

Hydrogen bonding in water under extreme confinement unveiled by nanoscale vibrational spectroscopy and simulations

Xintong Xu^{†1}, Xin Jin^{†2,3}, Matthias Kuehne⁴, De-Liang Bao², Joel Martis¹, Yu-Ming Tu⁴, Cody L. Ritt⁴, Juan Carlos Idrobo⁵, Michael S. Strano⁴, Arun Majumdar^{*1,6,7}, Sokrates T. Pantelides^{*2,8}, Jordan A. Hachtel^{*9}

[†]Equally Contributing First Authors

¹Department of Mechanical Engineering, Stanford University, Stanford, CA, USA

²Department of Physics and Astronomy, Vanderbilt University, Nashville, TN, USA

³University of the Chinese Academy of Sciences, Beijing 100049, China

⁴Department of Chemical Engineering, Massachusetts Institute of Technology, MA, USA

⁵Materials Science & Engineering, University of Washington, Seattle, WA, USA

⁶Precourt Institute for Energy, Stanford University, Stanford, CA, USA

⁷Department of Photon Science, SLAC National Laboratory, Menlo Park, CA, USA

⁸Department of Electrical and Computer Engineering, Vanderbilt University, Nashville, TN, USA

⁹Center for Nanophase Materials Sciences, Oak Ridge National Laboratory, Oak Ridge, TN, USA

*Correspondence to: arunava@stanford.edu

*Correspondence to: pantelides@vanderbilt.edu

*Correspondence to: hachtelja@ornl.gov

Notice: This manuscript has been authored by UT-Battelle, LLC, under Contract No. DE-AC0500OR22725 with the U.S. Department of Energy. The United States Government retains and the publisher, by accepting the article for publication, acknowledges that the United States Government retains a non-exclusive, paid-up, irrevocable, world-wide license to publish or reproduce the published form of this manuscript, or allow others to do so, for the United States Government purposes. The Department of Energy will provide public access to these results of federally sponsored research in accordance with the DOE Public Access Plan (<http://energy.gov/downloads/doe-public-access-plan>).

Fluids under extreme confinement exhibit distinctly new properties compared to their bulk analogs¹⁻⁵. Understanding the structure and intermolecular bonding of confined water lays the foundation for creating and improving applications at the water-energy nexus⁶⁻⁸. However, probing confined water experimentally at the length scale of intermolecular and surface forces has remained a challenge. Here, we report a combined experiment/theory framework to reveal changes in H-bonding environment and the underlying molecular structure of confined water inside individual carbon nanotubes. H-bonding is directly probed through the O-H stretch frequency with vibrational electron energy-loss spectroscopy and compared to spectra from molecular-dynamics simulations based on density-functional-theory. Experimental spectra show that water in larger carbon nanotubes exhibit the bonded O-H vibrations of bulk water, but at smaller diameters, the frequency blueshifts to near the ‘free’ O-H stretch found in water vapor and hydrophobic surfaces. The matching simulations reveal that, in addition to steric confinement, the tube’s vibrations play a key role in breaking up the H-bond network, resulting in an orientationally-dispersed, non-H-bonded phase. Furthermore, the temperature-dependence of the vibrations is investigated, providing insights into phase transitions and the confined-water density. This

research demonstrates the potential of the experiment/theory framework to explore unprecedented aspects of structure and bonding in confined fluids.

Introduction

Exotic behaviors in fluids emerge when they are under extreme confinement in nanoscale channels, cavities and porous media, whose length scales match the fundamental range of intermolecular and surface forces. Carbon nanotubes (CNTs) with atomically smooth inner surfaces and diameters in the range of 1-2 nm, resemble biological water channels, and give rise to significant enhancement of water transport, orders of magnitude faster than that in bulk¹⁻⁵. The anomalous behaviors rely on the structure of water confined water, which can be characterized by the hydrogen-bond (H-bond) network - a subtle interplay of localized bonding and long-range interactions, where the varied H-bond networks give rise to diverse phases of water layers at surfaces and interfaces⁹⁻¹¹. Deeper understanding of the complex structure of water in CNTs and the interactions of confined fluids with their bounding surfaces would facilitate new technologies at the water-energy nexus⁶⁻⁸.

Experimental examinations of the structure of water in CNTs has mostly been conducted with macroscopic optical and beam-line techniques on ensembles of CNTs with non-uniform diameters¹²⁻¹⁸. Even in experiments that leverage sparsity to isolate CNTs from one another¹⁹, the limited cross-section of the macroscopic beam with a single tube prevents direct analysis of water within. Transmission electron microscopy has been used to examine individual CNTs at high spatial resolution²⁰. However, given the mobile nature of liquid water and light atomic weight of H, directly imaging the H-bond network using electron microscopy is a major challenge.

As a result, molecular-dynamics (MD) simulations have been the primary method to access the atomic-scale structure and H-bond network information of water inside individual CNTs. The predicted structures demonstrate a strong dependence on the inner diameter; ranging from bulk-like water in large-diameter CNTs ($d > 2$ nm) to ordered ‘ice-tubes’ or disordered tubular structures in medium-diameter CNTs ($d \sim 1-2$ nm) to one-dimensional chains in small-diameter CNTs ($d < 1$ nm)^{12,15,21-30}. Both classical²¹ and density functional theory (DFT)-based²⁶ MD found that, in medium-diameter CNTs, water features vibrational modes at ~ 420 meV (‘bonded’ O-H stretch as in bulk water) and ~ 460 meV (‘free’ O-H stretch as found in water vapor³¹ and at hydrophobic interfaces⁹), where the primary difference between the two stretch modes is whether the H atom is bonded to a neighboring water molecule’s O atom. Early MD simulations in 2000, based on classical potentials³², led to the conclusion that the confinement drove the structural changes and that the CNT vibrations have minimal effects, leading to a large fraction of subsequent simulations employing rigid CNTs. While flexible CNTs have been more utilized in recent years, the focus on CNT vibrations has mainly been on their influence on transport^{27,33-35}. Possible effects of CNT vibrations on the confined-water H-bond network have not been addressed. Furthermore, the above

theoretical results have not been validated by experiments which can access the water vibrations of individual CNTs.

A spectroscopic option that matches the length scale of individual CNTs is vibrational electron energy-loss spectroscopy (vEELS) in the monochromated scanning transmission electron microscope (STEM). vEELS can currently attain energy resolution in the range of 3-4 meV ($25\text{-}30\text{ cm}^{-1}$)³⁶, while maintaining sub-nanometer spatial resolution³⁷, which allows us to directly measure molecular vibrations³⁸⁻⁴¹, including the O-H stretch of water⁴². Since *intermolecular* H \cdots O bonds mediate the vibrational frequency of the *intramolecular* O-H stretch¹⁰, the O-H stretch frequency is a natural probe of the H-bonding environment. Here, we combine vEELS with DFT-MD simulations to unveil the H-bonding and molecular structure of confined water. Our results show that the vibrational response is highly dependent on the diameter of CNTs, the vibrations of the CNT wall, the density of the water inside the tube, and the temperature of the system.

Visualizing Water in Individual CNTs with vEELS

A schematic of the vEELS experiments is shown in Fig. 1a. The CNTs are directly grown on SiN_x TEM grids with arrays of 200 nm holes by chemical vapor deposition (CVD). Afterwards, grown tubes are cut open by focused ion beam and placed in a humidifier to allow water infiltration (Supplementary Fig. S1). The CNTs are sparse, millimeters long, and cross the membrane in parallel, making them easy to identify and isolate, as shown in Fig. 1b. STEM reference images are acquired with a high-angle annular dark-field (HAADF) detector, shown in Fig. 1c, enabling

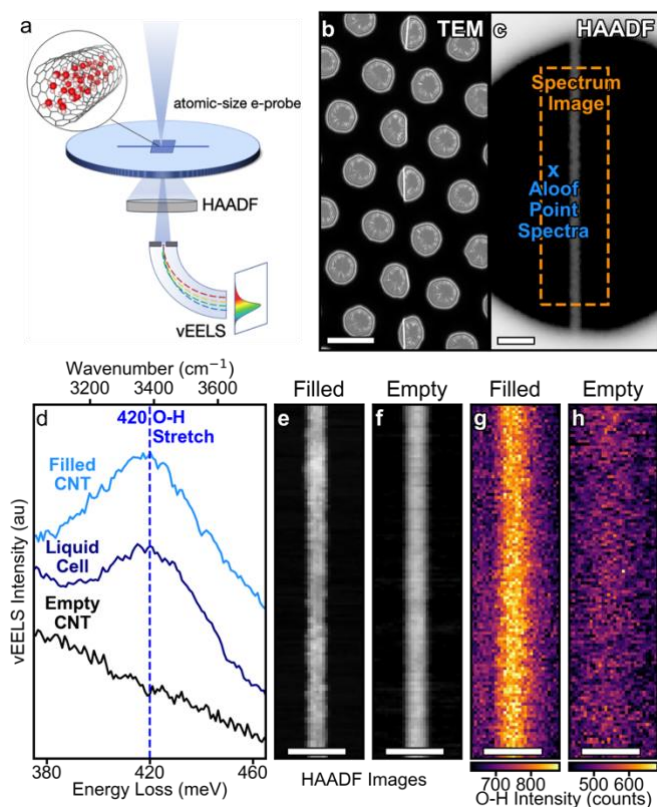


Fig. 1. Visualization of water confined in a single carbon nanotube. (a) Schematic of the vibrational electron energy-loss spectroscopy (vEELS) experimental setup. (b) Low-magnification TEM image of nanotubes on 200 nm diameter holey SiN grid. Scale bar is 500 nm. (c) HAADF image of a CNT. Annotations denote representative probe position for aloof point spectra acquisitions, and the scanned region for a spectrum. Scale bar – 50 nm. (d) Aloof vEEL spectra of a filled CNT (top), a bulk-water liquid cell (middle) and an empty CNT (bottom); the filled tube features a single peak at 420 meV that matches the peak of the bulk-water vEEL spectrum. (e-h) vEEL spectrum images of filled and empty tubes from (d). Scale bars – 20 nm. (e,f) HAADF images of filled (e) and empty (f) CNTs. (g,h) Spectrum image slices integrating the intensity of the O-H stretch vibrations (between 400 and 500 meV) for the filled (g) and empty (h) tubes, showing the clear spatial signature of water confined inside the tube.

precision control of the beam for vEELS acquisitions. To minimize beam damage, we primarily acquire ‘aloof’ point spectra, where the beam is placed closed to the sample (~ 30 nm), without directly intersecting it, and the vibrations are probed through the evanescent interactions⁴³. We also acquire spectrum images, where EEL spectra are acquired at each probe position in a 2D grid to create a full hyperspectral dataset, which enables the localization of the vibrations to be directly measured.

Figure 1d shows vEEL spectra from two different nominally water-filled CNTs compared with vEELS recorded from a bulk liquid cell. One CNT (bottom) appears empty, with no peak in the O-H stretch regime. However, the other CNT (top) shows a dominant peak at 420 meV, consistent in both linewidth and frequency to the bulk-water O-H stretch obtained from a liquid cell. The match verifies the existence of water in the CNT and demonstrates the capacity of vEELS to directly interrogate water vibrations in a confined CNT environment. Spectrum images are also acquired from the CNTs from Fig. 1d. The HAADF images are shown in Fig. 1e (filled) and Fig. 1f (empty) exhibiting no clear differences. By integrating the spectrum in each pixel between 400 and 500 meV (the O-H stretch regime), we can see in Fig. 1g that the filled tube lights up, while Fig. 1h shows that the empty tube has barely any variation from the background.

The Effect of Confinement and CNT Vibrations on H-Bonding

To explore the H-bonding of water under extreme confinement, we probed the frequency of O-H stretch modes in water-filled CNTs with different diameters. Figure 2a compares the room temperature (RT) vibrational spectra of water within CNTs with inner diameters (d) of 2.3 and 1.4 nm. TEM images of the tubes used to measure the inner diameters are shown in the Supplementary Fig. S2. The 2.3-nm-diameter CNT spectrum matches with the spectrum of bulk water, *i.e.*, a single vibrational peak at 420 meV (3400 cm^{-1}), while in the more confined system, namely the 1.4-nm-diameter CNT, the vibrational peak blueshifts to ~ 455 meV ($\sim 3700\text{ cm}^{-1}$). This is the frequency of the free O-H stretch which is observed in vapor and hydrophobic surfaces/interfaces^{9,31}. The domination of the vibrational response by the free O-H stretch shows that the water molecules are weakly or non-H-bonded, indicating the emergence of an unusual phase of confined water with an almost total disruption of the H-bond network.

The origin of this change in H-bonding can be revealed by comparisons with the vibrational densities of states (vDOS) generated by DFT-MD simulations. In Fig. 2b, we compare the vDOS of bulk water to that of water-filled-CNTs simulated under two conditions: one where the CNT wall is held rigid and one where the wall is free to vibrate during the MD run. To reduce computation costs, accurate DFT-MD simulations were performed for CNTs with a diameter of 1.1 nm. Select simulations for diameters of 1.4 nm verify that the results are essentially identical, as shown in Supplemental Fig. S3, indicating that the 1.1 nm diameter simulations are representative of the medium-diameter range, $d=1.1-1.4$ nm.

The computationally predicted bulk water vDOS (Fig. 2b top) is in excellent agreement with the experimental vEELS of bulk water and the 2.3 nm CNT. The vDOS of the rigid CNT displays a sharp high-frequency peak at ~ 460 meV while retaining a broad peak at 420 meV (Fig. 2b middle), corresponding to free and bonded O-H respectively. This result is consistent with previous reports^{21,26}, which found that the steric constraints of a rigid hydrophobic CNT produce a partial breakdown of the H-bond network that causes the emergence of the free O-H stretch. On the other hand, when the vibrations of the CNT walls are included, the vDOS exhibits a single broad peak at ~ 455 meV (Fig 2b bottom) in full accord with the experimental vEELS. We note that the vEELS energy-resolution (~ 8.5 meV) is demonstrably sufficient to distinguish between the two spectra shown in Fig. 2b (Supplemental Fig. S4).

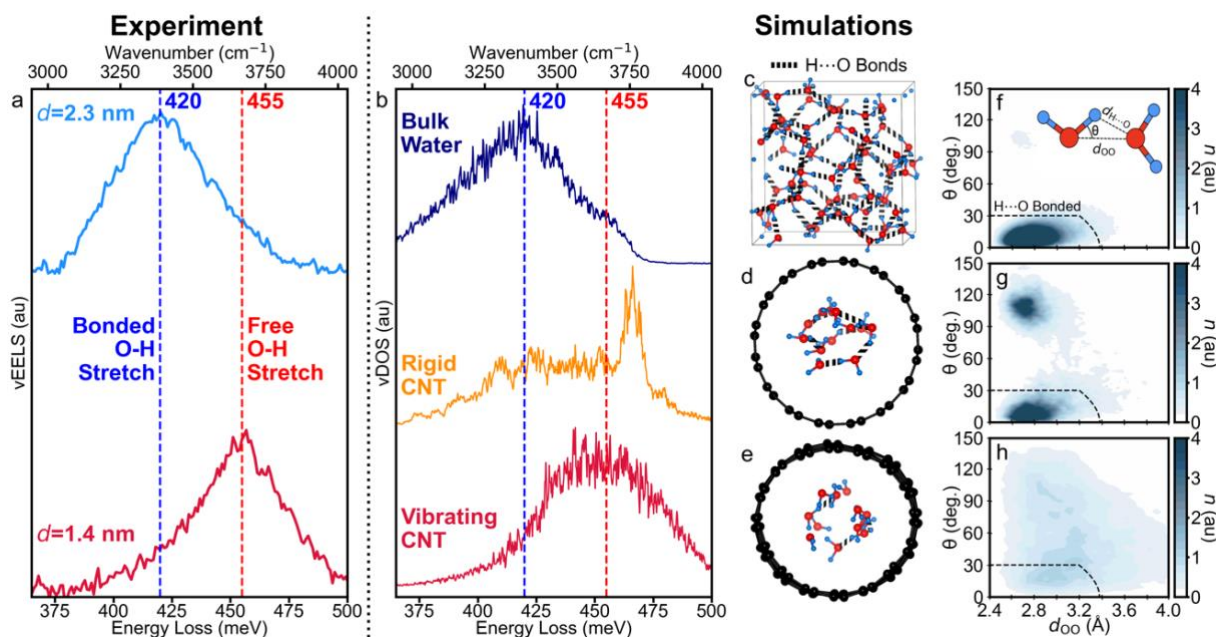


Figure 2. Vibrational properties and hydrogen bonding of water confined in medium diameter CNTs. (a) vEEL spectra from tubes with different inner diameters: 2.3 nm – top (same as Fig. 1) and 1.4 nm – bottom. The larger tube exhibits the ‘bonded’ O-H stretch, i.e., the O-H \cdots O stretch at 420 meV (3400 cm^{-1}) while the smaller tube exhibits ‘free’ O-H stretch frequency 455 meV (3670 cm^{-1}). (b) Calculated vibrational densities of states (vDOS): bulk water (top), water in a rigid-walled tube CNT (middle), and water in a vibrating-walled CNT (bottom). Both simulated CNTs have an inner diameter of 1.1 nm which is representative of medium diameter CNTs, $d=1.1$ -1.4 nm. (c-e) DFT-MD snapshots for the bulk water (c), rigid CNT (d) and vibrating CNT (e) in (b). Here, the intermolecular H \cdots O bonds are highlighted with black dotted lines, showing that the vibrating tube results in near-total elimination of H \cdots O bonds. (f-g) d_{OO} vs. θ heatmaps corresponding to the relative distances and orientations of water molecules throughout the simulations. Dashed line indicates region where H \cdots O bonding occurs, corresponding to $\theta < 30^\circ$ and $d_{\text{H}\cdots\text{O}} < 2.4 \text{ \AA}$. The quantities d_{OO} and θ are defined as the nearest neighbor O distances and H-bond angles, as indicated in the schematic in the inset of (f). All experiments and simulations at 300 K.

The molecular structure that corresponds to the vDOS of the vibrating CNT can now be extracted from the atomic positions in the MD simulations, highlighted in Figs. 2c-h. Representative snapshots of the MD simulations for vDOS in Fig. 2b are shown for bulk water, a rigid CNT, and a vibrating CNT in Figs. 2c-e, respectively. Here, intermolecular H \cdots O bonds are marked with

dark dotted lines when the H \cdots O distance is less than 2.4 Å and the bond angle (as defined on the inset in Fig. 2f) is less than 30°³². In the rigid CNT snapshot, Fig. 2d, we can see that, while the H-bond network is less ubiquitous compared to bulk water (Fig 2c), a large fraction of the molecules are still H-bonded and many of the non-H-bonded molecules are oriented towards the CNT wall. However, in the vibrating CNT snapshot, Fig. 2e, there are hardly any H \cdots O bonds, indicating a near-total disruption of the H-bond network.

For better visualization, statistical heatmaps of the hydrogen bonding throughout the course of each MD simulation are shown in Fig. 2f-h, for bulk water, the rigid CNT, and the vibrating CNT respectively. To generate the heatmap, in every snapshot of the MD simulations, we identify the first (intramolecular) and second (intermolecular) O neighbor of every H atom and measure this OO distance (d_{OO}) and the tilt angle of the H atom to this line (see the inset in Fig. 2f). The heatmap of bulk water has an average d_{OO} of 2.7 ± 0.3 Å and θ of $10^\circ\pm 5^\circ$. The heatmap of the rigid CNT shows a bimodal distribution, with a mixture of molecules with O-H in the bonded configuration, as in bulk water, and a group with O-H in a fundamentally different orientation, where d_{OO} is still less than 3 Å but now the bond angles are also between 90° and 120°. These orientations are consistent with molecules oriented towards the CNT wall, as seen in the rigid-CNT snapshot in Fig. 2d. In the heatmap of the vibrating CNT, on the other hand, the statistical distributions in d_{OO} and θ are broad, extending well past 3 Å and populating all angles between 0° and 120°, *i.e.*, the molecular orientations are relatively evenly and randomly spread throughout the angle/distance parameter space. The agreement between the experimental vEELS and simulated vDOS for the vibrating CNT suggests that the single broad peak observed at ~455 meV, along with the disruptions in the H-bond network observed in the MD simulations, correspond to an unusual new phase of water we term ‘non-H-bonded water’. Furthermore, the lack of agreement between the experimental vEELS and simulated vDOS for the rigid CNT demonstrates that the vibrations of the tube are critical to achieving this non-H-bonded phase. The vibrations further equalize the energy between water molecules and breaks the H bond network through water-wall interactions.

MD simulations were performed for water densities ranging from $\rho = 0.5$ to 1.5 g/cm³. They show that the non-H-bonded phase occurs for all densities if the CNT carbon atoms are allowed to vibrate, while the bimodal bonding phase occurs for all densities if the CNT is held rigid. Extensive tests using best-of-breed DFT functionals further confirmed the robustness of the results (see Methods). The complete results for vDOS, MD snapshots, and heatmaps for all densities and functionals, and both rigid and vibrating CNTs are shown in Supplementary Figs. S5-S12. While all densities produce similar results at 300 K significant variations are observed between densities at 100 K, which will be expanded upon in the following section. The vDOS in the above figure (Fig. 2b-h) shows representative results for $\rho = 0.5$ g/cm³, which we will show exhibits the best spectral match to vEELS on the 1.4 nm diameter CNT at 100 K in the following section.

Temperature-Dependent Response of Confined Fluids

For water under extreme confinement, subtle changes in the competition between molecule-wall and molecule-molecule interactions can fundamentally change the phase diagram since they are of comparable strengths in these systems. This competition opens many possibilities of variations in the H-bond network and of numerous phases of water and ice⁴⁴. Here we report initial vEELS at 100 K for the 1.4-nm-diameter and 2.3-nm-diameter CNTs that we studied at room temperature (Fig. 2) and select MD simulations that apply to these cases.

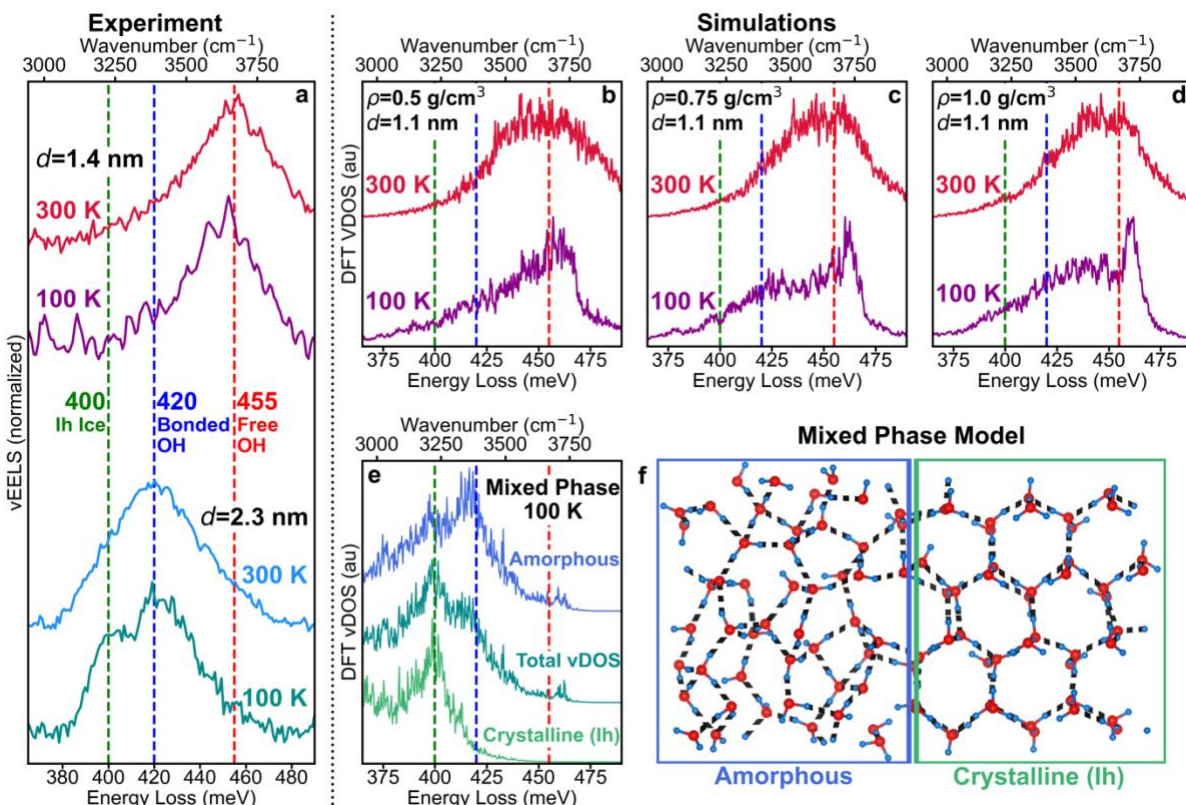


Fig. 3. Vibrational response at cryogenic and room temperature in filled CNTs. (a) vEEL spectra at 300 K and 100 K for the 1.4-nm-diameter CNT (top) and 2.3-nm-diameter CNT (bottom). (b-d) Calculated vibrational densities of states (vDOS) at 300 K (top) and 100 K (bottom) for medium diameter CNTs ($d=1.1$ nm) with water densities of $\rho=0.5$ g/cm³ (b), 0.75 g/cm³ (c), and 1.0 g/cm³ (d), demonstrating the evolution of the vibrational spectrum of water in medium-diameter tubes as a function of water density. (e,f) vDOS for a mixed ice model composed of amorphous and crystalline regions. vDOS for amorphous region (top), total supercell (center), and crystalline region (bottom) in (e), supercell used for calculation with amorphous and crystalline regions marked in (f).

The vEEL spectra were taken by lowering the temperature from 300 K to 100 K with a cryogenic STEM holder. The vEEL spectra are plotted in Fig. 3a. They show that the 1.4-nm-diameter CNT undergoes no significant change in peak frequency or lineshape, while the 2.3-nm-diameter CNT exhibits a secondary peak at 400 meV that emerges only at cryogenic temperatures. The change also appears to be reversible, as the vEEL spectrum acquired upon returning to room temperature does not exhibit the 400 meV peak (shown in Supplementary Figure S13). These observations

indicate that, for the smaller-diameter CNT, the non-H-bonded water phase from the RT measurements in Fig. 2 appears to persist to 100 K, while for the higher diameter CNT, water undergoes a partial phase transition. Similar effects have been observed in nano-droplets and mesoporous membranes, and the Raman spectra of filled CNTs, where reformation of the H-bond network is suppressed when lowering temperature for small droplet diameters and pore sizes^{19,45,46}.

For the smaller-diameter CNT, we performed MD simulations for several water densities, since it impacts the ratio of molecule-wall and molecule-molecule interactions and hence influence the temperature-dependence of the system. The vDOS for the 1.1-nm-diameter CNT is shown for three different water densities (0.5, 0.75, and 1.0 g/cm³) at both 300 K and 100 K in Figs 3b-d. As already mentioned at the end of the previous section, at 300 K, the vDOS for all three water densities are qualitatively quite similar, but at 100 K, the vDOS of the two higher water densities transform from the non-H-bonded water phase to the bimodal line-shape of water in rigid CNTs (see Supplementary Fig. S5). The MD snapshots and heatmaps for these densities at 100 K also exhibit a strong match to the 300 K rigid CNT simulations (see Supplementary Figs. S6-S7), indicating that structure strongly matches the mixed-bonding water phase. Conversely, for the lowest water density (0.5 g/cm³) at 100 K, the confined water remains in the non-H-bonded phase, resulting in a single-peak vDOS that agrees with the vEELS in Fig. 3a. The MD simulations demonstrate that the density-dependent evolution of the vibrational response reveals itself at cryogenic temperatures, which, in conjunction with vEELS, can potentially be a mechanism to measure density in confined fluids (see Supplementary Fig. S14).

For the 2.3-nm-diameter CNT, we note that the emergent peak at 400 meV is consistent with the Ih phase of ice with tetrahedrally-coordinated molecules¹² and that vEELS experiments on bulk amorphous ice have shown vibrations at 420 meV⁴⁷. A combination of different phases of ice would naturally lead to the combined peaks at 400 and 420 meV as we observed here in vEELS. Moreover, previous predictions have indicated that different phases of ice with different average H-bond numbers can exist simultaneously inside layered nanotube-ice⁴⁸. To visualize this effect, the vDOS at 100 K of a mixed ice supercell is calculated and shown in Fig. 3e, with the schematic of the supercell in Fig. 3f. The projected vDOS from the amorphous region (top) exhibits a broad peak with its maximum intensity at 420 meV while the crystalline region (bottom) exhibits a sharp peak at 400 meV. As a result, the total vDOS (center) features both peaks, albeit with a different ratio of intensities on the two peaks, demonstrating that the experiment is consistent with a transition to a phase of ice with a mixed and complex H-bond network.

We note that in a repeat experiment, we observed a qualitatively similar, but far less pronounced, phase change signature in a 4.2 nm-diameter CNT. The repeat experiment as well as additional discussion on the advantages and limitations of the present analysis are included in Supplementary Discussion 2.

Our results reveal how the H-bonding and structures of confined water change with the unexpected effects of CNT wall vibrations, along with the size-, temperature- and density-dependence, as they synergistically alter the competition of molecule-molecule and molecule-wall interactions. The powerful combination of high-energy/spatial-resolution vEELS experiments with cryo capabilities and DFT-MD simulations can reveal the likely organization as well as intermolecular and surface interactions of confined liquids, thus offering the promising prospects of new scientific advances in multiple disciplines.

Acknowledgments

This research was supported as part of the Center for Enhanced Nanofluidic Transport (CENT), an Energy Frontier Research Center funded by the U.S. Department of Energy (DOE), Office of Science, Basic Energy Sciences (BES), under Award # DE-SC0019112. Vibrational EELS research was supported by the Center for Nanophase Materials Sciences, (CNMS), which is a DOE Office of Science User Facility using instrumentation within ORNL's Materials Characterization Core provided by UT-Battelle, LLC, under Contract No. DE-AC05-00OR22725 with the DOE and sponsored by the Laboratory Directed Research and Development Program of Oak Ridge National Laboratory, managed by UT-Battelle, LLC, for the U.S. Department of Energy. Theoretical work at Vanderbilt University (X. J., D.-L. B., S. T. P.) was supported by the U.S. Department of Energy Office of Science, Basic Energy Sciences, Materials Science and Engineering Directorate Grant No. DE-FG02-09ER46554 and by the McMinn Endowment. X. J. is partially supported by the Fundamental Research Funds for the Central Universities. Computations were carried out in part at the National Energy Research Scientific Computer Center (NERSC), a U.S. Department of Energy Office of Science User Facility located at Lawrence Berkeley National Laboratory, operated under contract no. DE-AC02-05CH11231 and in part at the Beijing Three Axis Space Technology Co. Ltd. This work was led equally by Stanford University, Vanderbilt University and Oak Ridge National Laboratory.

Author Contributions

Experiments were conceived of and designed by XX, JCI, AM, and JAH. VEELS data was acquired and analyzed by XX and JAH with guidance from JM and AM. DFT calculations were conducted by XJ with guidance from DLB and STP. Samples were synthesized and prepared by XX, MK, YMT, CLR, and MSS. Manuscript and supplementary materials were written by XX, XJ, STP, and JAH. All authors contributed to the editing and revision of the manuscript.

Competing Interests Statement

The authors declare no competing interests.

Supplementary Information

Supplementary Information is available for this paper.

Correspondence

Correspondence and requests for materials should be addressed to arunava@stanford.edu, pantelides@vanderbilt.edu, or hachtelja@ornl.gov.

References

1. Hummer, G., Rasaiah, J. C. & Noworyta, J. P. Water conduction through the hydrophobic channel of a carbon nanotube. *Nature* **414**, 188–190 (2001).
2. Majumder, M., Chopra, N., Andrews, R. & Hinds, B. J. Enhanced flow in carbon nanotubes. *Nature* **438**, 44–44 (2005).
3. Holt, J. K. *et al.* Fast Mass Transport Through Sub-2-Nanometer Carbon Nanotubes. *Science* **312**, 1034–1037 (2006).
4. Secchi, E. *et al.* Massive radius-dependent flow slippage in carbon nanotubes. *Nature* **537**, 210–213 (2016).
5. Tunuguntla, R. H. *et al.* Enhanced water permeability and tunable ion selectivity in subnanometer carbon nanotube porins. *Science* **357**, 792–796 (2017).
6. Faucher, S. *et al.* Critical Knowledge Gaps in Mass Transport through Single-Digit Nanopores: A Review and Perspective. *J. Phys. Chem. C* **123**, 21309–21326 (2019).
7. Bocquet, L. Nanofluidics coming of age. *Nat. Mater.* **19**, 254–256 (2020).
8. Aluru, N. R. *et al.* Fluids and Electrolytes under Confinement in Single-Digit Nanopores. *Chem. Rev.* **123**, 2737–2831 (2023).
9. Scatena, L. F., Brown, M. G. & Richmond, G. L. Water at Hydrophobic Surfaces: Weak Hydrogen Bonding and Strong Orientation Effects. *Science* **292**, 908–912 (2001).
10. Montenegro, A. *et al.* Asymmetric response of interfacial water to applied electric fields. *Nature* **594**, 62–65 (2021).
11. Kapil, V. *et al.* The first-principles phase diagram of monolayer nanoconfined water. *Nature* **609**, 512–516 (2022).
12. Kolesnikov, A. I. *et al.* Anomalously Soft Dynamics of Water in a Nanotube: A Revelation of Nanoscale Confinement. *Phys. Rev. Lett.* **93**, 035503 (2004).
13. Maniwa, Y. *et al.* Ordered water inside carbon nanotubes: formation of pentagonal to octagonal ice-nanotubes. *Chemical Physics Letters* **401**, 534–538 (2005).
14. Matsuda, K., Hibi, T., Kadowaki, H., Kataura, H. & Maniwa, Y. Water dynamics inside single-wall carbon nanotubes: NMR observations. *Phys. Rev. B* **74**, 073415 (2006).
15. Byl, O. *et al.* Unusual Hydrogen Bonding in Water-Filled Carbon Nanotubes. *J. Am. Chem. Soc.* **128**, 12090–12097 (2006).
16. Kyakuno, H. *et al.* Confined water inside single-walled carbon nanotubes: Global phase diagram and effect of finite length. *The Journal of Chemical Physics* **134**, 244501 (2011).
17. Ohba, T. Size-Dependent Water Structures in Carbon Nanotubes. *Angewandte Chemie International Edition* **53**, 8032–8036 (2014).
18. Dalla Bernardina, S. *et al.* Water in Carbon Nanotubes: The Peculiar Hydrogen Bond Network Revealed by Infrared Spectroscopy. *J. Am. Chem. Soc.* **138**, 10437–10443 (2016).
19. Agrawal, K. V., Shimizu, S., Draushuk, L. W., Kilcoyne, D. & Strano, M. S. Observation of extreme phase transition temperatures of water confined inside isolated carbon nanotubes. *Nature Nanotech* **12**, 267–273 (2017).

20. Ye, H., Naguib, N. & Gogotsi, Y. TEM Study of Water in Carbon Nanotubes. *JEOL News* **39**, 38–43 (2004).
21. Martí, J. & Gordillo, M. C. Effects of confinement on the vibrational spectra of liquid water adsorbed in carbon nanotubes. *Phys. Rev. B* **63**, 165430 (2001).
22. Koga, K., Gao, G. T., Tanaka, H. & Zeng, X. C. Formation of ordered ice nanotubes inside carbon nanotubes. *Nature* **412**, 802–805 (2001).
23. Mashl, R. J., Joseph, S., Aluru, N. R. & Jakobsson, E. Anomalous Immobilized Water: A New Water Phase Induced by Confinement in Nanotubes. *Nano Lett.* **3**, 589–592 (2003).
24. Wang, J., Zhu, Y., Zhou, J. & Lu, X.-H. Diameter and helicity effects on static properties of water molecules confined in carbon nanotubes. *Phys. Chem. Chem. Phys.* **6**, 829–835 (2004).
25. Souza, N. R. de, Kolesnikov, A. I., Burnham, C. J. & Loong, C.-K. Structure and dynamics of water confined in single-wall carbon nanotubes. *J. Phys.: Condens. Matter* **18**, S2321 (2006).
26. Cicero, G., Grossman, J. C., Schwegler, E., Gygi, F. & Galli, G. Water Confined in Nanotubes and between Graphene Sheets: A First Principle Study. *J. Am. Chem. Soc.* **130**, 1871–1878 (2008).
27. Thomas, J. A. & McGaughey, A. J. H. Water Flow in Carbon Nanotubes: Transition to Subcontinuum Transport. *Phys. Rev. Lett.* **102**, 184502 (2009).
28. Pascal, T. A., Goddard, W. A. & Jung, Y. Entropy and the driving force for the filling of carbon nanotubes with water. *Proceedings of the National Academy of Sciences* **108**, 11794–11798 (2011).
29. Liang, C., Rayabharam, A. & Aluru, N. R. Structural and Dynamical Properties of H₂O and D₂O under Confinement. *J. Phys. Chem. B* **127**, 6532–6542 (2023).
30. Calegari Andrade, M. F. & Pham, T. A. Probing Confinement Effects on the Infrared Spectra of Water with Deep Potential Molecular Dynamics Simulations. *J. Phys. Chem. Lett.* **14**, 5560–5566 (2023).
31. Darling, B. T. & Dennison, D. M. The Water Vapor Molecule. *Phys. Rev.* **57**, 128–139 (1940).
32. Gordillo, M. C. & Martí, J. Hydrogen bond structure of liquid water confined in nanotubes. *Chemical Physics Letters* **329**, 341–345 (2000).
33. Alexiadis, A. & Kassinos, S. Influence of water model and nanotube rigidity on the density of water in carbon nanotubes. *Chemical Engineering Science* **63**, 2793–2797 (2008).
34. Joseph, S. & Aluru, N. R. Why Are Carbon Nanotubes Fast Transporters of Water? *Nano Lett.* **8**, 452–458 (2008).
35. Tao, J., Song, X., Zhao, T., Zhao, S. & Liu, H. Confinement effect on water transport in CNT membranes. *Chemical Engineering Science* **192**, 1252–1259 (2018).
36. Krivanek, O. L. *et al.* Progress in ultrahigh energy resolution EELS. *Ultramicroscopy* **203**, 60–67 (2019).
37. Hage, F. S., Kepaptsoglou, D. M., Ramasse, Q. M. & Allen, L. J. Phonon Spectroscopy at Atomic Resolution. *Phys. Rev. Lett.* **122**, 016103 (2019).
38. Rez, P. *et al.* Damage-free vibrational spectroscopy of biological materials in the electron microscope. *Nature Communications* **7**, 10945 (2016).
39. Haiber, D. M. & Crozier, P. A. Nanoscale Probing of Local Hydrogen Heterogeneity in Disordered Carbon Nitrides with Vibrational Electron Energy-Loss Spectroscopy. *ACS Nano* **12**, 5463–5472 (2018).
40. Hachtel, J. A. *et al.* Identification of site-specific isotopic labels by vibrational spectroscopy in the electron microscope. *Science* **363**, 525–528 (2019).

41. Hachtel, J. A. *et al.* A New Path to Nanoscale Cellular Analysis with Monochromated Electron Energy-Loss Spectroscopy. Preprint at <https://doi.org/10.48550/arXiv.2206.04191> (2022).
42. Jokisaari, J. R. *et al.* Vibrational Spectroscopy of Water with High Spatial Resolution. *Advanced Materials* **30**, 1802702 (2018).
43. Crozier, P. A. Vibrational and valence aloof beam EELS: A potential tool for nondestructive characterization of nanoparticle surfaces. *Ultramicroscopy* **180**, 104–114 (2017).
44. Travalloni, L., Castier, M., Tavares, F. W. & Sandler, S. I. Critical behavior of pure confined fluids from an extension of the van der Waals equation of state. *The Journal of Supercritical Fluids* **55**, 455–461 (2010).
45. Hudait, A. & Molinero, V. Ice Crystallization in Ultrafine Water–Salt Aerosols: Nucleation, Ice-Solution Equilibrium, and Internal Structure. *J. Am. Chem. Soc.* **136**, 8081–8093 (2014).
46. Malfait, B. *et al.* Structure of Water at Hydrophilic and Hydrophobic Interfaces: Raman Spectroscopy of Water Confined in Periodic Mesoporous (Organo)Silicas. *J. Phys. Chem. C* **126**, 3520–3531 (2022).
47. Krivanek, O. L. *et al.* Probing Biological Materials by Vibrational Analysis in the Electron Microscope. *Microscopy and Microanalysis* **28**, 1196–1197 (2022).
48. Takaiwa, D., Hatano, I., Koga, K. & Tanaka, H. Phase diagram of water in carbon nanotubes. *Proceedings of the National Academy of Sciences* **105**, 39–43 (2008).

Methods

Sample Preparation: SiN_x liquid cells were K-kit (Silicon-based Micro Channel Device) purchased from Electron Microscopy Sciences (EMS) with membrane thickness of 30 nm and gap height of 100 nm. The liquid cells were opened, filled with DI water, and sealed with TorrSeal following the instructions provided by EMS. CNTs were directly grown as described previously¹ except on holey SiN_x TEM grids (500 nm or 200 nm pore (21583-10 or 21586-10 respectively, TED Pella) using a low gas flow variant² of a chemical vapor deposition (CVD) method that results in a sparse array of gas flow-aligned ultralong CNTs³. For this work, CH₄ was utilized as a carbon precursor and iron particles contained in 25 Series APT Carbon Nanotubes from Nano-C were used as catalysts. For this, a CNT dispersion is produced as described elsewhere⁴, then drop cast onto the upstream side of the growth substrate. Substrates were placed in a tube furnace during growth in a manner such that the catalyst was located upstream of the holey SiN_x membrane so that the synthesized ultralong CNTs cross the TEM grid and suspended across its windows. After CVD synthesis, the CNTs were then subjected to a previously introduced Focused Ion Beam (FIB) cutting procedure to induce CNT opening^{5,6}. Briefly, the focused Ga⁺ beam of a dual beam FIB/scanning electron microscope (FEI Helios Nanolab 600) is used to cut the ultralong CNTs between the catalyst and TEM window and once beyond the same window. We use the following FIB patterning parameters: 9 pA, 30 kV, 100 passes, 5 μs dwell time, and 4 nm pitch. Any exposure of the membrane-supported CNT segments in between the two cut locations to electron or ion beams was carefully avoided. The CNTs were then transported and exposed to above 99% RH conditions in a custom-built humidity chamber (Supplementary Fig. S1a) using an ultrasonic humidifier as a standardized water filling process. We subsequently applied TorrSeal (Agilent Technologies) to the two FIB-cut regions of the sample (Supplementary Fig. S1b), again avoiding

the region between, as a CNT sealing method. Distinctive, temperature dependent Raman RBM trajectories were observed for CNTs before and after the water filling process, as described elsewhere⁶.

Transmission Electron Microscopy: TEM images were acquired on an FEI Titan 80-300 environmental transmission electron microscope operated at 80 kV, with an aberration corrector for the objective lens tuned before each session. The electron dose rate during HRTEM image acquisitions was measured at $\sim 300 \text{ e}^-/\text{\AA}^2/\text{s}$. TEM images were analyzed using GATAN DigitalMicrograph and ImageJ software.

Vibrational Electron Energy Loss Spectroscopy: The vibrational EELS in this manuscript is acquired with the Nion high energy-resolution monochromated EELS-STEM (HERMES) located at Oak Ridge National Laboratory. The spectra shown here are acquired from different experimental sessions, operating at both 60 kV and 30 kV accelerating voltages. However, the 1.4-nm-diameter CNT and the 2.3-nm-diameter CNT are acquired from the same sample during the same session (accelerating voltage 60 kV) to insure minimum experimental variance. All spectra acquired with a convergence angle of 30 mrad and a collection angle of 25 mrad. Energy resolutions for these acquisitions varied from 8-15 meV. The beam current for these experiments monochromation is approximately 4 pA, and while acquiring reference images to prepare spectrum images or point spectra, dwell times are kept extremely low to minimize sample irradiation. Due to the presence of the combination bands, we focus exclusively on the region between 350 meV and 500 meV to highlight the behavior of the O-H stretching. Bands of vibrations both below and above the O-H stretch are observed in the filled CNT system that are not present in the bulk-water liquid cell measurements or the empty CNT that we assign to combination bands, as explained in Supplementary Discussion 1. Also due to the presence of combination bands and the conductive continuum present in the spectra, a number of different background normalization methodologies are implied. Full details and validation of all background subtraction and quantitative normalization methodologies, as well as the energy resolution of each spectrum and spectrum image shown in this manuscript is tabulated in Supplementary Discussion 3. All experiments are conducted in ultrahigh vacuum which minimizes ice build up during cryo-experiments. The lack of ice-like peaks in the 1.4-nm-diameter CNT cryo experiment shown in Fig. 3a serves as proof that ice is not building up significantly during the experiments.

DFT calculations: We performed density-functional-theory molecular-dynamics (DFT-MD) simulations for water confined in carbon nanotube (CNT) using the Vienna ab initio simulation package (VASP)⁷⁻⁹ and the projected augmented wave (PAW) method^{10,11}. The exchange-correlation functional for electrons was described by the generalized gradient approximation (GGA) in the Perdew-Burke-Ernzerhof (PBE) form¹² and the Grimme D3 method was included to describe van der Waals (vdW) interactions¹³. The PBE-D3 functional has been validated as

showing very good performance in describing the water-water and water-CNT interactions while keeping a reasonable computational-resources cost^{14,15}.

It is known that for water, the DFT description of properties is affected by the choice of functional. To further assess the effects of the functional choice on our key results, we also calculated the vDOS and d_{00}/θ heatmap of water/CNT (water density $\rho=0.5$ g/cm³, CNT diameter 1.1 nm) using two additional functionals: PBE-D4, which uses the Gimme D4 version of the van der Waals contribution, and TPSS-D4, which is a computationally expensive meta-GGA functional. The three functionals have previously been found to be the best-performing functionals for water/CNT systems within each functional class^{14,15}. The calculated room-temperature vDOS and d_{00}/θ heatmaps using the three different functionals are very similar to each other, as shown in Supplementary Fig. S12 and S15, demonstrating the effectiveness of the PBE-D3 functional for our purposes. Additionally, the low-temperature (100 K) vDOS and d_{00}/θ heatmaps of water/CNT at different water densities ($\rho=0.4, 0.45,$ and 0.5 g/cm³) were also calculated using PBE-D3 and TPSS-D4 functionals (PBE-D4 always gives the same results as the PBE-D3). As shown in Supplementary Fig. S15a, at $\rho=0.5$ g/cm³, the TPSS-D4-calculated vDOS exhibits two peaks, differing from the PBE-D3 vDOS and the cryo-vEELS. However, when the density is further decreased to 0.45 g/cm³ or lower (Supplementary Fig. S15b, c), the vDOS calculated by PBE-D3 and TPSS-D4 are quite similar and consistent with the cryogenic experiment.

The plane-wave cutoff was set as 400 eV and a Γ -centered ($1\times 1\times 1$) k-mesh was applied for all the calculations. A (8,8) single-walled CNT (diameter 1.1 nm) with length of 1.9 nm was used to simulate the medium-diameter CNT used in experiments, while other cases, including a (10, 10) single-walled CNT (diameter 1.4 nm) and a (8,8)@(13,13) double-walled CNT (outer diameter 1.7 nm) were also studied to check the effect of CNT diameter and outer wall. The effect of the CNT length on the confined water VDOS was also checked and found there very little different between the VDOS calculated by 1.9 and 2.9 nm long CNT, as shown in Fig. S16. Periodic boundary conditions were applied along the axis-direction (z -direction), while a vacuum distance larger than 10 Å was set along the in-plane direction to separate the periodic neighbor.

The density of water in a CNT is defined as the ratio of the mass of water molecules and the volume of the CNT, estimated by removing a 2-Å-wide shell from the CNT radius defined by the carbon nuclei. In order to control the computational costs, we used a fixed CNT length (see above) and controlled the water density by changing the number of molecules. Water densities of 1.5, 1.0, 0.75 and 0.5 g/cm³ cases, were studied by including 36, 24, 18 and 12 water molecules into the (8,8) CNT, where the initial configurations of water molecules were random. In the case of 12 water molecules, we tested the statistical accuracy of the number by performing simulations for 18 molecules in a CNT that was 1.5 times longer.

Then 10 ps DFT-MD simulations with time step of 0.5 fs were performed at both 300 K and 100 K using the Nosé algorithm^{16,17}, for both rigid-CNT and vibrating-CNT cases. The vibrational densities of states of the confined water were obtained through Fourier transform of the velocity

autocorrelation function^{18,19} of the H and O atoms by using VASPKIT²⁰. The frequency and d_{oo}/θ heatmap was calculated by taking two water molecules as a model, as shown schematically in Supplementary Fig. S7m (top panel), where only the H atom between the two O atoms was allowed to vibrate, while other atoms were kept fixed.

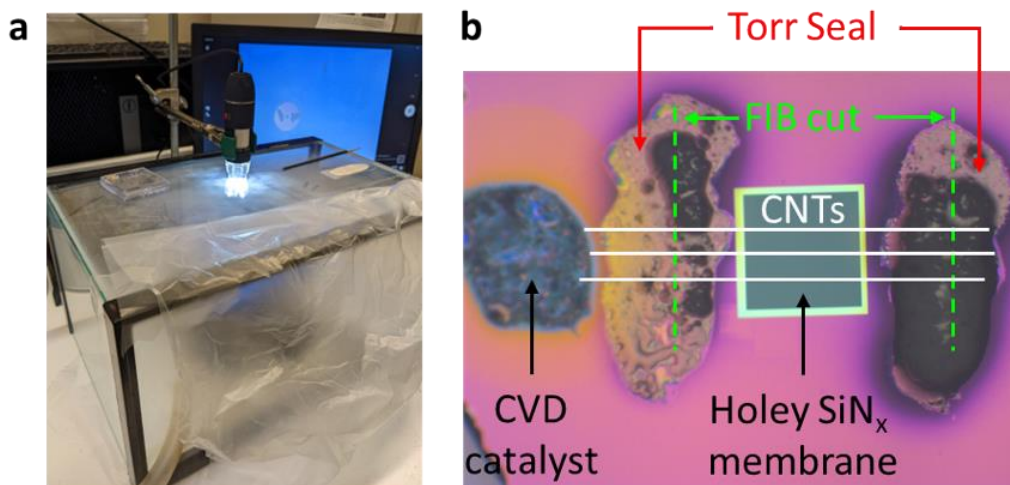
Methods References

1. Agrawal, K. V., Shimizu, S., Drahushuk, L. W., Kilcoyne, D. & Strano, M. S. Observation of extreme phase transition temperatures of water confined inside isolated carbon nanotubes. *Nature Nanotech* **12**, 267–273 (2017).
2. Jin, Z. *et al.* Ultralow Feeding Gas Flow Guiding Growth of Large-Scale Horizontally Aligned Single-Walled Carbon Nanotube Arrays. *Nano Lett.* **7**, 2073–2079 (2007).
3. Huang, S., Cai, X. & Liu, J. Growth of Millimeter-Long and Horizontally Aligned Single-Walled Carbon Nanotubes on Flat Substrates. *J. Am. Chem. Soc.* **125**, 5636–5637 (2003).
4. Jain, R. M. *et al.* Polymer-Free Near-Infrared Photovoltaics with Single Chirality (6,5) Semiconducting Carbon Nanotube Active Layers. *Advanced Materials* **24**, 4436–4439 (2012).
5. Kuehne, M. *et al.* Impedance of Thermal Conduction from Nanoconfined Water in Carbon Nanotube Single-Digit Nanopores. *J. Phys. Chem. C* **125**, 25717–25728 (2021).
6. Faucher, S. *et al.* Observation and Isochoric Thermodynamic Analysis of Partially Water-Filled 1.32 and 1.45 nm Diameter Carbon Nanotubes. *Nano Lett.* **23**, 389–397 (2023).
7. Kresse, G. & Furthmüller, J. Efficiency of ab-initio total energy calculations for metals and semiconductors using a plane-wave basis set. *Computational Materials Science* **6**, 15–50 (1996).
8. Kresse, G. & Hafner, J. Ab initio molecular dynamics for liquid metals. *Phys. Rev. B* **47**, 558–561 (1993).
9. Kresse, G. & Hafner, J. Ab initio molecular dynamics for open-shell transition metals. *Phys. Rev. B* **48**, 13115–13118 (1993).
10. Blochl, P. E. Projector Augmented-Wave Method. *Phys. Rev. B* **50**, 17953–17979 (1994).
11. Kresse, G. & Joubert, D. From ultrasoft pseudopotentials to the projector augmented-wave method. *Phys. Rev. B* **59**, 1758–1775 (1999).
12. Perdew, J. P., Burke, K. & Ernzerhof, M. Generalized Gradient Approximation Made Simple. *Phys. Rev. Lett.* **77**, 3865–3868 (1996).
13. Grimme, S., Antony, J., Ehrlich, S. & Krieg, H. A consistent and accurate ab initio parametrization of density functional dispersion correction (DFT-D) for the 94 elements H-Pu. *The Journal of Chemical Physics* **132**, 154104 (2010).
14. Gillan, M. J., Alfè, D. & Michaelides, A. Perspective: How good is DFT for water? *The Journal of Chemical Physics* **144**, 130901 (2016).
15. Brandenburg, J. G., Zen, A., Alfè, D. & Michaelides, A. Interaction between water and carbon nanostructures: How good are current density functional approximations? *The Journal of Chemical Physics* **151**, 164702 (2019).
16. Nosé, S. A molecular dynamics method for simulations in the canonical ensemble. *Molecular Physics* **52**, 255–268 (1984).
17. Nosé, S. A unified formulation of the constant temperature molecular dynamics methods. *The Journal of Chemical Physics* **81**, 511–519 (1984).
18. DICKEY, J. M. & PASKIN, A. Computer Simulation of the Lattice Dynamics of Solids. *Phys. Rev.* **188**, 1407–1418 (1969).

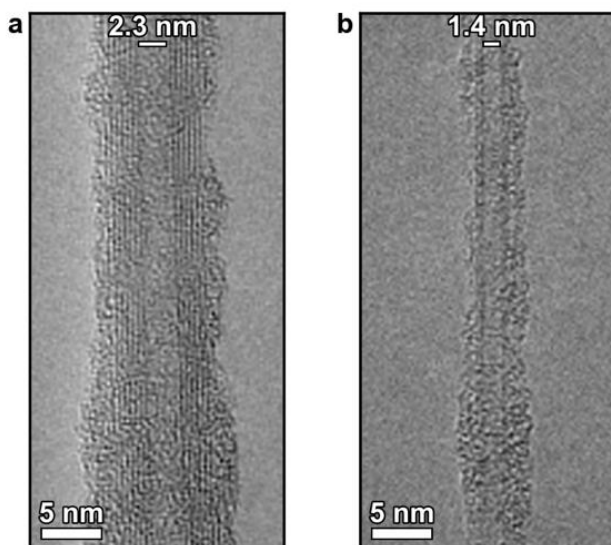
19. Lin, S.-T., Blanco, M. & Goddard, W. A., III. The two-phase model for calculating thermodynamic properties of liquids from molecular dynamics: Validation for the phase diagram of Lennard-Jones fluids. *The Journal of Chemical Physics* **119**, 11792–11805 (2003).
20. Wang, V., Xu, N., Liu, J.-C., Tang, G. & Geng, W.-T. VASPKIT: A user-friendly interface facilitating high-throughput computing and analysis using VASP code. *Computer Physics Communications* **267**, 108033 (2021).

Supplementary Information for The structure of highly confined water unveiled by nanoscale vibrational spectroscopy and simulations

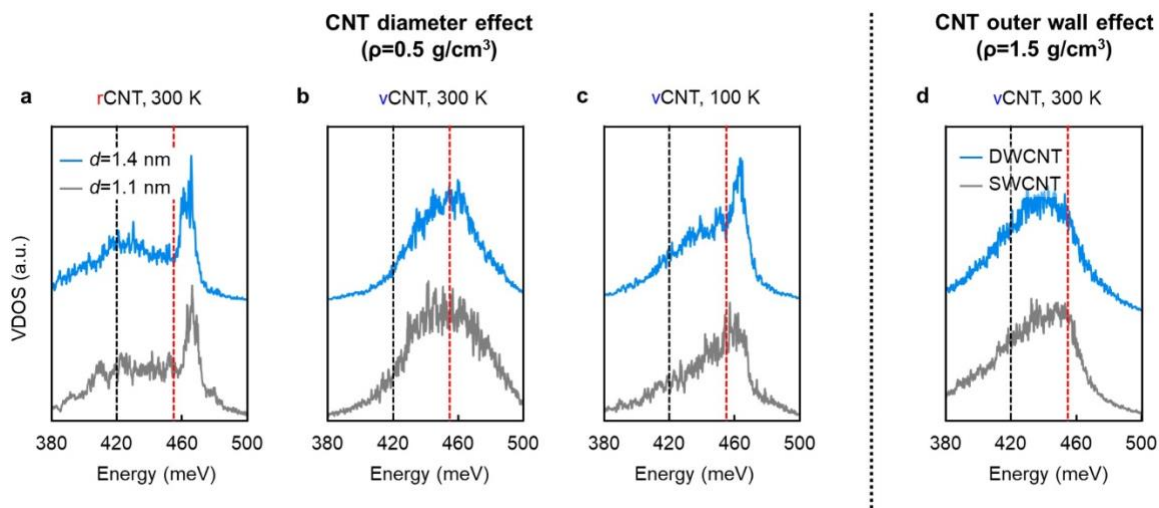
Supplementary Figures



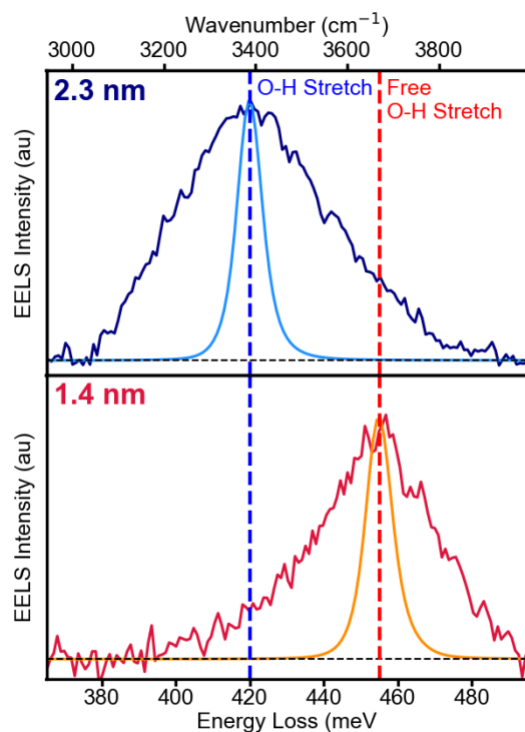
Supplementary Figure S1. Procedure for CNT water filling. (a) A custom-built humidity chamber with a microscope. (b) Optical micrograph of a holey SiN_x TEM chip after CVD growth and FIB cutting (along green dashed lines) of CNTs (schematically illustrated as continuous white lines) as well as their exposure to above 99% RH conditions and Torr Seal application. Note that Torr Seal covers the FIB cut regions but not the holey SiN_x membrane.



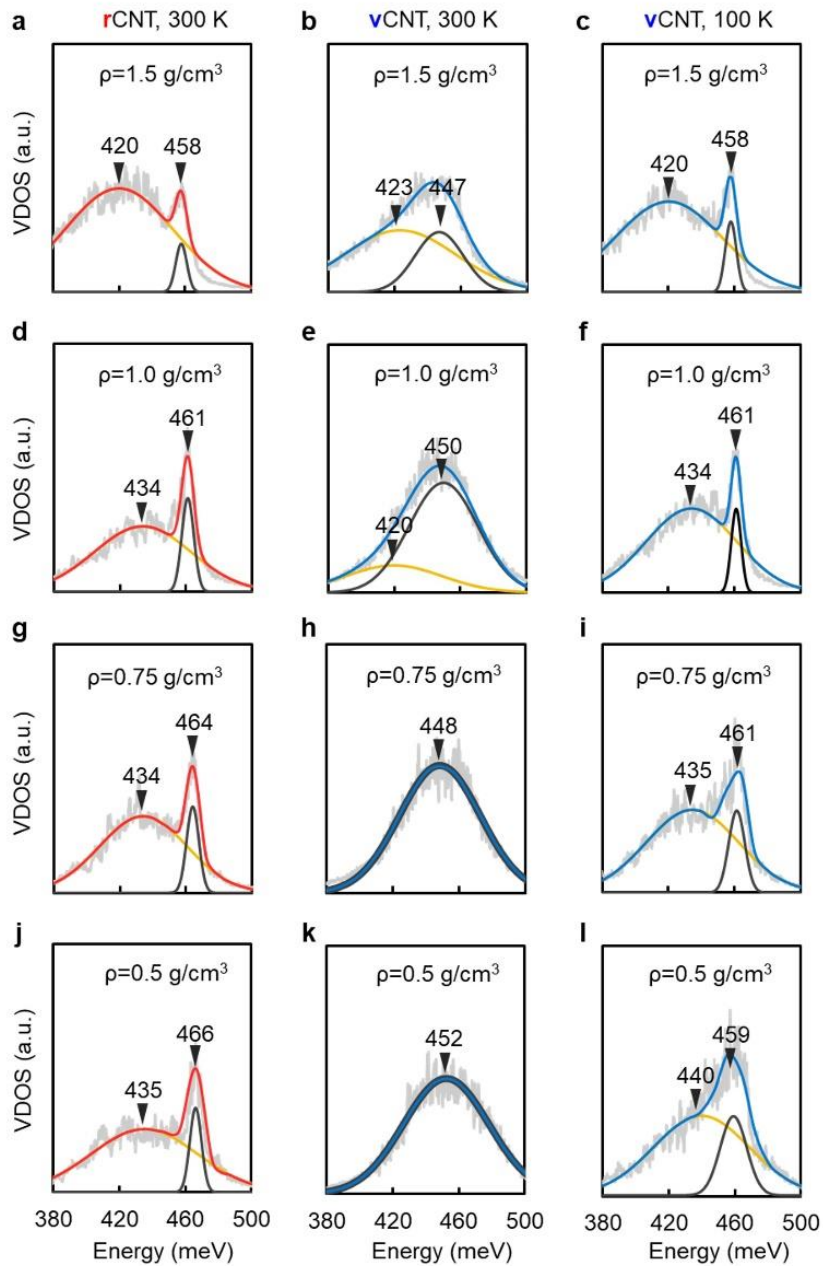
Supplementary Figure S2. Sample preparation. TEM images of the most examined CNTs in the main text with large and medium diameters. (a) The filled large-diameter tube from Fig. 1d-h, Fig. 2a, and Fig. 3a is measured to have an average inner diameter of ~2.3 nm. (b) The filled medium-diameter tube from Figs. 2a and 3a is measured to have an inner diameter of ~1.4 nm.



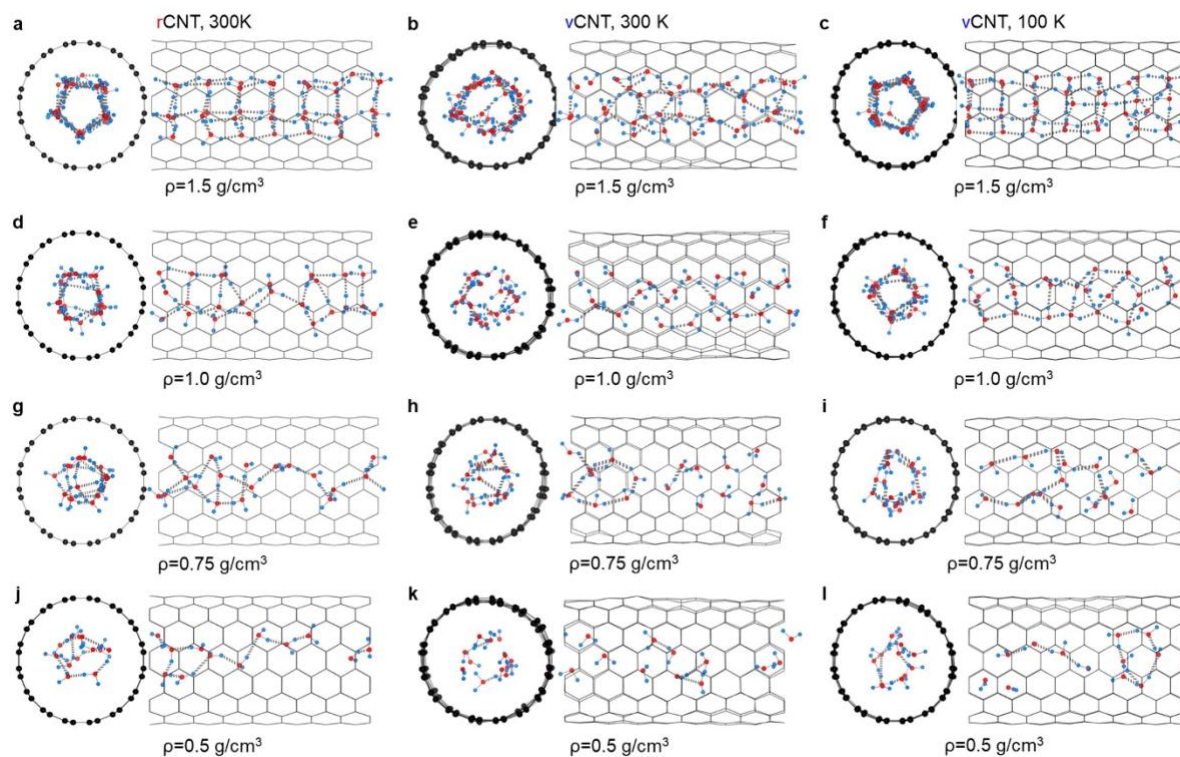
Supplementary Figure S3. VDOS of water confined in single-wall CNT (SWCNT) with larger diameter ($d=1.4$ nm) and double wall CNT (DWCNT). (a)-(c): VDOS of water confined in rigid- and vibrating-SWCNT with diameter 1.4 nm at 300 K and 100 K. The VDOS of the 1.4 nm CNT for both the rigid and vibrating cases compare very well with the corresponding vDOS of the 1.1 nm CNT. The density of the confined water is 0.5 g/cm³. (d) Demonstration that a vibrating double-wall CNT behaves the same way as a vibrating single-wall CNT. The density of the confined water is 1.5 g/cm³.



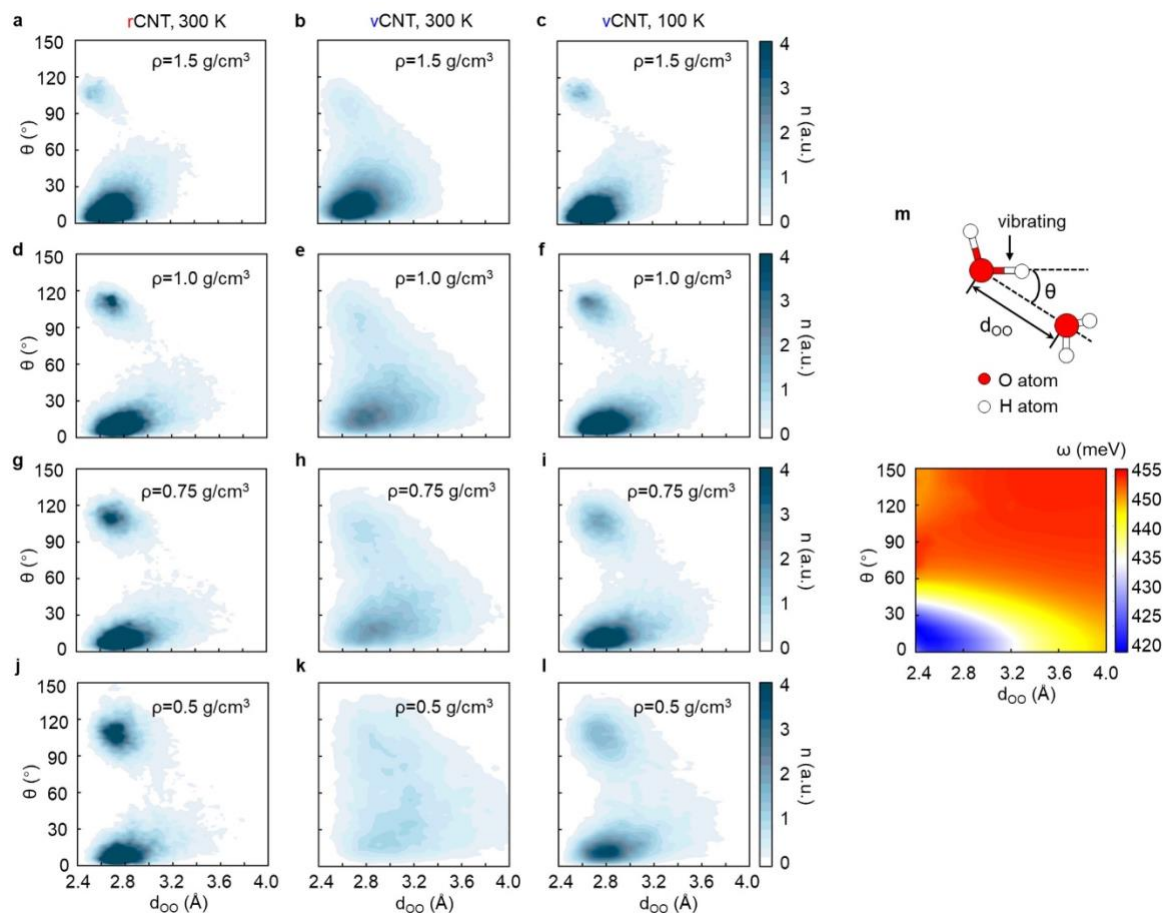
Supplementary Figure S4. Instrumental broadening vs. Spectral Linewidth. In this figure we show that our instrumental resolution is significantly below the measured linewidth of the vibrational spectra for the vibrational spectra shown in the large (2.3 nm) diameter tube and the smaller (1.4 nm) diameter tube from the main text figures. For the 2.3 nm tube the full-width at half-maximum (FWHM) of the O-H stretch is 50.1 meV, while the FWHM of the 1.4 nm tube is 34.0 meV. For all EEL spectra the energy resolution can be quantified by measuring the FWHM of the zero-loss peak (ZLP), which corresponds to all electrons in the EEL that have either elastically scattered off the sample or not interacted with the sample at all. As a result, this peak represents the spread of electron energies in the beam with which all peaks are convolved with and represents the instrumental broadening. For both spectra the FWHM of the ZLP is 8.5 meV, indicating that the vibrational peak width is dominated by the native linewidth of the peak, not instrumental broadening.



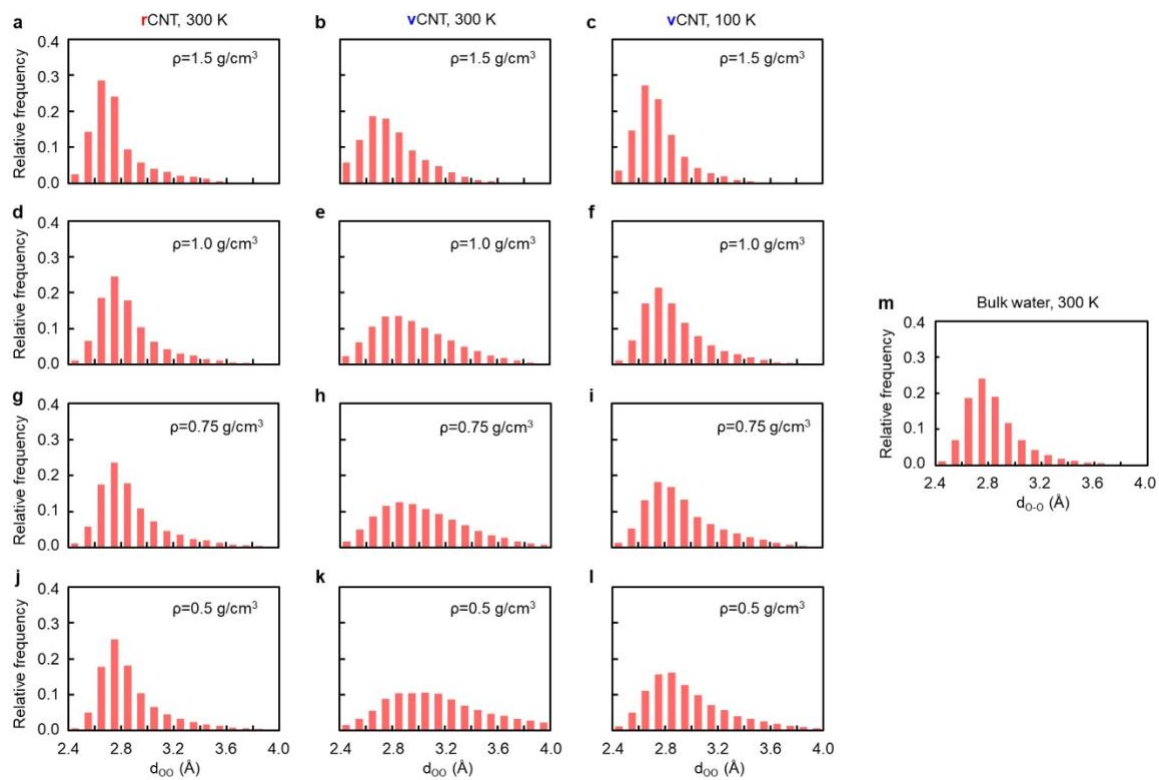
Supplementary Figure S5. VDOS of water/CNT ($d=1.1 \text{ nm}$) at different densities and temperatures as indicated. Here the VDOS are deconvoluted by two Gaussian peaks, shown in yellow and black colors. The centers of the two peaks are marked by the numbers. We note, here the two Gaussian peaks can be used to estimate the ratio between the high and low frequency component (centered at ~ 455 and ~ 420 meV, respectively) in the VDOS.



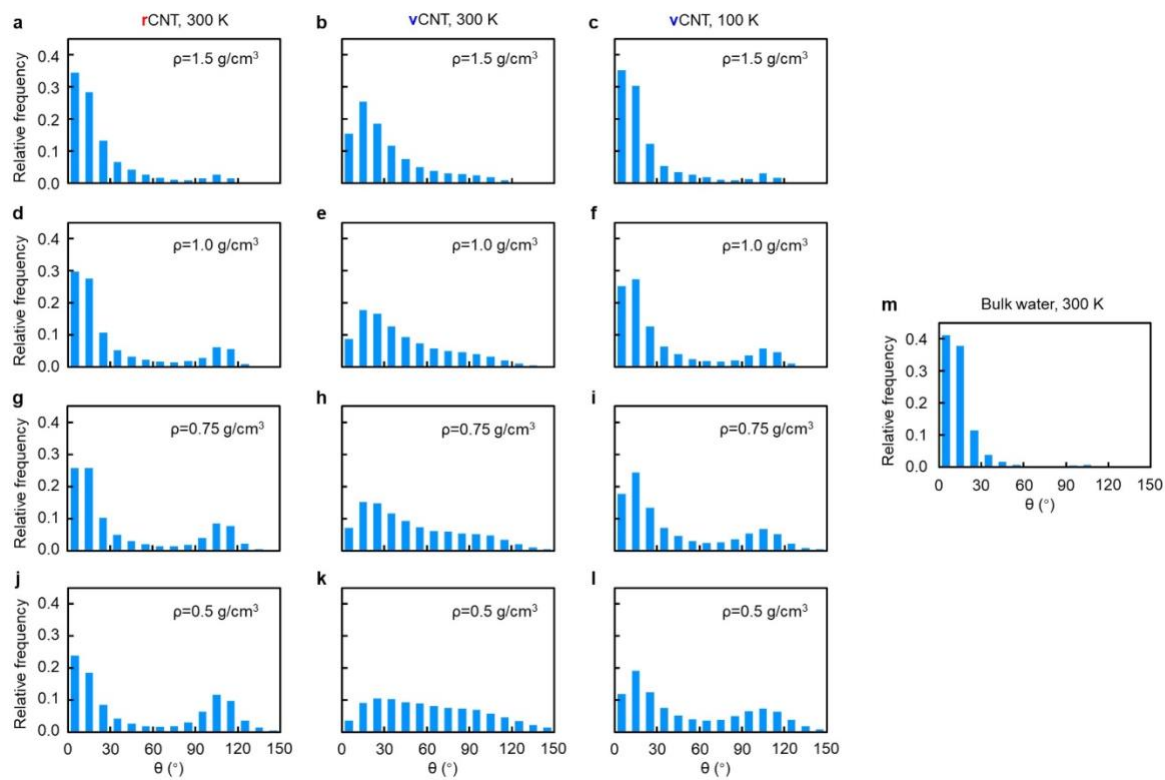
Supplementary Figure S6. MD Snapshots from Simulations. Axial and cross-sectional snapshots of the MD simulations at as-labeled water densities and temperatures. In each snapshot, intermolecular H \cdots O bonds are highlighted by dashed lines. Here, we see that, even for the higher densities, the CNT vibrations cause significant disruption of the H-bond network and the formation of more ‘free’ O-H bonds. Red atoms are oxygen and blue atoms are hydrogen.



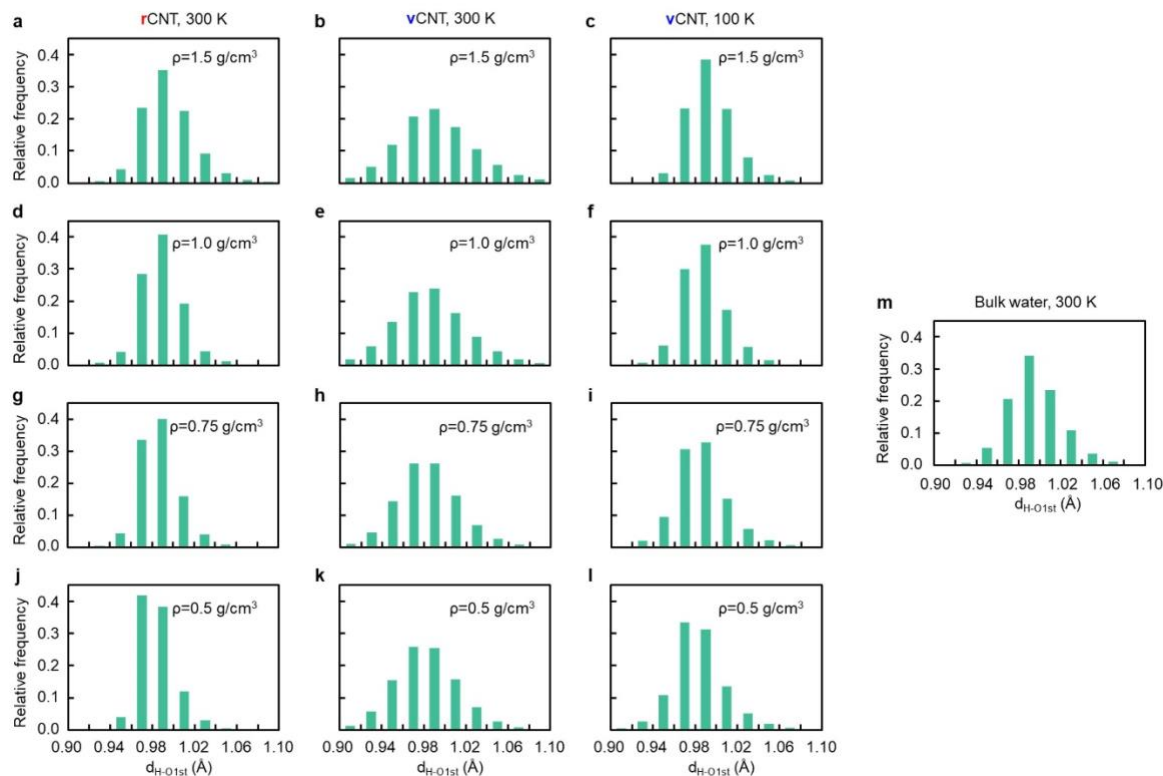
Supplementary Figure S7. Statistical heatmaps from Simulations. (a-l) d_{oo}/θ heatmaps from MD simulations for the as labeled water densities and temperatures (the color bars are normalized to be quantitatively comparable to one another). The values plotted in the heat maps are obtained from molecules in all the snapshots of the corresponding MD simulations. (m) Top panel shows a schematic of the nearest-neighbor molecular structure used to define d_{oo} and θ the heatmaps in (a-l) and the O-H stretch frequency ω as a functional of d_{oo} and θ . Since the color map in panel m is constructed using the two-water molecule model, it is only qualitatively indicative of the frequencies that correspond to the heat maps in panels a-l.



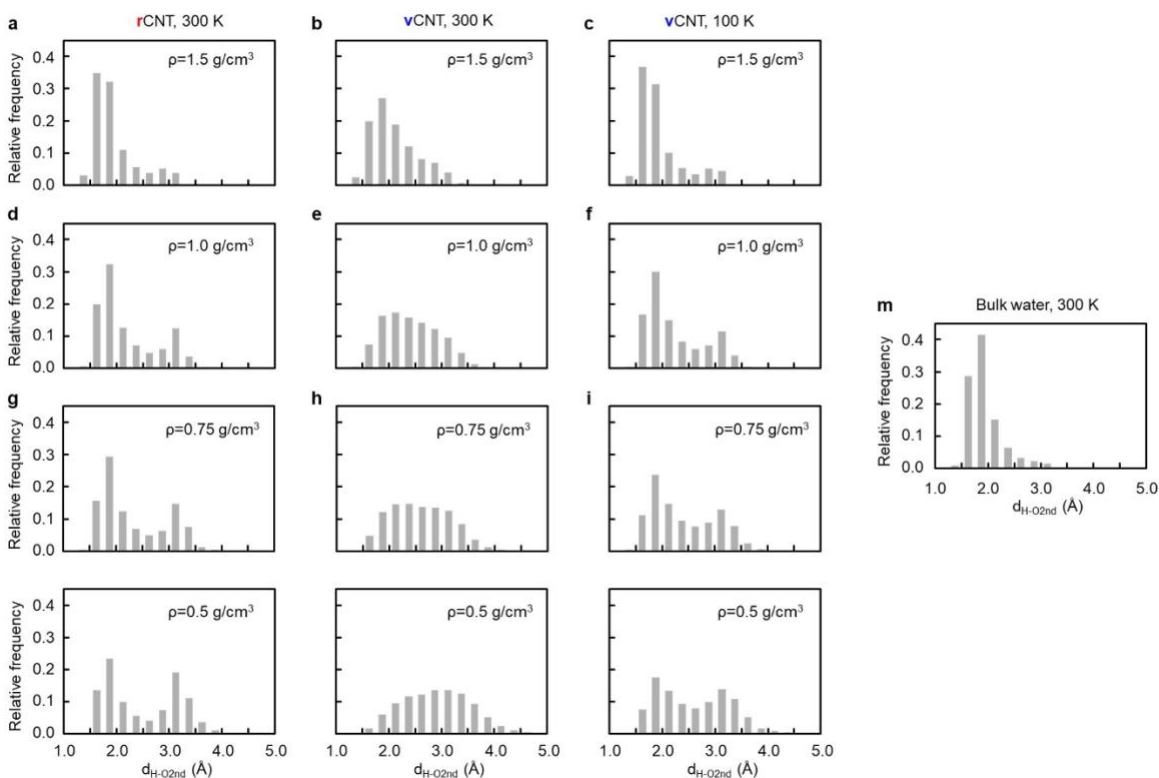
Supplementary Figure S8. H-O-O angle θ as defined in Fig. S7m. θ distribution histogram of water confined in CNT ($d=1.1$ nm) for all the densities and temperatures presented in the main text and SI.



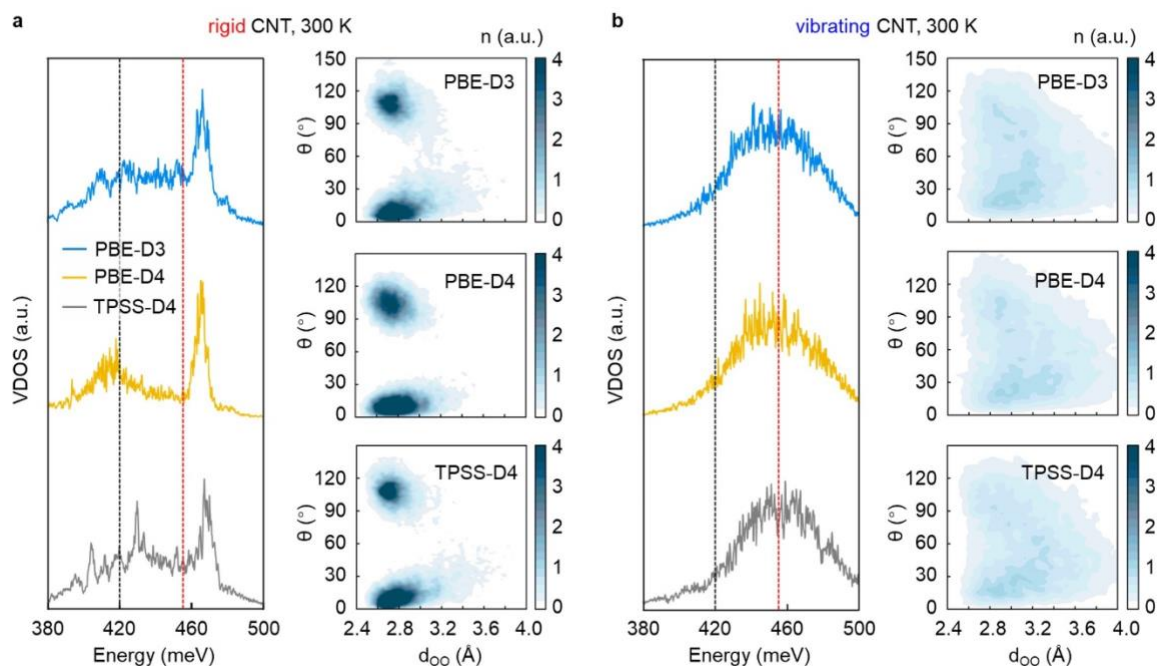
Supplementary Figure S9. Oxygen-oxygen d_{O-O} . d_{O-O} distribution histogram of water confined in CNT ($d=1.1 \text{ nm}$) for all the densities and temperatures presented in the main text and SI.



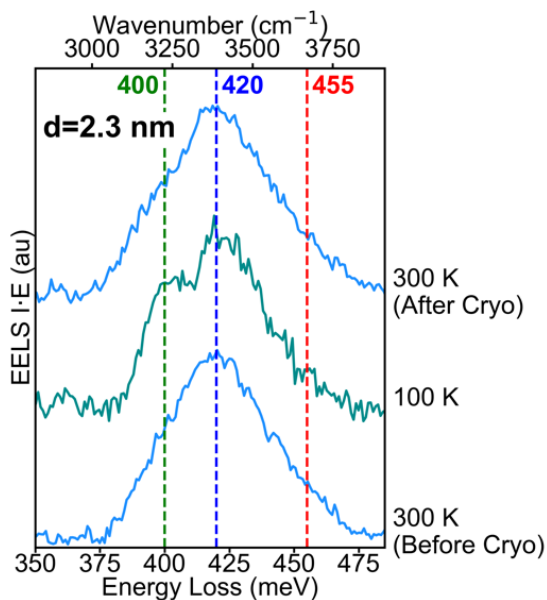
Supplementary Figure S10. O-H bond lengths. d_{H-O1st} distribution histogram of water confined in CNT ($d=1.1$ nm) for all the densities and temperatures presented in the main text and SI. Here, O_{1st} represents the oxygen atom closest to the H atom, as in the oxygen atom on the same molecule as the H-atom. These are the *intramolecular* O-H bonds. These calculations critically show while there is some change in the variation of the O-H bond length as a function of tube vibration the average length remains unchanged (~ 0.98 Å).



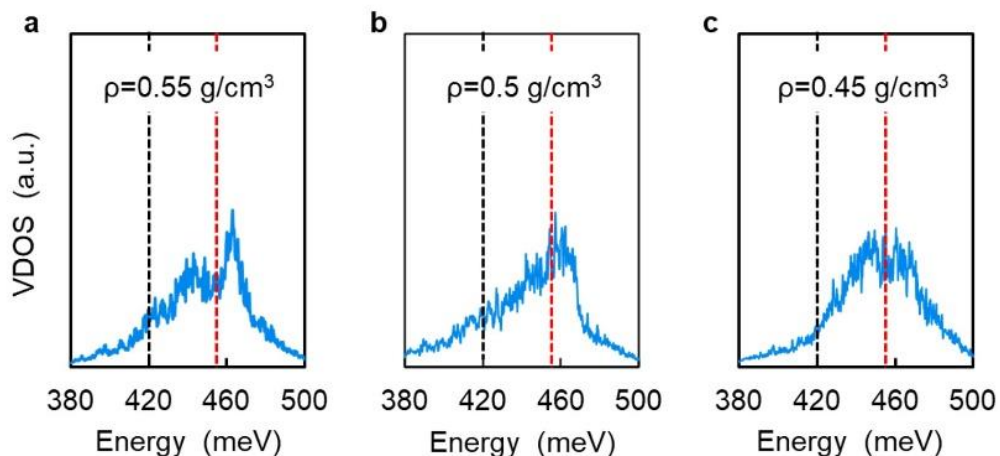
Supplementary Figure S11. H-O bond lengths. d_{H-O2nd} distribution histogram of water confined in CNT ($d=1.1$ nm) for all the densities and temperatures presented in the main text. Here, O_{2nd} represents the second closest oxygen atom to the H atom, as in the oxygen atom on the nearest neighbor molecule. These are the *intermolecular* O-H bonds. These simulations show the same split between bimodal and singular distributions due to disordering induced by the CNT vibrations as the heat maps in the main text.



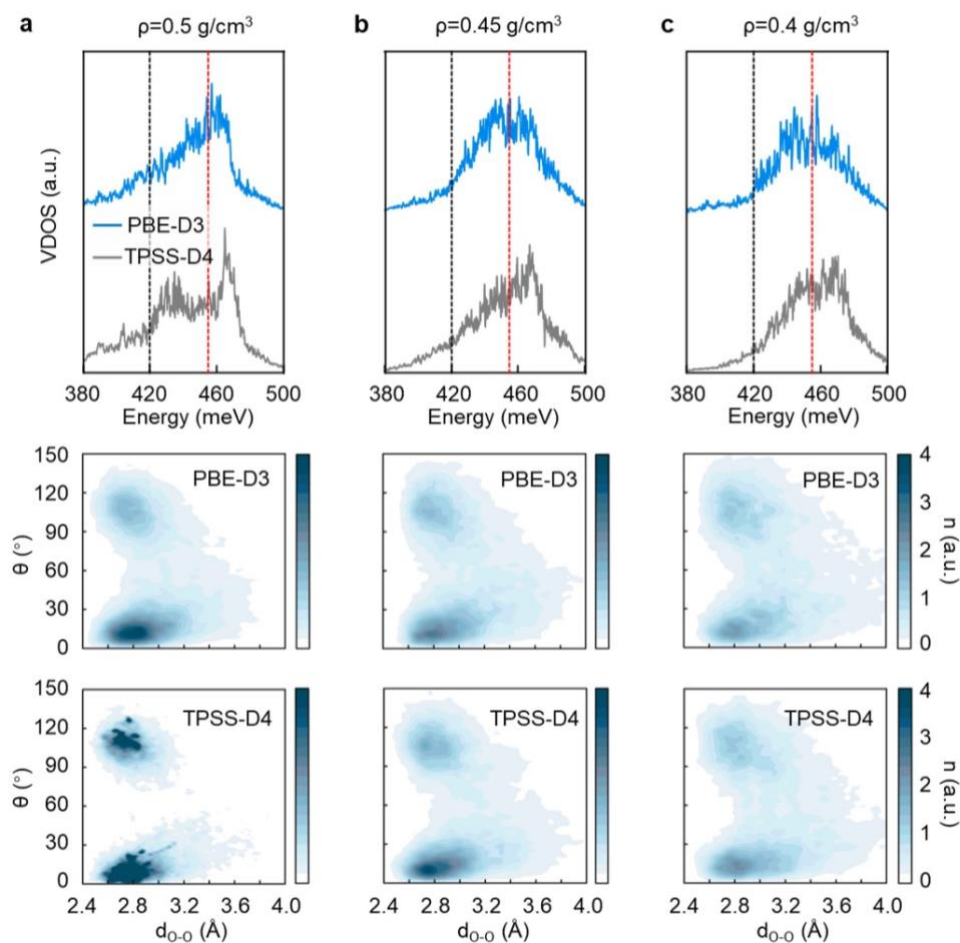
Supplementary Figure S12. Room temperature VDOS and d_{oo}/θ map of water confined in rigid/vibrating-CNT (diameter 1.1 nm) calculated using different functionals. The density of the confined water is 0.5 g/cm^3 in all the cases. The calculated VDOS and heat map using three different functionals are quite similar to each other, demonstrating the choice of functionals has minimal effects on the structure and properties of the confined water.



Supplementary Figure S13. Reversibility of the crystalline phase change. vEELS on the 2.3-nm-diameter CNT for a full cryo-cycle, meaning measurements at 300 K, 100 K, then back to 300 K, showing the emergence and disappearance of a ice-like peak at 400 meV.



Supplementary Figure S14. Density-dependent evolution of the cryogenic vibrational spectrum. vDOS at 100 K for three different water densities showing that $\rho = 0.5 \text{ g/cm}^3$ is the critical water density for which a single peak is observed in the vibrational DOS (indicating that the non-H-bonded water phase persists) at 100 K. These differences show that small differences in the density ($\sim 0.05 \text{ g/cm}^3$) can significantly impact the resulting vibrational response.

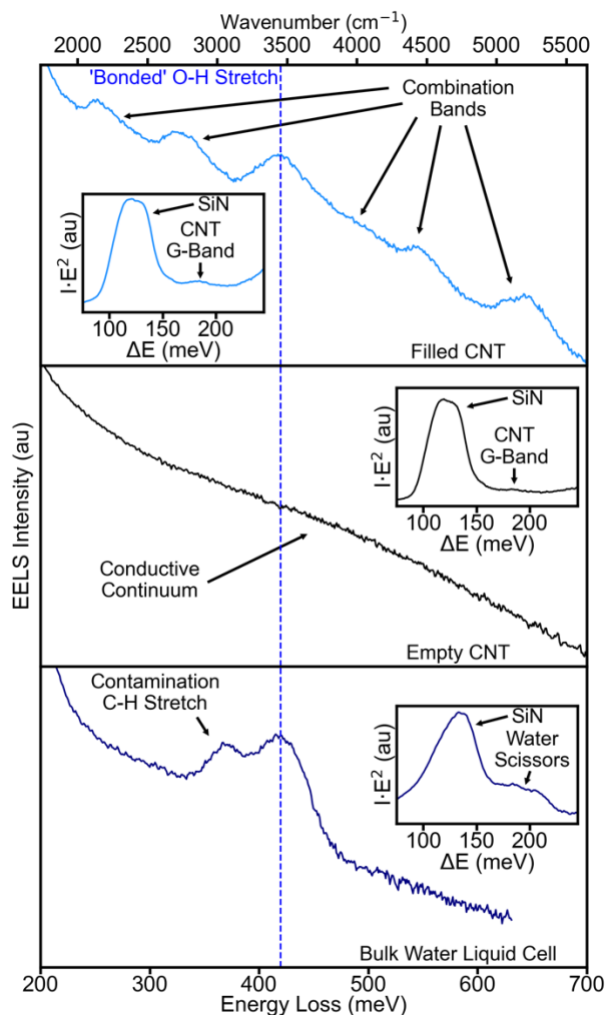


Supplementary Figure S15. Low temperature (100 K) vDOS and d_{oo}/θ map of water confined in vibrating-CNT (diameter 1.1 nm) calculated using different functionals. The densities of the confined water are 0.5, 0.45 and 0.4 g/cm^3 for the three cases. The 100 K vDOS calculated by PBE-D3 and TPSS-D4 differ from each other when $\rho = 0.5 \text{ g/cm}^3$, but consistent with each other when the density further decreases.

Supplementary Discussion 1: Additional Peaks Outside of the O-H Stretch Regime

As stated in the main text, there are more peaks in the measured vibrational spectra aside from just the O-H stretching modes. We assign these peaks as combination bands as other IR absorption spectroscopy techniques, as well as other vEELS experiments on ice have reported peaks in these regimes^{1,2}. In the main text, we focus exclusively on the O-H stretch regime between 370-500 meV due to the presence of these additional bands. We have not rigorously determined the origin of these bands, but believe the response is largely consistent with combination bands/overtones. Here, we present additional discussion on these vibrational peaks. In Figure S16, we show the three spectra from the main text Figure 1 from a filled CNT (Top), an empty CNT (Middle), and the bulk liquid cell (Bottom). The vast difference between the filled tube and the empty tube is even more dramatic in the full range picture, with the empty tube showing absolutely no sharp features, and only a broad sloping continuum that is present in any amorphous/conductive material corresponding to low-energy electronic transitions. We also note that the empty CNT and the filled CNT are from the same sample, and hence prepared under identical conditions. This serves as a strong piece of evidence that the main 420 meV peak discussed in the main text, and the other bands are both originating from the water. The tube filling rate is not predicted to be 100%, so one being full and the other being empty is a highly likely scenario, and perhaps no other physical scenario could result in such a dramatic difference between the vibrational spectra.

In the comparison to bulk water in Fig. S16, the bonded O-H stretch matches well, but these other features do not. Analyzing bulk water is much more straightforward since larger scale volumes of water can be confined in liquid cells. Our comparison is done on a bulk liquid cell with a macroscopic volume of water confined between two SiN windows. Due to the dirty nature of the sample preparation, and our inability to perform standard contamination mitigation protocols (such as baking and plasma cleaning), a large amount of hydrocarbons accumulate

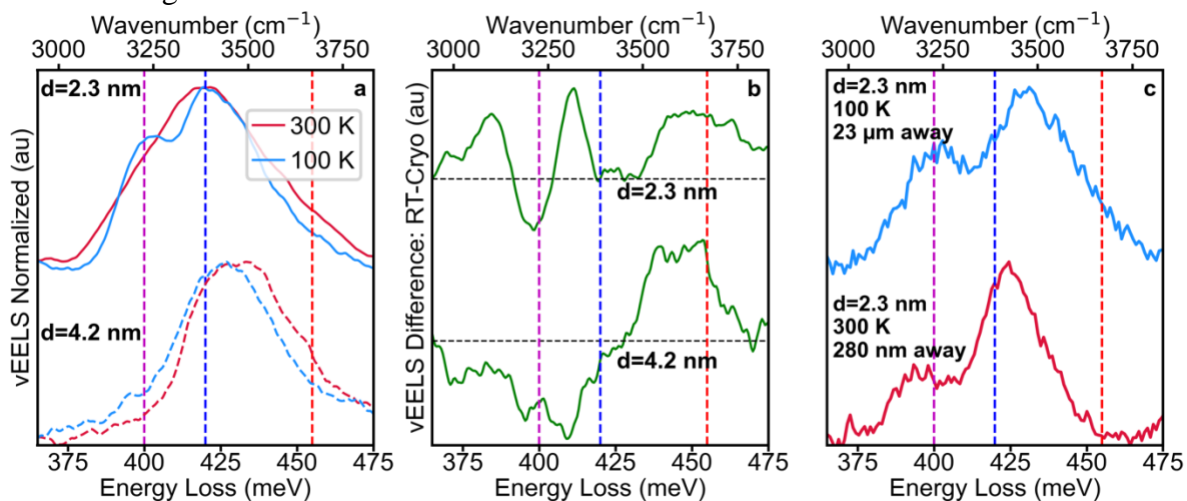


Supplementary Figure S16. Full vibrational spectrum of Filled CNT, Empty CNT, and Bulk Water. Here we show the full vibrational response of all three spectra shown in the main text of Figure 1. In each we show the spectrum in log-scale and in the inset we show the SiN/G-Band vibrations of the substrate/CNT. (Top) filled CNT, (Middle) Empty CNT, (Bottom) bulk liquid cell.

under the beam during acquisition. As a result, for the liquid cells we see two peaks, at 420 meV and 365 meV which are consistent with the O-H and C-H stretches respectively. In bulk water, we see no other peaks anywhere in the bulk water spectrum other than the C-H and O-H stretches, which is consistent with our previous work on the vibrational spectroscopy of water in graphene/h-BN liquid cells³. While this does not directly connect the additional peaks to combination bands, it directly connects the changed nature of the vibrational response to the confinement induced by the nanotube. Moreover, it shows that even in the case of a larger CNT diameter where the water shows the ‘bonded’ O-H stretch frequency of 420 meV, the vibrations in the water are still fundamentally different from those found bulk water. These peaks are in the spectral regime consistent with combination bands and potentially overtones of lower-frequency vibrations potentially indicating that the confinement of the CNT could increase the cross-section of these second order effects. However, this remains an open question that requires further validation and future study to understand better.

Supplementary Discussion 2: Repeatability of Temperature-Dependence Experiments

In the main text we present two cryogenic experiments, one for the 1.4 nm diameter tube and one for the 2.3-nm-diameter tube. We further go on to examine the reversibility of the phase transition in the 2.3-nm-diameter CNT in Figure S12. Each is summarized with two spectra, and more experiments were conducted to verify the repeatability of these measurements. Given the low filling rate of the CNTs, and a natural variance of the inner diameter of the tubes, finding filled tubes with similar diameters is challenging. Nevertheless, we managed to repeatedly observe both the 455 meV and the 420 meV peak phenomena on multiple independent tubes. We additionally take advantage of the length of the tubes (mm scale) to examine different parts of the same tubes. We report our observation as an initial experiment demonstrating the potential of vEELS (and especially cryo vEELS) and expect future development of new platforms for confined fluids will help obtain more robust analyses. A summary of our additional experiments is shown in Figure S17.



Supplementary Figure S17. Repeatability of phase change signatures in large diameter CNTs.

(a) Comparison of the room temperature (300 K) and cryogenic (100 K) spectra for the CNT shown in the main text and the other cryo experiment. (b) Difference spectra of the 300 K and 100 K spectra for each CNT. (c) shows other measurements on the 2.3 nm CNT. The top (blue) spectra shows a cryo measurement conducted many microns away from the original position of the spectra and the bottom (red) spectra shows a room-temperature measurement very close

We compare the results of the 2.3-nm-diameter CNT examined in the main text, to a larger 4.2-nm-diameter CNT in Fig. S17a and S17 b. On first glance, the 4.2 nm CNT does not appear to exhibit a significant phase change, as the peak has not changed in line-shape to nearly the same extent as the in the lower diameter tube. However, by normalizing the spectra and taking the difference (300 K spectrum minus the 100 K spectrum) we can see there is a strong similarity between the two experiments. Both have exhibited an overall redshift at cryogenic temperatures, as evidenced by the dip in intensities at around 400 meV and the increase in intensities at 455 meV. While the distinct 400 meV feature (corresponding to Ih ice) is less pronounced in the 4.2-nm-diameter CNT, this could easily be a factor of different phases of ice with different frequencies being present, or different ratios of crystalline and amorphous phases due to the difference in diameter.

The other piece of evidence that the phase change in the 2.3 nm tube is genuine is obtained by examining a position on the same CNT under cryogenic conditions very far away from the original spot. Figure S17c shows such a spectrum on the top, which exhibits a clear bimodal distribution with peaks near the 400 meV and 420 meV observed in the main text spectra. The ability to go so far away from the initial position and return a spectrum so similar to the initial spectrum is encouraging that these peaks are genuine features of the water inside the tube. It is important to note, that the bottom spectrum in Fig. S17c shows a room temperature spectrum from the CNT extremely close to where the original room temperature spectrum from Fig. S17a and all the main text figures is obtained, that shows a slight peak at 400 meV. The peak is much lower in intensity compared to the cryogenic spectrum, and peaks at both 400 meV and 420 meV have been observed room temperature water through vibrational sum frequency spectroscopy⁴, all of which still indicates that the reversible phase change shown for the 2.3-nm-diameter CNT does correspond to crystalline ice formation. However, this observation highlights the necessity to discuss potential artifacts that could influence our analysis. Contamination from hydrocarbons and combination bands have already been discussed Supplementary Discussion 1, however, beam-induced irradiation is possibly the largest potential for artifacts in our system.

We note that experiments were conducted in a mindset of limiting total exposure of the CNTs to the electron beam at all time, however, it is not possible to identify CNTs and align images without subjecting the areas to a small amount of electron dose before the initial acquisition. As a result radiolysis byproducts are certainly produced to some extent the electron beam interacting with the water⁵. By returning to the same positions we risk the possibility of dose directly driving the emergence of the 400 meV peak, and we cannot disprove this conjecture directly. However, in addition to the reversibility of the 400 meV peak emergence (highlighted in Fig. S13) the top spectrum in Fig. S17c shows the 400 meV and 420 meV peaks (both extremely pronounced) in a brand new area of the tube that had not been exposed to the electron beam, so we know it is not solely driven by beam irradiation.

Additionally, many other effects, such as the rate of cooling, or tensioning in the nanotube, or impurities in the confined water, or defects in the CNT, could also influence phase changes in confined fluids. We believe this result to be a powerful demonstration of the potential to monitor phase changes using vEELS, but to conclusively link the cryogenic phase changes (or lack thereof) identified through vEELS to specific physical origins and mechanisms, extensive statistics and follow up experiments controlling these variables will be needed. More controllable nanofluidic platforms and cooling processes that can be integrated with the vEELS workflow would be very helpful in future studies of phase transitions in fluids.

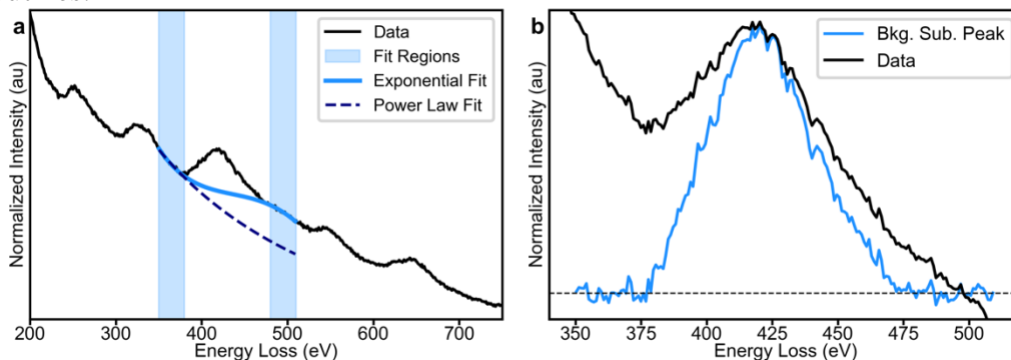
Supplementary Discussion 3: Data Processing of EEL Spectra

Figure 1 Spectrum Image Slices: In Figure 1, we compare 100 meV wide slices from two different spectrum-images to demonstrate the strength of the O-H vibrations in the filled tubes. For the filled CNT in Fig. 1 a 181 x 75 pixel spectrum-image was acquired with a 20 ms dwell time, for the empty tube a 151 x 78 pixel spectrum image was acquired with a 10 ms dwell time. In order to normalize, we use the maximum intensity of the ZLP in the pixel furthest away from the CNT, and find that the empty tube dataset had a total current a factor of 3.12 times less than the filled tube current. For the ‘counts’ reported in Main Text Fig. 1 for the empty tube we have multiplied the total counts in the empty tube slice by this factor of 3.12 to make it directly comparable to the filled tube slice, the filled tube slice intensity is as acquired. The spectra are not background subtracted to make sure the difficulties described in the following section do not influence the slices.

Additionally, due to our desire to minimize total beam-exposure on the CNTs between exposure, final preparations for the EELS acquisitions are done on a region of the sample a micron or two away from the CNT, then the stage is moved to get the CNT in range. As a result, a significant amount of drift is present in the spectrum-images. We assume the drift to be isotropic, fit the CNT positions as a function of the SI and then correct it using a linear fit. As a result, we have to cut out the areas of the dataset that are not aligned well between the top and bottom, and also cut out areas influenced by the SiN grid. The slices shown in the main text a fractional 120 x 36 pixel aligned region for both datasets.

The point spectra in Fig. 1d had energy resolutions of 8.5 meV for both CNTs, and for the bulk liquid cell. The spectrum images had energy resolutions of 9.5 meV for the filled CNT dataset, and 8.5 for the empty CNT dataset.

Background Subtraction for Spectra: All excitations in EELS are convolved with a background signal. For low-loss the excitations are convolved with the tail of the ZLP, and for core-loss they are convolved with the bulk plasmon tail. As a result, background subtraction is commonly employed to isolate the signal from the background. In core-loss EELS this is conventionally done with a power law, however, it has been demonstrated that in the low-loss region the ZLP tail is often better fit with more complex functions^{6,7}. Here, due to the combination bands discussed in Supplementary Discussion 1, fitting is challenging as strong peaks are in the regions directly before and after the ideal fitting regime, necessitating the use of one of these advanced fitting routines.



Supplementary Figure S18. Background Subtraction in vEELS. (a) A vEEL spectrum with the fit regions for a two-region, third-order exponential fit, and the resulting background. (b) Comparison of the background subtracted data and the actual peak.

We use the two-region, third-order exponential fit described in Ref. ⁶, which possesses the form $I(E) = e^{ax^3+bx^2+cx+d}$. The fitting regions are taken to be in regions on the tail or after the peak

of the combination band on the low-energy side of the O-H stretch regime (400-460) and before the onset of the next combination band on the high-energy side of the regime. An example of the fitting for the spectrum shown in Fig. S16 is shown in Fig. S18.

Figure S18a shows how the background fitting actual works. It is important to note that this background is not physical, it can clearly be seen that the pre-peak fitting region overlaps the preceding combination band. Moreover, the background level before the O-H stretch peak is not consistent with the background intensity after the peak. An example of how consistent background intensity would look is shown by fitting a power law in the pre-peak fitting region. The ZLP tail in this region follows this general line shape (continuous exponential decrease), the s-shape of the exponential fit is not a phenomenon that can originate directly from the elastic scattering intensity. We use this background subtraction method as a means of isolating the O-H stretch peak, which despite the non-physical nature of the background applied, does an excellent job of capturing the line-shape and frequency of the peak, as can be seen in the comparison between the raw data and the background subtracted peak shown in Fig. S18b.

Supplementary References

1. Bertie, J. E. & Lan, Z. Infrared Intensities of Liquids XX: The Intensity of the OH Stretching Band of Liquid Water Revisited, and the Best Current Values of the Optical Constants of H₂O(l) at 25°C between 15,000 and 1 cm⁻¹. *Appl. Spectrosc.* **50**, 1047–1057 (1996).
2. Krivanek, O. L. *et al.* Probing Biological Materials by Vibrational Analysis in the Electron Microscope. *Microsc. Microanal.* **28**, 1196–1197 (2022).
3. Jokisaari, J. R. *et al.* Vibrational Spectroscopy of Water with High Spatial Resolution. *Adv. Mater.* **30**, 1802702 (2018).
4. Scatena, L. F., Brown, M. G. & Richmond, G. L. Water at Hydrophobic Surfaces: Weak Hydrogen Bonding and Strong Orientation Effects. *Science* **292**, 908–912 (2001).
5. Abellan, P., Gautron, E. & LaVerne, J. A. Radiolysis of Thin Water Ice in Electron Microscopy. *J. Phys. Chem. C* **127**, 15336–15345 (2023).
6. Hachtel, J. A., Lupini, A. R. & Idrobo, J. C. Exploring the capabilities of monochromated electron energy loss spectroscopy in the infrared regime. *Sci. Rep.* **8**, 5637 (2018).
7. Fung, K. L. Y. *et al.* Accurate EELS background subtraction – an adaptable method in MATLAB. *Ultramicroscopy* **217**, 113052 (2020).

Exploring Charge Transport Dynamics in a Cryogenic P-Type Germanium Detector

P. Acharya,¹ M. Fritts,² D.-M. Mei,^{1,*} G.-J. Wang,¹ R. Mahapatra,³ and M. Platt³

¹*Department of Physics, The University of South Dakota, Vermillion, SD 57069, USA*

²*School of Physics and Astronomy, University of Minnesota, Minneapolis, MN, 55455, USA*

³*Department of Physics & Astronomy, Texas A & M University, College Station, TX 77843, USA*

(Dated: February 29, 2024)

This study explores the dynamics of charge transport within a cryogenic P-type Ge particle detector, fabricated from a crystal cultivated at the University of South Dakota (USD). By subjecting the detector to cryogenic temperatures and an Am-241 source, we observe evolving charge dynamics and the emergence of cluster dipole states, leading to the impact ionization process at 40 mK. Our analysis focuses on crucial parameters: the zero-field cross-section of cluster dipole states and the binding energy of these states. For the Ge detector in our investigation, the zero-field cross-section of cluster dipole states is determined to be $8.45 \times 10^{-11} \pm 4.22 \times 10^{-12} \text{ cm}^2$. Examination of the binding energy associated with cluster dipole states, formed by charge trapping onto dipole states during the freeze-out process, reveals a value of $0.034 \pm 0.0017 \text{ meV}$. These findings shed light on the intricate charge states influenced by the interplay of temperature and electric field, with potential implications for the sensitivity in detecting low-mass dark matter.

I. INTRODUCTION

Recent astronomical investigations consistently highlight the pivotal role of dark matter (DM) in the cosmos, characterized by its non-luminous and non-baryonic nature, constituting the majority of the universe's material composition [1–4]. Strong evidence supports the notion that DM influences the cosmos by creating expansive halos around galaxies, as observed in the Milky Way [5–8]. The quest for direct evidence lies within laboratory research, exploring potential interactions between DM particles and ordinary matter beyond gravitational forces. While weakly interacting massive particles (WIMPs) have been a focus, recent theoretical frameworks like asymmetric DM and dark sectors prompt exploration of low-mass DM particles. Thus, the MeV-scale particle emerges as a noteworthy candidate for low-mass DM [9–11], yet detecting them poses challenges. The need for detectors with exceptional sensitivity to discern a solitary electron-hole (e-h) pair complicates matters due to the narrow energy span involved. Overcoming this hurdle requires leveraging modern technology and innovative methodologies for precise and reliable capture and quantification of these minute energy signals. The relentless pursuit of sophisticated detectors and pioneering detection techniques continues as researchers delve deeper into the mysteries surrounding low-mass DM [12]. These advancements hold the promise of unraveling one of the universe's profound enigmas, potentially bringing us closer to understanding its intricate tapestry.

Owing to their exceptional sensitivity, germanium (Ge) detectors have emerged as a promising avenue for addressing the challenge of low-mass DM detection, presenting a compelling alternative to conventional method-

ologies [13]. These detectors possess a distinct advantage for probing low-mass DM due to their remarkable ability to efficiently generate electron-hole pairs, each requiring an average energy of 3 eV. Complementing this characteristic is Ge's narrow band gap of $\sim 0.7 \text{ eV}$, further bolstering its suitability for such investigations at millikelvin (mK) temperatures [14]. Leveraging the concept of doping, it becomes possible to significantly expand the parameter space for detecting low-mass DM using Ge detectors. By judiciously introducing impurities into the Ge matrix, particularly shallow-level impurities boasting binding energies around 0.01 eV, a fascinating phenomenon emerges: the creation of dipole states and cluster dipole states in conditions below 6.5 K [15]. What distinguishes these dipole states and cluster dipole states is their binding energy, which plunges even lower than that of the impurities themselves [16, 17]. This intriguing aspect opens a pathway to potentially detecting low-mass DM.

Yet, despite well-explored knowledge concerning the binding energies of impurities in Ge, a conspicuous gap remains regarding the binding energies of these dipole states and cluster dipole states at cryogenic temperatures, especially those hovering below 100 mK. When Ge is cooled to these frigid temperatures, as experienced in the vicinity of liquid helium, a compelling process unfolds: the expulsion of residual impurities from its conduction or valence bands. These expelled impurities then find solace in localized states, giving rise to electric dipoles (denoted as D^{0*} for donors and A^{0*} for acceptors) or neutral states (D^0 and A^0). These states signify excited neutral impurity configurations, tethered by binding energies less than 10 meV. The captivating implication here is the capacity of these dipole states to ensnare charge, thereby orchestrating the formation of cluster dipole states (D^+ and D^- for donors, and A^+ and A^- for acceptors), which exhibit even lower binding energy levels. The specifics of these states depend on the operational temperature [15, 18, 19].

* Corresponding author.
Email: Dongming.Mei@usd.edu

As temperatures decrease, a remarkable exponential reduction in the density of free charge carriers becomes apparent [20]. Approaching temperatures lower than 10 K, donor (or acceptor) atoms predominantly maintain their unionized configuration, confining fifth electrons (or vacant holes) within these atomic entities. The extent of this encapsulation is governed by the Onsager radius, denoted as $R = \frac{e^2}{4\pi\epsilon\epsilon_0 K_B T}$, where ϵ represents the relative permittivity of Ge (with a value of 16.2), ϵ_0 is the permittivity of free space, K_B is the Boltzmann constant, and T is the temperature. Remarkably, at temperatures below 10 K, R can significantly exceed the dimensions of the donor or acceptor atom [21]. Consequently, the fifth electrons (or vacant holes) associated with the donor (or acceptor) atoms may undergo thermal dissociation from the atomic nucleus, initiating the formation of electric dipoles due to the segregation of opposing charges [20]. This sequential progression leads to the generation of dipole states with the capacity to trap charge through Coulombic attraction, giving rise to the emergence of cluster dipole states [15]. As depicted in Figure 1, this visualization illustrates the formation of excited dipole states and cluster dipole states in n-type Ge or p-type Ge, respectively. Within an excited dipole state, whether associated with a positively charged donor ion or a negatively charged acceptor ion, a state of profound confinement prevails due to the lattice deformation potential. Consequently, the phase space available for capturing charge carriers is inherently more constrained than that of bound electrons (or holes), which retain the capability to traverse within the bounds set by the Onsager radius (R) [15, 20].

This intricate interplay foretells a higher likelihood of generating D^{+*} states (or A^{-*} states) within an n-type detector (or a p-type detector) than the likelihood of yielding D^{-*} states (or A^{+*} states) [20]. This asymmetry implies that within an n-type detector, holes undergo more pronounced entrapment effects compared to electrons, whereas electrons experience greater susceptibility to entrapment than holes within a p-type detector [22, 23]. At the University of South Dakota (USD), our research has delved extensively into the binding energy characteristics of cluster dipole states, as documented in recent studies [16, 17]. This investigation unfolded at a low temperature of 5.2 K, uncovering a binding energy threshold consistently below 10 meV, a parameter intricately linked to the prevailing electric fields. Notably, our analysis has spotlighted the pivotal role played by the Onsager radius in shaping the spatial confines conducive to the emergence of cluster dipole states, with temperature exerting a significant influence on this parameter. The intricate interplay between temperature and the Onsager radius serves as a governing factor in determining the binding energy of cluster dipole states. Our research transcends the microscopic realm, carrying macroscopic implications. It reveals that lower temperatures engender an expansion of the Onsager region, consequently leading to a reduction in binding energies.

Conversely, higher temperatures induce a contraction of this region, resulting in heightened binding energies. Our commitment to advancing this knowledge extends further, as we seek to validate these findings across distinct temperature regimes, including conditions exceeding 800 mK and those as low as 40 mK. Through this empirical exploration, we aim to offer concrete evidence for the intricate thermal dynamics that influence the binding energy within cluster dipole states.

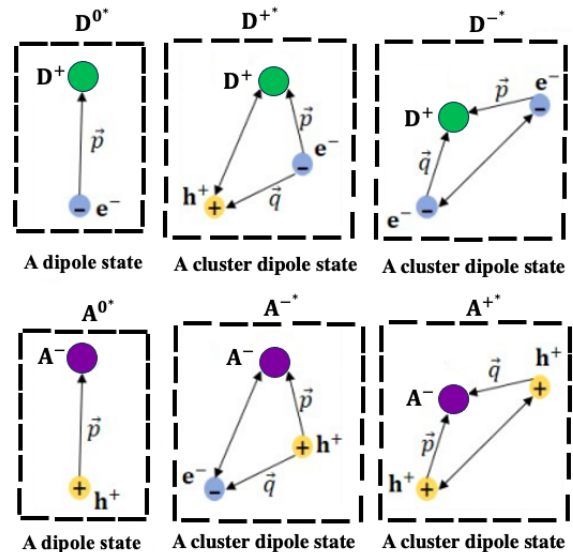


Figure 1. The procedural framework delineating the progression towards the genesis of both excited dipole states and cluster dipole states within a dual-tiered Ge detector — encompassing an upper tier (n-type) and a lower tier (p-type) — operational within sub-10 K temperatures, is embodied by the subsequent stages. Herein, \vec{p} and \vec{q} symbolize the distinct dipole moments affiliated with each state.

II. EXPERIMENTAL METHODS AND OBSERVED PHYSICAL PHENOMENON

Leveraging cutting-edge infrastructure, USD boasts an avant-garde platform for crystal growth and detector development. Central to this system is the employment of a zone refining technique, artfully harnessed to attain exceptional purification levels in commercial ingots [24, 25]. These meticulously purified ingots lay the foundation for crystal growth through the renowned Czochralski method. With over a decade of research and development experience, we have achieved increased consistency in growing detector-grade crystals. It is noteworthy that we have integrated advanced machine learning techniques into this process to further enhance the growth of large-size detector-grade crystals, aiming to attain a level of purity conducive to exploring low-mass DM phenomena [26]. The crux of this study lies in a crystal cultivated in 2014 at USD, revealing a net impu-

rity level of $|N_A - N_D| = 4 \times 10^{11} \text{ cm}^{-3}$. This particular crystal assumes a p-type configuration. The subsequent fabrication of the detector, orchestrated at Texas A & M University, boasts a configuration encompassing four channels for charge readout positioned atop the detector. Departing from conventional paradigms, the detector's grounding component integrates a uniform aluminum (Al) electrode as opposed to a grid arrangement. This innovative design choice, while safeguarding the electric field's integrity, acts as a bulwark against charge leakage, thereby sustaining an unwavering and uniformly distributed electric field. Notably, this departure might have implications for the detector's susceptibility to effective neutralization through light-emitting diodes (LEDs). The detector's geometric layout mirrors the essence of SuperCDMS-style detectors, as pictured in Figure 2. Following meticulous wire-bonding, the detector seamlessly integrates into a dilution refrigerator, embarking on a comprehensive testing regimen hosted at the K100 Detector Testing Facility at the University of Minnesota (UMN).

The phenomenon of impact ionization prompted by impurities within Ge specimens has received extensive attention from researchers, particularly at temperatures surpassing 4 K [27, 28]. Noteworthy contributions to this knowledge pool have been made by various scholars. Recently, Phipps et al. have achieved a significant breakthrough by investigating the impact ionization of impurities using SuperCDMS-style detectors at an ultracold temperature of $\sim 40 \text{ mK}$ [29]. Furthermore, F. Ponce et al. demonstrated a room temperature pulsed laser's effect on a SuperCDMS silicon HVeV detector, unveiling coherent probabilities for charge trapping and impact ionization within the high-purity Si substrate under specific conditions [30]. Aligned with these pioneering works, our endeavor delves into the realm of time-dependent impact ionization, mirroring the ultracold environment at $\sim 40 \text{ mK}$. We employ a detector constructed from a distinctive and ultra-stable Ge crystal. This detector experiences gradual cryogenic cooling, eventually reaching an extraordinary temperature of approximately 40 mK. The ensuing meticulous evaluations transpire over two separate refrigeration runs: Run 67 in 2018 and Run 74 in 2021. In the context of Run 67, the arrangement involved situating four ^{241}Am sources directly above individual channels on the detector, an arrangement aptly illustrated in Figure 2. These setups employ lead collimators sporting 0.2 mm apertures, strategically permitting the transmission of 59.54 keV γ rays while adeptly blocking alpha particles through source encapsulation. Our findings manifest in the spectra from each channel, displaying distinct 59.54 keV peaks, with comprehensive measurements conducted diligently over a two-week interval. Contrastingly, Run 74 deploys a singular ^{241}Am source, ingeniously mounted on a carriage facilitated by a superconducting stepper motor, as graphically represented in Figure 3. This inventive source design incorporates a 0.5 mm collimator hole, leading to a

reduced flux of incident γ rays on the detector, constituting approximately 75% of the sources utilized in Run 67. Notably, the two runs unfold over extended time spans, inherently introducing fluctuations in the detector's operational state. These fluctuations can wield considerable influence over the detector's charge collection efficiency and trapping characteristics. For an all-encompassing comprehension of the nuanced intricacies underpinning these experiments, an in-depth analysis is available in the research paper authored by Acharya et al [18].

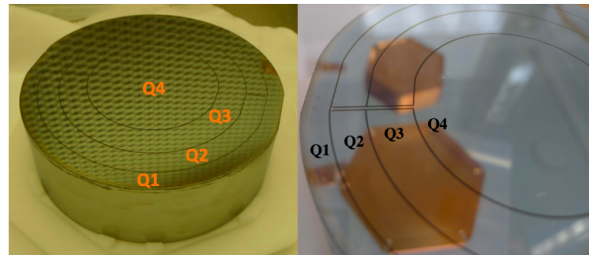


Figure 2. This illustration features the detector scrutinized in our investigation, equipped with four read-out electrodes labeled as Q_1 , Q_2 , Q_3 , and Q_4 . The detector boasts dimensions of 10 cm in diameter and 3.3 cm in thickness, ending it with a mass of approximately 1.34 kg.

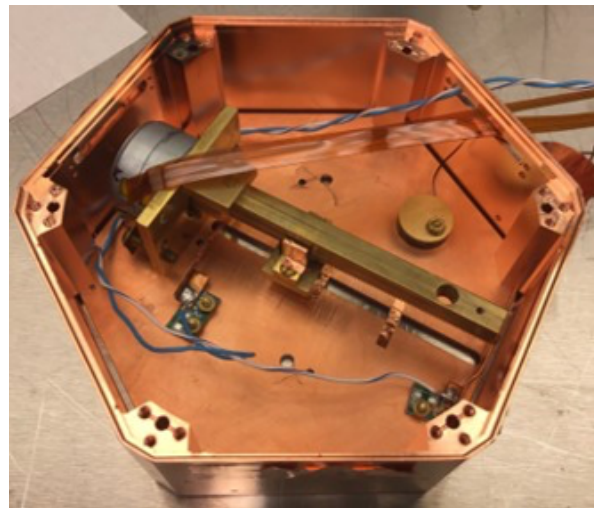


Figure 3. Presented here is the arrangement of the ^{241}Am source manipulator, ingeniously crafted utilizing superconducting mobile coil technology. This groundbreaking design facilitates meticulous control and positioning of the radioactive source, thereby significantly augmenting its effectiveness across a spectrum of scenarios [31].

III. EXPERIMENTAL DATA ANALYSIS AND RESULTS

We embarked on a thorough analysis, utilizing data collected at various bias voltages to comprehensively de-

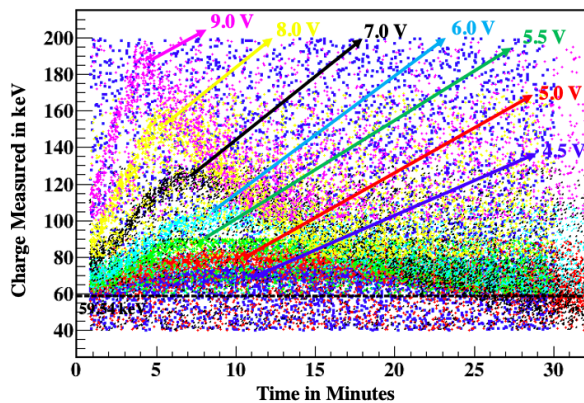


Figure 4. Depicted here is the evolving charge response from Q4, discernible across time when subjected to favorable biases during Run-67. The foundational signal associated with the 59.54 keV gamma-ray emission from Q4 exhibited an initial linear rise within a matter of minutes, which swiftly transitioned into an exponential decline spanning tens of minutes.

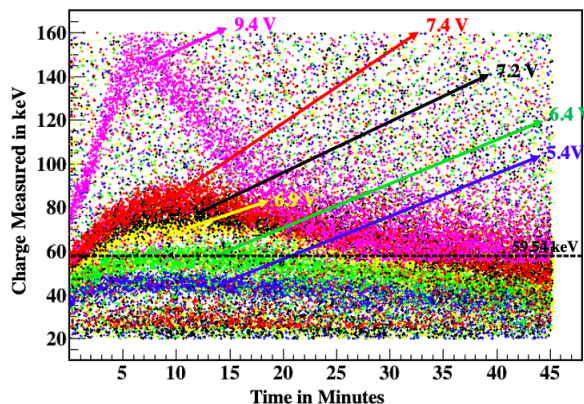


Figure 5. Provided is the temporal progression of the charge response in Q4, witnessed under positive biases throughout Run-74. The initial climb of the 59.54 keV gamma ray baseline stemming from Q4 displayed a linear trajectory during the initial moments, rapidly transitioning into an almost exponential decay pattern spanning a maximum duration of approximately 10 minutes.

lineate the charge collection efficiency for each channel, scrutinizing its interplay with bias and time. This investigation has yielded intriguing insights into the behavior of the 59.54 keV calibration line, as depicted in Figure 4 and Figure 5. Our observations unveiled a multitude of time-dependent phenomena: signal amplitudes from the 59.54 keV line exhibiting an initial increase post-bias application, succeeded by a subsequent descent towards a steady-state value. This distinctive phenomenon exclusively manifested under positive biases, owing to the strategic positioning of ^{241}Am sources on the biased side of the crystal, instigating the immediate collection of electrons and the subsequent drift of holes across the entirety of the detector's thickness.

Remarkably, this effect displayed varying degrees of

potency across channels, with its most pronounced manifestation occurring in the central channel (Q4), while its presence was faintest in the outer ring channel (Q1), indicative of a radial dependence. In light of this, our study centered its focus on the 59.54 keV line within the central channel (Q4) under positive biases, as it showcased the most promising outcomes.

Upon delving into the equilibrium state at $t=0$, where $p - n = N_D^+ + N_A^- = 0$, representing the charge neutralization state [32, 33], with p signifying free holes, n indicating free electrons, N_D^+ representing positively ionized donor atoms, and N_A^- representing negatively ionized acceptor atoms. We also introduce expressions for the density of acceptor impurities: $p + p_d = N_A$, where p_d signifies the unionized holes bound to the atom; similarly, $n + n_d = N_D$, with n_d representing the unionized donor electrons. When weaving these expressions together, they coalesce into a coherent depiction.

Figure 4 and Figure 5 visually articulate the temporal evolution of the impact ionization phenomenon, underscored by the drift of hole carriers under positive bias conditions. The process unfolds with hole impact ionization exhibiting a linear surge, modulated by bias and event rate. This amplified charge signal experiences an exponential decay, the timescale of which is intrinsically linked to the prevailing bias. This behavior is attributed to the attenuation of charge collection efficiency, stemming from the disruption of the bulk electric field due to the presence of trapped charges. The linear enhancement in the signal arising from hole impact ionization, in conjunction with the absence of comparable electron impact ionization, suggests that the spectrum of plausible sites for hole impact ionization is modest at its inception, originating from the capture of drifting electrons.

This intricate phenomenon encompasses the interplay of three distinct processes: $e^- + A^{0*} \rightarrow A^{-*}$, $h^+ + A^{-*} \rightarrow e^- + 2h^+ + A^-$, and $h^+ + A^- \rightarrow A^{0*}$. The first process entails the creation of cluster dipole states as a consequence of electron migration within the detector, spurred by background radiation. The second corresponds to the ionization of cluster dipole states initiated by hole carriers, while the third involves the confinement of h^+ carriers, culminating in the cessation of neutralization in the series' denouement [34]. These intricate mechanisms find graphical representation in Figure 1.

IV. THE THEORETICAL FRAMEWORK

To comprehensively understand the intricate nuances influencing the detector's performance under low-temperature conditions, it is crucial to subject various theoretical models to rigorous testing. The insights gained from these systematic evaluations have the potential to provide invaluable information, shaping our understanding of the detector's efficacy in low-mass DM detection. We have extensively explored several theoretical frameworks, supplementing our investigation with calcu-

lations. A detailed presentation of these comprehensive findings and discussions are outlined below.

A. Impact Ionization

At low cryogenic temperatures, the Ge detector showcases intriguing phenomena related to impact ionization (Fig. 4). Our earlier analysis of the impact ionization phenomenon employed a well-defined physical model that accounted for the observed behavior of charge carriers. We have established a relationship between the detected charge energy, denoted as $E(t)$, and the input 59.54 keV γ rays through the following equation [18]:

$$E(t) = E_\gamma \{ p_0 + p_1 \exp[\frac{p_2}{p_3} (1 - \exp(-p_3 t))] \} \exp(-p_4 t), \quad (1)$$

where $E_\gamma = 59.54$ keV. Our focus lies on two parameters, p_0 and p_1 , where $p_0 + p_1$ signifies the impact ionization factor, specifically for absolute impact ionization observation. If $p_0 + p_1 > 1$, it indicates a gain in charge energy due to impact ionization.

The sole instance of observed absolute impact ionization transpired at $t = 0$ during Run-67. Consequently, our analysis will center on understanding the detector's distinctive signature for impact ionization at low temperatures, leveraging the data obtained from Run-67. Upon applying the data from Run-67 to fit the model outlined in Equation 1, the fitted parameters for p_0 and p_1 under various biases were determined as,

Run 67		
Bias	p_0	p_1
4.5 V	1.05	0.015
5 V	1.07	0.018
5.5 V	1.09	0.019
6 V	1.13	0.020
7 V	1.22	0.028
8 V	1.28	0.032
9 V	1.39	0.038

Table I. Summary of the fitting for parameters p_0 and p_1 under various biases in Run-67 [18].

Figure 6 represents the correlation between two parameters, p_0 and p_1 , and the applied electric field at 40 mK. Regression analysis demonstrates a strong correlation, indicating these parameters vary according to the applied bias. The sum of these parameters, $p_0 + p_1$, defines an amplification factor, A . If n_t represents the charge carriers at any time t , it can be expressed as $n_t = n_0 e^{t/\tau_{\text{imp}}}$, where n_0 denotes the charge carriers at time $t = 0$ [20]. Here, $\tau_{\text{imp}} = \frac{1}{N_a \sigma_{\text{imp}}(E) v_d}$ stands for the charge generation time through impact ionization. Here, N_a represents the impurity concentration, $\sigma_{\text{imp}}(E)$ is the impact ionization scattering cross-section as a function of the electric field, and v_d signifies the drift velocity, given by $v_d = d/t$, where d denotes the detector width

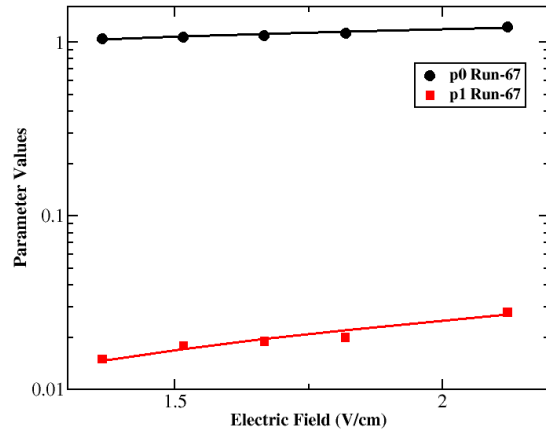


Figure 6. Shown are the fitting parameters, p_0 and p_1 using equation 1 as a function of the applied field, E , and fits a linear regression model, which demonstrates the correlation of the parameters with the electric field using the data from Run-67. The fitting functions for those parameters in Run 67 are: $p_0 = 0.25E + 0.69$, $p_1 = 0.017E - 0.0087$.

and t is the drift time. It should be noted that the amplification factor, $A = n_t/n_0$. After incorporating the equations $n_t = n_0 e^{t/\tau_{\text{imp}}}$ and $\tau_{\text{imp}} = \frac{1}{N_a \sigma_{\text{imp}}(E) v_d}$ alongside the amplification factor, the derived equation elucidating impact ionization due to the cluster dipole at cryogenic temperatures is succinctly expressed as:

$$\log(A) = N_a \times \sigma_{\text{imp}}(E) \times d, \quad (2)$$

B. Zero Field Cross-Section

The zero-field impact ionization cross-section for charged carriers within a detector denotes the detector's effective interaction area in the absence of an external electric field and quantifies the likelihood per unit area of charged carriers inducing an impact ionization event within the detector material. This parameter is intricately impacted by several factors, including the characteristics of the particle (such as charge and energy), alongside the specific properties inherent to the detecting material. Notably, the zero-field cross-section for cluster dipoles unveils a captivating domain within low-temperature physics. Understanding and harnessing this cross-section hold considerable potential for advancing our comprehension of elusive particles and their interaction dynamics within the context of low-temperature environments. If σ_0 denotes the zero field cross-section, its mathematical expression can be written as [35–38]:

$$\sigma_0 = \frac{\pi}{2} \times \frac{\hbar^2}{2m_h^* E_{BB'}}, \quad (3)$$

Here, m_h^* represents the effective mass of holes in the conduction band, and $E_{BB'}$ denotes the binding energy for the cluster dipole state, which will be discussed in detail later in the section dedicated to calculating the binding energy of cluster dipole states, as defined by Equation 8. Considering $m_h^* = 0.21m_e$, where m_e represents the mass of an electron, equivalent to $0.51 \text{ MeV}/c^2$. We can plug these parameters into Equation 3 to obtain $\sigma_0 = \frac{2.85 \times 10^{-15}}{E_{BB'}} \text{ cm}^2$, where $E_{BB'}$ has the unit in eV.

C. Impurity Freeze-Out

In a recent study, Mei et al. demonstrated a freeze-out process in both an n-type detector with $N_d = 7.02 \times 10^{10}/\text{cm}^3$ and a p-type detector with $N_a = 6.2 \times 10^9/\text{cm}^3$ [15, 20]. In these detectors, as the temperature falls below 11 K, there is a notable decrease in relative capacitance in the Ge detectors. Simultaneously, impurities in the detectors freeze out of the conduction or valence band, leading to a decrease in free charges within the detector volume as it is cooled down to 6.5 K [20]. Further cooling towards 5.2 K maintains a constant capacitance, indicating the absence of free charges. Nearly all impurity atoms then form electric dipole states (D^{0*} for donors and A^{0*} for acceptors) [20].

In the case of a p-type Ge detector, if an impurity atom is in its ground state, it is unable to capture charges. Nevertheless, when the detector is cooled to 5.2 K, this impurity atom undergoes a transition to a dipole state, gaining the ability to capture charges and forming a cluster dipole state. During this freeze-out process, impurity atoms, previously responsible for generating free carriers above 11 K, undergo a transition into bound states. These bound states manifest as electrically neutral, reflecting the transformation of impurities in the Ge detector into localized states. This phenomenon is commonly referred to as "freeze-out" in the context of semiconductor physics [20].

If the same detectors continue to cool down, as the detector temperature reaches 40 mK, it is anticipated that the dipole moments of these dipole states will increase, influenced by the temperature-dependent size of dipoles. These enhanced dipole states may weakly trap charge carriers, potentially resulting in the formation of cluster dipole states (D^{+*} , D^{-*} for donors, and A^{+*} , A^{-*} for acceptors) [15–17]. Figure 7 illustrates both a p-type dipole state and a p-type cluster dipole state [20].

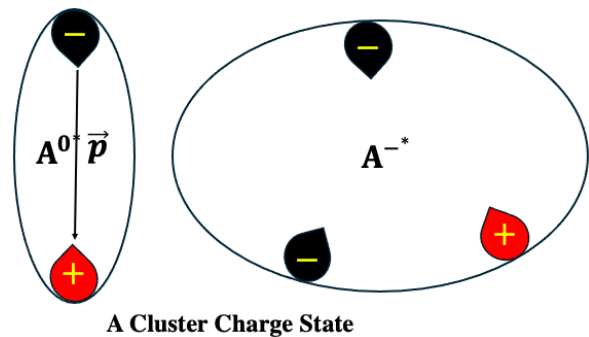


Figure 7. Shown are a p-type dipole state and a p-type cluster dipole state.

The freeze-out phenomenon significantly influences the behavior of Ge detectors at extremely low temperatures. In the state of freeze-out, the proportion of holes associated with acceptor levels in a p-type material with an impurity density of N_a is [20]:

$$\frac{p_a}{p + p_a} = \frac{1}{\frac{N_V}{4N_a} \exp\left[-\frac{E_a - E_v}{k_B T}\right] + 1}, \quad (4)$$

where p signifies the number density of free holes in the valence band and p_a denotes the number density of holes bound to acceptors, the mathematical relationship is expressed as $N_a = p + p_a$. Here, N_V signifies the density of states in the valence band, and $E_a - E_v \simeq 0.01 \text{ eV}$ represents the ionization energy of acceptors. The fraction of holes bound to acceptors, as defined by Equation 4, is visually represented in Figure 8.

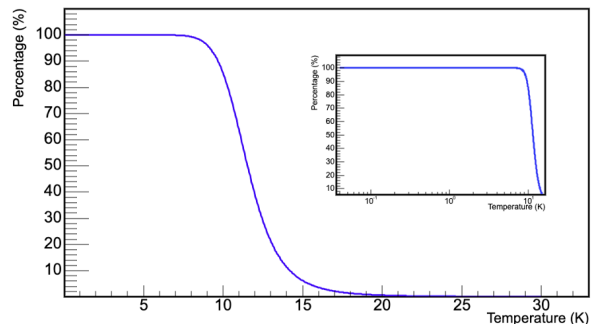


Figure 8. The presented graph illustrates the temperature-dependent ratio of holes bound to the acceptors, with $N_A = 4 \times 10^{11} \text{ cm}^{-3}$ and $E_a - E_v \simeq 0.01 \text{ eV}$ as the parameters for generating this plot. Additionally, it's important to observe that the inset plot conveys the same information across a wider temperature range, displayed in a logarithmic scale.

The graph vividly illustrates a significant rise in the percentage of holes bound to acceptors within the temperature range of 20 K to 8 K. It's important to note that this freeze-out range in temperature slightly deviates from the observations in Mei et al. [15, 20] due to variations in detector impurity levels. This dependence on impurity levels is also evident from Equation 4. By

rearranging the terms, Equation 4 can be reformulated as:

$$p = \frac{p_a N_V}{4N_a} \exp\left[-\frac{E_a - E_V}{K_B T}\right], \quad (5)$$

While residual impurity atoms remain ionized until approximately 20 K, a distinctive phenomenon emerges within the temperature range of 20 K to 8 K. During this period, these impurity atoms undergo a freeze-out process, transitioning into bound states that manifest as effectively charge-neutral entities. This abrupt transformation is intricately linked to the band structures illustrated in Figure 9, where $E_c - E_d \simeq 0.01$ eV and $E_a - E_V \simeq 0.01$ eV [39].

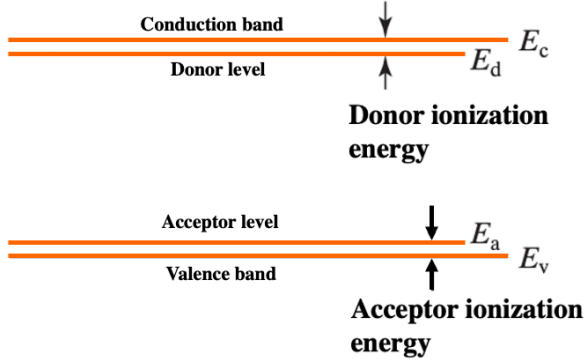


Figure 9. Displayed are the energy levels of donors and acceptors within semiconductor materials [40, 41].

The abrupt transition depicted in Figure 8 highlights the intricate relationship between temperature fluctuations and the corresponding band structures. It reveals a significant shift in the behavior of impurity atoms within this particular temperature range (20 K to 8 K). Under such circumstances, the expression for the number density of free holes (p) existing within the valence band can also be delineated as [9, 42]:

$$p = \left[\frac{N_a N_V}{4}\right]^{1/2} \exp\left[-\frac{E_a - E_V}{2K_B T}\right], \quad (6)$$

where N_V is the effective density of states in the valence band for Ge materials, which is given by $N_V = 9.6 \times 10^{14} T^{3/2} \text{ cm}^{-3}$.

In situations where the temperature drops below 8 K for the p-type detector under investigation, the number density of free holes is significantly smaller, by several orders of magnitude, than the number density of holes bound to acceptors. Consequently, it is reasonable to assume that p_a equals N_a and $E_a - E_V = E_B$, where E_B is the binding energy of the bound states. Therefore, combining Equations 5 and 6 facilitates the determination of the binding energy for the bound states - dipole states:

$$E_{BB} = K_B T \log\left(\frac{N_V}{4p_a}\right), \quad (7)$$

Please note that the binding energy of dipole states, represented by E_{BB} , differs from the ionization energy of acceptors, as illustrated in Figure 9. This distinction arises due to the formation of dipole states within a particular range of the Onsager radius when holes bound to acceptors. Consequently, the binding energy of these dipole states, influenced by the size of the dipole, may differ from the ionization energy of impurity atoms.

Utilizing Equation 7, we can assess the binding energy for various bound states, including dipole states and cluster dipole states, as a function of energy. As an illustrative example, Equation 7 is employed to calculate the binding energy of dipole states. Figure 10 portrays the binding energy of a dipole state with a dipole density of $N_a = 4 \times 10^{11} \text{ cm}^{-3}$ across different temperatures. Two specific temperature points are highlighted in the plot to emphasize the dipole state's binding energy. At a temperature of 5.2 K, the binding energy of the dipole states is calculated at 3.98 meV. However, as the temperature drops to 40 mK, the binding energy decreases substantially to 0.005 meV, reaching a level comparable to thermal energy.

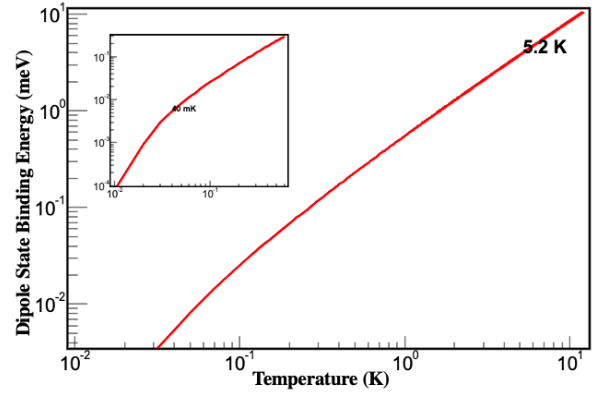


Figure 10. The plot illustrates the binding energy of the dipole state, while the inset plot extends the representation across a broader temperature range. Additionally, the plot furnishes details on the binding energy of the dipole state at two distinct temperatures, namely 5.2 K and 40 mK.

The binding energy of dipole states and cluster dipole states was measured at 5.2 K using both an n-type detector and a p-type detector in our previous study [16, 17]. The obtained values were found to be similar, as demonstrated in our research at 5.2 K [16, 17]. Generally, the binding energy of cluster dipole states is expected to differ from that of dipole states at the same temperature. This expectation arises because the binding energy of dipole states is confined by the Coulomb potential associated with the dipole size, whereas the binding energy of cluster dipole states is influenced by both the Coulomb potential determined by the trapping distance between two charge carriers with opposite charges and the dipole size. This was demonstrated by the previous measurements at 5.2 K [16, 17], where the dipole size and

the trapping distance between two mobile charge carriers with opposite charges are slightly different. However, this scenario may change when the detector is operated at 40 mK, where the dipole size becomes significantly larger than the trapping distance of two opposite charge carriers. In this scenario, the binding energy of dipole states is anticipated to be smaller than that of cluster dipole states. To assess the binding energy of cluster dipole states at 40 mK, we utilize the data obtained from Run-67.

D. Binding Energy of Cluster Dipole States

The presence of dipole states and cluster dipole states within the detector is influenced by both the detector's configuration and its operational mode. For this p-type detector, during the dilution refrigeration process, as the temperature approaches 40 mK, 100% of impurity atoms precipitate out from the conduction band, leading to the formation of electric dipole states identified as A^{0*} . Subsequently, electrons generated by the background radiation from the environment become trapped by the excited dipole state (A^{0*}), resulting in the emergence of the cluster dipole state labeled as A^{-*} . This phenomenon was observed during Run-67 when the detector was exposed to a ^{241}Am source in two operational modes. The creation of electron-hole pairs near the surface of the detector, primarily induced by 59.54 keV gamma rays, was a key aspect. In the first mode, a negative bias was applied to the detector, prompting electrons to drift across its surface. Conversely, in the second mode, a positive bias was employed, leading to the drift of holes across the detector. For illustration, Figure 11 depicts the detector operating at both -4 V and +4 V. The figure clearly indicates that electrons become trapped, whereas holes do not exhibit the same behavior.

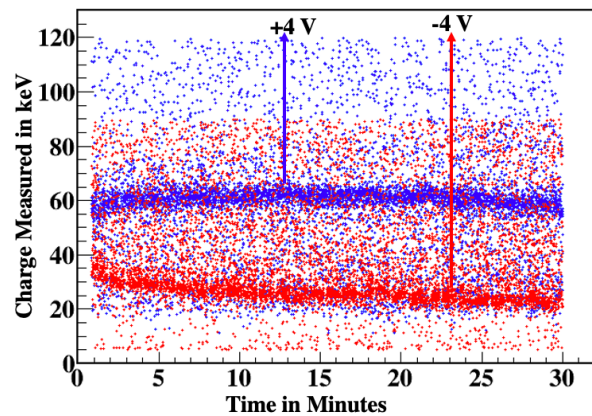


Figure 11. The depicted figure showcases the dynamic charge response of Q4 over time, influenced by two opposing biases: +4 V and -4 V. These biases symbolize the migration of holes under positive bias and electrons under negative bias across the entire detector during Run-67. The data unveils that the detection of electron-hole pairs originating from Q4, induced by 59.54 keV gamma rays, is fully realized under a +4 V bias. Conversely, under a -4 V bias, the energy detection is notably lower than 59.54 keV throughout a 30-minute period. This observation suggests a substantial entrapment of electrons within the p-type Ge detector.

In the UMN K100 laboratory, we contend with the environmental background of gamma-rays inducing electron-hole pairs within the detector. Additionally, cosmic-ray muons interact with the detector, resulting in the generation of electron-hole pairs. These background electrons become ensnared in a dipole state, leading to the formation of cluster dipole states, while holes experience less entrapment in a p-type detector subjected to the same bias voltage. This discrepancy arises from the limited space available for immobilized negative ions, responsible for trapping charge carriers, compared to the ample space for mobile bound holes.

The mobility of holes is dictated by the Onsager radius, denoted as R as defined earlier. Since the trapping probability is proportional to the available space where charges can be trapped, the likelihood of trapping for immobilized negative ions is smaller than that of mobile holes. Consequently, the probability of creating A^{-*} states is greater than that of forming A^{+*} states in a p-type detector. Note that A^{+*} and A^{-*} represent excited states that differ from the ground states of A^+ and A^- . This elucidates why electrons are more profoundly trapped than holes in a p-type detector, as clearly articulated in the recent publication [20].

Under a sufficiently electric field, holes traverse the detector undergoing impact ionization of a dipole state or a cluster dipole state at low temperatures. At a temperature of 40 mK, despite the binding energy of dipole states being comparable to thermal energy, the impact ionization of holes takes place in conjunction with a cluster dipole state. This phenomenon arises due to Coulomb repulsion among holes, which inhibits the occurrence of

this process at the operational voltage employed within the investigation, limited to a few volts.

Upon applying a positive bias voltage from the upper region of the detector and exposing it to an ^{241}Am source positioned above, hole carriers traverse the detector. Subsequently, these drifting holes engage in impact ionization interactions with the cluster dipole states (A^{-*}). As the bias voltage increases, the holes, serving as liberated charge carriers, accumulate greater kinetic energy, leading to the emission of electrons from the traps. This phenomenon results in a decrease in the count of cluster dipole states (A^{-*}), inducing the transition of A^{-} states, as depicted in Figure 7. The amplification of a single hole to two holes per reaction ($h^+ + A^{-*} \rightarrow e^- + 2h^+ + A^-$) tangibly demonstrates the occurrence of hole impact ionization within the detector.

Our investigation has revealed the presence of a cluster dipole state at the low cryogenic temperature of 40 mK. While the exact density of the cluster dipole state requires determination, we can utilize Equation 7 to calculate the binding energy associated with this state. To ascertain the density of the cluster dipole state, we will employ the relationship provided by Equation 2. Consequently, the updated equation for calculating the binding energy of the cluster dipole state is as follows:

$$E_{\text{BB}'} = K_{\text{B}}T \log\left(\frac{N_{\text{V}}}{4p_{\text{cd}}}\right), \quad (8)$$

where $E_{\text{BB}'}$ represents the binding energy for the cluster dipole state, and p_{cd} denotes the density of the cluster dipole state. Considering the model in Equation 2 to determine the density of the cluster dipole state at a cryogenic temperature of 40 mK, when the detector response is in an impact ionization mode with sufficient bias voltage and some cluster dipole states (A^{-*}) are ionized through impact ionization, we can express Equation 2 as $\log(A) = p_{\text{cd}} \times \sigma_0 E^{[p_1]} \times d$. Here, $\sigma_{\text{imp}}(E) = \sigma_0 E^{[p_1]}$, with $[p_1]$ as a fitting parameter. To simplify further, let's assume $[p_0] = p_{\text{cd}} \times \sigma_0$. Now, the simplified expression for calculating the binding energy for fitting the observed data is:

$$\log(A) = [p_0] \times E^{[p_1]} \times d, \quad (9)$$

Figure 12 displays the fitting line of Equation 9. From this, we obtained the values of two fitting parameters: $[p_0] = 8.9 \times 10^{-3} \pm 4.7 \times 10^{-4}$ and $[p_1] = 2.5 \pm 7.7 \times 10^{-2}$. We know that $[p_0]$ equals $p_{\text{cd}} \times \sigma_0$. By substituting the values of σ_0 and $[p_0]$, we find $p_{\text{cd}} = 3.12 \times 10^{12} \times E_{\text{BB}'} \text{ cm}^{-3}$. Thus, according to Equation 8, the binding energy for cluster dipole states (A^{-*}) at a cryogenic temperature can be expressed as:

$$E_{\text{BB}'} = K_{\text{B}}T \log\left(\frac{N_{\text{V}}}{4 \times 3.12 \times 10^{12} E_{\text{BB}'}}\right), \quad (10)$$

Plugging in all the constant values and solving Equation 10 numerically at a cryogenic temperature of 40 mK, we obtain $E_{\text{BB}'} = 0.034 \pm 0.0017$ meV. This ultra-low binding energy of cluster dipole states (A^{-*}) at cryogenic temperatures suggests a delicate balance between the forces holding these clusters together. At such low temperatures, the energy states of these clusters exhibit minimal thermal agitation, revealing a fundamental characteristic of their stability.

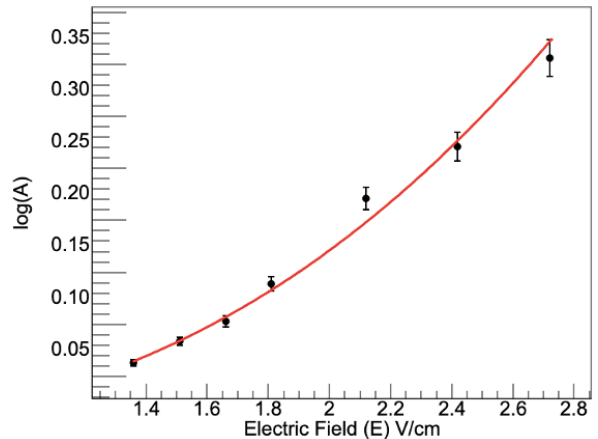


Figure 12. Displayed is the logarithmic value of the amplification factor, A , obtained by summing two fitting parameters, p_0 and p_1 from Table I. $\log(A)$ is plotted against the applied electric field. The error in $\log(A)$ was calculated, with the error in the electric field measurement primarily influenced by the precision of the applied bias voltage.

Calculating the binding energy of the cluster dipole state enabled us to determine the density of cluster dipole states, which is found to be $p_{\text{cd}} = 3.12 \times 10^{12} E_{\text{BB}'}$. Consequently, the density of cluster dipole states is found to be $1.05 \times 10^8 \pm 5.25 \times 10^6 \text{ cm}^{-3}$. Similarly, the zero-field impact ionization cross-section for charged carriers within the detector is computed using Equation 3, resulting in a value of $8.45 \times 10^{-11} \pm 4.22 \times 10^{-12} \text{ cm}^2$.

V. CONCLUSION

We conducted an experimental investigation into the time-dependent impact ionization phenomenon within a p-type Ge detector. Our findings unveil that temporal fluctuations in charge amplification, particularly concerning the 59.54 keV emission line from an ^{241}Am source, mainly arise from impact ionization induced by drifting holes traversing the detector. Our study delved into understanding the potential mechanisms driving this impact ionization, primarily attributing it to the generation and subsequent impact ionization of cluster dipole states.

Our study focused on a critical examination of binding energy and zero-field impact ionization cross-section of cluster dipole states within a low-temperature p-type Ge detector. At 40 mK, the zero-field cross-section of

cluster dipole states was determined to be $8.45 \times 10^{-11} \pm 4.22 \times 10^{-12} \text{cm}^2$, representing a two-order-of-magnitude increase compared to the cross-section of neutral impurity in Ge reported by Phipps et al.[29], which stands at $5 \times 10^{-13} \text{cm}^2$. This discrepancy is attributed to the notable difference in binding energy between cluster dipole states at 40 mK (0.034 meV) and neutral impurity states (approximately 10 meV). We also calculated the binding energy of cluster dipole states (A^{-*}), resulting in 0.034 ± 0.0017 . This ultra-low binding energy is distinctive to the detector state and plays a crucial role in the exploration of low-mass dark matter (DM) at the MeV scale. The low-scale binding energy, arising from impact ionization occurrences via intrinsic amplification, has the potential to enhance the detector's capability to achieve an ultra-low energy threshold, reaching as low as sub-meV.

The calculated cluster dipole state (A^{-*}) binding energy, observed when the detector operated at cryogenic temperatures, is lower than the typical binding energy associated with ground-state impurities in Ge, which is ~ 10 meV for the detector in our study. However, this binding energy is higher than the thermal energy at 40 mK, which is 0.005 meV. This suggests that these cluster dipole states might not significantly contribute to the usual impurity-related effects observed in the detector at higher temperatures. Additionally, it implies that these cluster dipole states might remain stable and distinguishable from thermal fluctuations at this low temperature. This stability hints at the potential for these states to maintain a distinct identity, unaffected by thermal agitation, thus offering a stable feature or characteristic in

the detector's behavior at cryogenic temperatures.

At electric fields below 3 V/cm, our calculations yield a density of cluster dipole states (A^{-*}), denoted as p_{cd} , at $1.05 \times 10^8 \pm 5.25 \times 10^6 \text{cm}^{-3}$. This value signifies the density of states associated with cluster dipole states formed by trapping electrons from background radiation. Our findings underscore the capacity of energetic charge carriers to ionize these cluster dipole states, thereby generating additional charge carriers. This phenomenon holds particular significance in facilitating impact ionization, especially in scenarios characterized by low electric fields.

In summary, our study offers crucial insights into the behavior of impurities within Ge detectors. These revelations have the potential to influence the design of innovative detectors, particularly those crafted for tasks such as MeV-scale DM searches. Additionally, the observation of low binding energies suggests the feasibility of utilizing appropriately doped impurities in Ge for the creation of low-threshold detectors capable of detecting low-mass MeV scale DM particles.

VI. ACKNOWLEDGEMENT

The authors extend their sincere gratitude to Vuk Mandic for his invaluable support in facilitating this research, providing access to his dilution refrigerator, and contributing to the data acquisition system. This research received partial support from NSF OISE 1743790, NSF PHYS 1902577, NSF PHYS 2310027, DOE DE-SC0024519, DOE grants DE-FG02-10ER46709 and DE-SC0004768, as well as a research center funded by the State of South Dakota.

-
- [1] Felix Kahlhoefer. Review of lhc dark matter searches. *International Journal of Modern Physics A*, 32(13):1730006, 2017.
 - [2] Troy A Porter, Robert P Johnson, and Peter W Graham. Dark matter searches with astroparticle data. *Annual Review of Astronomy and Astrophysics*, 49:155–194, 2011.
 - [3] Paul L Brink, B Cabrera, CL Chang, J Cooley, RW Ogburn, DS Akerib, CN Bailey, PP Brusov, MR Dragowsky, DR Grant, et al. Beyond the cdms-ii dark matter search: Supercdms. *arXiv preprint astro-ph/0503583*, 2005.
 - [4] P Agnes, Ivone Freire da Mota Albuquerque, T Alexander, AK Alton, GR Araujo, David M Asner, M Ave, Henning O Back, B Baldin, G Batignani, et al. Low-mass dark matter search with the darkside-50 experiment. *Physical review letters*, 121(8):081307, 2018.
 - [5] Oscar Agertz and Andrey V Kravtsov. The impact of stellar feedback on the structure, size, and morphology of galaxies in milky-way-sized dark matter halos. *The Astrophysical Journal*, 824(2):79, 2016.
 - [6] Paul H Frampton. *Did Time Begin? Will Time End? Maybe the Big Bang Never Occurred*. World Scientific, 2009.
 - [7] Jürg Diemand, Michael Kuhlen, and Piero Madau. Dark matter substructure and gamma-ray annihilation in the milky way halo. *The Astrophysical Journal*, 657(1):262, 2007.
 - [8] Fabio Iocco, Miguel Pato, and Gianfranco Bertone. Evidence for dark matter in the inner milky way. *Nature Physics*, 11(3):245–248, 2015.
 - [9] D-M Mei, G-J Wang, H Mei, G Yang, J Liu, M Wagner, R Panth, K Kooi, Y-Y Yang, and W-Z Wei. Direct detection of mev-scale dark matter utilizing germanium internal amplification for the charge created by the ionization of impurities. *The European Physical Journal C*, 78(3):187, 2018.
 - [10] G Angloher, P Bauer, A Bento, C Bucci, L Canonica, X Defay, A Erb, F v Feilitzsch, N Ferreiro Iachellini, P Gorla, et al. Results on mev-scale dark matter from a gram-scale cryogenic calorimeter operated above ground. *The European Physical Journal C*, 77(9):1–6, 2017.
 - [11] Haipeng An, Maxim Pospelov, Josef Pradler, and Adam Ritz. Directly detecting mev-scale dark matter via solar reflection. *Physical review letters*, 120(14):141801, 2018.
 - [12] Phillip S Barbeau, Petra Merkel, Jinlong Zhang, Darin Acosta, Anthony A Affolder, Artur Apresyan, Marina

- Artuso, Vallary Bhopatkar, Stephen Butalla, Gabriella A Carini, et al. Report of the instrumentation frontier working group for snowmass 2021. *arXiv preprint arXiv:2209.14111*, 2022.
- [13] J Gascon, E Armengaud, Q Arnaud, C Augier, A Benoit, L Bergé, J Billard, A Broniatowski, P Camus, A Cazes, et al. Low-mass dark matter searches with edelweiss. *arXiv preprint arXiv:2112.05467*, 2021.
- [14] Seong Woo Oh, Artem O Denisov, Pengcheng Chen, and Jason R Petta. Cryogen-free scanning gate microscope for the characterization of si/si0. 7ge0. 3 quantum devices at milli-kelvin temperatures. *AIP Advances*, 11(12), 2021.
- [15] D-M Mei, R Panth, K Kooi, H Mei, S Bhattarai, M Raut, P Acharya, and G-J Wang. Evidence of cluster dipole states in germanium detectors operating at temperatures below 10 k. *AIP Advances*, 12(6), 2022.
- [16] Mathbar Singh Raut, Dongming Mei, Sanjay Bhattarai, Rajendra Panth, Kyler Kooi, Hao Mei, and Guojian Wang. Development of low-threshold detectors for low-mass dark matter searches with a p-type germanium detector operated at cryogenic temperature. *Journal of Low Temperature Physics*, pages 1–15, 2023.
- [17] Sanjay Bhattarai, Dongming Mei, Mathbar Raut, Rajendra Panth, Kyler Kooi, Hao Mei, and Guojian Wang. Investigating binding energies and trapping cross-sections in an n-type ge detector at low temperatures. *Frontiers in Detector Science and Technology*, 1:1275385, 2023.
- [18] P Acharya, M Fritts, D-M Mei, V Mandic, C-J Wang, R Mahapatra, and M Platt. Observation of time-dependent internal charge amplification in a planar germanium detector at cryogenic temperature. *The European Physical Journal C*, 83(4):278, 2023.
- [19] Marco Klinkigt, Rudolf Weeber, Sofia Kantorovich, and Christian Holm. Cluster formation in systems of shifted-dipole particles. *Soft Matter*, 9(13):3535–3546, 2013.
- [20] Dongming Mei. Exploring the potential of residual impurities in germanium detectors for low-mass dark matter detection. *arXiv preprint arXiv:2310.11955*, 2023.
- [21] Simon M Sze, Yiming Li, and Kwok K Ng. *Physics of semiconductor devices*. John wiley & sons, 2021.
- [22] IJ Arnuist, FT Avignone III, AS Barabash, CJ Barton, FE Bertrand, E Blalock, B Bos, M Busch, M Buuck, TS Caldwell, et al. α -event characterization and rejection in point-contact hpge detectors. *The European Physical Journal C*, 82(3):226, 2022.
- [23] EJ Meijer, DM De Leeuw, Saeed Setayesh, E Van Veenendaal, B-H Huisman, PWM Blom, JC Hummelen, Ullrich Scherf, and TM Klapwijk. Solution-processed ambipolar organic field-effect transistors and inverters. *Nature materials*, 2(10):678–682, 2003.
- [24] Guojian Wang, Mark Amman, Hao Mei, Dongming Mei, Klaus Irscher, Yutong Guan, and Gang Yang. Crystal growth and detector performance of large size high-purity ge crystals. *Materials Science in Semiconductor Processing*, 39:54–60, 2015.
- [25] G Yang, YT Guan, FY Jian, MD Wagner, H Mei, GJ Wang, SM Howard, DM Mei, A Nelson, J Marshal, et al. Zone refinement of germanium crystals. In *Journal of Physics: Conference Series*, volume 606, page 012014. IOP Publishing, 2015.
- [26] PRAMOD ACHARYA, Sanjay Bhattarai, Mathbar Raut, Hao Mei, and Dongming Mei. Machine learning model identification on a single hpge crystal growth dynamics-based lstm neural networks. *Bulletin of the American Physical Society*, 2023.
- [27] A Zylbersztejn. Theory of low-temperature impact ionization in high-purity germanium. *Physical Review*, 127(3):744, 1962.
- [28] W Pickin. Impact ionization of shallow donor states in germanium, 4–7° k. *Solid-State Electronics*, 21(1):309–314, 1978.
- [29] A Phipps, B Sadoulet, and KM Sundqvist. Observation of impact ionization of shallow states in sub-kelvin, high-purity germanium. *Journal of Low Temperature Physics*, 184:336–343, 2016.
- [30] F Ponce, C Stanford, S Yellin, W Page, C Fink, M Pyle, B Sadoulet, B Serfass, SL Watkins, PL Brink, et al. Measuring the impact ionization and charge trapping probabilities in supercdms hvev phonon sensing detectors. *Physical Review D*, 101(3):031101, 2020.
- [31] N Mast, M Fritts, DJ Sincavage, P Cushman, and V Mandic. An in-situ movable calibration source for cryogenic particle detectors. *Nuclear Instruments and Methods in Physics Research Section A: Accelerators, Spectrometers, Detectors and Associated Equipment*, 971:164070, 2020.
- [32] Homer D Hagstrum. Theory of auger neutralization of ions at the surface of a diamond-type semiconductor. *Physical Review*, 122(1):83, 1961.
- [33] GH Wei, ZX Yang, XQ Dai, SY Wei, M Wang, and T Zhang. Ion neutralization at an si-or ge-type semiconductor surface. *Journal of Physics: Condensed Matter*, 6(27):4991, 1994.
- [34] Pramod Acharya, Matthew Fritts, Dongming Mei, Vuk Mandic, and Pire-Gemadarc Team. Observation of time-dependent impact ionization in a large-size ge detector made from a crystal grown at usd. In *APS April Meeting Abstracts*, volume 2022, pages T08–005, 2022.
- [35] JF Palmier. Impurity ionization in n-type germanium. *Physical Review B*, 6(12):4557, 1972.
- [36] Edmundo A Gutierrez-D, Jamal Deen, and Cor Claeys. *Low temperature electronics: physics, devices, circuits, and applications*. Elsevier, 2000.
- [37] Arran Thomas James Phipps. *Ionization collection in detectors of the cryogenic dark matter search PhD thesis*. University of California, Berkeley, 2016.
- [38] Kyle Michael Sundqvist. *Carrier transport and related effects in detectors of the cryogenic dark matter search PhD thesis*. University of California, Berkeley, 2012.
- [39] DM Mei, RB Mukund, WZ Wei, Rajendra Panth, Jing Liu, Hao Mei, YY Li, Pramod Acharya, Sanjay Bhattarai, Kyler Kooi, et al. Impact of charge trapping on the energy resolution of ge detectors for rare-event physics searches. *Journal of Physics G: Nuclear and Particle Physics*, 47(10):105106, 2020.
- [40] David K Ferry. *Semiconductors*. IoP Publishing, 2013.
- [41] Lev I Berger. *Semiconductor materials*. CRC press, 2020.
- [42] W Van Roosbroeck. Theory of the flow of electrons and holes in germanium and other semiconductors. *The Bell System Technical Journal*, 29(4):560–607, 1950.

A Tampering Risk of Fiber-Based Frequency Synchronization Networks and Its Countermeasures

Hongfei Dai, Yufeng Chen, Wenlin Li, Fangmin Wang, Guan Wang, Zhongwang Pang, and Bo Wang

Abstract—Fiber optic networks are used worldwide and have been regarded as excellent media for transmitting time-frequency (TF) signals. In the past decades, fiber-based TF synchronization techniques have been extensively studied. Instruments based on these techniques have been successfully applied. With the increasing application of TF synchronization instruments, their security has become an important issue. Unfortunately, the security risks of fiber-based frequency synchronization (FbFS) instruments have been overlooked. This paper proposes a frequency tampering method called “frequency lens”. On a 200 km fiber link, we demonstrate a frequency tampering scenario using a frequency lens-enabled frequency tampering module (FTM). On the user side, the frequency value of the recovered 100 MHz signal can be stealthily altered within a range of $100 \text{ MHz} \pm 100 \text{ Hz}$, while the frequency dissemination stability of the system remains normal. Related to this tampering risk, potential hazards in three different application scenarios, which rely on precise frequency references, are analyzed. Two countermeasures are also proposed to solve this tampering risk.

Index Terms—Fiber-based frequency synchronization; fiber network; tampering risk.

I. INTRODUCTION

At present, optical fiber networks are used worldwide and have been one of the largest infrastructures for human utilization. As an excellent transmission medium, the optical fiber has unique advantages in transmitting time-frequency (TF) reference. In the past decades, fiber-based TF synchronization techniques have been widely studied [1]–[10]. The related instruments have been successfully applied in various fields, such as metrology [6], [8], [11], communication [12], navigation [13], and radio astronomy [14], [15], as shown in Fig. 1. In the near future, fiber-based TF synchronization instruments will support strict timing requirements in the fields of fifth-generation/sixth-generation communication [16], smart cities [17], global seismic monitoring [18], [19], and distributed computation [20].

With the increasing applications of fiber-based TF synchronization instruments, their security has become an important issue that must be considered in advance [21]. There have been previous studies on attacks and countermeasures related to fiber-based time synchronization (FbTS) systems [22]–[26].

This work was supported in part by the National Natural Science Foundation of China under Grant 62171249, in part by the National Key Project of Research and Development under Grant 2021YFA1402102, and in part by Tsinghua Initiative Scientific Research Program. (*Corresponding author: Bo Wang.*)

The authors are with State Key Laboratory of Precision Space-time Information Sensing Technology, Department of Precision Instrument, Tsinghua University, Beijing 100084, China, and also with the Key Laboratory of Photonic Control Technology (Tsinghua University), Ministry of Education, Beijing 100084, China (e-mail: bo.wang@tsinghua.edu.cn).

However, research on corresponding aspects of fiber-based frequency synchronization (FbFS) systems is limited. Notably, those methods designed for attacking FbTS cannot be directly applied to FbFS. The primary method in attacking FbTS is to partially disrupt the symmetry of the fiber link in both forward and backward directions, causing asymmetry in the delay of time signals within the link. However, the asymmetry of a small portion of the fiber link cannot cause a disastrous effect on frequency synchronization. For FbFS instruments, the disastrous attack is covertly and slightly tampering with the disseminated frequency reference without affecting its stability. This means that third parties can control important applications with a frequency tampering module (FTM), as shown in Fig. 1. It would not disrupt the normal operation of applications relying on frequency synchronization but could lead to incorrect or biased results.

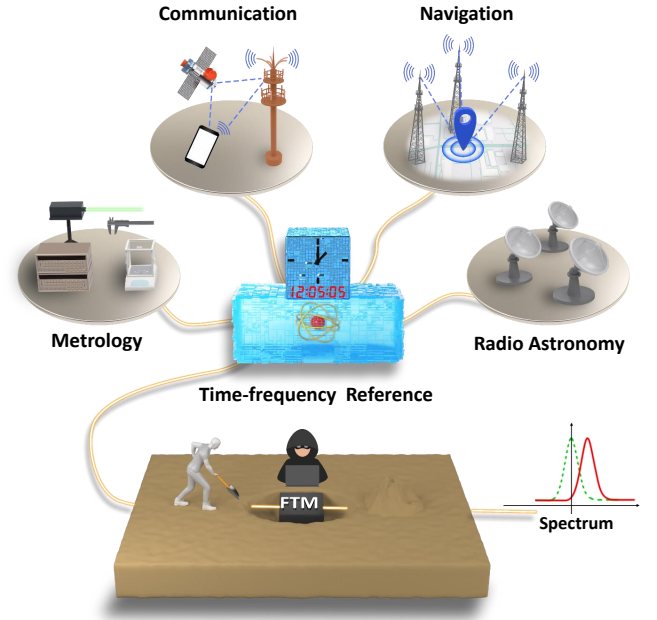


Fig. 1. Schematic diagram of the fiber-based TF synchronization network and tampering risk behavior. FTM, frequency tampering module.

For FbFS systems, there are normally two phase-locked loops (PLLs), as shown in Fig. 2(a). PLL1 is used to compensate for the phase fluctuation induced by fiber dissemination. PLL2 is used as a clean oscillator to optimize the phase noise spectrum of the recovered frequency signal [4], [27]. Monitoring the locking status of PLL1 normally serves as an effective method for system security monitoring. PLL1

compares the returned frequency signal from the user site with the local frequency reference, making it sensitive to any alterations in the transmitted signal. Typically, tampering with the transmitted frequency signal results in a significant change in the locking status of PLL1. Although this monitoring method seems simple and effective, it has inherent flaws. Once a tampering method can make the returned frequency signal unbiased and bypass the locking status monitoring, tampering activities will become undetectable.

In this paper, we propose a frequency tampering method called “frequency lens” and give countermeasures against it. With a frequency lens-enabled FTM, it can controllably alter the value of the disseminated frequency at any point along the fiber link. This alteration does not compromise the relative stability of frequency dissemination and can bypass locking status monitoring. In our case, tampering with the recovered 100 MHz signal within ± 100 Hz is demonstrated on a 200 km fiber link. The relative stability of the recovered biased frequency (compared with the reference at the server site) is maintained at the same level as the normal state, i.e., $2.2 \times 10^{-14}/1$ s and $2.2 \times 10^{-17}/10^5$ s. We analyze its damaging effects on timekeeping, metrology, and astronomical observation, respectively. To solve the security issue of FbFS systems, we propose two countermeasures against frequency tampering methods. We anticipate this article will provoke research interest in the security issue of FbFS instruments and provide instructive insights for future investigations.

II. METHOD

We consider a typical fiber-based radio frequency synchronization system. The schematic diagram is shown in Fig. 2(a), which includes a reference $V_{ref} = \cos(2\pi f_{ref}t + \phi_{ref})$, a server $V_S = \cos(2\pi f_S t + \phi_S)$, a user $V_U = \cos(2\pi f_U t + \phi_U)$, and a fiber link with one-way loop noise ϕ_n [4]. For convenience, the amplitude items of these signals are disregarded. When the frequency synchronization system is active by PLL1, the frequency f_S is aligned with f_{ref} . The phase ϕ_S is locked to the difference between ϕ_{ref} and ϕ_n , i.e., $\phi_S = \phi_{ref} - \phi_n$. After transmission, the signal V_U is recovered at the user site, and the one-way loop noise is automatically eliminated. As a consequence, the following relationship can be applied:

$$\phi_U = \phi_S + \phi_n = \phi_{ref}, \quad (1)$$

$$f_U = f_S = f_{ref}. \quad (2)$$

Under normal conditions, it enables highly stable frequency synchronization between the user and reference. If an intruder attempts to break the synchronization scenario, such as tampering with the recovered frequency, the locking status of PLL1 is affected. However, if the tampering operation can bypass the locking status monitoring, the recovered frequency can be slightly and covertly altered.

Here, we use a “frequency lens” to achieve this covert intrusion. The concept of the frequency lens is inspired by an optical lens. In geometrical optics, the reversibility principle states that light will follow exactly the same path if its direction of travel is reversed. An optical lens can form an enlarged image, as shown in Fig. 2(b). It can also form a

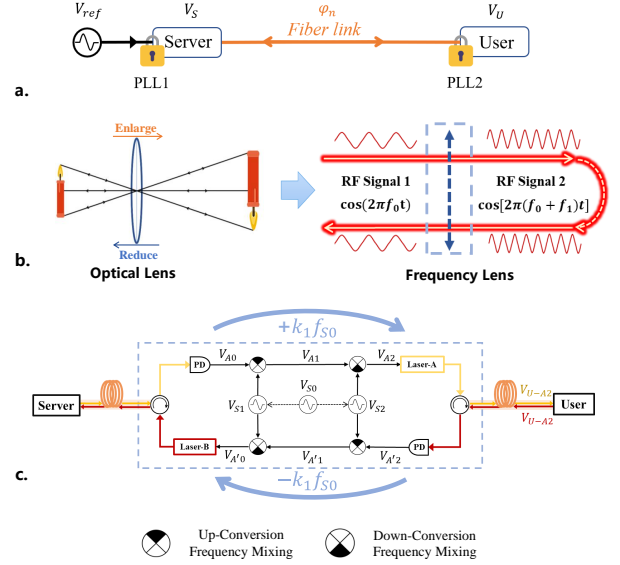


Fig. 2. Principles of FbFS and the frequency lens. (a) Structure of a typical FbFS system. (b) Comparison between the optical lens and frequency lens. (c) Schematic diagram of the frequency lens. PD, photodetector.

reduced image by switching the position of the object and image. Thus, if the disseminated frequency can be changed in a similar way, the monitoring of the locking status will be bypassed, and stealthy frequency tampering will be achieved. Fig. 2(c) illustrates the detailed structure of the frequency lens. There is an oscillator V_{S0} , i.e., $V_{S0} = \cos(2\pi f_{S0}t + \phi_{S0})$. The signals V_{S1} and V_{S2} are synthesized via V_{S0} , as follows:

$$V_{S1} = \cos(2\pi f_{S1}t + \phi_{S1}) \\ = \cos[2\pi(k + k_1)f_{S0}t + (k + k_1)\phi_{S0}], \quad (3)$$

$$V_{S2} = \cos(2\pi f_{S2}t + \phi_{S2}) \\ = \cos(2\pi k f_{S0}t + k\phi_{S0}), \quad (4)$$

where k and k_1 are the frequency synthesis factors. Compared with k , the factor k_1 is very small, which is usually smaller than 2.1×10^{-4} .

Using the frequency lens, the input signal V_{A0} (the disseminated RF signal modulated on the laser carrier, i.e., $V_{A0} = \cos(2\pi f_{A0}t + \phi_{A0})$) can be parametrically converted to the output signal V_{A2} in the forward direction. Conversely, in the backward direction, the signal $V_{A'2}$ (the same frequency as V_{A2}) can be parametrically converted to the signal $V_{A'0}$ again (the same frequency as V_{A0}). Specifically, the parametrical conversion process is accomplished by using second-order nonlinear electronic devices, such as electric mixers, to generate signals V_{A1} and V_{A2} . In the forward direction, V_{A1} is generated by up-mixing V_{A0} and V_{S1} , while V_{A2} is generated by down-mixing V_{A1} and V_{S2} , as follows:

$$V_{A1} = \cos(2\pi f_{A1}t + \phi_{A1}) \\ = \cos\{2\pi[(k + k_1)f_{S0} + f_{A0}]t + (k + k_1)\phi_{S0} + \phi_{A0}\}, \quad (5)$$

$$V_{A2} = \cos(2\pi f_{A2}t + \phi_{A2}) \\ = \cos[2\pi(k_1 f_{S0} + f_{A0})t + k_1\phi_{S0} + \phi_{A0}]. \quad (6)$$

Consequently, the disseminated frequency is shifted from f_{A0} to $(k_1 f_{S0} + f_{A0})$. The output signal V_{A2} can be used to modulate the laser carrier again, which is transmitted to the user site along the optical fiber link. Referring to Appendix A, the RF signal V_{U-A2} is recovered at the user side, i.e., $V_{U-A2} = \cos[2\pi(k_1 f_{S0} + f_{A0})t + k_1 \phi_{S0} + \phi_{A0} + \phi_{n2}]$, where ϕ_{n2} is the phase noise introduced by this part of the fiber link between the frequency lens and the user site. Notably, the application of the frequency lens induces $k_1 \phi_{S0}$ in phase noise. For example, if the frequency stability of V_{S0} is $1 \times 10^{-11}/1s$ is chosen, $k_1 \phi_{S0}$ is $2 \times 10^{-15}/1s$ when k_1 is set as 2×10^{-4} . It proves that it does not significantly affect the relative stability of the frequency dissemination.

At the user site, the RF signal V_{U-A2} is also modulated on another laser carrier, whose wavelength is different, and returned to the frequency lens along the fiber. In the backward direction, signal $V_{A'2}$ is detected by the frequency lens, as follows:

$$\begin{aligned} V_{A'2} &= \cos(2\pi f_{A'2} t + \phi_{A'2}) \\ &= \cos[2\pi(k_1 f_{S0} + f_{A0})t + k_1 \phi_{S0} + \phi_{A0} + 2\phi_{n2}]. \end{aligned} \quad (7)$$

In the lower part of Fig. 2(c), $V_{A'0}$ can be obtained by similar treatments to that of Eq. (5) and Eq. (6), as follows:

$$\begin{aligned} V_{A'1} &= \cos(2\pi f_{A'1} t + \phi_{A'1}) \\ &= \cos\left\{2\pi[(k + k_1)f_{S0} + f_{A0}]t \right. \\ &\quad \left. + (k + k_1)\phi_{S0} + \phi_{A0} + 2\phi_{n2}\right\}, \end{aligned} \quad (8)$$

$$\begin{aligned} V_{A'0} &= \cos(2\pi f_{A'0} t + \phi_{A'0}) \\ &= \cos(2\pi f_{A0} t + \phi_{A0} + 2\phi_{n2}). \end{aligned} \quad (9)$$

In this way, we achieve symmetrical enlargement and reduction of the disseminated frequency, such as $f_{A0} \rightarrow f_{A2}$ and $f_{A'2} \rightarrow f_{A'0}$. Considering the relationship between $f_{A0} = f_{A'0}$ and $f_{A2} = f_{A'2}$, the insertion of the frequency lens does not affect the normal operation of the frequency synchronization system. In other words, the disseminated frequency can be altered by slightly changing the parameter k_1 , and the locking status will be maintained.

The premise of this tampering operation is to covertly insert a tampering module with a frequency lens function into the fiber link. Considering the operation status of optical fiber networks, link outages due to natural disasters, human accidents, and extreme weather are common. Moreover, according to the above description, the intrusion position of the tampering module can be arbitrary along the fiber link. All of these conditions provide ample opportunities for tampering module intrusion, making the possibility of these risky situations much more likely.

III. EXPERIMENTAL SETUP

As shown in Fig. 3(a), we have established a fiber-based radio frequency synchronization system. The frequency synchronization system consists of a server and a user, which are connected by a 200 km fiber link. The server is referenced to a 100 MHz output of a hydrogen maser. The system builds 2 PLLs to recovered a frequency signal at the user

that is synchronized with the hydrogen maser. To improve the detection resolution of phase noise during transmission, the transmitted signal is 2.1 GHz RF signal modulated on the laser carriers, whose wavelengths are 1546.92 nm (C38) and 1546.12 nm (C39). A detailed description of the principles of this system can be found in Appendix A. For attenuation and dispersion, the erbium-doped fiber amplifier (EDFA) and the chirped fiber Bragg grating (CFBG) have emerged as effective solutions [27]. In the experiment, we insert two CFBG-enhanced bidirectional EDFA (Bi-EDFAs) into the fiber link to amplify the laser signals transmitted in both directions and to compensate for dispersion. The structure of Bi-EDFA is shown in Fig. 3(b), and two CFBGs are used together with EDFA-1 and EDFA-2, respectively.

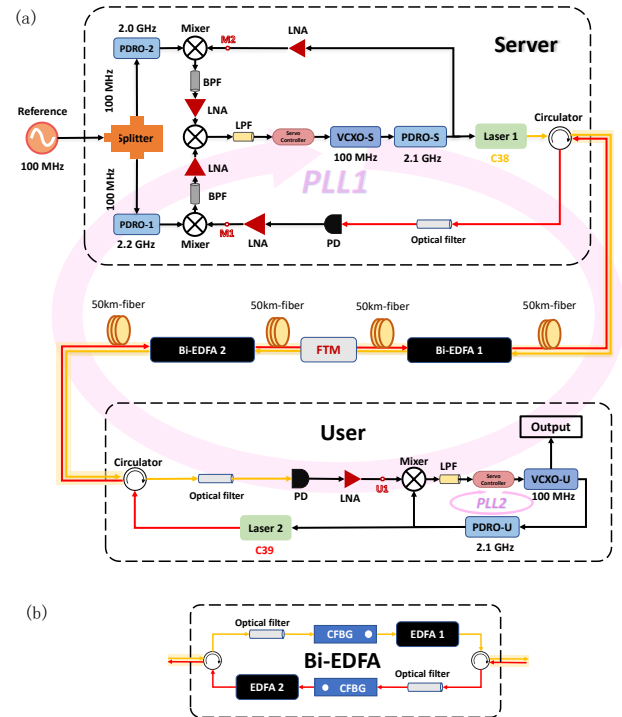


Fig. 3. Schematic diagram of the frequency synchronization system, bidirectional erbium-doped fiber amplifier (Bi-EDFA). (a) Frequency synchronization system, containing a server, a user and a fiber link. The black line represents RF signals. The yellow line represents the optical signal with the wavelength of 1546.92 nm (C38), and the red line represents the optical signal with the wavelength of 1546.12 nm (C39). (b) Chirped fiber grating enhanced Bi-EDFA, which plays the role of optical power amplification and dispersion elimination in the fiber link. EDFA, erbium-doped fiber amplifier; VCXO, voltage-controlled crystal oscillator; PDRO, phase-locked dielectric resonant oscillator; LNA, low noise amplifier; CFBG, chirped fiber grating.

To realize the frequency tampering, we insert the frequency lens-enabled FTM into the fiber link, whose structure is shown in the gray board of Fig. 4. This FTM is composed of two dense wavelength division multiplexing (DWDM) modules, two optical switches, a short fiber connected to the ‘other’ ports of DWDM modules, and the key part of the FTM connected to the C38/C39 ports of DWDM modules. Inside the frequency lens, the optical signals from both directions are detected by photodetectors (PDs). A 10 MHz oscillator V_{S0} is used to synthesize the signals V_{S1} and V_{S2} as shown in

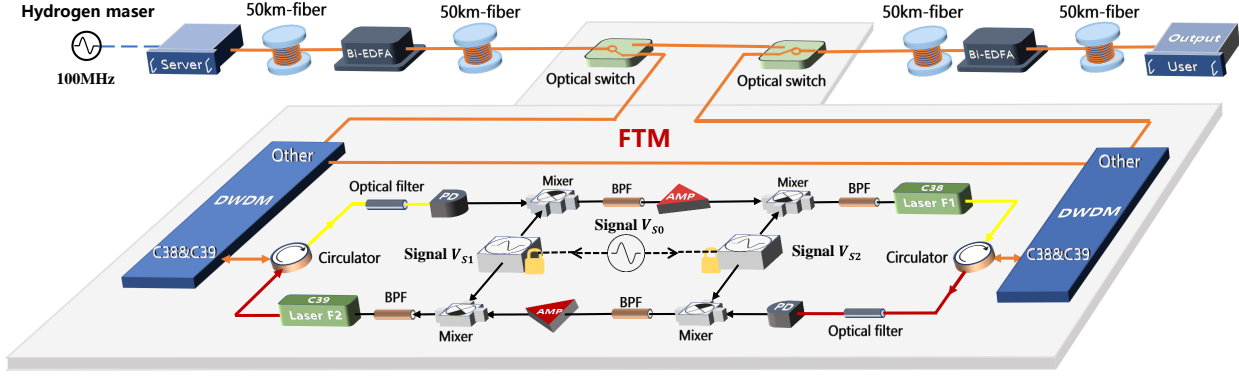


Fig. 4. Schematic diagram of frequency lens-enabled FTM. The orange lines represent optical fiber links. The black line represents RF signals. DWDM, dense wavelength division multiplexing; PD, photodetector; BPF, band-pass filter; AMP, amplifier.

Eq. (3) and Eq. (4), where $k = 90$, and k_1 can be set within $\pm 2.1 \times 10^{-4}$. Specifically, f_{S1} is set to $(900 + 10k_1)$ MHz, and f_{S2} is set to 900 MHz.

IV. RESULT

In our experiment, k_1 is the key to achieving frequency tampering, and k is also selected to avoid harmonic interference in the frequency mixing process. Based on our experimental system, we obtain that the frequency f_U recovered by the user satisfies the following equation:

$$f_U = \left(100 + \frac{10k_1}{21}\right) \text{MHz}, \quad (10)$$

whose derivation process is provided in Appendix A. For example, when k_1 is set as 2.1×10^{-4} , the recovered frequency at the user will be altered to 100 MHz+100 Hz. An experimental frequency tampering result is found in the video in Supplemental Material. We can observe from the video that the frequency value of the recovered 100 MHz signal can be stealthily altered within a range of 100 MHz \pm 100 Hz over the 200 km fiber link. At the same time, the locking status remains normal. It is worth noting that, for numerous scientific applications, even small frequency offsets, as small as 1 Hz, are unacceptable. The 100 Hz offset is deliberately chosen in the experiment to illustrate the destructive capability of this method.

Next, we further investigate the effect of the FTM on frequency dissemination stability. We select three different values of k_1 to set the corresponding recovered frequency f_U to 100 MHz+1 Hz, 100 MHz+10 Hz, and 100 MHz+100 Hz. As a comparison, under the same experimental conditions, we also measure the frequency dissemination stability without the FTM insertion. The experimental results are shown in Fig. 5, and the duration of each test is approximately six days. When the FTM is not added to the fiber link, relative stability results are $1.4 \times 10^{-14}/1$ s and $2.0 \times 10^{-17}/10^5$ s. When the FTM is added, the relative stability results under three different values of k_1 remain at $2.2 \times 10^{-14}/1$ s and $2.2 \times 10^{-17}/10^5$ s. Thus, the insertion of the FTM has almost no effect on the frequency

dissemination stability and the relative stability of the recovery signal is also almost the same when k_1 takes different values.

To show the characteristics of arbitrary adjustment and fast response of the frequency lens-enabled FTM, we carry out another frequency tampering experiment. The corresponding result is shown in Fig. 6, where the parameter k_1 is changed 10 times within 7000 s. The recovered frequency f_U can be

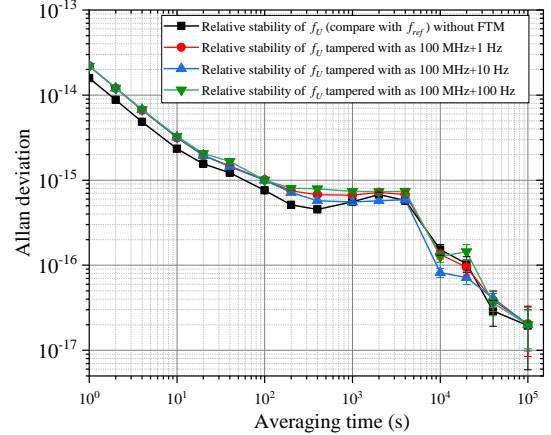


Fig. 5. Relative stability of the recovered frequency signal under the different parameter settings of the FTM. With the FTM, f_U is altered to 100 MHz + 1 Hz, 100 MHz + 10 Hz, and 100 MHz + 100 Hz, respectively. A comparison is made with the scenario without FTM insertion.

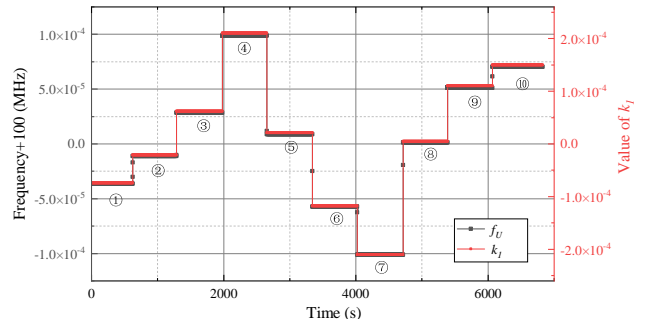


Fig. 6. Variation in f_U during the fast adjustment of k_1 . k_1 is randomly changed 10 times, indicated by the black line.

accurately and quickly altered, and the locking status of FbFS system is effectively maintained. Moreover, we measure the short-term relative stability of the recovered f_U during each change, as shown in Table I; thus, the relative stability of the recovered frequency is kept at the same level after the adjustment.

TABLE I
SHORT-TERM RELATIVE STABILITY OF THE RECOVERED FREQUENCY SIGNAL.

Test sequence		1	2	3	4	5
Allan Deviation	$\times 10^{-14}/1\text{ s}$	2.5	2.9	2.7	2.8	3.1
	$\times 10^{-15}/100\text{ s}$	1.8	2.0	1.4	3.0	0.8
Test sequence		6	7	8	9	10
Allan Deviation	$\times 10^{-14}/1\text{ s}$	3.4	3.3	2.8	2.3	2.1
	$\times 10^{-15}/100\text{ s}$	1.3	0.7	1.1	1.5	1.0

V. IMPACT OF FREQUENCY TAMPERING

Frequency reference synchronization is important in time-keeping, metrology, astronomical observation, etc. If the recovered frequency is covertly altered, severe hazards can occur. In the following, we present three frequency tampering scenarios, where the function of these applications is still normal, but the results provided are highly biased.

For the case of the timekeeping network, the frequency tampering directly affects the length of second [8], due to the relationship of $\frac{\Delta t}{t} = \frac{\Delta f}{f}$. Considering a scenario of two timekeeping systems at the server and user of Fig. 3, if the recovered frequency at the user side is altered from 100 MHz to 100 MHz+1 Hz, the time difference between 2 timekeeping systems increases 0.1 ms every 10^4 s, as shown in Fig. 7. From the viewpoint of the user side, its timekeeping function is normal because the timing output is stable and reproducible, which is found in the Allan deviation plot of Fig. 7. From the viewpoint of the whole timekeeping network, the cumulated time difference destroys the synchronization of the timekeeping network.

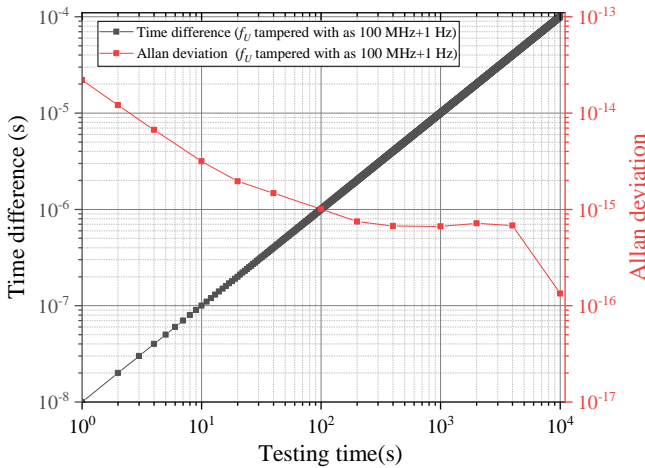


Fig. 7. Impact of frequency tampering on the timekeeping system. The recovery frequency signal to be used as the reference for the user-side timekeeping system is altered from 100 MHz to 100 MHz+1 Hz.

For the new definition of the International System of Units (SI) [28], all SI units (except for mole and second itself) can be

traced to corresponding fundamental constants with the aid of second, which is the most precise SI unit. The unit of length is defined by using the fixed numerical value of the speed of light in vacuum c to be 299792458 expressed in m/s. If the recovered frequency in Fig. 6 is used as the reference of the meter recovery system, the tampering action on frequency transfers to the tampering action on the length. As shown in Fig. 8, the corresponding error of the recovered SI unit-meter is altered with within the range of $\pm 1 \times 10^{-6}$ m. In this case, the function of the meter recovery system remains normal, while the induced by frequency tampering causes a large error.

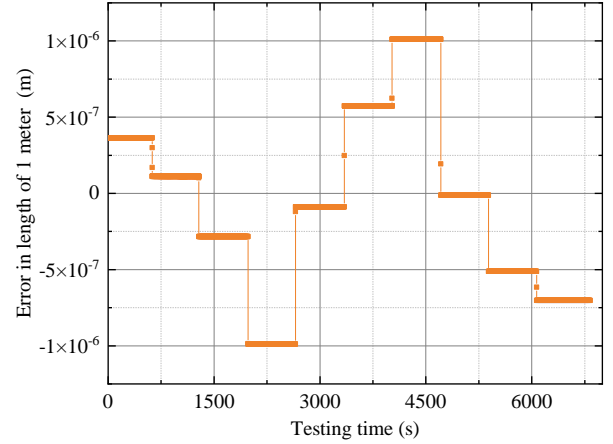


Fig. 8. Simulation result of the corresponding error of the recovered SI unit-meter using the tampered frequency signal shown in Fig. 6 as the reference for the unit of length tracing.

Another scenario is radio astronomy. In radio astronomy, multiple radio telescopes can be combined using radio interferometry [29], [30] and aperture synthesis techniques [31] to improve measurement accuracy. To reduce the coherent loss of the observation system, interference measurement arrays, such as the Square Kilometre Array (SKA), have a high requirement for frequency synchronization [32]. If there is a fixed frequency difference Δf between the two observation

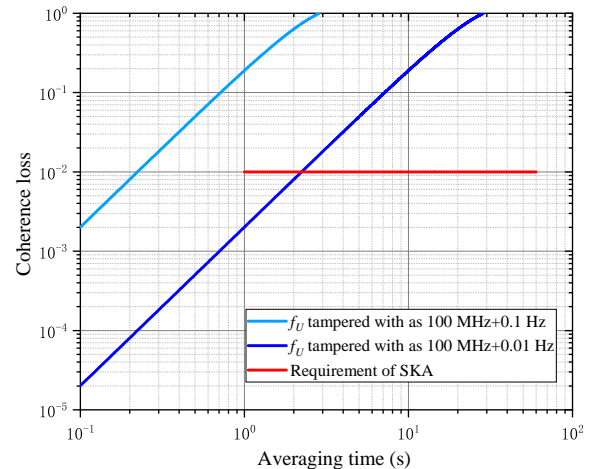


Fig. 9. Coherence loss of the radio telescope array under different frequency tampering cases, which are compared with the requirements of the Square Kilometre Array (SKA).

stations caused by the FTM, the coherent loss $Lc(T)$ between the two stations follows the relationship: $Lc(T) = 1 - |\text{sinc}(\pi\Delta ft)|$. For example, when the observation frequency is 350 MHz, the calculation results of the coherent loss under different frequency tampering scenarios are shown in Fig. 9. To compare the impact of reference frequency tampering directly, we use the coherent loss requirement of SKA as a comparison. SKA requires that the coherent loss caused by the frequency transmission system does not exceed 1% within an integration time from 1 s to 1 min. The coherent loss caused by 0.01 Hz frequency tampering causes the SKA observation to be disabled at 2.5 s, and the observation is completely unfeasible at 0.1 Hz frequency tampering.

VI. DISCUSSION

The FbFS network is one of the most important infrastructures. However, the frequency-tampering scenarios expose its potential risks. To solve its security issue, countermeasures of this risk posed by the FTM need to be discussed.

In optical networks, signal encryption [33] and link integrity monitoring [34], [35] are commonly used security measures at the information and hardware layers, respectively. Unfortunately, neither of these methods cannot be used as security countermeasures for the disseminated frequency reference. First, signal encryption techniques have a negative impact on the relative stability of the disseminated frequency signal and introducing additional phase noise, which defeats the purpose of high-quality transmission of frequency references. Second, link integrity monitoring methods, represented by optical time domain reflectometry (OTDR) [36]–[38], can be circumvented by the FTM. DWDMs and controlled optical switches can ensure that the core structure of the FTM is not detected during OTDR detection. All these circumstances point to the need to identify new security countermeasures for FbFS.

There are two possible security countermeasures. One countermeasure is link patrolling combined with fiber vibration detection. Relying on fiber vibration sensing technology, such as distributed acoustic sensing (DAS) [39]–[42], it is possible to identify intrusions and quickly locate them. Every link interruption event needs to be taken seriously. Inspectors should inspect risky sections and ensure that no special devices, such as FTMs, are embedded in the link. Another countermeasure is to build a more robust FbFS network. Multiple links need to be established between a single server and a single user. Preferably, the user can receive frequency references disseminated by different servers. If the user can receive multiple frequency references, they can be compared with each other to ensure that problems with a particular frequency reference can be detected in time.

VII. CONCLUSION

On a 200 km fiber link, we demonstrate that the synchronized frequency reference can be altered using a frequency lens-enabled FTM. While bypassing the locking status monitoring, the 100 MHz frequency reference synchronized at the user side can be changed arbitrarily and stealthily within the range of 100 MHz \pm 100 Hz. Moreover, the relative stability

of the recovered frequency reference can be maintained at the same normal level when tampering occurs. To more intuitively show the consequences of using a tampered frequency reference, we constructed three application scenarios that rely on disseminated frequency reference. In these three scenarios, the application systems could still run stably, but the generated results deviated dramatically. To solve this tampering risk, we propose two possible countermeasures. We anticipate that this article will raise awareness of the risks faced by FbFS networks and improve risk prevention measures.

APPENDIX

APPENDIX A: DETAILS OF THE FIBER-BASED RADIO FREQUENCY SYNCHRONIZATION SYSTEM AND DERIVATION PROCESS OF EQ. (10)

To show the details of the fiber-based radio frequency synchronization system as shown in Fig. 3(a), we start the explanation from PLL1 and PLL2. For convenience, the amplitude terms of signals in Appendix A are also ignored. A 100 MHz voltage-controlled crystal oscillator (VCXO) at the server site generates the signal that can be expressed as $V_{SX} = V_{VCXO-S} = \cos(2\pi f_{SX}t + \phi_{SX})$. Then, V_{SX} is converted to 2.1 GHz by a phase-locked dielectric resonant oscillator (PDRO), i.e., $V_{PDRO-S} = \cos(2\pi \times 21 f_{SX}t + 21\phi_{SX})$, which is modulated to an optical carrier (C38), and sent to the user site via the fiber link.

In the following, we first analyze the normal operation of the system when the FTM does not join the link. At the user site, the optical signal transmitted along the fiber is received and demodulated. The 2.1 GHz RF signal can be obtained at U1 point of Fig. 3(a), i.e., $V_{U1} = \cos(2\pi \times 21 f_{SX}t + 21\phi_{SX} + \phi_n)$, where ϕ_n is the phase noise caused by the whole link. Another 100 MHz VCXO-U located at the user site generates a signal that can be expressed as $V_{UX} = V_{VCXO-U} = \cos(2\pi f_{UX}t + \phi_{UX})$. Similarly, V_{UX} is also multiplied to 2.1GHz by the PDRO-U, i.e., $V_{PDRO-U} = \cos(2\pi \times 21 f_{UX}t + 21\phi_{UX})$. V_{PDRO-U} is mixed with V_{U1} to generate the error signal, i.e., $V_{error-U} = \cos[2\pi(21f_{SX} - 21f_{UX})t + 21(\phi_{SX} - \phi_{UX}) + \phi_n]$. Then, PLL2 can be realized with a servo controller. As a consequence,

$$21f_{SX} - 21f_{UX} = 0, \quad (A1)$$

$$21\phi_{SX} + \phi_n - 21\phi_{UX} = 0. \quad (A2)$$

For the backward route, V_{PDRO-U} is modulated on another optical carrier (C39), and sent to the server site. After demodulation and amplification at the server site, a 2.1 GHz RF signal can be obtained at point M1. In addition, the phase noise introduced by the same fiber link for a short time can also be considered as ϕ_n too. Considering the above, the 2.1 GHz RF signal at M1 point can be expressed as $V_{M1} = \cos(2\pi \times 21 f_{UX}t + 21\phi_{UX} + \phi_n)$.

In the left part of Fig. 3(a), the reference frequency signal of 100 MHz, i.e., $V_{ref} = \cos(2\pi f_{ref}t + \phi_{ref})$, is split and sent to two PDROs to generate the RF signals of 2.2 GHz and 2.0 GHz, denoted as $V_{ref1} = V_{PDRO-1} = \cos(2\pi \times 22 f_{ref}t + 22\phi_{ref})$ and $V_{ref2} = V_{PDRO-2} = \cos(2\pi \times$

$20f_{ref}t + 20\phi_{ref}$), respectively. Subsequently, V_{ref1} is mixed with V_{M1} to generate a 100 MHz signal, i.e., $\cos[2\pi(22f_{ref} - 21f_{UX})t + (22\phi_{ref} - 21\phi_{UX}) - \phi_n]$. Similarly, V_{ref2} is mixed with $V_{M2} = V_{PDRO-S}$ to generate another 100 MHz signal, i.e., $\cos[2\pi(21f_{SX} - 20f_{ref})t + 21\phi_{SX} - 20\phi_{ref}]$. Finally, these two 100 MHz signals are mixed to obtain the error signal $V_{error-S}$, i.e., $V_{error-S} = \cos[2\pi(42f_{ref} - 21f_{SX} - 21f_{UX})t + (42\phi_{ref} - 21\phi_{SX} - 21\phi_{UX} - \phi_n)]$. PLL1 can be realized with a servo controller. As a consequence,

$$42f_{ref} - 21f_{SX} - 21f_{UX} = 0, \quad (A3)$$

$$42\phi_{ref} - 21\phi_{SX} - 21\phi_{UX} - \phi_n = 0. \quad (A4)$$

Considering Eq. (A1), Eq. (A2), Eq. (A3), and Eq. (A4), the output signal V_{Output} at the user site can be obtained as

$$\begin{aligned} V_{Output} &= V_{UX} = V_{VCXO-U} \\ &= \cos(2\pi f_{UX}t + \phi_U) \\ &= \cos(2\pi f_{ref}t + \phi_{ref}), \end{aligned} \quad (A5)$$

and frequency synchronization between the server site and the user site is realized.

In the following we consider the case after inserting the FTM and provide the derivation process of Eq. (10). Before entering the FTM, the RF signal carried by the optical signal (C38) is $\cos(2\pi \times 21f_{SX}t + 21\phi_{SX} + \phi_{n'1})$, where $\phi_{n'1}$ is the noise introduced by part of the fiber link between the FTM and the server site. Referring to Eq. (5) and Eq. (6), after passing the FTM, the RF signal carried by the optical signal (C38) is $\cos[2\pi(k_1f_{S0} + 21f_{SX})t + k_1\phi_{S0} + 21\phi_{SX} + \phi_{n'1}]$. As a consequence, V_{U1} changes, i.e., $V_{U1} = \cos[2\pi(k_1f_{S0} + 21f_{SX})t + k_1\phi_{S0} + 21\phi_{SX} + \phi_{n'1} + \phi_{n'2}]$, where $\phi_{n'2}$ is the noise introduced by another part of the fiber link. Due to PLL2, V_{UX} changes accordingly, i.e.,

$$f_{UX} = \frac{k_1f_{S0}}{21} + f_{SX}, \quad (A6)$$

$$\phi_{UX} = \frac{k_1\phi_{S0}}{21} + \phi_{SX} + \frac{\phi_{n'1} + \phi_{n'2}}{21}. \quad (A7)$$

Therefore, the RF signal modulated to laser-2 changes to $V_{PDRO-U} = \cos[2\pi(k_1f_{S0} + 21f_{SX})t + k_1\phi_{S0} + 21\phi_{SX} + \phi_{n'1} + \phi_{n'2}]$. In the backward direction, when entering the FTM, the RF signal carried by the optical signal (C39) is $\cos[2\pi(k_1f_{S0} + 21f_{SX})t + k_1\phi_{S0} + 21\phi_{SX} + \phi_{n'1} + 2\phi_{n'2}]$. Referring to Eq. (8) and Eq. (9), the RF signal modulated on the optical carrier changes back to $\cos[2\pi \times 21f_{SX}t + (21\phi_{SX} + \phi_{n'1} + 2\phi_{n'2})]$. Although the FTM tampers with the disseminated frequency reference in the fiber link, the frequency of the RF signal demodulated at the server site remains unchanged. After going through the same process described by Eq. (A3) and Eq. (A4), what can be obtained is

$$f_{SX} = f_{ref}, \quad (A8)$$

$$\phi_{SX} = \phi_{ref} - \frac{\phi_{n'1} + \phi_{n'2}}{21}. \quad (A9)$$

As a result,

$$\begin{aligned} V_{Output} &= \cos(2\pi f_{UX}t + \phi_{UX}) \\ &= \cos \left[2\pi \left(\frac{k_1f_{S0}}{21} + f_{ref} \right) t + \frac{k_1\phi_{S0}}{21} + \phi_{ref} \right]. \end{aligned} \quad (A10)$$

In the experimental setup, $f_{S0} = 10$ MHz and $f_{ref} = 100$ MHz, so that

$$f_{UX} = \left(100 + \frac{10k_1}{21} \right) \text{MHz}. \quad (A11)$$

REFERENCES

- [1] J. Ye, J. Peng, R. J. Jones, K. W. Holman, J. L. Hall, D. J. Jones, S. A. Diddams, J. Kitching, S. Bize, J. C. Bergquist, L. W. Hollberg, L. Robertsson, and L. S. Ma, "Delivery of high-stability optical and microwave frequency standards over an optical fiber network," *J. Opt. Soc. Am. B*, vol. 20, pp. 1459–1467, 2003.
- [2] P. A. Williams, W. C. Swann, and N. R. Newbury, "High-stability transfer of an optical frequency over long fiber-optic links," *J. Opt. Soc. Am. B*, vol. 25, pp. 1284–1293, Aug. 2008.
- [3] M. Amemiya, M. Imae, Y. Fujii, T. Suzuyama, and S.-i. Ohshima, "Simple time and frequency dissemination method using optical fiber network," *IEEE Trans. Instrum. Meas.*, vol. 57, no. 5, pp. 878–883, 2008.
- [4] B. Wang, C. Gao, W. L. Chen, J. Miao, X. Zhu, Y. Bai, J. W. Zhang, Y. Y. Feng, T. C. Li, and L. J. Wang, "Precise and continuous time and frequency synchronisation at the 5×10^{-19} Accuracy Level," *Sci. Rep.*, vol. 2, p. 556, 2012.
- [5] Y. Bai, B. Wang, X. Zhu, C. Gao, J. Miao, and L. J. Wang, "Fiber-based multiple-access optical frequency dissemination," *Opt. Lett.*, vol. 38, pp. 3333–3335, 2013.
- [6] C. Lisdat, G. Grosche, N. Quintin, C. Shi, S. Raupach, C. Grebing, D. Nicolodi, F. Stefani, A. Al-Masoudi, S. Dörscher *et al.*, "A clock network for geodesy and fundamental science," *Nat. Commun.*, vol. 7, no. 1, p. 12443, 2016.
- [7] M. Rizzi, S. Rinaldi, P. Ferrari, A. Flammini, D. Fontanelli, and D. Macci, "Enhancing accuracy and robustness of frequency transfer using synchronous ethernet and multiple network paths," *IEEE Trans. Instrum. Meas.*, vol. 65, no. 8, pp. 1926–1936, 2016.
- [8] F. Riehle, "Optical clock networks," *Nat. Photonics*, vol. 11, no. 1, pp. 25–31, 2017.
- [9] J. Wang, C. Yue, Y. Xi, Y. Sun, N. Cheng, F. Yang, M. Jiang, J. Sun, Y. Gui, and H. Cai, "Fiber-optic joint time and frequency transfer with the same wavelength," *Opt. Lett.*, vol. 45, no. 1, pp. 208–211, 2020.
- [10] B. Liu, X. Guo, W. Kong, T. Liu, R. Dong, and S. Zhang, "Stabilized time transfer via a 1000-km optical fiber link using high-precision delay compensation system," *Photonics*, vol. 9, no. 8, 2022.
- [11] M. Schioppa, J. Kronjaeger, A. Silva, R. Ilieva, J. Paterson, C. Baynham, W. Bowden, I. Hill, R. Hobson, A. Vianello *et al.*, "Comparing ultrastable lasers at 7×10^{-17} fractional frequency instability through a 2220 km optical fibre network," *Nat. Commun.*, vol. 13, no. 1, p. 212, 2022.
- [12] S. Johnson and O. A. Dobre, "Time and carrier frequency synchronization for coherent optical communication: Implementation considerations, measurements, and analysis," *IEEE Trans. Instrum. Meas.*, vol. 69, no. 8, pp. 5810–5820, 2020.
- [13] S. Lewis and M. Inggis, "Synchronization of coherent netted radar using white rabbit compared with one-way multichannel gpsdos," *IEEE Trans. Aerosp. Electron. Syst.*, vol. 57, no. 3, pp. 1413–1422, 2021.
- [14] Y. He, K. G. H. Baldwin, B. J. Orr, R. Bruce Warrington, M. J. Wouters, A. N. Luiten, P. Mirtschin, T. Tzioumis, C. Phillips, J. Stevens, B. Lennon, S. Munting, G. Aben, T. Newlands, and T. Rayner, "Long-distance telecom-fiber transfer of a radio-frequency reference for radio astronomy," *Optica*, vol. 5, pp. 138–146, 2018.
- [15] Y. Chen, B. Wang, L. Wang, K. Grainger, R. Oberland, R. Whitaker, and A. Wilkinson, "Integrated dissemination system of frequency, time and data for radio astronomy," *IEEE Photon. J.*, vol. 13, no. 1, pp. 1–7, 2021.
- [16] L. Sliwczynski, P. Krehlik, H. Imlau, H. Ender, H. Schnatz, D. Piester, and A. Bauch, "Fiber-based utc dissemination supporting 5g telecommunications networks," *IEEE Commun. Mag.*, vol. 58, no. 4, pp. 67–73, 2020.

- [17] Z. Zhou, J. Wei, Y. Luo, K. A. Clark, E. Sillekens, C. Deakin, R. Sohanpal, R. Slavik, and Z. Liu, "Communications with guaranteed bandwidth and low latency using frequency-referenced multiplexing," *Nat. Electron.*, vol. 6, no. 9, pp. 694–702, 2023.
- [18] G. Marra, C. Clivati, R. LUCKETT, A. Tampellini, J. Kronjager, L. Wright, A. Mura, F. Levi, S. Robinson, A. Xuereb, B. Baptie, and D. Calonico, "Ultrastable laser interferometry for earthquake detection with terrestrial and submarine cables," *Science*, vol. 361, p. 486, 2018.
- [19] J. Grotti, S. Koller, S. Vogt, S. Häfner, U. Sterr, C. Lisdat, H. Denker, C. Voigt, L. Timmen, A. Rolland *et al.*, "Geodesy and metrology with a transportable optical clock," *Nat. Phys.*, vol. 14, no. 5, pp. 437–441, 2018.
- [20] K. A. Clark, D. Cletheroe, T. Gerard, I. Haller, K. Jozwik, K. Shi, B. Thomsen, H. Williams, G. Zervas, H. Ballani, P. Bayvel, P. Costa, and Z. Liu, "Synchronous subnanosecond clock and data recovery for optically switched data centres using clock phase caching," *Nat. Electron.*, vol. 3, no. 7, pp. 426–433, 2020.
- [21] L. Narula and T. E. Humphreys, "Requirements for secure clock synchronization," *IEEE Journal of Selected Topics in Signal Processing*, vol. 12, no. 4, pp. 749–762, 2018.
- [22] J. Lee, L. Shen, A. Cerè, J. Troupe, A. Lamas-Linares, and C. Kurtsiefer, "Asymmetric delay attack on an entanglement-based bidirectional clock synchronization protocol," *Appl. Phys. Lett.*, vol. 115, no. 14, 2019.
- [23] Y. Li, J. Hu, Y. Pan, W. Huang, L. Ma, J. Yang, S. Zhang, Y. Luo, C. Zhou, C. Zhang, H. Wang, Y. Shao, Y. Zhang, X. Chen, Z. Chen, S. Yu, H. Guo, and B. Xu, "Secure two-way fiber-optic time transfer against sub-ns asymmetric delay attack with clock model-based detection and mitigation scheme," *IEEE Trans. Instrum. Meas.*, vol. 72, 2023.
- [24] X. Xu, Y. Zhang, Y. Bian, J. Hu, J. Dou, Y. Li, B. Xu, S. Yu, and H. Guo, "Controllable asymmetric attack against practical round-trip fiber time synchronization systems," *IEEE Photon. Technol. Lett.*, pp. 1263–6, 2023.
- [25] C. Zhang, Y. Li, X. Chen, Y. Zhang, L. Fu, Y. Gong, H. Wang, W. Huang, and B. Xu, "Controllable asymmetry attack on two-way fiber time synchronization system," *IEEE Photon. J.*, vol. 13, no. 6, 2021.
- [26] Z. Liu, Y. Bian, Y. Zhang, B. Xu, Y. Li, and S. Yu, "Asymmetric channel attack against practical round-trip fiber time synchronization system," in *2022 Joint Conference of the European Frequency and Time Forum and IEEE International Frequency Control Symposium (EFTF/IFCS)*, ser. Joint European Frequency and Time Forum and International Frequency Control Symposium, 2022.
- [27] Y. Chen, H. Dai, H. Si, F. Wang, B. Wang, and L. Wang, "Long-haul high precision frequency dissemination based on dispersion correction," *IEEE Trans. Instrum. Meas.*, vol. 71, pp. 1–7, 2022.
- [28] M. Stock, R. Davis, E. de Mirandés, and M. J. Milton, "The revision of the si—the result of three decades of progress in metrology," *Metrologia*, vol. 56, no. 2, p. 022001, 2019.
- [29] W.-H. Shang-Guan, R.-B. Zhao, J.-Q. Wang, Z.-C. Wang, Q.-H. Liu, X.-Y. Hong, G.-L. Wang, W.-M. Zheng, X.-Z. Zhang, T. Shuai, Z. Yan, Y.-D. Huang, X.-J. Lu, L.-F. Yu, Y.-B. Jiang, C. Zhang, M.-L. Ma, W.-Y. Zhong, R.-J. Zhu, W.-B. Wang, J. Zhang, B. Xia, and C.-Y. Zhang, "Lunar orbit vlbi experiment ground validation system," *IEEE Trans. Instrum. Meas.*, vol. 72, pp. 1–14, 2023.
- [30] C. M. Holler, M. E. Jones, A. C. Taylor, A. I. Harris, and S. A. Maas, "A 2–20-ghz analog lag correlator for radio interferometry," *IEEE Trans. Instrum. Meas.*, vol. 61, no. 8, pp. 2253–2261, 2012.
- [31] D. Le Vine, "Synthetic aperture radiometer systems," *IEEE Trans Microw Theory Tech*, vol. 47, no. 12, pp. 2228–2236, 1999.
- [32] B. Alachkar, A. Wilkinson, and K. Grainge, "Frequency reference stability and coherence loss in radio astronomy interferometers application to the ska," *J. Astron. Instrum.*, vol. 7, no. 01, p. 1850001, 2018.
- [33] D. Venu, A. Mayuri, S. Neelakandan, G. Murthy, N. Arulkumar, and N. Shelke, "An efficient low complexity compression based optimal homomorphic encryption for secure fiber optic communication," *Optik*, vol. 252, p. 168545, 2022.
- [34] X. Bao and L. Chen, "Recent progress in distributed fiber optic sensors," *SENSORS*, vol. 12, no. 7, pp. 8601–8639, 2012.
- [35] E. F. Williams, M. R. Fernández-Ruiz, R. Magalhaes, R. Vanthillo, Z. Zhan, M. González-Herráez, and H. F. Martins, "Distributed sensing of microseisms and teleseisms with submarine dark fibers," *Nat. Commun.*, vol. 10, no. 1, p. 5778, 2019.
- [36] Y. Lu, T. Zhu, L. Chen, and X. Bao, "Distributed vibration sensor based on coherent detection of phase-otdr," *J. Light. Technol.*, vol. 28, no. 22, pp. 3243–3249, 2010.
- [37] F. Peng, H. Wu, X. H. Jia, Y. J. Rao, Z. N. Wang, and Z. P. Peng, "Ultra-long high-sensitivity phi-OTDR for high spatial resolution intrusion Detection of pipelines," *Opt. Express*, vol. 22, pp. 13 804–13 810, 2014.
- [38] F. Peng, X. Zheng, and Q. Miao, "Large dynamic range and anti-fading phase-sensitive otdr using 2-d phase unwrapping via neural network," *IEEE Trans. Instrum. Meas.*, vol. 72, pp. 1–8, 2023.
- [39] T. Li, C. Fan, H. Li, T. He, W. Qiao, Z. Shi, Z. Yan, C. Liu, D. Liu, and Q. Sun, "Nonintrusive distributed flow rate sensing system based on flow-induced vibrations detection," *IEEE Trans. Instrum. Meas.*, vol. 70, pp. 1–8, 2021.
- [40] M. van den Ende, I. Lior, J.-P. Ampuero, A. Sladen, A. Ferrari, and C. Richard, "A self-supervised deep learning approach for blind denoising and waveform coherence enhancement in distributed acoustic sensing data," *IEEE Trans. Instrum. Meas.*, vol. 34, no. 7, pp. 3371–3384, 2023.
- [41] N. J. Lindsey, T. C. Dawe, and J. B. Ajo-Franklin, "Illuminating seafloor faults and ocean dynamics with dark fiber distributed acoustic sensing," *Science*, vol. 366, p. 1103, 2019.
- [42] G. Wang, Z. W. Pang, B. H. Zhang, F. M. Wang, Y. F. Chen, H. F. Dai, B. Wang, and L. J. Wang, "Time shifting deviation method enhanced laser interferometry: ultrahigh precision localizing of traffic vibration using an urban fiber link," *Photonics Res.*, vol. 10, pp. 1839–1839, 2022.

A Compact Anomaly Detection Solution for Science Instruments

Alfonso Lagares de Toledo
School of Aerospace Engineering
Georgia Institute of Technology
Atlanta, GA 30312
alagares@gatech.edu

Christopher E. Carr
School of Aerospace Engineering &
School of Earth and Atm. Sciences
620 Cherry St NW, Room G10
Atlanta, GA 30312
cecarr@gatech.edu

Abstract—Small, low-cost instruments enable new and exciting mission opportunities, yet their constrained volume and limited budgets make them especially susceptible to suffering anomalies during flight. Radiation effects, as well as sensor or actuator failure, can all pose a serious threat to the continued collection of scientific data as well as cause the partial or complete loss of a mission’s science payload. Onboard anomaly detection could allow instruments to recover from such events, but its ad-hoc development typically falls outside the mission’s timeline or monetary constraints. Here we describe a compact solution for the implementation of onboard anomaly detection meant for space science missions. The device is designed to be interoperable with a broad range of instruments, utilizing easily accessible power and logic signals to monitor the state of peripherals and actuators without disrupting their functionality. By leveraging a commercially-available microcontroller with a radiation-hardened alternative package, the device can be inexpensively sourced and assembled with minimal work, enabling instrument characterization on an expedited timeline. The system can then be exchanged for a radiation-hardened version, ensuring the replicability of observed anomalies in a laboratory environment during instrument operations. We also present currently implemented anomaly detection algorithms, which enable the system to detect anomalies in instruments with varying failure modes and allow mission designers to choose which detection approach best fits the specific needs of their instrument. Finally, we showcase an example application of this system in the detection of anomalies during the operation of a lysis motor designed for use in biological space instruments. The inclusion of the described anomaly detection system into new or existing instruments can effectively lower the risks associated with in-flight anomalies, improving their reliability while causing minimal impact on their development timeline or system complexity. This newfound capability can be leveraged to improve the resilience of existing science missions or to enable new missions to harsher space environments where anomaly detection is a requirement for successful instrument operation.

strained timelines. This creates exciting opportunities to pursue new mission concepts that were previously not achievable, where mass, volume, or cost constraints limit the use of larger instruments. Missions concepts similar to the Europa Lander [1], the Enceladus Orbilander Mission [2], or the Vertical Entry Robot for Navigating Europa (VERNE) [3] rely on small instruments to achieve their mission goals. Furthermore, instruments that are not yet implemented in specific mission architectures, like the ELIE [4] or SETG [5] instruments, have the potential to improve or enable new measurements and observations to answer still unanswered questions in planetary science. Small science missions are an integral part of current and future strategies to advance in-situ investigation of planetary or small-body environments, as they provide a valuable combination of launch cadence, complexity, and risk that enables them to respond to ongoing scientific development [6].

However, these instruments pose unique implementation challenges for mission designers, one of which is reliable anomaly detection that can adapt to the requirements of these instruments. During the course of a mission, instruments will encounter anomalies that can threaten their successful operation, the collection of data, and the achievement of scientific goals. An anomaly is an external or internal event that changes the state or configuration of an instrument to one that can cause temporary or permanent damage to the instrument, or under which the instrument was not designed to operate. Anomalies pose a risk to all spacecraft, but their impact on small missions can be severely detrimental: Between the years 2000 and 2016, 35 percent of small missions failed to meet their objectives [7]. Detecting an anomaly is vital to allow the instrument or spacecraft to respond to it, mitigating its disruption to ongoing operations and ensuring the safety and continuity of the mission.

TABLE OF CONTENTS

1. INTRODUCTION.....	1
2. METHODS	3
3. RESULTS	5
4. CONCLUSION	6
REFERENCES	7
BIOGRAPHY	7

1. INTRODUCTION

Small instruments are rapidly expanding our ability to achieve science objectives with reduced budgets and con-

The need for anomaly detection can be driven by multiple mission requirements. Recovery from anomalies into a functional or safe state can be a requirement for missions where the occurrence of an anomaly threatens the continuation of the mission or the achievement of its mission goals unless corrective action is taken. It can also be a requirement for instruments where the medium to sample is a-priori unknown. Detecting an anomaly in the instrument’s operation can indicate the presence of an unfamiliar sample medium, allowing mission controllers to halt operations and conduct further studies before the instrument proceeds with sample analysis, thus mitigating the risk of damage to the instrument. A requirement for increased reliability can also drive the need for anomaly detection capabilities. Resource restrictions drive instrument designers to use commercial-of-the-shelf (COTS) or low technology readiness level (TRL) technologies in instrument designs which increases the risk of anomalies

This work has been submitted to the IEEE for possible publication. Copyright may be transferred without notice, after which this version may no longer be accessible.

negatively impacting instrument operations. This can also affect the overall risk of the instrument and make it unsuitable for missions with low-risk tolerances. Anomaly detection can increase the reliability of these instruments and lower their overall risk. Furthermore, missions destined for harsh environments where a short mission duration is expected can leverage anomaly detection to maximize the total amount of data gathered by detecting and reporting anomalies that might affect the integrity of the data. Finally, missions requiring complete autonomy of the spacecraft and instrument due to limited or a complete lack of communication for extended periods of time must be able to react to anomalies that might threaten the successful completion of the mission objectives, which is enabled by anomaly detection. These driving factors for anomaly detection, as well as examples of missions enabled by anomaly detection capabilities, are summarized in Figure 1.





Driving Factor	Enables	Representative Missions
Anomaly Recovery	Missions with low-risk tolerance, interacting with unknown environments	Curiosity, Perseverance rovers 
Reliability	Use of COTS or low TRL technologies	Cubesat missions (Starling, ELaNu) 
Harsh Mission Environments	Maximizing data gathering during short-duration missions	Europa Lander 
Autonomy	Missions with limited or no communications where complete operational autonomy is required	Vertical Entry Robot for Navigating Europa (VERNE), Exobiology Extant Life Surveyor (EELS) 

Figure 1. Mapping of driving factors, capabilities, and representative missions enabled by anomaly detection. Mission renders sourced from [8], [9], [1] and [10]

Anomaly sources that impact an instrument can be caused by the environment the spacecraft operates in, like radiation-related latch-up events or bit flips, or by the failure or misconfiguration of a system or subsystem that is part of the spacecraft itself [11]. Finally, operator error and faulty hardware design threaten the correct function of the instrument. Due to this variability in anomaly sources, there is no single method that can detect all possible anomalies an instrument might experience during the duration of its mission.

Current anomaly detection solutions rely on the ad-hoc implementation of both custom hardware and software on the specific system to be protected from a subset of possible anomalies. This requires an investment of both resources and time for the development of this functionality, which is sometimes infeasible for small instruments due to their limited budgets and restricted timelines. Furthermore, identifiable results of anomalies are dependent on the specific implementation of actuators and peripherals that compose the instrument, and as such customized anomaly detection solutions are needed for each instrument or instrument implementation. This need for a customized detection solution clashes with the agile timelines expected from small instrument developers. This tight implementation schedule might also prohibit the inclusion of an independent anomaly detection system, opting instead for the implementation of anomaly detection as part of the instrument software or hardware system directly. Although this implementation approach might be preferable over the complete lack of anomaly detection, it does not

mitigate the risk of a fault in the instrument rendering all or part of the anomaly detection measures ineffective. Furthermore, the increased complexity of implementing anomaly detection might not be manageable for teams focused on the development of an instrument. It might also unnecessarily complicate the software and hardware design of an instrument, which itself poses a risk of faults. Current anomaly detection solutions thus fail to meet the requirements of small instruments.

Mitigating the risks of anomalies impacting small instruments would require an anomaly detection solution that is easy to integrate with a multitude of different instruments, eliminating the need for the development of unique anomaly detection solutions for each spacecraft or instrument implementation. This would reduce the time and resource commitment required by teams to implement anomaly detection, making it more accessible. To achieve this goal, the solution must also have a clear and defined interface to communicate with the rest of the instrument and be compact and inexpensive. It should also be easy to use by instrument designers and ground operators to reduce the chance of anomalies caused by improper implementation. Finally, this generic anomaly detection solution that provides this capability to multiple instruments must meet the diverging requirements found during instrument development in the laboratory and during flight while minimizing complexity and risk to replicability.

In the laboratory environment, the anomaly detection system must be easy to procure and inexpensive to enable fast development and simplify the instrument characterization process. Usability by operators also becomes a concern during laboratory testing, as the output of the anomaly detection system should be easily interpretable for rapid development. During flight, the need for systems to be radiation tolerant or radiation hardened becomes a top priority, especially for missions with objectives past low Earth orbit. These competing requirements would normally force teams to devise two separate systems: one to characterize their instrument in the laboratory and a separate system to provide anomaly detection during flight. This increases the complexity throughout the instrument's life cycle, but more importantly, it poses a risk to the replicability of unexpected fault states experienced during flight: As the flight and laboratory systems are fundamentally different, recreating an anomalous state in the laboratory using information from flight requires understanding how to translate the flight system's output into the expected input for the laboratory system.

The proposed anomaly detection solution allows instrument designers to use the same solution to characterize expected anomalies and other instrument parameters prior to hardware handoff and to detect anomalies during flight using the same instrument subsystem. During assembly and laboratory instrument testing, anomaly detection can be used to characterize the expected operational states of the instrument and profile known or expected failure states that might result from possible hardware design limitations or flaws. Failures resulting from random events like single event effects (latch-ups or bit flips) can also be emulated in the laboratory to determine the resiliency of the instrument to such faults. During the instrument's use in a mission, the anomaly detection system can be used to detect anomalous states during instrument operation, which allows the instrument to respond to failures and recover from states that might pose a risk to its safety and continued functionality. An anomaly detection solution can also provide instrument monitoring capabilities useful for instrument operation independent of the instrument itself.

2. METHODS

System Architecture

The proposed anomaly detection device follows a decoupled architecture, where the anomaly detection function is performed not as part of the instrument or power systems but as an independent device with separate hardware and software design. This allows the device to be used for different instruments without the need to have a specific hardware implementation for each one. Depending on the role anomaly detection is meant to play in the mission, the device can be used as the starting node of a more expansive monitoring and reliability system that oversees the functionality of the instrument. It can also be connected to the instrument or other systems on the spacecraft for closed-loop control of instrument modes or to a communication subsystem for off-board instrument monitoring, as shown in the system diagram presented on Figure 2.

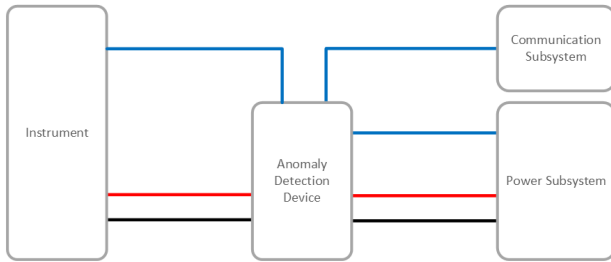


Figure 2. High-level anomaly detection system architecture, showing the connection between the anomaly detection device and other subsystems.

The device detects anomalies in the connected instrument by measuring its power consumption over time. This measurement is taken using an INA260 Precision Digital Current and Power Monitor, which is managed by an ARM M0 Cortex microcontroller. The data is processed by the microcontroller and time-tagged through the use of a real-time clock (RTC), after which it is stored in external flash memory and/or sent to a communication system through I2C or SPI. Multiple INA260 sensors can be connected to the same device as shown in Figure 3 if the instrument uses more than one power rail to operate. The detection of anomalies through this data is dependent on the specific implementation of the anomaly detection device and the type of anomaly to be detected. These will be discussed further in the System Use and Anomaly Detection Algorithms sections. The detection and monitoring of anomalies are performed by the microcontroller which can then alert the instrument or supporting systems through the aforementioned communication protocols.

The device can be used through two different hardware implementations, depending on its intended use: a laboratory implementation, which uses inexpensive and readily available COTS parts and microcontrollers; and a flight version which uses a radiation-hardened microcontroller to enable deep space missions. The device is implemented on two distinct pieces of hardware to best meet the design constraints of the laboratory and flight environments while minimizing the risk of fault replicability associated with utilizing different hardware. Figure 4 shows the connections between the

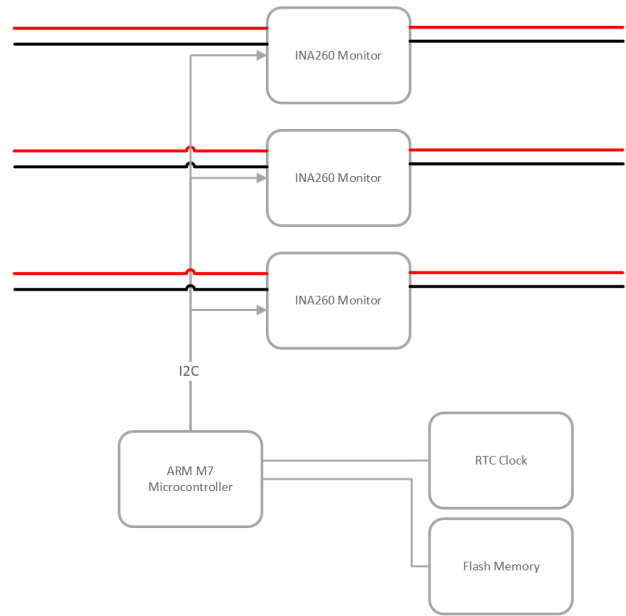


Figure 3. Anomaly detection device block diagram when connected to multiple INA260 sensors.

device, the instrument, and its power system under the two different hardware implementations. The current laboratory implementation fits within a $6.4 \times 2.4 \times 1.9$ inch volume, weighs 20 grams, and consumes an average of $25.2mW$ during active use.

Integration with an instrument

As the device relies on the INA260 sensor to monitor power, the device must be connected to the power supply of the instrument to monitor the instrument's state and detect anomalies. This can be done on either the high or low side of power, depending on other mission requirements, and will not interfere with any non-signal carrying power supply. The device can also be connected to the instrument's peripherals, actuators, or sensors which designers deem to be at the highest risk of experiencing a fault. This provides even more granularity in the detected anomalous states. A total of 16 INA260 sensors can be connected in parallel to a single monitoring device, enabling a wide survey of all potential sources of faults present in an instrument.

System utilization

The device is first connected to the instrument during final integration in the laboratory, after which the instrument can be put through functional testing. As part of this testing, expected modes of operation and known possible faults can be profiled, which allows the anomaly detection system to be configured for the specific needs of the instrument at hand. Expected modes of operation to be profiled might include the power draw from the instrument during standby, startup, or expected conditions during data collection. Faults to be tested can include possible actuator or active component failures, or mission subsystem failures that might threaten the nominal state of the instrument. During this process, the anomaly detection device is connected to a computer running a profiling and configuration application which collects data from the device in real time and allows for the tagging and archiving of instrument monitoring data. This data can then

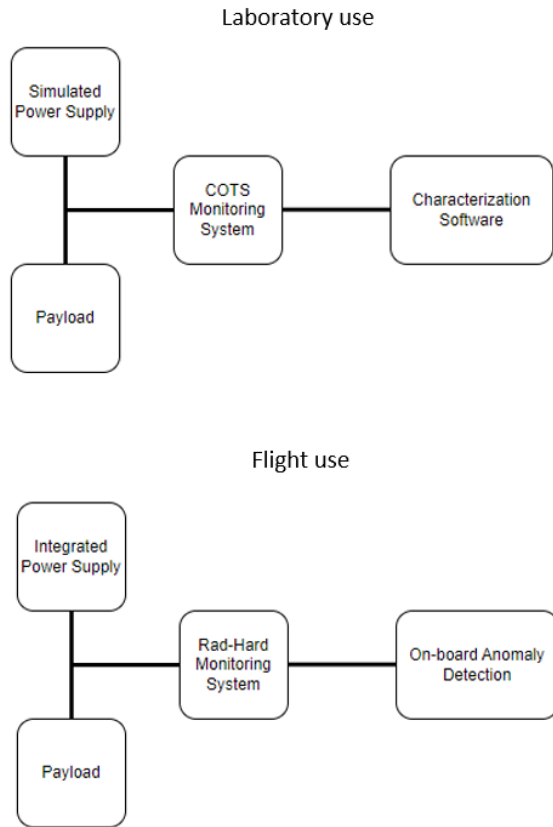


Figure 4. System diagrams for laboratory and flight use of the device, showing the connections to the instrument and supporting systems.

be used to produce a configuration for the anomaly detection device that can be used during flight.

Once the instrument has been characterized and possible fault modes have been used to configure the anomaly detection device, the corresponding configuration can be loaded onto the flight version of the anomaly detection device and subsequently integrated with the instrument before hardware hand-off. The application code used by both microcontrollers is reused, with only the Hardware Abstraction Layer (HAL) and middleware required to drive the anomaly detection peripherals (INA260 sensors, RTC, and flash memory) regenerated. Although this inherently poses a risk to the laboratory replicability of errors experienced in flight, sacrificing the use of a one-to-one replica of the instrument in exchange for lower costs, ease of procurement, and fast integration with the instrument might be a positive trade off for small instruments with lax code validation and verification requirements.

Anomaly detection algorithms

The capability of the anomaly detection device relies on its detection algorithms. There is no singular ideal anomaly detection algorithm that can detect anomalies in all possible instruments. As such multiple approaches have been implemented to allow instrument designers to tailor the algorithms

to their specific use cases. The algorithms rely on the voltage and current measurements to identify anomalous states of the instrument or instrument subsystems. The currently implemented algorithms include Out-of-limits and AutoEncoder-based anomaly detection. These were chosen as they lie on opposite sides of the available algorithm spectrum in terms of complexity, explainability, and ease of implementation, showcasing the flexible capabilities of the anomaly detection device.

Out-of-limits anomaly detection—For simple monitoring purposes or for anomalies that directly translate into overvoltage, overcurrent, undervoltage, or undercurrent of a system, an out-of-limits anomaly detection schema might be the most explainable and effective anomaly detection method. This involves quantifying the expected maximum and minimum values for a given voltage and current signal connected to the anomaly detection device. Once these limits have been determined, the anomaly detection device will flag an anomaly if the measured voltage and current exceed the defined limits. Figure 5 shows an example of the out-of-limits anomaly detection schema detecting the delivery of power to a sample load after it is connected to a power rail being monitored by the device. This can be implemented on the device’s microcontroller or as an alarm directly commanded by the INA260 sensor through an I/O signal. This second option minimizes the time taken by the system to detect and report an anomaly and can be especially useful if action must be taken by the instrument in a short time to correct the fault.

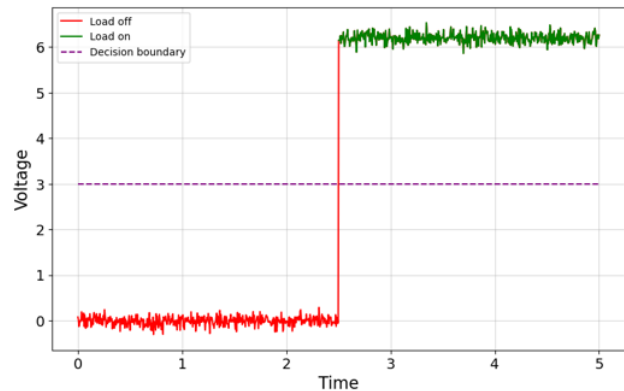


Figure 5. Example of out-of-limits anomaly detection on a power rail load off to load on transition.

Out-of-limits anomaly detection is easy to implement and easily explainable, but it lacks the ability to detect anomalies that primarily manifest in the time domain and not in the magnitude of the signal. Furthermore, it requires the boundaries of the signal to be known before the anomaly happens, which is not always feasible for more complex anomalies.

Autoencoder-based anomaly detection—Autoencoders are a type of neural network whose aim is to reconstruct the input signal with as little error as possible. An autoencoder is formed by a converging section that tapers down to a latent space of reduced dimensionality. This latent space is then followed by a diverging section where layers get progressively wider until they reach the same layer width as the input. During training, the network learns to compress the input data down to the latent space, and then reconstruct it back to its original form. This architecture is presented in Figure 6.

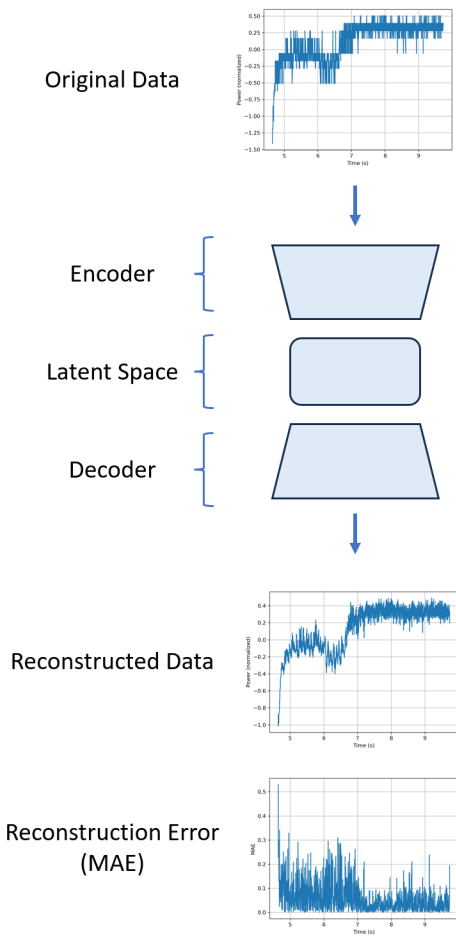


Figure 6. Sample autoencoder architecture, showing example data being reconstructed by the network.

Autoencoders have proven to be valuable tools for anomaly detection, as their ability to compress and reconstruct new data down to the dimensionality of the latent space is highly dependent on the characteristics of the training data [12]. The reconstruction error of the autoencoder can then be used to measure the similarity of new inputs to the training data. Anomalous data that does not match the characteristics of the training data will produce a high reconstruction error, which flags the data as anomalous. An example of this workflow is shown in Figure 7.

Autoencoders have the advantage of being able to detect anomalies not characterized during instrument testing, as any data that does not fit the training data will be flagged as an anomaly. Multiple autoencoders can be trained on different data sets to identify anomalies in instruments with multiple nominal states, providing instrument designers with a flexible anomaly detection solution that can accommodate multiple operation modes.

However, autoencoders suffer from a lack of explainability as their output cannot be easily interpreted to be meaningful or useful beyond characterizing an anomaly. They also require training data to be collected. The heavy computational cost of training a neural network is a limiting factor for the

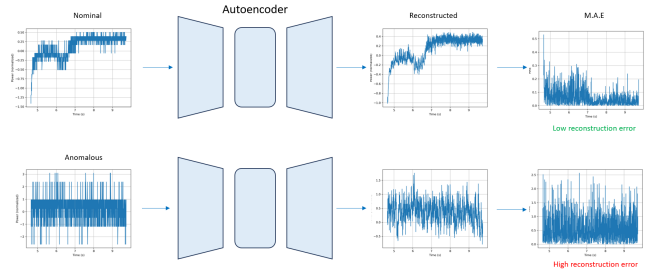


Figure 7. Example of autoencoder network applied to anomaly detection. The reconstruction MAE is used to determine if input data is anomalous.

complexity of the system in most microcontroller systems. These issues are mitigated in our implementation of the autoencoder by utilizing dense layers with no convolution and performing the training during the laboratory procedures on a separate device and not on the microcontroller itself. The trained weights are then loaded onto the anomaly detection device and used to compute the reconstruction error of newly measured data, which indicates whether the data is nominal or anomalous.

3. RESULTS

Here, we showcase the application of the anomaly detection device previously presented for the detection of anomalies in the operation of a lysis motor. This component is being used as part of the sample processing stage of the ELIE instrument [4] and is a common component in other life detection instrumentation under development. In principle, this lysis motor could be replaced with any given load that exhibits changing power draw as an unknown function of state. This includes most actuators, peripherals, or subsystems with electrical components present in instruments or spacecraft.

Background

Lysis is the process through which the membranes of cells are broken down, which makes materials only present inside the cell available for further analysis, such as DNA, RNA, proteins, or organelles. This process can be induced mechanically through the use of a lysis motor, which combines a small electrical brushed motor with a lysis chamber containing grinding beads through which a solution with the cells of interest is pumped. The motor stirs the grinding beads, which break down the cell walls and produce a lysate (solution containing the products of lysis) which can then be used for further analysis. The motor relies on the constant flow of fluid through the lysis chamber to avoid overheating during operation but does not pump the fluid itself and instead relies on a pumping system to continue feeding fluid through the lysis chamber.

A failure of the pumping system which starves the motor of fluid for a continued period of time will cause it to overheat, damaging it and preventing its further use. Furthermore, a latch-up event can maintain the motor running past the period through which the pumping system is providing it with fluid, causing it to overheat still. As fluid systems take up significant amounts of space and increase the complexity of an instrument, being able to reliably operate a single motor

and fluidic line is critical. These two possible failure modes were used to validate the anomaly detection algorithms currently implemented on the anomaly detection device while showcasing its setup, workflow, and features.

Experimental setup

The anomaly detection device was first connected between an OmniLyse® lysis motor and a power source, a benchtop power supply. A syringe connected to the motor was used to control the flow of fluid through the lysis chamber, as shown in the setup diagram presented by Figure 8. Instead of a cell solution, water was used as a cooling fluid. The microcontroller used for this setup was a Microchip SAMD21G18 Arm® Cortex®-M0 implemented on an IOT development board. The INA260 sensor was connected to the microcontroller through a Click development board and the power supply for the motor was routed through the sensor.

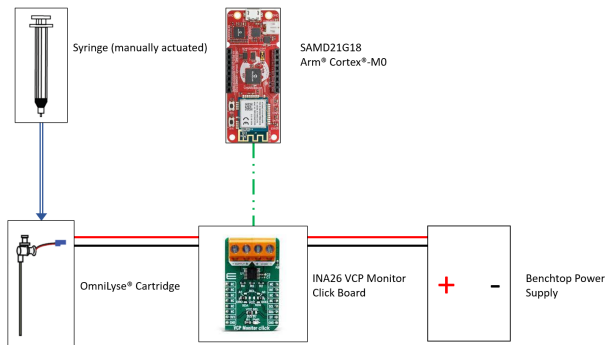


Figure 8. Lysis motor experimental setup used to collect training data.

The motor was first turned on and off repeatedly to capture data on the startup and shutdown behavior of the lysis motor. The motor was turned on and off roughly every 10 seconds by switching the power supply on and off, for a total duration of 50 seconds. This data was then used to determine a power threshold for when the motor was operating and when it was turned off. The state of the motor can be found utilizing the anomaly detection device and its out-of-bounds algorithm configured with the measured threshold.

The motor was then turned on constantly and run both with fluid constantly flowing through the lysis chamber (in wet conditions) and with no fluid flowing through (dry conditions). Readings for wet and dry conditions were captured in 60-second intervals, varying the voltage between 6V and 12V. An autoencoder network was trained on a subset of the wet conditions data. The rest of the wet and the dry data were then used as inputs to the network and the mean square error of the resulting data reconstruction was recorded.

Outcomes

Data from the first trial was processed using the out-of-bounds algorithm with an on/off threshold value of 3V. The algorithm was able to correctly determine the state of the motor, showing the anomaly detection device can correctly determine the running state of the motor from power consumption data, as shown in Figure 9. This capability is of special interest for anomalies that cause the commanded and actual state of a peripheral to not correspond to each other, such as latch-up events, as it provides a direct measurement

of the running state of the peripheral independent of the commanded value.

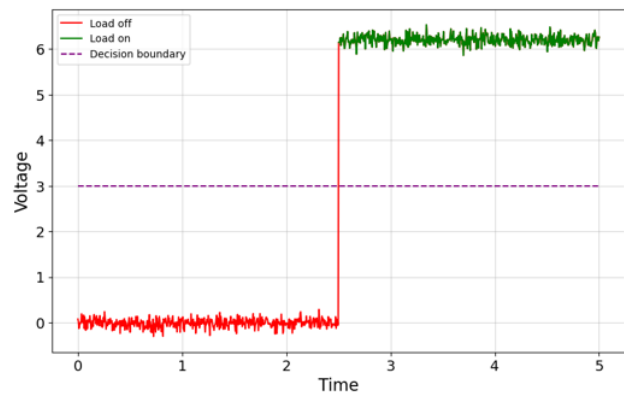


Figure 9. Detection of motor operation through out-of-limits anomaly detection.

Data from the second trial was first normalized and processed into rolling windows with a 5-second duration. The rolling windows resulting from the wet running conditions test were used to train an autoencoder network, which effectively reconstructed the rolling windows after training, with a mean absolute error of $0.1mW$ across all measured voltages under wet running conditions. This autoencoder network was then used to reconstruct dry running condition data, yielding reconstructions with an increased MAE (mean absolute error) of $0.64mW$ across all measured voltages. The mean absolute errors of all sampled windows were used to capture the distribution of the autoencoder reconstruction loss as a function of the operating conditions of the motor during data capture. The distribution of the wet windows was used to compute a limit of detection (LOD) for anomalies in the motor operating conditions, which was taken to be the mean plus three times the standard deviation of the wet conditions reconstruction MAE. The distributions of the MAE during dry and wet running, as well as the LOD are presented in Figure 10. The reconstruction loss of dry running condition data shows the effectiveness of the autoencoder at detecting anomalous motor operation conditions, as measurements taken during dry running conditions correctly lie past the LOD.

4. CONCLUSION

Anomaly detection is a critical component of any mission, as it protects instruments from irreparable damage caused by unexpected events that will inevitably occur during their lifetime. The presented anomaly detection device provides small instrument designers and integrators with an effective, inexpensive, and compact solution to add this capability to their instruments without investing large amounts of work implementing an ad-hoc solution for their instrument. The ability to use the same system in a laboratory setting as well as during flight gives users an edge to lower costs and reduce time to develop and deliver instruments, as well as ensuring anomalies observed in flight can be replicated. The proposed system was demonstrated for use with an instrument component that is analogous to actuators or peripherals readily present in other instruments and spacecraft, showcasing the ease of use and adaptability of the device. Continued development of this anomaly detection solution and its implementation in instruments through the use of

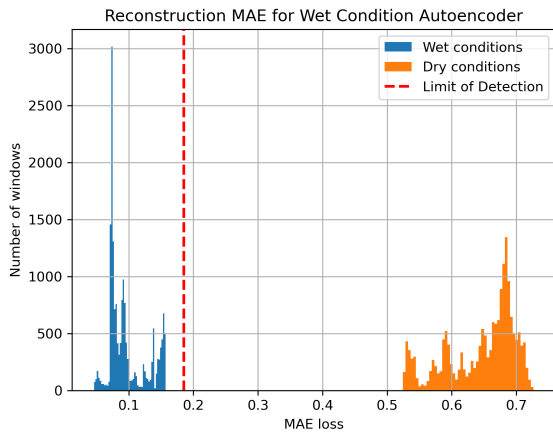


Figure 10. Detection of dry or wet conditions through autoencoder anomaly detection.

radiation-hardened hardware can enable new missions where anomaly recovery capabilities and heightened reliability are needed to access harsh mission environments autonomously, to further advance in-situ investigation of open questions in planetary science.

REFERENCES

- [1] Europa lander study 2016 report. [Online]. Available: <https://europa.nasa.gov/resources/58/europa-lander-study-2016-report>
- [2] S. M. MacKenzie, M. Neveu, A. F. Davila, J. I. Lunine, K. L. Craft, M. L. Cable, C. M. Phillips-Lander, J. D. Hofgartner, J. L. Eigenbrode, J. H. Waite, C. R. Glein, R. Gold, P. J. Greenauer, K. Kirby, C. Bradburne, S. P. Kounaves, M. J. Malaska, F. Postberg, G. W. Patterson, C. Porco, J. I. Núñez, C. German, J. A. Huber, C. P. McKay, J.-P. d. Vera, J. R. Brucato, and L. J. Spilker, “The encladus orbilander mission concept: Balancing return and resources in the search for life,” vol. 2, no. 2, p. 77, publisher: IOP Publishing. [Online]. Available: <https://iopscience.iop.org/article/10.3847/PSJ/abe4da/meta>
- [3] F. E. Bryson, M. Nassif, P. A. Szot, C. J. Chivers, N. Daniel, B. E. Wiley, T. Plattner, A. Hanna, Y. Tomar, S. Rapoport, E. M. Spiers, S. Pierson, A. Hodges, J. Lawrence, A. D. Mullen, D. Dichek, K. Hughson, M. R. Meister, E. G. Lightsey, and B. Schmidt, “Vertical entry robot for navigating europa (VERNE) mission and system design,” in *ASCEND 2020*. American Institute of Aeronautics and Astronautics, eprint: <https://arc.aiaa.org/doi/pdf/10.2514/6.2020-4061>. [Online]. Available: <https://arc.aiaa.org/doi/abs/10.2514/6.2020-4061>
- [4] C. E. Carr, J. L. Ramírez-Colón, D. Duzdevich, S. Lee, M. Taniguchi, T. Ohshiro, Y. Komoto, J. M. Soderblom, and M. T. Zuber, “Solid-state single-molecule sensing with the electronic life-detection instrument for encladus/europa (ELIE),” pages: 2022.08.31.505913 Section: New Results. [Online]. Available: <https://www.biorxiv.org/content/10.1101/2022.08.31.505913v1>
- [5] C. Lui, C. E. Carr, H. Rowedder, G. Ruvkun, and

M. Zuber, “SETG: An instrument for detection of life on mars ancestrally related to life on earth,” in *2011 Aerospace Conference*, pp. 1–12, ISSN: 1095-323X. [Online]. Available: <https://ieeexplore.ieee.org/document/5747299>

- [6] *Origins, Worlds, and Life: A Decadal Strategy for Planetary Science and Astrobiology 2023-2032*. National Academies Press. [Online]. Available: <https://www.nap.edu/catalog/26522>
- [7] S. A. Jacklin, “Small-satellite mission failure rates.” [Online]. Available: <https://ntrs.nasa.gov/api/citations/20190002705/downloads/20190002705.pdf>
- [8] mars.nasa.gov. Mars 2020 perseverance landing press kit. [Online]. Available: <https://mars.nasa.gov/resources/25529/mars-2020-perseverance-landing-press-kit>
- [9] NASA’s startling mission sending swarm of satellites into orbit - NASA. Running Time: 86 Section: Ames Research Center. [Online]. Available: <https://www.nasa.gov/centers-and-facilities/nasas-startling-mission-sending-swarm-of-satellites-into-orbit/>
- [10] Exobiology extant life surveyor (EELS). ISBN: 9780784483374. [Online]. Available: <https://ascelibrary.org/doi/epdf/10.1061/9780784483374.033>
- [11] “Satellite anomalies: benefits of a centralized anomaly database and methods for securely sharing information among satellite operators.”
- [12] M. Thill, W. Konen, H. Wang, and T. Bäck, “Temporal convolutional autoencoder for unsupervised anomaly detection in time series,” vol. 112, p. 107751. [Online]. Available: <https://www.sciencedirect.com/science/article/pii/S1568494621006724>

BIOGRAPHY



Alfonso Lagares de Toledo is an undergraduate researcher at Georgia Tech pursuing a B.S. degree in Aerospace Engineering. He is interested in leveraging system design to improve the way avionics are integrated into space missions.



Christopher E. Carr received his B.S. degree in Aero/Astro and Electrical Engineering in 1999, his Masters degree in Aero/Astro in 2001, and his Sc.D. degree in Medical Physics in 2005, all from MIT. He is an Assistant Professor in the Daniel Guggenheim School of Aerospace Engineering and the School of Earth and Atmospheric Sciences at the Georgia Institute of Technology. He is broadly interested in searching for and expanding the presence of life beyond Earth.

All-heavy pentaquarks in a nonrelativistic potential quark model

Zhi-Biao Liang¹, Feng-Xiao Liu^{2,3}*, and Xian-Hui Zhong^{1,3}†

1) Department of Physics, Hunan Normal University, and Key Laboratory of Low-Dimensional Quantum Structures and Quantum Control of Ministry of Education, Changsha 410081, China

2) Institute of High Energy Physics, Chinese Academy of Sciences, Beijing 100049, China and

3) Synergetic Innovation Center for Quantum Effects and Applications (SICQEA), Hunan Normal University, Changsha 410081, China

In a nonrelativistic potential quark model framework, we carry out a serious calculation of the all-heavy pentaquarks by adopting the explicitly correlated Gaussian method. A complete mass spectrum for the $1S$ states is obtained. For the $cccc\bar{c}$, $cccc\bar{b}$, $bbbb\bar{c}$, $bbbb\bar{b}$, $ccb\bar{c}$, and $bccb\bar{b}$ systems, the obtained states are compact and lie far above the lowest dissociation baryon-meson threshold. While, in the $ccb\bar{c}$, $ccb\bar{b}$, $bbc\bar{c}$, and $bbc\bar{b}$ systems with $\{123\}4\bar{5}$ symmetry, the two low-lying configurations with $J^P = 5/2^-$ and $3/2^-$ have a typical molecular structure due to the special role of the color-Coulomb interactions, they may be good candidates of stable states below the dissociation baryon-meson thresholds.

I. INTRODUCTION

Searching for genuine exotic multiquark states beyond the conventional meson ($q\bar{q}$) and baryon (qqq) states has been one of the most important initiatives since the establishment of quark model in 1964 [1–3]. Since the discovery of $X(3872)$ by Belle in 2003 [4], many tetraquark candidates, such as the series hidden-charmed/bottom XYZ states [5], the doubly-charmed state $T_{cc}(3875)^+$ [6, 7], and charmed-strange states [8, 9], have been observed in experiments. Furthermore, the exotic P_c [10–12] and P_{cs} [13] states as candidates of pentaquark states were also reported by the LHCb collaboration. All of these observed exotic states contains two or three light quarks, it is very difficult to determine whether they are hadronic molecular states or genuine multiquark states due to the role of light-meson exchanges. This dilemma should be largely alleviated for the all-heavy multiquarks. They are most likely to be genuine multiquark states since there is no light-meson exchange potential, which is often needed by the formation molecules. Thus, the study of the all-heavy multiquarks may provide an interesting way for establishing the genuine multiquark states.

Impressively, some all-heavy multiquark states have been observed in LHC experiments. In 2020, the LHCb Collaboration observed a narrow structure $X(6900)$ together a broad structure ranging from 6.2 to 6.8 GeV in the di- J/ψ invariant mass spectrum [14]. Later in 2022, the $X(6900)$ was confirmed in the same final state by both the ATLAS [15] and CMS [16] collaborations. Moreover, in the lower mass region the CMS measurements show that a clear resonance $X(6600)$ lies in the di- J/ψ spectrum. These clear structures may be evidences for genuine all-charmed tetraquark $cc\bar{c}\bar{c}$ states. The discovery of $cc\bar{c}\bar{c}$ states has demonstrated the powerful abilities of LHC in productions of fully-heavy hadrons, and also indicates that the all-heavy pentaquark should be exist. Thus, one may expect to observe some all-heavy pentaquarks in forthcoming experiments.

Stimulated by these, some relative studies of the all-heavy pentaquarks have been carried out within various models in recent years. The all-charmed and -bottom pentaquarks were studied with the QCD sum rules [17, 18]. For the baryon-meson type, the masses of $cccc\bar{c}$ and $bbbb\bar{b}$ are predicted to be ~ 7.41 GeV and ~ 21.60 GeV, respectively in Ref. [17], which are notably smaller than those of 7.93 ± 0.15 GeV and 23.91 ± 0.15 GeV predicted for the diquark-diquark-antiquark type in Ref. [18]. In Ref. [19], the mass spectra of the $1S$ -wave all-heavy pentaquarks were systematically studied with the simple chromomagnetic interaction (CMI) model. The masses of $cccc\bar{c}$ and $bbbb\bar{b}$ are predicted to be ~ 7.9 GeV and ~ 23.8 GeV, respectively, which are slightly above the lowest dissociation baryon-meson mass threshold. While, there may exist a stable $J^P = 3/2^-$ $bbcc\bar{b}$ states with a mass of ~ 17.4 MeV. In Ref. [20], the all-heavy pentaquarks were further studied within the MIT bag model by including the chromomagnetic interaction. In this framework, the masses of $cccc\bar{c}$ and $bbbb\bar{b}$ are predicted to be ~ 8.2 GeV and ~ 24.8 GeV, and no stable states below the dissociation baryon-meson thresholds are found.

In the recent two years, the all-heavy pentaquarks have been studied with more comprehensive potential quark models, where besides the chromomagnetic interaction, the confining and Coulomb-like potentials are also included in the calculations. In Refs. [21, 22], the authors studied the all-heavy pentaquarks by using the resonating group method (RGM), in which two-cluster approximation is adopted. They obtained one possible stable $J^P = 1/2^-$ $cccc\bar{c}$ state with a mass of ~ 7.9 GeV, and two possible stable $bbbb\bar{b}$ states with $J^P = 1/2^-$ and $J^P = 3/2^-$ in the mass range of ~ 23.8 GeV, and several possible stable candidates in the charmed-bottom pentaquarks. In Ref. [23], considering the baryon-meson and diquark-diquark-antiquark configurations, the authors obtained several narrow resonances above 8.0 GeV and 24.0 GeV for the $cccc\bar{c}$ and $bbbb\bar{b}$ pentaquarks, respectively, based on the Gaussian expansion method combined with a complex-scaling range approach. Recently, a more serious dynamical calculation beyond the cluster approximation has been carried out by using the variational method with the trial spatial wave function in a simple Gaussian form [24]. No stable pentaquarks states below the dissociation baryon-meson thresholds are found. The masses for the ground $cccc\bar{c}$ and $bbbb\bar{b}$ states are predicted

*E-mail: liufx@ihep.ac.cn

†E-mail: zhongxh@hunnu.edu.cn

to be ~ 8.2 GeV and ~ 24.2 GeV, respectively, which are consistent with those obtained with the trial function in the most general Gaussian form [25]. However, due to the simple Gaussian basis adopted in Ref [24], no stable solutions are obtained for many states in the all-heavy pentaquarks containing unequal mass quarks, such as $cccc\bar{b}$, $cccb\bar{c}$, $bbbb\bar{c}$, and $bbb\bar{c}\bar{b}$.

In this work, we carry out a dynamical calculation of the mass spectra of the $1S$ -wave all-heavy pentaquarks with a nonrelativistic potential quark model (NRPQM). This model is based on the Hamiltonian of the Cornell model [26], whose parameters have been well determined based on the successful description of the heavy quarkonium spectra [27–29], and triply charmed and bottom baryon spectra [30]. This model has been extended to study the mass spectra of all-heavy tetraquarks by our group in Refs. [31–33]. To solve the five-body problem accurately, we adopt the explicitly correlated Gaussian (ECG) method [34, 35], in which a variational trial spatial wave function is expanded with the most general nondiagonal Gaussian basis functions associated to the Jacobi coordinates. This is one of the most powerful approaches currently used for calculating the properties of few-body systems, and offers great flexibility, and high accuracy [35]. Based on the ECG numerical method, the mass spectrum of charmed-strange tetraquarks was successfully predicted by our group, recently [36]. The main purposes of this work are (i) to give a reliable prediction of the mass spectra for the fully-heavy pentaquarks based on our serious studies; (ii) to reveal the inner structure special properties of the pentaquark states due to the complex symmetry and dynamics; (iii) to assess the differences of the predictions from different potential models with different numerical methods.

As follows, we first give a brief introduction to our framework. We then give our numerical results and discussions for the S -wave all-heavy pentaquarks states in Sec. III. Finally, a summary is given in Sec. IV.

II. FRAMEWORK

In this section, we first give a brief review of the nonrelativistic potential quark model. Then, we introduce the quark model classification of the pentaquarks based on the symmetries. Finally, we give a brief introduction to the ECG method what we adopt in the calculations.

A. Hamiltonian

In NRPQM, the Hamiltonian for a pentaquark system is given by

$$H = \sum_i^5 (m_i + T_i) - T_{cm} + \sum_{i<j}^5 V_{ij}(r_{ij}), \quad (1)$$

where m_i and T_i represent the mass and kinetic energy of the i -th quark, respectively; T_{cm} represents the kinetic energy of the center of mass of the pentaquark system; $r_{ij} = |\mathbf{r}_i - \mathbf{r}_j|$ is the distance between the i -th and j -th quarks; while V_{ij} is an

effective potential between them. In this work, the effective potential V_{ij} is adopted a widely used form,

$$V_{ij}(r_{ij}) = -\frac{3}{16} (\boldsymbol{\lambda}_i \cdot \boldsymbol{\lambda}_j) \left(br_{ij} - \frac{4}{3} \frac{\alpha_{ij}}{r_{ij}} + C_0 \right) - \frac{\alpha_{ij}}{4} (\boldsymbol{\lambda}_i \cdot \boldsymbol{\lambda}_j) \cdot \left\{ \frac{\pi}{2} \cdot \frac{\sigma_{ij}^3 e^{-\sigma_{ij}^2 r_{ij}^2}}{\pi^{3/2}} \cdot \frac{16}{3m_i m_j} (\mathbf{S}_i \cdot \mathbf{S}_j) \right\}, \quad (2)$$

where $\boldsymbol{\lambda}_{i,j}$ are the color operators acting on the i, j -th quarks, $\mathbf{S}_{i,j}$ represent the spin operators of the i, j -th quarks; while C_0 represents the zero-point energy. The parameters b and α_{ij} denote the strength of the confinement and strong coupling of the one-gluon-exchange potential, respectively. In this work, the parameter set $\{b, \alpha_{ij}, C_0, \sigma_{ij}, m_i\}$ is taken the same as that in our previous works [30, 33] and are listed in Table I. These parameters were determined through the fitting of meson spectrum. Finally, it should be mentioned that in this work we only consider the low-lying $1S$ -wave pentaquark states without any orbital excitations, thus, the spin-orbit and tensor potentials are not included.

TABLE I: The potential model parameters.

$m_c/m_b(\text{GeV})$	1.483/4.852
$\alpha_{cc}/\alpha_{bc}/\alpha_{bb}$	0.5461/0.5021/0.4311
$\sigma_{cc}/\sigma_{bc}/\sigma_{bb}(\text{GeV})$	1.1384/1.3000/2.3200
$b(\text{GeV}^2)$	0.1425
$C_0(\text{GeV})$	0

B. Pentaquark configuration

The pentaquark configuration can be expressed as a product the flavor, spatial, spin, and color parts, i.e.,

$$|\Psi_{5q}\rangle = |flavor\rangle \otimes |spatial\rangle \otimes |spin\rangle \otimes |color\rangle. \quad (3)$$

In the flavor space, the available configurations for all-heavy pentaquarks are “ $cccc\bar{c}$, $cccc\bar{b}$, $bbbb\bar{b}$, $bbbb\bar{c}$, $cccb\bar{b}$, $cccb\bar{c}$, $bbbc\bar{c}$, $bbbc\bar{b}$, $ccbb\bar{c}$, $bbcc\bar{b}$ ”. The spin and color parts can be constructed according to the permutation symmetry. For the low-lying $1S$ pentaquark states without any excitations, their spatial wave functions are symmetrical when exchanging the coordinates of any two quarks. To obtain the spatial part of the pentaquarks, one should solve the Schrödinger equation.

Due to the pentaquark system containing identical quarks, it must satisfy the Pauli principle. Considering the permutation symmetry of identical quarks, the pentaquark configurations can be classified into three categories, which are denoted by

$$\begin{aligned} \{1234\}\bar{5} &: \{cccc\}\bar{c}, \{cccc\}\bar{b}, \{bbbb\}\bar{b}, \{bbbb\}\bar{c}, \\ \{123\}4\bar{5} &: \{ccc\}b\bar{b}, \{ccc\}b\bar{c}, \{bbb\}c\bar{c}, \{bbb\}c\bar{b}, \\ \{12\}\{34\}\bar{5} &: \{cc\}\{bb\}\bar{c}, \{bb\}\{cc\}\bar{b}. \end{aligned} \quad (4)$$

The quarks in $\{\}$ should satisfy the requirements of the permutation symmetry.

For a pentaquark system, one can construct three colorless configurations (color singlets) in the color space based on the $SU(3)$ -group representation theory. Their representations with Young tableaux are given by [39]

$$C_1 = \begin{array}{|c|c|} \hline 1 & 4 \\ \hline 2 & \\ \hline 3 & \\ \hline \end{array} \otimes (5)_3, \quad C_2 = \begin{array}{|c|c|} \hline 1 & 2 \\ \hline 3 & \\ \hline 4 & \\ \hline \end{array} \otimes (5)_3, \quad C_3 = \begin{array}{|c|c|} \hline 1 & 3 \\ \hline 2 & \\ \hline 4 & \\ \hline \end{array} \otimes (5)_3. \quad (5)$$

By using the C-G coefficients of $SU(3)$ group [37], one can explicitly write out the three color configurations, which are can be found in the literature, such as Ref. [20].

For a pentaquark system, the total spin quantum numbers are possibly $J = 5/2, 3/2, 1/2$. Based on the $SU(2)$ symmetry, one can construct the configurations with $J = 5/2, 3/2, 1/2$ in the spin space. Their representations with Young tableaux are given by

$$J = \frac{5}{2} : S_1 = \begin{array}{|c|c|c|c|} \hline 1 & 2 & 3 & 4 \\ \hline \end{array} 5. \quad (6)$$

$$J = \frac{3}{2} : S_2 = \begin{array}{|c|c|c|} \hline 1 & 2 & 3 & 4 \\ \hline 5 & & & \\ \hline \end{array}, \quad S_3 = \begin{array}{|c|c|c|} \hline 1 & 2 & 3 & 5 \\ \hline 4 & & & \\ \hline \end{array}, \quad (7)$$

$$S_4 = \begin{array}{|c|c|c|} \hline 1 & 3 & 4 & 5 \\ \hline 2 & & & \\ \hline \end{array}, \quad S_5 = \begin{array}{|c|c|c|} \hline 1 & 2 & 4 & 5 \\ \hline 3 & & & \\ \hline \end{array}.$$

$$J = \frac{1}{2} : S_6 = \begin{array}{|c|c|c|} \hline 1 & 2 & 3 \\ \hline 4 & 5 & \\ \hline \end{array}, \quad S_7 = \begin{array}{|c|c|c|} \hline 1 & 3 & 4 \\ \hline 2 & 5 & \\ \hline \end{array}, \quad S_8 = \begin{array}{|c|c|c|} \hline 1 & 2 & 4 \\ \hline 3 & 5 & \\ \hline \end{array}, \quad (8)$$

$$S_9 = \begin{array}{|c|c|} \hline 1 & 2 \\ \hline 3 & 4 \\ \hline \end{array} 5, \quad S_{10} = \begin{array}{|c|c|} \hline 1 & 3 \\ \hline 2 & 4 \\ \hline \end{array} 5.$$

Combining the C-G coefficient of $SU(2)$ group, one can obtain the spin wave function $\psi_{S_i|J_z}$ corresponding to a special Young tableau.

With the configurations of the color and spin spaces, one can further construct the configurations of the spin \otimes color space. For the low-lying $1S$ -wave pentaquark configurations, both the spatial and flavor parts are symmetric when one exchanges any two identical quarks, thus, the spin \otimes color part should be antisymmetric. To get the coupling configurations in the spin \otimes color space, we need the C-G coefficients of S_4 group, which are taken from Ref. [38].

For a pentaquark system with $\{1234\bar{5}$ symmetry, there are two configurations with $J^P = \frac{3}{2}^-$ and $\frac{1}{2}^-$:

$$1S_{\frac{3}{2}^-}(\{1234\bar{5}\}) = \frac{1}{\sqrt{3}} (C_1 S_3 + C_2 S_4 - C_3 S_5),$$

$$1S_{\frac{1}{2}^-}(\{1234\bar{5}\}) = \frac{1}{\sqrt{3}} (C_1 S_6 + C_2 S_7 - C_3 S_8).$$

It should be mentioned that there is no $J^P = \frac{5}{2}^-$ configurations. In this case, the $\{1234\bar{5}$ symmetry requires the color configurations are fully antisymmetric since the spin configurations are fully symmetric, however, the color configurations given in Eq. (5) cannot satisfy this requirement.

For a pentaquark system with $\{123\}4\bar{5}$ symmetry, one can obtain a $J^P = \frac{5}{2}^-$ configuration,

$$1S_{\frac{5}{2}^-}(\{123\}4\bar{5}) = C_1 S_1,$$

three $J^P = \frac{3}{2}^-$ configurations,

$$1S_{\frac{3}{2}^-}(\{123\}4\bar{5})_1 = \sqrt{\frac{1}{3}} (C_2 S_4 - C_3 S_5 + C_1 S_3),$$

$$1S_{\frac{3}{2}^-}(\{123\}4\bar{5})_2 = \sqrt{\frac{1}{6}} (-C_2 S_4 + C_3 S_5 + 2C_1 S_3),$$

$$1S_{\frac{3}{2}^-}(\{123\}4\bar{5})_3 = C_1 S_2,$$

and three $J^P = \frac{1}{2}^-$ configurations,

$$1S_{\frac{1}{2}^-}(\{123\}4\bar{5})_1 = \sqrt{\frac{1}{3}} (C_2 S_7 - C_3 S_8 + C_1 S_6),$$

$$1S_{\frac{1}{2}^-}(\{123\}4\bar{5})_2 = \sqrt{\frac{1}{6}} (-C_2 S_7 + C_3 S_8 + 2C_1 S_6),$$

$$1S_{\frac{1}{2}^-}(\{123\}4\bar{5})_3 = \sqrt{\frac{1}{2}} (C_2 S_{10} - C_3 S_9).$$

For a pentaquark system with $\{12\}\{34\bar{5}$ symmetry, there is a $J^P = \frac{5}{2}^-$ configuration,

$$1S_{\frac{5}{2}^-}(\{12\}\{34\bar{5}\}) = \sqrt{\frac{2}{3}} C_3 S_1 - \sqrt{\frac{1}{3}} C_1 S_1,$$

four $J^P = \frac{3}{2}^-$ configurations,

$$1S_{\frac{3}{2}^-}(\{12\}\{34\bar{5}\})_1 = \sqrt{\frac{1}{3}} (C_2 S_4 - C_3 S_5 + C_1 S_3),$$

$$1S_{\frac{3}{2}^-}(\{12\}\{34\bar{5}\})_2 = \sqrt{\frac{1}{3}} (C_1 S_5 - C_3 S_3) - \sqrt{\frac{1}{6}} (C_2 S_4 + C_3 S_5),$$

$$1S_{\frac{3}{2}^-}(\{12\}\{34\bar{5}\})_3 = \frac{\sqrt{2}}{6} (3C_2 S_4 + C_3 S_5 - 2C_1 S_3)$$

$$+ \frac{1}{3} (C_1 S_5 - C_3 S_3),$$

$$1S_{\frac{3}{2}^-}(\{12\}\{34\bar{5}\})_4 = \sqrt{\frac{2}{3}} C_3 S_2 - \sqrt{\frac{1}{3}} C_1 S_2,$$

and four $J^P = \frac{1}{2}^-$ configurations,

$$1S_{\frac{1}{2}^-}(\{12\}\{34\bar{5}\})_1 = \sqrt{\frac{1}{3}} (C_2 S_7 - C_3 S_8 + C_1 S_6),$$

$$1S_{\frac{1}{2}^-}(\{12\}\{34\bar{5}\})_2 = \sqrt{\frac{1}{3}} (C_1 S_8 - C_3 S_6) - \sqrt{\frac{1}{6}} (C_2 S_7 + C_3 S_8),$$

$$1S_{\frac{1}{2}^-}(\{12\}\{34\bar{5}\})_3 = \frac{\sqrt{2}}{6} (3C_2 S_7 + C_3 S_8 - 2C_1 S_6)$$

$$+ \frac{1}{3} (C_1 S_8 - C_3 S_6),$$

$$1S_{\frac{1}{2}^-}(\{12\}\{34\bar{5}\})_4 = \sqrt{\frac{2}{3}} C_3 S_9 - \sqrt{\frac{1}{3}} C_1 S_9.$$

To know more technical details for constructing the pentaquark configurations in the spin \otimes color space, one can refer to the works [19, 20, 24, 39].

C. Numerical method

To solve the five-body problem accurately, we adopt the ECG method [34, 35]. It is a well-established variational method to solve quantum few-body problems in molecular, atomic, and nuclear physics. The spatial part of the wave function for a pentaquark system without any angular momenta is expanded in terms of ECG basis set. Such a basis function can be expressed as

$$\psi(\mathbf{r}_1, \mathbf{r}_2, \mathbf{r}_3, \mathbf{r}_4, \mathbf{r}_5) = \exp\left[-\sum_{i<j}^5 a_{ij} r_{ij}^2\right], \quad (9)$$

where a_{ij} are variational parameters. For a pentaquark system with $\{1234\}\bar{5}$ symmetry, one has two independent variational parameters, i.e., $a_{12} = a_{13} = a_{14} = a_{23} = a_{24} = a_{34} = a$ and $a_{15} = a_{25} = a_{35} = a_{45} = b$, due to the symmetry of identical quarks. Similarly, for a pentaquark system with $\{123\}4\bar{5}$ -symmetry, there are four variational parameters, $a_{12} = a_{13} = a_{23} = a$, $a_{14} = a_{24} = a_{34} = b$, $a_{15} = a_{25} = a_{35} = c$ and $a_{45} = d$. While for a pentaquark system with $\{12\}\{34\}\bar{5}$ symmetry, there are also five independent variational parameters, $a_{12} = a$, $a_{13} = a_{14} = a_{23} = a_{24} = b$, $a_{15} = a_{25} = c$, $a_{34} = d$ and $a_{35} = a_{45} = f$.

It is convenient to use a set of the Jacobi coordinates $\xi = (\xi_1, \xi_2, \xi_3, \xi_4)$ instead of position vectors \mathbf{r}_i ($i = 1 - 5$). For example, one can take a set of Jacobi coordinates as follows,

$$\begin{aligned} \xi_1 &= \mathbf{r}_1 - \mathbf{r}_2, \\ \xi_2 &= \mathbf{r}_3 - \frac{m_1 \mathbf{r}_1 + m_2 \mathbf{r}_2}{m_1 + m_2}, \\ \xi_3 &= \mathbf{r}_4 - \mathbf{r}_5, \\ \xi_4 &= \frac{m_1 \mathbf{r}_1 + m_2 \mathbf{r}_2 + m_3 \mathbf{r}_3}{m_1 + m_2 + m_3} - \frac{m_4 \mathbf{r}_4 + m_5 \mathbf{r}_5}{m_4 + m_5}. \end{aligned} \quad (10)$$

Then, the correlated Gaussian basis function ψ can be rewritten as

$$G(\xi, A) = \exp(-\xi^T A \xi), \quad (11)$$

where A is a 4×4 matrix, which is related to the variational parameters. The spatial part of the trial wave function can be expanded with a set of correlated Gaussians:

$$\Psi(\xi, A) = \sum_{k=1}^N C_k G(\xi, A_k), \quad (12)$$

where N is the number of Gaussian basis functions. The accuracy of the trial function depends on the number N and the nonlinear parameter matrix A_k . In our calculations, following the method of Ref. [40], we let the variational parameters form a geometric progression. For example, for a variational parameter a , we take

$$a_i = \frac{1}{2(a_1 q^{i-1})^2} \quad (i = 1, \dots, n_{max}). \quad (13)$$

The Gaussian size parameters $\{a_1, q, n_{max}\}$ will be determined through the variation method. In the calculations, the final results should be stable and independent with these parameters.

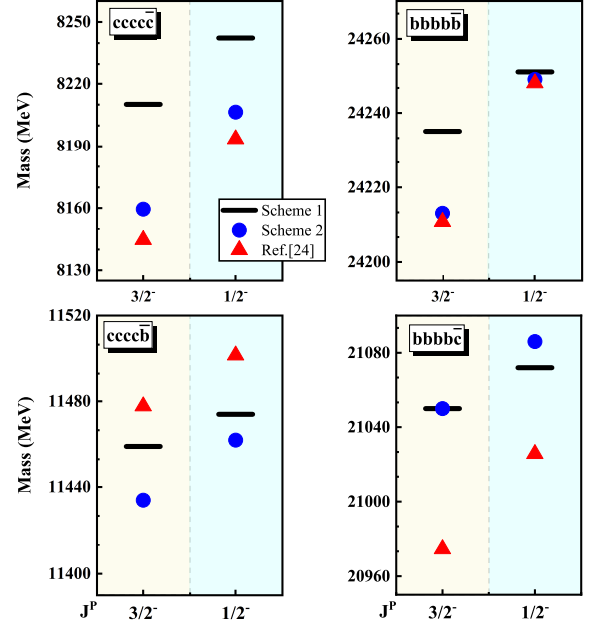


FIG. 1: Spectrum for all-heavy pentaquarks with $\{1234\}\bar{5}$ symmetry. The black short solid lines stand for the predictions based on the potential model of the present work with the ECG numerical method (Scheme 1). The solid circles and triangles stand for the predictions based on the potential model of Ref. [24], which are solved with the ECG numerical method in this work (Scheme 2) and with the simple diagonal Gaussian basis in Ref. [24], respectively.

For a given pentaquark configuration, one can work out the Hamiltonian matrix elements,

$$H_{kk'} = \langle \psi_{CS} G(\xi, A_k) | H | \psi_{CS} G(\xi, A_{k'}) \rangle, \quad (14)$$

where ψ_{CS} is the spin-color wave function. Then, by solving the generalized matrix eigenvalue problem,

$$\sum_{k'=1}^N (H_{kk'} - E N_{kk'}) C_{k'} = 0, \quad (15)$$

one can obtain the eigenenergy E , and the expansion coefficients $\{C_k\}$. Where $N_{kk'}$ is an overlap factor defined by $N_{kk'} = \langle G(\xi, A_k) | G(\xi, A_{k'}) \rangle$.

Finally, it should be mentioned that in the calculations we can obtain stable solutions when we take $N = n_{max}^a \times n_{max}^b = 8 \times 8 = 64$ for the system with $\{1234\}\bar{5}$ symmetry, $N = n_{max}^a \times n_{max}^b \times n_{max}^c \times n_{max}^d = 5 \times 5 \times 5 \times 5 = 625$ for the system with $\{123\}4\bar{5}$ symmetry, while $N = n_{max}^a \times n_{max}^b \times n_{max}^c \times n_{max}^d \times n_{max}^f = 4 \times 4 \times 4 \times 4 \times 4 = 1024$ for the system with $\{12\}\{34\}\bar{5}$ symmetry.

III. RESULTS AND DISCUSSIONS

A. States with $\{1234\}\bar{5}$ symmetry

In the all-heavy pentaquarks, the $cccb\bar{c}$, $cccb\bar{b}$, $bbbb\bar{c}$, and $bbbb\bar{b}$ systems have the $\{1234\}\bar{5}$ symmetry. Considering the

TABLE II: Predicted mass spectra of $1S$ states for the $cccc\bar{c}$, $bbbb\bar{b}$, $cccc\bar{b}$, and $bbbb\bar{c}$ systems compared with those of other works. The unit is MeV. ‘‘Scheme 1’’ stands for the results obtained with the ECG method based on the potential model of the present work, while ‘‘Scheme 2’’ stands for the results obtained with the ECG method based on the potential model of Ref. [24].

	J^P	Configuration	Scheme 1	Scheme 2	[24]	[19]	[20]	[23]	[21]	[18]	[17]
$cccc\bar{c}$	$3/2^-$	$1S_{\frac{3}{2}}-\{(1234)5\}$	8210	8159	8145	7864	8229	8095			7410^{+270}_{-310}
	$1/2^-$	$1S_{\frac{1}{2}}-\{(1234)5\}$	8242	8206	8193	7949	8262	8045	7892	7930 ± 150	
$bbbb\bar{b}$	$3/2^-$	$1S_{\frac{3}{2}}-\{(1234)5\}$	24235	24213	24211	23775	24761	24035	23748		21600^{+730}_{-220}
	$1/2^-$	$1S_{\frac{1}{2}}-\{(1234)5\}$	24251	24249	24248	23821	24770	24035	23810	23910 ± 150	
$cccc\bar{b}$	$3/2^-$	$1S_{\frac{3}{2}}-\{(1234)5\}$	11459	11434	11478	11130	11569				
	$1/2^-$	$1S_{\frac{1}{2}}-\{(1234)5\}$	11474	11462	11502	11177	11582				
$bbbb\bar{c}$	$3/2^-$	$1S_{\frac{3}{2}}-\{(1234)5\}$	21050	21050	20975	20652	21472				
	$1/2^-$	$1S_{\frac{1}{2}}-\{(1234)5\}$	21072	21086	21026	20699	21491				

TABLE III: The average contributions of each part of the Hamiltonian (in MeV) and the root mean square radii (in fm) for the $1S$ -wave all-heavy pentaquark configurations with the $\{1234\}\bar{5}$ symmetry.

	J^P	Configuration	Each part contribution of Hamiltonian					RMS Radius	
			Mass	$\langle T \rangle$	$\langle V^{Conf} \rangle$	$\langle V^{Coul} \rangle$	$\langle V^{SS} \rangle$	$r_{12}, r_{13}, r_{14},$ r_{23}, r_{24}, r_{34}	$r_{15}, r_{25},$ r_{35}, r_{45}
$cccc\bar{c}$	$3/2^-$	$1S_{\frac{3}{2}}-\{(1234)\bar{5}\}$	8210	886	860.7	-977.8	26.1	0.5248	0.5176
	$1/2^-$	$1S_{\frac{1}{2}}-\{(1234)\bar{5}\}$	8242	846	879.8	-954.9	56.3	0.5327	0.5337
$cccc\bar{b}$	$3/2^-$	$1S_{\frac{3}{2}}-\{(1234)\bar{5}\}$	11459	858	800	-1017	34	0.5135	0.4413
	$1/2^-$	$1S_{\frac{1}{2}}-\{(1234)\bar{5}\}$	11474	842	807	-1007	48	0.5172	0.4467
$bbbb\bar{c}$	$3/2^-$	$1S_{\frac{3}{2}}-\{(1234)\bar{5}\}$	21050	919	548	-1317	9	0.2988	0.3864
	$1/2^-$	$1S_{\frac{1}{2}}-\{(1234)\bar{5}\}$	21072	889	557	-1296	30	0.3017	0.3957
$bbbb\bar{b}$	$3/2^-$	$1S_{\frac{3}{2}}-\{(1234)\bar{5}\}$	24235	931	467	-1436	14	0.2842	0.2839
	$1/2^-$	$1S_{\frac{1}{2}}-\{(1234)\bar{5}\}$	24251	905	473	-1416	29	0.2870	0.2890

permutation symmetry of identical quarks, there are two states with $J^P = 3/2^-$ and $J^P = 1/2^-$ for each pentaquark system. The mass splitting between them is very small ($\sim 15 - 30$ MeV), the $J = 1/2^-$ slightly lies above the $J = 3/2^-$ state. The predicted mass spectrum has been given in Table II and also shown in Fig. 1.

For the $cccc\bar{c}$ system, the masses of the ground ($1S$) states are predicted to be ~ 8.2 GeV, which is ~ 300 MeV above the mass threshold of $J/\psi\Omega_{ccc}(3/2^+)$ according to the predictions of the triply heavy baryon spectrum [30]. For the $bbbb\bar{b}$ system, the masses of the $1S$ states are predicted to be ~ 24.2 GeV, which is ~ 340 MeV above the mass threshold of $\Upsilon(1S)\Omega_{bbb}(3/2^+)$. For the $cccc\bar{b}$ system, the masses of the $1S$ states are predicted to be ~ 11.5 GeV, which is ~ 400 MeV above the mass threshold of $B_c\Omega_{ccc}(3/2^+)$. While, for the $bbbb\bar{c}$ system, the masses of the two $1S$ states are predicted to be ~ 21.1 GeV, which is ~ 400 MeV above the mass threshold of $B_c\Omega_{bbb}(3/2^+)$.

Similar studies have been carried out within another potential model approach in a recent work by An *et al.* [24]. For a comparison, we listed their results in Table II and also shown in Fig. 1. It is seen that our predicted mass spectra are con-

sistent with those in Ref. [24]. The differences of the predictions between ours and those in Ref. [24] are within 100 MeV. To further see the numerical method dependency of the predictions, by using the same Hamiltonian of Ref. [24] we calculate the mass spectrum with the ECG method as well. The results are listed in Table II and shown in Fig. 1. From Fig. 1, one can see that the results for the $cccc\bar{c}$ and $bbbb\bar{b}$ systems obtained with the ECG method (solid circles) are very close to those (solid triangles) obtained with the simple diagonal Gaussian basis in Ref. [24]. However, for the $cccc\bar{b}$ and $bbbb\bar{c}$ systems containing unequal mass quarks, there is a considerable difference of $\sim 40 - 80$ MeV in the results obtained with the two different numerical methods. Some other studies about these pentaquarks can be found in the literature based on the MIT bag model [20], CMI model [19], Lattice-QCD inspired quark model [23], chiral quark model/quark delocalization color screening model [21], and QCD sum rule approach [17, 18], the results are collected in Table II for a comparison. There are large discrepancies (about 100 – 1000 MeV) in the predictions from various models.

Moreover, to know some details of the inner structure of the predicted pentaquark states, we calculate the root mean square

TABLE IV: Predicted mass spectra of $1S$ states for the $cccb\bar{c}$, $cccb\bar{b}$, $bbcb\bar{c}$ and $bbcb\bar{b}$ systems.

J^P	$cccb\bar{c}$			$cccb\bar{b}$			Configuration		
	Mass	Eigenvector			Mass	Eigenvector			
$5/2^-$	(11160)	(1)			(14322)	(1)			$(1S_{\frac{5}{2}} - (\{123\}4\bar{5}))$
$3/2^-$	(11124)	$\begin{pmatrix} -0.02 & -0.09 & 1 \\ 0.57 & 0.82 & 0.08 \\ -0.82 & 0.57 & 0.03 \end{pmatrix}$			(14282)	$\begin{pmatrix} -0.04 & -0.08 & 1 \\ 0.56 & 0.83 & 0.09 \\ -0.83 & 0.56 & 0.02 \end{pmatrix}$			$1S_{\frac{3}{2}} - (\{123\}4\bar{5})_1$
	(11349)				(14522)				$1S_{\frac{3}{2}} - (\{123\}4\bar{5})_2$
	(11482)				(14737)				$1S_{\frac{3}{2}} - (\{123\}4\bar{5})_3$
$1/2^-$	(11356)	$\begin{pmatrix} 0.46 & 0.85 & 0.26 \\ -0.23 & -0.17 & 0.96 \\ -0.86 & 0.50 & -0.12 \end{pmatrix}$			(14534)	$\begin{pmatrix} 0.53 & 0.84 & 0.06 \\ -0.07 & -0.03 & 1 \\ -0.84 & 0.54 & -0.05 \end{pmatrix}$			$1S_{\frac{1}{2}} - (\{123\}4\bar{5})_1$
	(11419)				(14645)				$1S_{\frac{1}{2}} - (\{123\}4\bar{5})_2$
	(11506)				(14745)				$1S_{\frac{1}{2}} - (\{123\}4\bar{5})_3$
J^P	$bbcb\bar{c}$			$bbcb\bar{b}$			Configuration		
	Mass	Eigenvector			Mass	Eigenvector			
$5/2^-$	(20767)	(1)			(17540)	(1)			$(1S_{\frac{5}{2}} - (\{123\}4\bar{5}))$
$3/2^-$	(20731)	$\begin{pmatrix} -0.04 & -0.09 & 1 \\ 0.54 & 0.84 & 0.10 \\ -0.84 & 0.54 & 0.01 \end{pmatrix}$			(17465)	$\begin{pmatrix} -0.08 & -0.14 & 0.99 \\ 0.55 & 0.82 & 0.16 \\ -0.83 & 0.55 & 0.01 \end{pmatrix}$			$1S_{\frac{3}{2}} - (\{123\}4\bar{5})_1$
	(20951)				(17740)				$1S_{\frac{3}{2}} - (\{123\}4\bar{5})_2$
	(21120)				(17913)				$1S_{\frac{3}{2}} - (\{123\}4\bar{5})_3$
$1/2^-$	(20964)	$\begin{pmatrix} 0.52 & 0.86 & 0.05 \\ -0.05 & -0.03 & 1 \\ -0.86 & 0.52 & -0.03 \end{pmatrix}$			(17761)	$\begin{pmatrix} 0.51 & 0.85 & 0.10 \\ -0.08 & -0.7 & 0.99 \\ -0.86 & 0.52 & -0.03 \end{pmatrix}$			$1S_{\frac{1}{2}} - (\{123\}4\bar{5})_1$
	(21051)				(17837)				$1S_{\frac{1}{2}} - (\{123\}4\bar{5})_2$
	(21128)				(17928)				$1S_{\frac{1}{2}} - (\{123\}4\bar{5})_3$

TABLE V: Predicted mass spectra of $1S$ states for the $ccbb\bar{c}$ and $bbcb\bar{b}$ systems.

J^P	$ccbb\bar{c}$				$bbcb\bar{b}$				Configuration		
	Mass	Eigenvector				Mass	Eigenvector				
$5/2^-$	(14691)	1				(17831)	1				$(1S_{\frac{5}{2}} - (\{12\}\{34\}\bar{5}))$
$3/2^-$	(14584)	$\begin{pmatrix} -0.16 & -0.01 & -0.39 & 0.91 \\ 0.52 & 0.85 & -0.04 & 0.09 \\ 0.19 & 0.11 & -0.89 & -0.41 \\ -0.82 & 0.51 & 0.25 & -0.04 \end{pmatrix}$				(17815)	$\begin{pmatrix} 0.03 & 0.05 & -0.30 & 0.95 \\ 0.40 & 0.91 & -0.05 & -0.08 \\ 0.37 & -0.09 & 0.88 & 0.27 \\ -0.84 & 0.40 & 0.36 & 0.11 \end{pmatrix}$				$1S_{\frac{3}{2}} - (\{12\}\{34\}\bar{5})_1$
	(14625)					(17835)					$1S_{\frac{3}{2}} - (\{12\}\{34\}\bar{5})_2$
	(14651)					(17856)					$1S_{\frac{3}{2}} - (\{12\}\{34\}\bar{5})_3$
	(14665)					(17880)					$1S_{\frac{3}{2}} - (\{12\}\{34\}\bar{5})_4$
$1/2^-$	(14585)	$\begin{pmatrix} 0.12 & 0.77 & -0.29 & -0.56 \\ -0.15 & -0.58 & -0.09 & -0.79 \\ -0.17 & -0.15 & -0.94 & 0.24 \\ -0.97 & 0.22 & 0.14 & 0.01 \end{pmatrix}$				(17815)	$\begin{pmatrix} -0.13 & -0.53 & -0.15 & -0.83 \\ -0.19 & -0.82 & 0.10 & 0.53 \\ 0.25 & -0.06 & 0.95 & -0.18 \\ -0.94 & 0.22 & 0.26 & -0.04 \end{pmatrix}$				$1S_{\frac{1}{2}} - (\{12\}\{34\}\bar{5})_1$
	(14606)					(17819)					$1S_{\frac{1}{2}} - (\{12\}\{34\}\bar{5})_2$
	(14655)					(17858)					$1S_{\frac{1}{2}} - (\{12\}\{34\}\bar{5})_3$
	(14684)					(17891)					$1S_{\frac{1}{2}} - (\{12\}\{34\}\bar{5})_4$

(RMS) radii between two quarks, i.e., $\sqrt{\langle r_{ij}^2 \rangle}$. The results are listed in Tables III. It is found that $1S$ states with $\{1234\}\bar{5}$ symmetry should have a compact structure. The RMS radii for the $cccc\bar{c}$, $cccc\bar{b}$, $bbbb\bar{c}$, and $bbbb\bar{b}$ systems are in the ranges of (0.51, 0.54), (0.44, 0.52), (0.29, 0.40), and (0.28, 0.29) fm, respectively. The $bbbb\bar{b}$ system is much more compact than $cccc\bar{c}$ due to the much stronger attractive color-Coulomb potential.

We further analyze the contributions from each part of the Hamiltonian for the pentaquark states. The results are listed in Table III. It shows that the averaged kinetic energy $\langle T \rangle$ is nearly a stable value ~ 900 MeV for all of the states. The color-Coulomb potential contributes to a large negative

value $\langle V^{Coul} \rangle$, about $-950, -1000, -1300, -1400$ MeV for the $cccc\bar{c}$, $cccc\bar{b}$, $bbbb\bar{c}$, and $bbbb\bar{b}$ systems, respectively. The linear confining potential $\langle V^{Conf} \rangle$ has the same order of magnitude as $\langle T \rangle$, which cannot be neglected. For the $cccc\bar{c}$ system, the value of confining potential $\langle V^{Conf} \rangle$, ~ 870 MeV, is comparable with that of $\langle T \rangle$. While for the $bbbb\bar{b}$ system, the confining potential $\langle V^{Conf} \rangle$, ~ 470 MeV, is about one half of the $cccc\bar{c}$ system. It is interesting to find that for a pentaquark system the value of $\langle T \rangle + \langle V^{Conf} \rangle + \langle V^{Coul} \rangle$ for the $J^P = 1/2^-$ state is equal to that of the $J^P = 3/2^-$ state, although each parts for these two states are different. From this point of view, the mass splitting between the $J^P = 1/2^-$ and $3/2^-$ states is caused by the chromo-magnetic interaction.

As a whole, in the $cccc\bar{c}$, $bbbb\bar{b}$, $cccc\bar{b}$, and $bbbb\bar{c}$ systems,

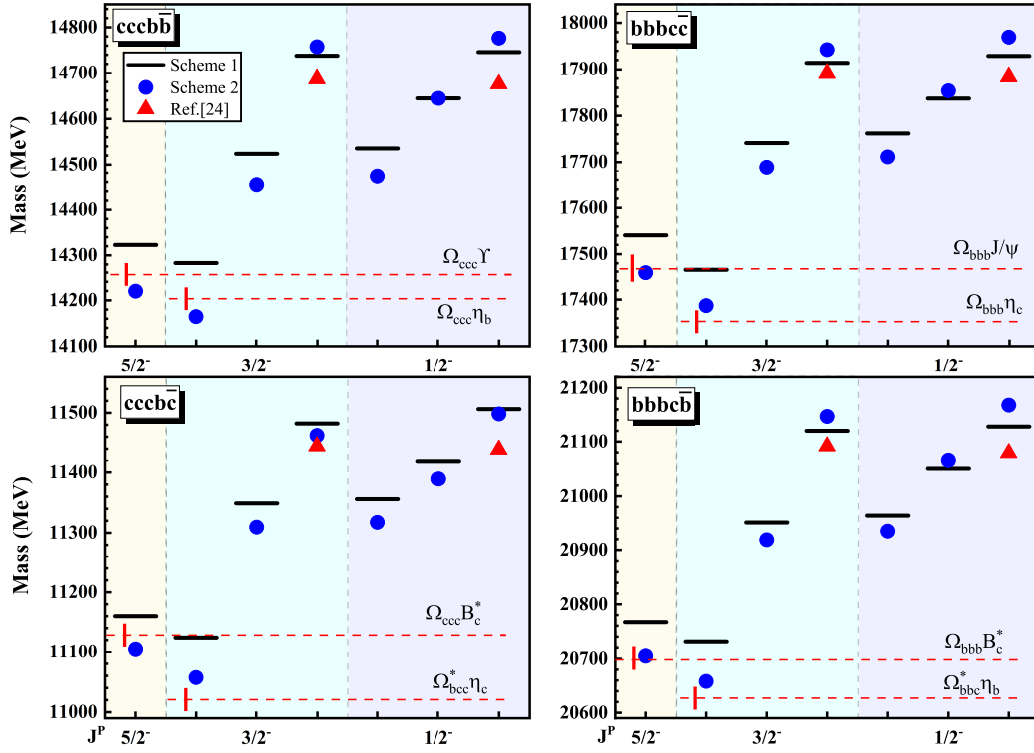


FIG. 2: Spectrum for all-heavy pentaquarks with $\{123\}4\bar{5}$ symmetry. The black short solid lines stand for the predictions based on the potential model of the present work with the ECG numerical method. The solid circles and triangles stand for the predictions based on the potential model of Ref. [24], which are obtained with the ECG numerical method in this work and with the simple diagonal Gaussian basis in Ref. [24], respectively. The red dashed lines represent the lowest $1S$ -wave dissociation baryon-meson thresholds for the two low-lying states with $J^P = 5/2^-$ and $3/2^-$ in each system. The short red solid lines represent the uncertainties according to the Lattice predictions of the triply heavy baryons [41].

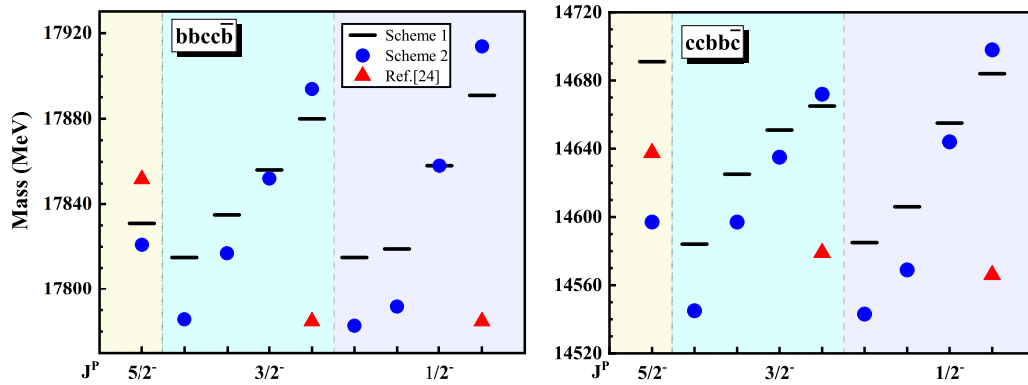


FIG. 3: Spectrum for all-heavy pentaquarks with $\{12\}\{34\}5\bar{}$ symmetry. The short solid lines stand for the predictions based on the potential model of the present work with the ECG numerical method. The solid circles and triangles stand for the predictions based on the potential model of Ref. [24], which are obtained with the ECG numerical method in this work and with the simple diagonal Gaussian basis in Ref. [24], respectively.

there are no stable states below the dissociation baryon-meson thresholds. The $1S$ states should have a compact structure. For each pentaquark system, the mass splitting between the $J^P = 1/2^-$ and $3/2^-$ states is no more than 30 MeV.

B. States with $\{123\}4\bar{5}$ symmetry

In the all-heavy pentaquarks, the $ccb\bar{b}\bar{b}$, $ccb\bar{c}\bar{b}$, $bbb\bar{c}\bar{c}$, and $bbb\bar{c}\bar{b}$ systems have the $\{123\}4\bar{5}$ symmetry. Considering

the permutation symmetry of identical quarks, for each pentaquark system there are seven $1S$ states, one with $J^P = 5/2^-$, three with $J^P = 3/2^-$, and three with $J^P = 1/2^-$. The predicted mass spectrum has been given in Table IV and also shown in Fig. 2. From Table IV, one can see that there exist large mixing between the two configurations $1S_{J^P}(\{123\}4\bar{5})_1$ and $1S_{J^P}(\{123\}4\bar{5})_2$ with the same spin-parity J^P numbers. The splitting between the two mixed states are notably increased to $\sim 150 - 200$ MeV due to the configuration mixing effect, while without this effect the splitting between the two pure states is $\sim 50 - 90$ MeV. The $1S_{1/2^-}(\{123\}4\bar{5})_3$ and $1S_{3/2^-}(\{123\}4\bar{5})_3$ are nearly two pure configurations. For a given pentaquark system, the lowest state is the $J^P = 3/2^-$ configuration $1S_{\frac{3}{2}^-}(\{123\}4\bar{5})_3$, which is slightly ($\sim 40 - 60$ MeV) lower than the $J^P = 5/2^-$ state. The masses of the other five states are notably larger than these two low-lying states, the mass gap reaches up to about $200 - 500$ MeV.

The masses of the $1S$ states for the $cccb\bar{c}$, $cccb\bar{b}$, $bbbc\bar{c}$, and $bbbc\bar{b}$ systems scatter in the range of $\sim (11.1, 11.5)$, $\sim (14.3, 14.8)$, $\sim (17.5, 17.9)$, and $\sim (20.7, 21.1)$ GeV, respectively. In Ref. [24], the authors given their predictions of the masses for the highest $J^P = 1/2^-$ and $J^P = 3/2^-$ states. For a comparison, we shown their results (denoted by the solid triangles) in Fig. 2 as well. It is seen that these predictions in Ref [24] are generally consistent with ours. However, in Ref [24], no stable solutions for the other low-lying states are obtained by taking a simple Gaussian form for the trial spatial wave function. By using the same Hamiltonian adopted in Ref. [24], we calculate the mass spectrum with the ECG method as well. We obtain stable solutions for all of the $1S$ states, which are shown in Fig. 2 with solid circles as the scheme 2. It is found that mass spectra predicted with the two different potential models adopted in Ref. [24] (scheme 2) and present work (scheme 1) are similar, it shows only a small model dependency. The difference for most of the predictions between the two potential models is no more than 40 MeV. Some other studies about these pentaquarks can be found in the literature based on the MIT bag model [20], chromo-magnetic interaction model [19], and chiral quark model [22]. It is interesting to find that the four $J^P = 5/2^-$ states for the $cccb\bar{c}$, $cccb\bar{b}$, $bbbc\bar{c}$, and $bbbc\bar{b}$ systems reported in Ref. [22] are comparable with our predictions.

To know about the inner structure of the pentaquark states, in Tables VI we further give the root mean square (RMS) radii between two quarks. It is found that the five high-lying $1S$ states with $J^P = 1/2^-$ and $J^P = 3/2^-$ for a given pentaquark system are compact states, their RMS radii are no more than 0.52 fm. While the two low-lying $J^P = 3/2^-$ and $J^P = 5/2^-$ states have a typical molecular structure. From Table VI, one can see that in these states the three identical quarks $Q_1Q_2Q_3$ and the two non-identical quarks $Q_4\bar{Q}_5$ form two compact clusters, respectively. The RMS radii between two quarks in each cluster are no more than 0.5 fm. However, the RMS radii between two compact clusters reaches up to a fairly large value, ~ 2 fm. The molecular structure of the $J^P = 5/2^-$ states is also found in Ref. [22].

The contributions from each part of the Hamiltonian for the pentaquark states are listed in Table VI of the appendix.

Taking the $cccb\bar{c}$ system as an example, from the Table VI, one can see that the kinetic energy $\langle T \rangle \sim (900, 1000)$ MeV, the confining potential $\langle V^{Conf} \rangle \sim (700, 800)$ MeV, and the color-Coulomb potential $\langle V^{Coul} \rangle \sim -(1000, 1300)$ MeV have the same order of magnitude. The sums of these contributions for different states are usually very different. Thus, one cannot give a reliable prediction of the mass splitting when only considering the chromo-magnetic interaction. It should be pointed out that for the two low-lying $J^P = 3/2^-$ and $J^P = 5/2^-$ states, the color-Coulomb potential $\langle V^{Coul} \rangle$ is much more attractive ($\sim 200 - 300$ MeV) than that for the other five high-lying states, which leads to the fairly large gap between the two low-lying states and the five high-lying states.

The molecular structure of the low-lying $J^P = 3/2^-$ and $J^P = 5/2^-$ states is also mainly caused by the color-Coulomb interactions. In these two states, the color-Coulomb interactions between quarks in the colored subsystems $Q_4\bar{Q}_5$ and $Q_1Q_2Q_3$ are very strong. The color-Coulomb potentials from $Q_4\bar{Q}_5$ and $Q_1Q_2Q_3$ are about $\sim 5-6$ and $\sim 2-3$ times stronger than those for the other states, respectively. Thus, the subsystems $Q_4\bar{Q}_5$ and $Q_1Q_2Q_3$ forms two compact clusters. However, the color-Coulomb interactions between the two clusters are zero. Due to no attractive color-Coulomb interactions, the distance between the two clusters $Q_4\bar{Q}_5$ and $Q_1Q_2Q_3$ become very large.

Except for the special molecular structures, the two low-lying states with $J^P = 5/2^-$ and $J^P = 3/2^-$ in a given pentaquark system may be good candidates of stable states below the dissociation baryon-meson thresholds what we are looking for. If taking the masses for the triply-heavy baryons predicted by Lattice QCD [41], from Fig. 2, one can see that for a given pentaquark system the masses of the low-lying states with $J^P = 5/2^-$ and $J^P = 3/2^-$ are close to their lowest S -wave strong decay channels. With the potential model of the present work (scheme 1), the predicted masses of the two low-lying states with $J^P = 5/2^-$ and $J^P = 3/2^-$ are about a few tens MeV larger than the thresholds of their lowest S -wave strong decay channels, while with the potential model of Ref. [24] (scheme 2), the predicted masses are much more closer to or slightly below these thresholds. Considering the model uncertainty, the two low-lying $J^P = 5/2^-$ and $J^P = 3/2^-$ states with $\{123\}4\bar{5}$ symmetry may lie below the dissociation baryon-meson thresholds. Similar feature of the $J^P = 5/2^-$ states is also predicted in Ref. [22].

As a whole, a complete spectrum for the $1S$ -wave all-heavy pentaquarks with $\{123\}4\bar{5}$ symmetry is given based on the potential models. For the $J^P = 1/2^-$ and $3/2^-$ states, there exist large mixing between the two different color-spin configurations $1S_{J^P}(\{123\}4\bar{5})_1$ and $1S_{J^P}(\{123\}4\bar{5})_2$. Besides the compact structures, there also exist two molecular structures for each pentaquark system, which correspond to the two low-lying $J^P = 5/2^-$ and $J^P = 3/2^-$ states. They may be candidates of the stable states below the dissociation baryon-meson thresholds.

C. States with $\{12\}\{34\}\bar{5}$ symmetry

In the all-heavy pentaquarks, the $cbb\bar{c}$ and $bbcc\bar{b}$ systems have the $\{12\}\{34\}\bar{5}$ symmetry. Considering the permutation symmetry of identical quarks, for each pentaquark system there are nine $1S$ states, one with $J^P = 5/2^-$, four with $J^P = 3/2^-$, and four with $J^P = 1/2^-$. The predicted mass spectrum has been given in Table V and also shown in Fig. 3. For the $J^P = 3/2^-$ and $1/2^-$ states, there is sizeable mixing in the different color-spin configurations. The masses of the $1S$ states for the $cbb\bar{c}$ and $bbcc\bar{b}$ systems are predicted to be in the ranges of $\sim (14.6, 14.7)$ and $\sim (17.8, 17.9)$ GeV, respectively, which are included in the mass range of the five high-lying states for the $cccb\bar{b}$ ($bbbc\bar{c}$) system. These $1S$ states are far above the dissociation baryon-meson thresholds.

By adopting the same Hamiltonian of Ref. [24], we calculate the mass spectrum with the ECG method as well. The results (scheme 2) are shown with solid circles in Fig. 3 for comparing with our potential model results (scheme 1). It is found that two different potential models give very similar results. The difference for most of the predictions is no more than 50 MeV. It should be mentioned that in Ref. [24], the authors did not give the whole mass spectrum of the $1S$ states for the $cbb\bar{c}$ and $bbcc\bar{b}$ systems due to the limitation of their numerical method, where a simple diagonal Gaussian basis is adopted. The discrepancy between the results obtained with the diagonal Gaussian basis (solid triangles) [24] and the ECG method (solid circles) can reach up to ~ 100 MeV. Thus, to deal with the $cbb\bar{c}$ and $bbcc\bar{b}$ systems containing unequal mass quarks, the ECG method is suggested. Some other studies about these pentaquarks can be found in the literature based on the MIT bag model [20], CMI model [19], and chiral quark model [22]. There are large discrepancies (about 300 – 800 MeV) in the predictions from various models.

To know about the inner structure of the pentaquark states, in Table VII we further give the root mean square (RMS) radii between two quarks. It is found that the $1S$ states of the $cbb\bar{c}$ and $bbcc\bar{b}$ systems are compact states, the RMS radii are predicted to be in the range of $\sim 0.28 - 0.51$ fm.

The contributions from each part of the Hamiltonian for the pentaquark states are given in Table VII as well. Taking the $cbb\bar{c}$ system as an example, from the table one can see that the kinetic energy $\langle T \rangle \sim 900$ MeV, the confining potential $\langle V^{Conf} \rangle \sim 700$ MeV, and the color-Coulomb potential $\langle V^{Coul} \rangle \sim -(1100, 1200)$ MeV have the same order of magnitude. By summing these contributions, $\langle T \rangle + \langle V^{Conf} \rangle + \langle V^{Coul} \rangle$, for each $1S$ state, one obtains three nearly degenerate values 443, 472, and 486 MeV. These values together with the small spin-spin potential $\langle V^{SS} \rangle$ determine the mass splittings between the different configurations.

As a whole, a complete spectrum for the $1S$ -wave all-heavy pentaquarks $cbb\bar{c}$ and $bbcc\bar{b}$ with $\{12\}\{34\}\bar{5}$ symmetry is given based on the potential models. For the $J^P = 1/2^-$ and $3/2^-$ states, there exists sizeable mixing between the differ-

ent color-spin configurations. The $1S$ pentaquark states in the $cbb\bar{c}$ and $bbcc\bar{b}$ systems should be compact structures, and far above the dissociation baryon-meson thresholds.

IV. SUMMARY

In this work, we carry out a dynamical calculation of the mass spectra for the all-heavy pentaquarks with a non-relativistic potential model. To precisely treat a five-body system, we apply the ECG method, in which a variational trial spatial wave function is expanded with nondiagonal Gaussians associated to the Jacobi coordinates. A complete mass spectrum for the $1S$ states is obtained.

In the all-heavy pentaquarks with $\{1234\}\bar{5}$ symmetry, the masses of the $1S$ -wave states for $cccc\bar{c}$ and $bbbb\bar{b}$ are predicted to be in the ranges of ~ 8.2 and ~ 24.2 GeV, respectively; while the masses for $cccc\bar{b}$ and $bbbb\bar{c}$ are predicted to be in the ranges of ~ 11.5 and ~ 21.1 GeV, respectively. These pentaquark states have a compact structure, and lie far above the lowest dissociation baryon-meson mass threshold.

For the $cccb\bar{c}$, $cccb\bar{b}$, $bbbc\bar{c}$, and $bbbc\bar{b}$ systems with $\{123\}4\bar{5}$ symmetry, the masses of the $1S$ states scatter in the range of $\sim (11.1, 11.5)$, $\sim (14.3, 14.8)$, $\sim (17.5, 17.9)$, and $\sim (20.7, 21.1)$ GeV, respectively. For each system, the five high-lying states with $J^P = 1/2^-$ and $3/2^-$ are compact states, and lie far above the lowest dissociation baryon-meson mass threshold. However, the two low-lying states with $J^P = 5/2^-$ and $3/2^-$ have a typical molecular structure, $(Q_1 Q_2 Q_3)-(Q_4 Q_5)$, due to the special role of the color-Coulomb interactions. They may be good candidates of stable states below the dissociation baryon-meson thresholds what we are looking for.

For the $cbb\bar{c}$ and $bbcc\bar{b}$ systems with $\{12\}\{34\}\bar{5}$ symmetry, the masses of the $1S$ states scatter in the ranges of $\sim (14.6, 14.7)$ and $\sim (17.8, 17.9)$ GeV, respectively. These pentaquark states have a compact structure, and lie far above the lowest dissociation baryon-meson mass threshold.

Finally, it should be emphasized that with a serious consideration of the five-body problem, the results obtained from different potential models should be similar. To reliably deal with the all-heavy pentaquarks containing unequal mass quarks, it is necessary to be expanded the spatial wave functions with the most general Gaussian form rather than a simple diagonal Gaussian form.

Acknowledgements

We thank Yan-Rui Liu for part contributions to this work. We also thank Hong-Tao An for useful discussions about the pentaquark configurations. This work is supported by the National Natural Science Foundation of China under Grants Nos.12175065 and 12235018.

[1] M. Gell-Mann, A Schematic Model of Baryons and Mesons, Phys. Lett. **8**, 214-215 (1964).

[2] G. Zweig, An SU(3) model for strong interaction symmetry and

TABLE VI: The average contributions of each part of the Hamiltonian (in MeV) and the root mean square radii (in fm) for the $1S$ -wave all-heavy pentaquark configurations with the $\{123\}4\bar{5}$ symmetry.

J^P	Configuration	Each part contribution of Hamiltonian					RMS Radius					
		Mass	$\langle T \rangle$	$\langle V^{Conf} \rangle$	$\langle V^{Coul} \rangle$	$\langle V^{SS} \rangle$	r_{12}, r_{13}, r_{23}	r_{14}, r_{24}, r_{34}	r_{15}, r_{25}, r_{35}	r_{45}		
$cccb\bar{c}$	$5/2^-$	$1S_{\frac{5}{2}}-\{(123)4\bar{5}\}$	11160	962	681	-1302	35	0.4846	2.2071	2.2156	0.3267	
		$3/2^-$	$1S_{\frac{3}{2}}-\{(123)4\bar{5}\}_1$	11439	886	789	-1038	19	0.5088	0.4410	0.5018	0.4334
			$1S_{\frac{3}{2}}-\{(123)4\bar{5}\}_2$	11390	913	771	-1092	14	0.5000	0.4706	0.5285	0.3810
	$1S_{\frac{3}{2}}-\{(123)4\bar{5}\}_3$		11126	1000	673	-1332	1	0.4847	2.2563	2.2637	0.3134	
	$1/2^-$	$1S_{\frac{1}{2}}-\{(123)4\bar{5}\}_1$	11470	847	806	-1015	48	0.5164	0.4471	0.5168	0.4462	
		$1S_{\frac{1}{2}}-\{(123)4\bar{5}\}_2$	11395	906	773	-1087	20	0.4993	0.4702	0.5284	0.3861	
		$1S_{\frac{1}{2}}-\{(123)4\bar{5}\}_3$	11416	885	781	-1047	11	0.5145	0.4332	0.5025	0.4769	
	$cccb\bar{b}$	$5/2^-$	$1S_{\frac{5}{2}}-\{(123)4\bar{5}\}$	14322	936	646	-1447	34	0.5103	1.7147	1.7146	0.2292
			$3/2^-$	$1S_{\frac{3}{2}}-\{(123)4\bar{5}\}_1$	14670	873	718	-1101	27	0.4953	0.4256	0.4232
$1S_{\frac{3}{2}}-\{(123)4\bar{5}\}_2$				14587	927	695	-1201	14	0.4927	0.4507	0.4514	0.2667
$1S_{\frac{3}{2}}-\{(123)4\bar{5}\}_3$		14284		991	638	-1494	-5	0.5104	1.7257	1.7256	0.2184	
$1/2^-$		$1S_{\frac{1}{2}}-\{(123)4\bar{5}\}_1$	14685	853	726	-1088	41	0.4993	0.4291	0.4288	0.3355	
		$1S_{\frac{1}{2}}-\{(123)4\bar{5}\}_2$	14595	915	697	-1191	21	0.4924	0.4510	0.4516	0.2713	
		$1S_{\frac{1}{2}}-\{(123)4\bar{5}\}_3$	14645	879	712	-1112	13	0.4945	0.4179	0.4197	0.3793	
$bbbc\bar{c}$		$5/2^-$	$1S_{\frac{5}{2}}-\{(123)4\bar{5}\}$	17540	1058	506	-1584	38	0.2491	2.0011	1.9992	0.4195
			$3/2^-$	$1S_{\frac{3}{2}}-\{(123)4\bar{5}\}_1$	17859	895	634	-1202	9	0.3180	0.4093	0.4039
	$1S_{\frac{3}{2}}-\{(123)4\bar{5}\}_2$			17787	953	606	-1291	-3	0.2898	0.4327	0.4350	0.4439
	$1S_{\frac{3}{2}}-\{(123)4\bar{5}\}_3$	17472		1140	484	-1642	-31	0.2490	2.1234	2.1214	0.3847	
	$1/2^-$	$1S_{\frac{1}{2}}-\{(123)4\bar{5}\}_1$	17884	862	646	-1180	34	0.3211	0.4145	0.4138	0.4849	
		$1S_{\frac{1}{2}}-\{(123)4\bar{5}\}_2$	17806	929	614	-1275	16	0.2900	0.4373	0.4391	0.4568	
		$1S_{\frac{1}{2}}-\{(123)4\bar{5}\}_3$	17837	893	631	-1202	-6	0.3368	0.3964	0.3996	0.4854	
	$bbbc\bar{b}$	$5/2^-$	$1S_{\frac{5}{2}}-\{(123)4\bar{5}\}$	20767	1071	454	-1676	27	0.2580	1.9594	1.9473	0.3269
			$3/2^-$	$1S_{\frac{3}{2}}-\{(123)4\bar{5}\}_1$	21071	865	566	-1267	16	0.3058	0.3950	0.3180
$1S_{\frac{3}{2}}-\{(123)4\bar{5}\}_2$				20998	946	536	-1374	-1	0.2835	0.4035	0.3327	0.3613
$1S_{\frac{3}{2}}-\{(123)4\bar{5}\}_3$		20733		1110	446	-1706	-8	0.2581	2.0506	2.0402	0.3135	
$1/2^-$		$1S_{\frac{1}{2}}-\{(123)4\bar{5}\}_1$	21084	848	572	-1255	29	0.3077	0.3982	0.3214	0.3998	
		$1S_{\frac{1}{2}}-\{(123)4\bar{5}\}_2$	21008	934	539	-1365	9	0.2836	0.4062	0.3336	0.3668	
		$1S_{\frac{1}{2}}-\{(123)4\bar{5}\}_3$	21051	847	568	-1250	-6	0.3210	0.3860	0.3223	0.4096	

its breaking. Version 1, CERN-TH-401.

- [3] G. Zweig, An $SU(3)$ model for strong interaction symmetry and its breaking. Version 2, CERN-TH-412.
- [4] S. K. Choi *et al.* [Belle], Observation of a narrow charmonium-like state in exclusive $B^{\pm} \rightarrow K^{\pm}\pi^{\pm}J/\psi$ decays, Phys. Rev. Lett. **91**, 262001 (2003).
- [5] R. L. Workman *et al.* [Particle Data Group], Review of Particle Physics, PTEP **2022**, 083C01 (2022).
- [6] R. Aaij *et al.* [LHCb], Study of the doubly charmed tetraquark T_{cc}^+ , Nature Commun. **13**, 3351 (2022).
- [7] R. Aaij *et al.* [LHCb], Observation of an exotic narrow doubly

charmed tetraquark, Nature Phys. **18**, 751-754 (2022).

- [8] R. Aaij *et al.* [LHCb], First Observation of a Doubly Charged Tetraquark and Its Neutral Partner, Phys. Rev. Lett. **131**, 041902 (2023).
- [9] R. Aaij *et al.* [LHCb], A model-independent study of resonant structure in $B^+ \rightarrow D^+D^-K^+$ decays, Phys. Rev. Lett. **125**, 242001 (2020).
- [10] R. Aaij *et al.* [LHCb], Observation of $J/\psi p$ Resonances Consistent with Pentaquark States in $\Lambda_b^0 \rightarrow J/\psi K^- p$ Decays, Phys. Rev. Lett. **115**, 072001 (2015).
- [11] R. Aaij *et al.* [LHCb], Model-independent evidence for $J/\psi p$

TABLE VII: The average contributions of each part of the Hamiltonian (in MeV) and the root mean square radii (in fm) for the 1S-wave all-heavy pentaquark configurations with the $\{12\}\{34\}\bar{5}$ symmetry.

J^P	Configuration	Each part contribution of Hamiltonian					RMS Radius					
		Mass	$\langle T \rangle$	$\langle V^{Conf} \rangle$	$\langle V^{Coul} \rangle$	$\langle V^{SS} \rangle$	r_{12}	$r_{13}, r_{14},$ r_{23}, r_{24}	r_{15}, r_{25}	r_{34}	r_{35}, r_{45}	
$c\bar{c}bb\bar{c}$	5/2 ⁻	$1S_{\frac{5}{2}}-\{12\}\{34\}\bar{5}$	14619	903	702	-1162	23	0.4780	0.4493	0.5043	0.2902	0.4227
		$1S_{\frac{3}{2}}-\{12\}\{34\}\bar{5}_1$	14652	898	709	-1121	14	0.4918	0.4220	0.4860	0.3299	0.4168
	3/2 ⁻	$1S_{\frac{3}{2}}-\{12\}\{34\}\bar{5}_2$	14636	908	704	-1140	11	0.4813	0.4258	0.4943	0.3083	0.4206
		$1S_{\frac{3}{2}}-\{12\}\{34\}\bar{5}_3$	14642	910	704	-1128	3	0.4923	0.4115	0.4833	0.3440	0.4196
		$1S_{\frac{3}{2}}-\{12\}\{34\}\bar{5}_4$	14595	935	690	-1182	-1	0.4725	0.4432	0.4920	0.2881	0.4131
		$1S_{\frac{1}{2}}-\{12\}\{34\}\bar{5}_1$	14680	860	724	-1098	41	0.4990	0.4277	0.5000	0.3336	0.4287
	1/2 ⁻	$1S_{\frac{1}{2}}-\{12\}\{34\}\bar{5}_2$	14598	960	685	-1172	-27	0.4722	0.4178	0.4760	0.3042	0.4055
		$1S_{\frac{1}{2}}-\{12\}\{34\}\bar{5}_3$	14649	900	708	-1122	10	0.4942	0.4129	0.4868	0.3451	0.4227
		$1S_{\frac{1}{2}}-\{12\}\{34\}\bar{5}_4$	14602	926	694	-1176	6	0.4733	0.4428	0.4970	0.2883	0.4175
$b\bar{b}cc\bar{b}$	5/2 ⁻	$1S_{\frac{5}{2}}-\{12\}\{34\}\bar{5}$	17831	895	626	-1231	19	0.2824	0.4300	0.3142	0.4647	0.4205
		$1S_{\frac{3}{2}}-\{12\}\{34\}\bar{5}_1$	17869	884	636	-1194	20	0.3162	0.4081	0.3156	0.4781	0.4061
	3/2 ⁻	$1S_{\frac{3}{2}}-\{12\}\{34\}\bar{5}_2$	17842	909	626	-1220	5	0.2967	0.4093	0.3130	0.4662	0.4081
		$1S_{\frac{3}{2}}-\{12\}\{34\}\bar{5}_3$	17855	904	629	-1205	5	0.3284	0.3975	0.3174	0.4767	0.3998
		$1S_{\frac{3}{2}}-\{12\}\{34\}\bar{5}_4$	17819	913	621	-1243	7	0.2808	0.4264	0.3103	0.4617	0.4154
		$1S_{\frac{1}{2}}-\{12\}\{34\}\bar{5}_1$	17885	864	643	-1179	35	0.3189	0.4116	0.3204	0.4822	0.4118
	1/2 ⁻	$1S_{\frac{1}{2}}-\{12\}\{34\}\bar{5}_2$	17822	937	617	-1239	-15	0.2939	0.4045	0.3070	0.4611	0.4007
		$1S_{\frac{1}{2}}-\{12\}\{34\}\bar{5}_3$	17859	898	631	-1201	9	0.3292	0.3984	0.3186	0.4778	0.4012
		$1S_{\frac{1}{2}}-\{12\}\{34\}\bar{5}_4$	17818	913	620	-1244	6	0.2806	0.4246	0.3113	0.4608	0.4157

- contributions to $\Lambda_b^0 \rightarrow J/\psi p K^-$ decays, Phys. Rev. Lett. **117**, 082002 (2016).
- [12] R. Aaij *et al.* [LHCb], Observation of a narrow pentaquark state, $P_c(4312)^+$, and of two-peak structure of the $P_c(4450)^+$, Phys. Rev. Lett. **122**, 222001 (2019).
- [13] R. Aaij *et al.* [LHCb], Observation of a $J/\psi\Lambda$ Resonance Consistent with a Strange Pentaquark Candidate in $B^- \rightarrow J/\psi\Lambda\bar{p}$ Decays, Phys. Rev. Lett. **131**, 031901 (2023).
- [14] R. Aaij *et al.* [LHCb], Observation of structure in the J/ψ -pair mass spectrum, Sci. Bull. **65**, 1983-1993 (2020).
- [15] G. Aad *et al.* [ATLAS], Observation of an Excess of Dicharmonium Events in the Four-Muon Final State with the ATLAS Detector, Phys. Rev. Lett. **131**, 151902 (2023).
- [16] A. Hayrapetyan *et al.* [CMS], Observation of new structure in the $J/\psi J/\psi$ mass spectrum in proton-proton collisions at $\sqrt{s} = 13$ TeV, [arXiv:2306.07164 [hep-ex]].
- [17] J. R. Zhang, Fully-heavy pentaquark states, Phys. Rev. D **103**, 074016 (2021).
- [18] Z. G. Wang, Analysis of the fully-heavy pentaquark states via the QCD sum rules, Nucl. Phys. B **973**, 115579 (2021).
- [19] H. T. An, K. Chen, Z. W. Liu and X. Liu, Fully heavy pentaquarks, Phys. Rev. D **103**, 074006 (2021).
- [20] W. X. Zhang, H. T. An and D. Jia, Masses and magnetic moments of exotic fully heavy pentaquarks, Eur. Phys. J. C **83**, 727 (2023).
- [21] Y. Yan, Y. Wu, X. Hu, H. Huang and J. Ping, Fully heavy pentaquarks in quark models, Phys. Rev. D **105**, 014027 (2022).
- [22] Y. Yan, Y. Wu, H. Huang, J. Ping and X. Zhu, Prediction of charmed-bottom pentaquarks in quark model, Eur. Phys. J. C **83**, 610 (2023).
- [23] G. Yang, J. Ping and J. Segovia, Fully charm and bottom pentaquarks in a lattice-QCD inspired quark model, Phys. Rev. D **106**, 014005 (2022).
- [24] H. T. An, S. Q. Luo, Z. W. Liu and X. Liu, Fully heavy pentaquark states in constituent quark model, Phys. Rev. D **105**, 074032 (2022).
- [25] M. C. Gordillo and J. M. Alcaraz-Pelegrina, Asymptotic mass limit of large fully heavy compact multiquarks, Phys. Rev. D **108**, 054027 (2023).
- [26] E. Eichten, K. Gottfried, T. Kinoshita, K. D. Lane and T. M. Yan, Charmonium: The Model, Phys. Rev. D **17**, 3090 (1978) [erratum: Phys. Rev. D **21**, 313 (1980)].
- [27] Q. Li, M. S. Liu, Q. F. Lü, L. C. Gui and X. H. Zhong, Canonical interpretation of $Y(10750)$ and $Y(10860)$ in the Y family, Eur. Phys. J. C **80**, 59 (2020).
- [28] W. J. Deng, H. Liu, L. C. Gui and X. H. Zhong, Charmonium spectrum and their electromagnetic transitions with higher multipole contributions, Phys. Rev. D **95**, 034026 (2017).
- [29] Q. Li, M. S. Liu, L. S. Lu, Q. F. Lü, L. C. Gui and X. H. Zhong, Excited bottom-charmed mesons in a nonrelativistic quark model, Phys. Rev. D **99**, 096020 (2019).
- [30] M. S. Liu, Q. F. Lü and X. H. Zhong, Triply charmed and bottom baryons in a constituent quark model, Phys. Rev. D **101**, 074031 (2020).

- [31] M. S. Liu, F. X. Liu, X. H. Zhong and Q. Zhao, Full-heavy tetraquark states and their evidences in the LHCb $di\text{-}J/\psi$ spectrum, [arXiv:2006.11952 [hep-ph]].
- [32] F. X. Liu, M. S. Liu, X. H. Zhong and Q. Zhao, Higher mass spectra of the fully-charmed and fully-bottom tetraquarks, Phys. Rev. D **104**, 116029 (2021).
- [33] M. S. Liu, Q. F. Lü, X. H. Zhong and Q. Zhao, All-heavy tetraquarks, Phys. Rev. D **100**, 016006 (2019).
- [34] K. Varga and Y. Suzuki, Precise Solution of Few Body Problems with Stochastic Variational Method on Correlated Gaussian Basis, Phys. Rev. C **52**, 2885-2905 (1995).
- [35] J. Mitroy, S. Bubin, W. Horiuchi, Y. Suzuki, L. Adamowicz, W. Cencek, K. Szalewicz, J. Komasa, D. Blume and K. Varga, Theory and application of explicitly correlated Gaussians, Rev. Mod. Phys. **85**, 693-749 (2013).
- [36] F. X. Liu, R. H. Ni, X. H. Zhong and Q. Zhao, Charmed-strange tetraquarks and their decays in the potential quark model, Phys. Rev. D **107**, 096020 (2023).
- [37] T. A. Kaeding, Tables of SU(3) isoscalar factors, Atom. Data Nucl. Data Tabl. **61**, 233-288 (1995).
- [38] F. Stancu and S. Pepin, Isoscalar factors of the permutation group, Few Body Syst. **26**, 113-133 (1999).
- [39] W. Park, A. Park, S. Cho and S. H. Lee, $P_c(4380)$ in a constituent quark model, Phys. Rev. D **95**, 054027 (2017).
- [40] E. Hiyama, Y. Kino and M. Kamimura, Gaussian expansion method for few-body systems, Prog. Part. Nucl. Phys. **51**, 223-307 (2003).
- [41] Z. S. Brown, W. Detmold, S. Meinel and K. Orginos, Charmed bottom baryon spectroscopy from lattice QCD, Phys. Rev. D **90**, 094507 (2014).

Next-to-next-to-leading-order QCD corrections to pion electromagnetic form factors

Long-Bin Chen ^{*,1}, Wen Chen ^{†,2,3}, Feng Feng ^{‡,4,5} and Yu Jia ^{§5,6}

¹ School of Physics and Materials Science, Guangzhou University, Guangzhou 510006, China

² Institute of Quantum Matter, South China Normal University, Guangzhou 510006, China

³ Zhejiang Institute of Modern Physics, School of Physics, Zhejiang University, Hangzhou, Zhejiang 310027, China

⁴ China University of Mining and Technology, Beijing 100083, China

⁵ Institute of High Energy Physics and Theoretical Physics Center for Science Facilities, Chinese Academy of Sciences, Beijing 100049, China

⁶ School of Physical Sciences, University of Chinese Academy of Sciences, Beijing 100049, China

(Dated: February 28, 2024)

We investigate the next-to-next-to-leading order (NNLO) QCD radiative corrections to the pion electromagnetic form factor with large momentum transfer. We explicitly verify the validity of the collinear factorization to two-loop order for this observable, and obtain the respective IR-finite two-loop hard-scattering kernel in the closed form. The NNLO QCD correction turns to be positive and significant. Incorporating this new ingredient of correction, we then make a comprehensive comparison between the finest theoretical predictions and numerous pion form factor measurements in both space-like and time-like regions. Our phenomenological analysis provides strong constraint on the second Gegenbauer moment of the pion light-cone distribution amplitude (LCDA) obtained from recent lattice QCD studies.

Introduction. Originally proposed by Yukawa as the strong nuclear force carrier in 1935 [1], subsequently discovered in the cosmic rays in 1947 [2], the π mesons have always occupied the central stage throughout the historic advancement of the strong interaction. As the lightest particles in the hadronic world (hence the highly-relativistic bound systems composed of light quark and gluons), π mesons entail extremely rich QCD dynamics, exemplified by the color confinement and chiral symmetry breaking. Notwithstanding extensive explorations during the past decades, there still remain some great myths about the internal structure of the π mesons.

A classic example of probing the internal structure of the charged pions is the pion electromagnetic (EM) form factor:

$$\langle \pi^+(P') | J_{\text{em}}^\mu | \pi^+(P) \rangle = F_\pi(Q^2)(P^\mu + P'^\mu), \quad (1)$$

with $Q^2 \equiv -(P' - P)^2$. The electromagnetic current defined by $J_{\text{em}}^\mu = \sum_f e_f \bar{f} \gamma^\mu f$, with $e_u = 2/3$ and $e_d = -1/3$ indicating the electric charges of the u and d quarks.

During the past half century, the pion EM form factor has been intensively studied experimentally [3–29]. From the theoretical perspective, the pion EM form factor at small Q^2 can be investigated in chiral perturbation theory [30] and lattice QCD [31–35], from which one can infer the pion charge radius. On the other hand, at

large momentum transfer, the $F_\pi(Q^2)$ is expected to be adequately described by perturbative QCD. Within the collinear factorization framework tailored for hard exclusive reactions [36–42] (for a review, see [43]), at the lowest order in $1/Q$, the pion EM form factor can be expressed in the following form:

$$F_\pi(Q^2) = \iint dx dy \Phi_\pi^*(x, \mu_F) T(x, y, \frac{\mu_R^2}{Q^2}, \frac{\mu_F^2}{Q^2}) \Phi_\pi(y, \mu_F), \quad (2)$$

where $T(x, y)$ signifies the perturbatively calculable hard-scattering kernel, and $\Phi_\pi(x, \mu_F)$ represents the nonperturbative yet universal leading-twist pion light-cone distribution amplitude (LCDA), *i.e.*, the probability amplitude of finding the valence u and \bar{d} quark inside π^+ carrying the fractional momenta x and $\bar{x} \equiv 1 - x$, respectively. The leading-twist pion LCDA assumes the following operator definition:

$$\Phi_\pi(x, \mu_F) = \int \frac{dz^-}{2\pi i} e^{iz^- x P^+} \langle 0 | \bar{d}(0) \gamma^+ \gamma_5 \times \mathcal{W}(0, z^-) u(z^-) | \pi^+(P) \rangle, \quad (3)$$

with \mathcal{W} signifies the light-like gauge link to ensure the gauge invariance. Conducting the UV renormalization for (3), one is led to the celebrated Efremov-Radyushkin-Brodsky-Lepage (ERBL) evolution equation [38, 40]:

$$\frac{d\Phi_\pi(x, \mu_F)}{d \ln \mu_F^2} = \int_0^1 dy V(x, y) \Phi_\pi(y, \mu_F), \quad (4)$$

with $V(x, y)$ referring to the perturbatively calculable ERBL kernel.

Eq. (2) is expected to hold to all orders in perturbative expansion. The hard-scattering kernel

* chenlb@gzhu.edu.cn

† chenwenphy@gmail.com

‡ f.feng@outlook.com

§ jiay@ihep.ac.cn

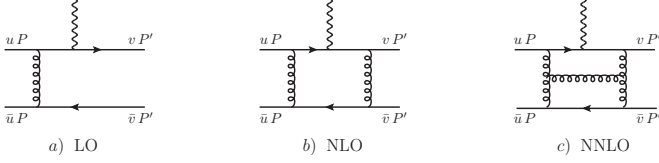


FIG. 1: Sample parton-level Feynman diagrams for the reaction $\gamma^* \pi(P) \rightarrow \pi(P')$ at various perturbative orders.

$T(x, y, \mu_R^2/Q^2, \mu_F^2/Q^2)$ can thus be expanded in the power series:

$$T = \frac{16C_F\pi\alpha_s}{Q^2} \left\{ T^{(0)} + \frac{\alpha_s}{\pi} T^{(1)} + \left(\frac{\alpha_s}{\pi} \right)^2 T^{(2)} + \dots \right\}, \quad (5)$$

with $C_F = \frac{N_c^2 - 1}{2N_c}$, and $N_c = 3$ is the number of colors.

The leading order (LO) result was known shortly after the advent of QCD [37, 38, 40, 42]. The next-to-leading order (NLO) correction was originally computed by three groups in early 80s [44–46]. Unfortunately these results are not compatible with each other. In 1987, scrutinizing the previous calculations, Braaten and Tse traced the origin of the discrepancies among the earlier work and presented the correct expression of the NLO hard-scattering kernel [47]. In 1998, Melić, Nizić, and Passek conducted a comprehensive phenomenological study by incorporating the NLO correction as well as the evolution effect of pion LCDA [48]. The central goal of this work is to compute the next-to-next-to-leading order (NNLO) perturbative correction to pion EM form factor, and critically examine its phenomenological impact.

Setup of perturbative matching. The strategy of deducing the short-distance coefficients is through the standard matching procedure. Since the hard-scattering kernel is insensitive to the long-distance physics, it is legitimate to replace the physical $|\pi^+\rangle$ state by a fictitious pion state, *i.e.*, a free massless quark-antiquark pair $|u\bar{d}\rangle$, and compute both sides of (2) in perturbation theory. To make things simpler, we neglect the transverse motion, assign the momenta of the u and \bar{d} in the incoming “pion” to be uP and $\bar{u}P$, and assign the momenta of the u and \bar{d} in the outgoing “pion” to be vP and $\bar{v}P$, with u, v range from 0 to 1.

In the left-hand side of (2), we extract the scalar form factor $F(u, v)$ through the partonic reaction $\gamma^* + u(uP)\bar{d}(\bar{u}P) \rightarrow u(vP')\bar{d}(\bar{v}P')$. Some typical Feynman diagrams through two-loop are depicted in Fig. 1. It is subject to a perturbative expansion:

$$F(u, v) = F^{(0)}(u, v) + \frac{\alpha_s}{\pi} F^{(1)}(u, v) + \left(\frac{\alpha_s}{\pi} \right)^2 F^{(2)}(u, v) + \dots \quad (6)$$

In the right-hand side of (2), one can expand the renormalized “pion” LCDA as

$$\Phi(x|u) = \Phi^{(0)}(x|u) + \frac{\alpha_s}{\pi} \Phi^{(1)}(x|u) + \left(\frac{\alpha_s}{\pi} \right)^2 \Phi^{(2)}(x|u) + \dots \quad (7)$$

At tree level, the fictitious pion DA in (3) simply reduces to $\Phi^{(0)}(x|u) = \delta(x-u)$ (Note that we have omitted the same overall factor which also appears in $F(u, v)$). By equating both sides of (2), one reproduces the well-known tree-level expression $T^{(0)}(x, y)$ [36–42]

$$T^{(0)}(x, y) = \frac{e_u}{x\bar{y}}(1 - \epsilon) - \left[\frac{e_u \rightarrow e_d}{\bar{x} \rightarrow x, \bar{y} \rightarrow y} \right], \quad (8)$$

which holds true in $d = 4 - 2\epsilon$ spacetime dimension.

Once beyond the tree level, the UV and IR divergences inevitably arise and we use the dimensional regularization to regularize both types of divergences. Nevertheless, the bare “pion” LCDA remains intact due to the scaleless integrals vanish in the dimensional regularization scheme. The renormalized “pion” LCDA is related to the bare one via

$$\Phi(x|u) = \int dy Z(x, y) \Phi_{\text{bare}}(y|u) = Z(x, u), \quad (9)$$

which is solely comprised of various IR poles.

$Z(x, y)$ in (9) signifies the renormalization function in the $\overline{\text{MS}}$ scheme, which can be cast into the following Laurent-expanded form in ϵ :

$$Z(x, y) = \delta(x - y) + \sum_{k=1}^{\infty} \frac{1}{\epsilon^k} Z_k(x, y), \quad (10)$$

Note that the prefactor of single pole in (10) is related to the ERBL kernel $V(x, y)$ in (4) via [49]

$$V(x, y) = -\alpha_s \frac{\partial Z_1}{\partial \alpha_s}. \quad (11)$$

Note that the two-loop [46, 50–53] and three-loop corrections [54] to the ERBL kernel $V(x, y)$ have been known.

The two-loop renormalized LCDA $\Phi^{(2)}$ also contains double IR pole. The Z_2 can be obtained through the recursive relation [55]

$$\alpha_s \frac{\partial Z_2}{\partial \alpha_s} = \alpha_s \frac{\partial Z_1}{\partial \alpha_s} \otimes Z_1 + \beta(\alpha_s) \frac{\partial Z_1}{\partial \alpha_s}, \quad (12)$$

where $d\alpha_s/d\ln\mu^2 = -\epsilon\alpha_s + \beta(\alpha_s)$.

With the aid of (9) and (10), we then determine the $\mathcal{O}(\alpha_s)$ and $\mathcal{O}(\alpha_s^2)$ corrections to the renormalized “pion” LCDA in (7).

At one-loop order, the matching condition for fictitious pion states becomes

$$\begin{aligned} Q^2 F^{(1)}(u, v) &= T^{(1)}(u, v) + \Phi^{(1)}(x|u) \otimes_x T^{(0)}(x, v) \\ &\quad + \Phi^{(1)}(y|v) \otimes_y T^{(0)}(u, y), \end{aligned} \quad (13)$$

where \otimes_x signifies the shorthand for the convolution over x . Note that the renormalized scalar form factor $F^{(1)}(u, v)$ still contains single collinear pole. However, the renormalized $\Phi^{(1)}(x|u)$ and $\Phi^{(1)}(y|v)$ also contains

the same IR poles. Upon solving this matching equation, one ends with both UV and IR-finite $T^{(1)}(x, y)$. Our expressions agree with the known NLO result [48].

To the desired two-loop order, the following matching equation descends from (2):

$$\begin{aligned}
Q^2 F^{(2)}(u, v) = & T^{(2)}(u, v) + \Phi^{(2)}(x|u) \otimes_x T^{(0)}(x, v) \\
& + \Phi^{(2)}(y|v) \otimes_y T^{(0)}(u, y) \\
& + \Phi^{(1)}(x|u) \otimes_x T^{(1)}(x, v) \\
& + \Phi^{(1)}(y|v) \otimes_y T^{(1)}(u, y) \\
& + \Phi^{(1)}(x|u) \otimes_x T^{(0)}(x, y) \otimes_y \Phi^{(1)}(y|v),
\end{aligned} \tag{14}$$

More severe IR divergences are expected to arise in both $F^{(2)}(u, v)$ and $\Phi^{(1,2)}(x|u)$. Clearly, one also needs compute $T^{(1)}(x, y)$ to $\mathcal{O}(\epsilon)$.

Description of the calculation. We use `HepLib` [56] and `FeynArts` [57] to generate Feynman diagrams and the corresponding amplitudes for the partonic reaction $\gamma^* + u(uP)\bar{d}(\bar{u}P) \rightarrow u(vP')\bar{d}(\bar{v}P')$. We then employ the covariant projector technique to enforce each $u\bar{d}$ pair to bear zero helicity. For our purpose it suffices to adopting the naive anticommutation relation to handle γ_5 . There are about 1600 two-loop diagrams. We employ the package `Apart` [58] to conduct partial fraction, and `FIRE` [59] for integration-by-part reduction. We end up with 116 independent master integrals (MIs). The MIs are calculated by utilizing the differential equations method [60–62]. Note that these MIs are considerably more involved than those in the two-loop corrections for the $\pi - \gamma$ transition form factor [63, 64]. We have attempted two independent ways to construct and solve the differential-equation systems, one of which is based on the method developed in [65–68]. The analytic results are expressed in terms of the Goncharov Polylogarithms (GPLs) [69]. Two independent calculations yield the identical answer. We also numerically check our results against the package `AMFLOW` [70] and found perfect agreement. Technical details will be included in the future long write-up.

Upon renormalizing the QCD coupling in $\overline{\text{MS}}$ scheme, we end up with a rather lengthy expression for $F^{(2)}(u, v)$. Being UV finite, it still contains severe IR divergences which start at order- $1/\epsilon_{\text{IR}}^2$. Inspecting the matching equation (14), piecing all the known ingredients together, we are able to solve for the intended two-loop hard-scattering kernel. Hearteningly, $T^{(2)}(x, y)$ is indeed IR finite. Therefore, our explicit calculation verifies that the collinear factorization does hold at two-loop level for the pion EM form factor. The analytical expression of $T^{(2)}(x, y)$ is too lengthy to be reproduced here. For the sake of clarity, in the supplementary material we provide the asymptotic expressions for $T^{(1,2)}(x, y)$ near the end point regions.

Master formula for pion EM form factor at NNLO. Given a certain parametrized form of pion LCDA, the two-fold

convolution integration in (2) turns out to be difficult to conduct numerically, mainly due to numerical instability caused by the spurious singularity as $x \rightarrow y$ and $x \rightarrow \bar{y}$ in $T^{(2)}(x, y)$. Our recipe to circumvent this challenge is to predict the two-loop pion EM form factor in an analytical manner, which enables us to achieve exquisite precision.

The leading-twist pion LCDA can be conveniently expanded in the Gegenbauer polynomial basis:

$$\Phi_\pi(x, \mu_F) = \frac{f_\pi}{2\sqrt{2}N_c} \sum_{n=0}' a_n(\mu_F) \psi_n(x), \tag{15a}$$

$$\psi_n(x) = 6x\bar{x}C_n^{3/2}(2x-1) \tag{15b}$$

where the pion decay constant $f_\pi = 0.131$ GeV, and \sum' signifies the sum over even integers. Note all the nonperturbative dynamics is encoded in the Gegenbauer moments $a_n(\mu_F)$.

Substituting (15) into (2), conducting two-fold integration, we can reexpress the pion EM form factor as

$$\begin{aligned}
Q^2 F_\pi(Q^2) = & \frac{2C_F\pi^2(e_u - e_d)f_\pi^2}{3} \times \\
& \sum_{k=0} \left(\frac{\alpha_s}{\pi}\right)^{k+1} \sum_{m,n}' a_n(\mu_F) a_m(\mu_F) \mathcal{T}_{mn}^{(k)},
\end{aligned} \tag{16}$$

with $\mathcal{T}_{mn}^{(k)}$ defined by

$$\mathcal{T}_{mn}^{(k)} = \frac{1}{e_u - e_d} \psi_m(x) \otimes_x T^{(k)} \left(x, y, \frac{\mu_R^2}{Q^2}, \frac{\mu_F^2}{Q^2} \right) \otimes_y \psi_n(y). \tag{17}$$

For simplicity, we will set $\mu_R = \mu_F = \mu$ and $n_L = 3$ from now on. The two-fold convolution integrals in (17) can be readily worked out at tree and one-loop levels. For instance, we have

$$\mathcal{T}_{mn}^{(0)} = 9, \tag{18a}$$

$$\mathcal{T}_{00}^{(1)} = \frac{1}{4}(81L_\mu + 237), \tag{18b}$$

with $L_\mu \equiv \ln(\mu^2/Q^2)$.

(m,n)	c_1	c_2	d_1	d_2	d_3
(0,0)	20.25	59.25	91.1250	478.436	696.210
(0,2)	32.75	112.473	170.118	1094.39	2025.84
(0,4)	38.45	147.638	211.902	1541.23	3206.98
(0,6)	42.2571	174.359	241.822	1901.22	4265.06
(2,2)	45.25	192.871	266.472	2178.25	4953.36
(2,4)	50.95	240.181	316.173	2875.57	7237.52
(2,6)	54.7571	274.974	351.380	3415.43	9172.70
(4,4)	56.65	292.970	369.484	3704.29	10222.5
(4,6)	60.4571	331.411	407.102	4337.65	12698.8
(6,6)	64.2643	372.282	446.331	5037.27	15588.4

TABLE I: The numerical values for $\mathcal{T}_{mn}^{(1)} = (c_1 L_\mu + c_2)$ and $\mathcal{T}_{mn}^{(2)} = (d_1 L_\mu^2 + d_2 L_\mu + d_3)$, with $0 \leq m, n \leq 6$.

It is remarkable that the coefficients $\mathcal{T}_{mn}^{(2)}$ can also be computed analytically, thanks to the fact that $T^{(2)}$ can be

expressed in terms of the GPLs. Although the integrand involving $T^{(2)}$ in (17) contain about $\mathcal{O}(10^5)$ individual terms, the final result after two-fold integration becomes

$$\mathcal{T}_{00}^{(2)} = \frac{729L_\mu^2}{8} - (8\zeta_3 + \frac{35\pi^2}{6} - \frac{4365}{8})L_\mu + 205\zeta_5 - \frac{3\pi^4}{20} - \frac{759\zeta_3}{2} - \frac{1829\pi^2}{96} + \frac{36559}{32}. \quad (19)$$

Due to the length restriction, we refrain from providing the analytical expressions for other $\mathcal{T}_{mn}^{(1,2)}$. For reader's convenience, in Table I we tabulate the numerical values of $\mathcal{T}_{mn}^{(1,2)}$ for $0 \leq m, n \leq 6$, which is sufficient for most phenomenological analysis.

With the input from Table I, Eq. (16) constitutes our master formula for yielding phenomenological predictions through the two-loop accuracy. Compared with the original factorization formula (2), we have simplified an integration task into an algebraic one.

It is straightforward to adapt our master formula for the space-like pion EM form factor to the time-like one, provided that one makes the replacement $L_\mu \rightarrow L_\mu + i\pi$ in Table I, with Q^2 now indicating the squared invariant mass of the $\pi^+\pi^-$ pair.

Input parameters. As the key nonperturbative input, our knowledge on the pion LCDA is still not confirmative enough. In the early days, it is popular to assume asymptotic form, CZ parametrization [43] and the BSM parameterizations [71, 72]. In recent years there have emerged extensive investigations on the profile of the pion DA from different methodologies, including QCD light-cone sum rule [73] with nonlocal condensate [71, 74] or fitted from dispersion relation [75] or Platykurtic [76], Dyson-Schwinger equation [77, 78], basis light-front quantization [79], light-front quark model [80], holographic QCD [81], and very recently, from the lattice simulation [82, 83]. Various Gegenbauer moments predicted from these approaches are scattered in a wide range.

Since lattice QCD provides the first-principle predictions, in this Letter we will take the recent lattice results as inputs. In 2019 RQCD Collaboration has presented a precise prediction for the second Gegenbauer moment of pion LCDA in $\overline{\text{MS}}$ scheme [82]:

$$a_2(2 \text{ GeV}) = 0.116_{-0.020}^{+0.019}, \quad (20)$$

An important progress in lattice QCD is expedited by the advent of the Large-momentum effective theory (LaMET) a decade ago [84, 85], which allows one to access the light-cone distributions in Euclidean lattice directly in the x space. Very recently, the LPC Collaboration has presented the whole profile of the pion LCDA [83], from which various Gegenbauer moments can

exceedingly compact, which can be expressed in terms of the rational numbers and Riemann zeta function. For instance, the expression of $\mathcal{T}_{00}^{(2)}$ reads

be inferred:

$$\begin{aligned} a_2(2 \text{ GeV}) &= 0.258 \pm 0.087, \\ a_4(2 \text{ GeV}) &= 0.122 \pm 0.056, \\ a_6(2 \text{ GeV}) &= 0.068 \pm 0.038. \end{aligned} \quad (21)$$

It is curious that the value of a_2 reported by LPC Collaboration is about twice greater than that reported by the RQCD Collaboration. This discrepancy might be attributed to the fact that the LaMET approach receives large power correction in the endpoint region. On the other hand, it is very challenging for the local operator matrix element approach [82] to compute the higher Gegenbauer moments, thus difficult to reconstruct the whole profile of the LCDA.

Phenomenological exploration. We use the three-loop evolution equation [54, 86] to evolve each a_n evaluated at 2 GeV by lattice simulation to any intended scale μ . In the phenomenological study, we only retain those Gegenbauer moments with n up to 6. We also use the package FAPT [87] to evaluate the running QCD coupling constant to three-loop accuracy.

For the sake of comparison, we take the pion EM form factor data in the spacetime region from NA7 collaboration [11], Corne11 data compiled by Bebek *et al.* [5], and the reanalyzed JLab data [16], and take the pion EM form factor data in the timelike region entirely from the BaBar experiment [27]. We discard many irrelevant data at low momentum transfer.

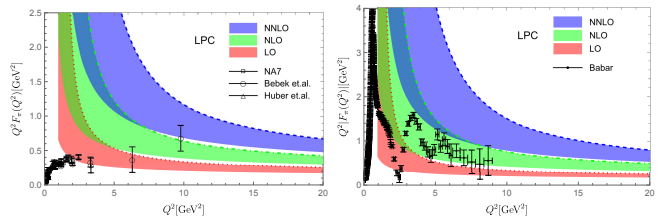


FIG. 2: Theoretical predictions vs. data for $Q^2 F_\pi(Q^2)$ in the space-like (left panel) and time-like (right panel) regimes. We take the various Gegenbauer moments of pion LCDA from the central values of (21) given by LPC collaboration. The red, green and blue curves correspond to the LO, NLO and NNLO results, and the respective bands are obtained by sliding μ from $Q/2$ to Q . Experimental data points are taken from NA7 [11], Bebek *et al.* [5], Huber *et al.* [16] and BaBar [27].

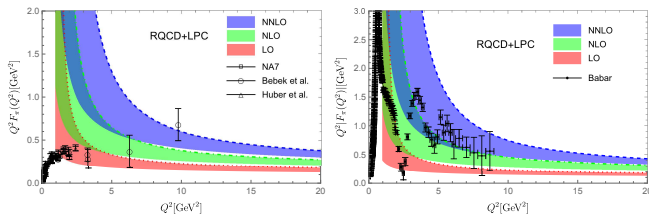


FIG. 3: Same as Fig. 2, except the predictions are made by taking a_2 from (20) by RQCD, and taking the values of a_4 and a_6 as the lower bounds in (21) by LPC.

In Fig. 2 and Fig. 3, we confront our predictions at various perturbative accuracy with the available data, including both space-like and time-like regime. One clearly visualizes that NNLO correction is important and positive. In Fig. 2, we set the various Gegenbauer moments of pion LCDA to the central values of (21) given by LPC Collaboration [83]. It appears the NNLO predictions are significantly overshooting the experimental data at large Q^2 ($> 5 \text{ GeV}^2$), especially for the time-like regime with high statistics data. This symptom is mainly due to the large value of a_2 given in (21).

In Fig. 3 we present our predictions with a_2 taken from (20) given by RQCD, yet still quote the LPC values for a_4 and a_6 (as the lower bounds in (21)). We find satisfactory agreement between the NNLO predictions and the data, both in space-like and time-like regimes. This might indicate that the value of a_2 given by RQCD might be more trustworthy. It is of utmost importance for RQCD and LPC collaborations to settle the discrepancy in the value of a_2 .

The prospective Electron-Ion Collider (EIC) program plans to measure the space-like pion EM form factor with Q^2 as large as 30 GeV^2 [88], where perturbative QCD should be very reliable. We are eagerly awaiting to confronting our NNLO predictions with the future EIC data.

Summary. In this work we report the first calculation of the NNLO QCD corrections to the pion electromagnetic form factor. We have explicitly verified the validity of the

collinear factorization to two-loop order for this process, and obtain the UV, IR-finite two-loop hard-scattering kernel in closed form. The NNLO QCD correction turns to be positive and substantial. We then confront our finest theoretical predictions with various space-like and time-like pion form factor data. Our phenomenological study reveals that adopting the second Gegenbauer moment computed by RQCD can yield a decent agreement with large- Q^2 data (above the resonance region in the time-like case). Nevertheless, to make a definite conclusion, it seems imperative to resolve the discrepancy between LPC and RQCD Collaboration for the value of a_2 in the future study. Furthermore, we look forward to the future high-statistics larger- Q^2 pion EM form factor data for critically testing our NNLO predictions. It is also interesting to confront our NNLO predictions with the available kaon EM form factor data.

Acknowledgments

We are indebted to Jun Hua for providing the value of the Gegenbauer moment a_6 based on the recent LPC study [83]. The work of L.-B. C. is supported by the NNSFC Grant No. 12175048. The work of W.C. is supported by National Natural Science Foundation of China under contract No. 11975200. The work of F. F. is supported by the NNSFC Grant No. 12275353. The work of Y. J. is supported in part by the NNSFC Grants No. 11925506, No. 12070131001 (CRC110 by DFG and NSFC).

Appendix A: Asymptotical expressions of the hard-scattering kernel

The analytic expressions of the hard-scattering kernels are too lengthy to be presented in the text. Nevertheless, it is instructive to present their asymptotic expressions near the endpoint regimes. For the one-loop hard-scattering kernel, we have

$$\lim_{\substack{x \rightarrow 0 \\ y \rightarrow 0}} T^{(1)}(x, y, \mu) = -\frac{e_d}{36xy} \left[12 \ln^2(xy) - 18 \ln(xy) - \pi^2 + 30 - 3(8 \ln(xy) - 3)L_\mu \right], \quad (\text{A1a})$$

$$\begin{aligned} \lim_{\substack{x \rightarrow 0 \\ y \rightarrow 1}} T^{(1)}(x, y) &= -\frac{e_d}{12x} \left[4 \ln^2 x - \ln x \ln \bar{y} - 7 \ln x - \ln \bar{y} + 15 - (8 \ln x - 3)L_\mu \right] \\ &+ [x \rightarrow \bar{y}, \bar{y} \rightarrow x, e_d \rightarrow -e_u]. \end{aligned} \quad (\text{A1b})$$

The limiting behavior of $T^{(1)}(x, y, \mu)$ in two other corners, $x \rightarrow 1, y \rightarrow 1$ and $x \rightarrow 1, y \rightarrow 0$, can be obtained from the above formulas by making the substitutions

$x \rightarrow \bar{x}, y \rightarrow \bar{y}$ and $e_u \leftrightarrow -e_d$.

For the two-loop hard-scattering kernel, we have

$$\begin{aligned}
\lim_{\substack{x \rightarrow 0 \\ y \rightarrow 0}} T^{(2)}(x, y, \mu) &= -\frac{e_d}{18xy} \left[\ln^4(xy) - \frac{33}{2} \ln^3(xy) - \left(\frac{5}{3}\pi^2 - \frac{313}{8} \right) \ln^2(xy) - 81 \ln x \ln y \right. \\
&\quad + (73\zeta_3 + \frac{461}{48}\pi^2 - \frac{1925}{8}) \ln(xy) + \frac{83}{60}\pi^4 - 123\zeta_3 - \frac{619}{48}\pi^2 + \frac{3681}{16} \\
&\quad + \frac{1}{4}(8 \ln(xy) - 3)(2 \ln(xy) - 21)L_\mu^2 \\
&\quad \left. - (4 \ln^3(xy) - 48 \ln^2(xy) - \frac{1}{3}(10\pi^2 - 228) \ln(xy) + 4\zeta_3 + \frac{17}{2}\pi^2 - \frac{513}{4})L_\mu \right]. \quad (\text{A2a})
\end{aligned}$$

$$\begin{aligned}
\lim_{\substack{x \rightarrow 0 \\ y \rightarrow 1}} T^{(2)}(x, y, \mu) &= -\frac{e_d}{18x} \left[\ln^4 x - \frac{1}{2} \ln^3 x \ln \bar{y} - \frac{5}{32} \ln^2 x \ln^2 \bar{y} - \frac{1}{6} \ln x \ln^3 \bar{y} \right. \\
&\quad - 17 \ln^3 x + \frac{51}{8} \ln^2 x \ln \bar{y} + \frac{23}{4} \ln x \ln^2 \bar{y} - \frac{1}{6} \ln^3 \bar{y} \\
&\quad - \frac{1}{48} ((89\pi^2 - 2019) \ln^2 x + 2(225 - 14\pi^2) \ln x \ln \bar{y} - 327 \ln^2 \bar{y}) \\
&\quad - \frac{1}{8} ((-395\zeta_3 - 83\pi^2 + 1700) \ln x + (29\zeta_3 + \pi^2 + 186) \ln \bar{y}) \\
&\quad + \frac{1}{80} (32\pi^4 - 7670\zeta_3 - 745\pi^2 + 15105) + \\
&\quad + (4 \ln^2 x - \frac{87}{2} \ln x - \frac{2}{3}\pi^2 + \frac{47}{4})L_\mu^2 - (4 \ln^3 x - \ln^2 x \ln \bar{y} \\
&\quad - \frac{1}{2} \ln^2 \bar{y} \ln x - 49 \ln^2 x + \frac{21}{2} \ln x \ln \bar{y} - \frac{1}{2} \ln^2 \bar{y} + (\frac{165}{2} - 4\pi^2) \ln x \\
&\quad \left. + \frac{23}{2} \ln \bar{y} - 7\zeta_3 + \frac{14}{3}\pi^2 - \frac{471}{4})L_\mu \right] \\
&\quad + [x \rightarrow \bar{y}, \bar{y} \rightarrow x, e_d \rightarrow -e_u]. \quad (\text{A2b})
\end{aligned}$$

Similar to the one-loop case, the limiting behavior of $T^{(2)}(x, y, \mu)$ in two other corners, $x \rightarrow 1, y \rightarrow 1$ and $x \rightarrow 1, y \rightarrow 0$, can also be deduced by making the substitutions $x \rightarrow \bar{x}, y \rightarrow \bar{y}$ and $e_u \leftrightarrow -e_d$.

Inspecting (A1) and (A2), one observes that $T^{(1)}(x, y, \mu)$ contains double endpoint logarithms exemplified by $\ln^2(xy)$ and $\ln^2 x$, while $T^{(2)}(x, y, \mu)$ of entail quartic endpoint logarithms $\ln^4(xy)$ and $\ln^4 x$. It is curious whether such endpoint logarithms can be resummed to all orders in α_s or not.

As an interesting exercise, we use the asymptotic expressions (A1) and (A2) to evaluate the convolution integrals as defined in (17) of the main text. We divide

the integrate regions into four parts: $0 < x, y < \frac{1}{2}$, $\frac{1}{2} < x, y < 1$, as well as $(0 < x < \frac{1}{2}, \frac{1}{2} < y < 1)$ and $(\frac{1}{2} < x < 1, 0 < y < \frac{1}{2})$. It is found that the contributions from the last two regions cancel with each other, and the first two regions yield identical results once the replacement $e_d \leftrightarrow -e_u$ is made. For the sake of clarity, we also tabulate the numerical results of $\mathcal{T}_{mn}^{(k)}|_{\text{asy}}$ in Table II. In comparison with Table I in the main text, we observe that the agreement between $\mathcal{T}_{mn}^{(1,2)}|_{\text{asy}}$ and the exact results becomes increasingly satisfactory as m, n increase.

-
- [1] H. Yukawa, Proc. Phys. Math. Soc. Jap. **17**, 48-57 (1935)
[2] C. M. G. Lattes, H. Muirhead, G. P. S. Occhialini and C. F. Powell, Nature **159**, 694-697 (1947)
[3] C. J. Bebek, C. N. Brown, M. Herzlinger, S. D. Holmes, C. A. Lichtenstein, F. M. Pipkin, S. Raither and L. K. Sisterson, Phys. Rev. D **13** (1976), 25
[4] C. J. Bebek, A. Browman, C. N. Brown, K. M. Hanson, S. D. Holmes, R. V. Kline, D. Larson, F. M. Pipkin, S. W. Raither and A. Silverman, *et al.* Phys. Rev. Lett.

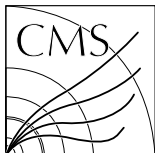
- 37** (1976), 1326
[5] C. J. Bebek, C. N. Brown, S. D. Holmes, R. V. Kline, F. M. Pipkin, S. Raither, L. K. Sisterson, A. Browman, K. M. Hanson and D. Larson, *et al.* Phys. Rev. D **17** (1978), 1693
[6] H. Ackermann, T. Azemoon, W. Gabriel, H. D. Mertiens, H. D. Reich, G. Specht, F. Janata and D. Schmidt, Nucl. Phys. B **137** (1978), 294-300
[7] P. Brauel, T. Canzler, D. Cords, R. Felst, G. Grind-

(m,n)	\tilde{c}_1	\tilde{c}_2	\tilde{d}_1	\tilde{d}_2	\tilde{d}_3
(0,0)	13.8194	39.4375	68.0646	365.132	620.076
(0,2)	27.1946	94.1639	145.758	963.722	1888.2
(0,4)	29.925	118.728	170.843	1301.75	2870.32
(0,6)	33.65	142.097	197.967	1613.8	3800.59
(2,2)	49.3167	204.84	287.84	2301.52	5188.99
(2,4)	52.2326	244.914	323.918	2934.33	7386.29
(2,6)	58.0254	286.907	369.88	3548.01	9469.42
(4,4)	54.25	284.119	356.587	3618.4	10078.1
(4,6)	59.879	328.872	403.889	4313.49	12661.6
(6,6)	65.949	378.914	456.09	5111.96	15759.8

TABLE II: The numerical values for $\mathcal{T}_{mn}^{(1)}|_{\text{asy}} = (\tilde{c}_1 L_\mu + \tilde{c}_2)$ and $\mathcal{T}_{mn}^{(2)}|_{\text{asy}} = (\tilde{d}_1 L_\mu^2 + \tilde{d}_2 L_\mu + \tilde{d}_3)$, with $0 \leq m, n \leq 6$, which are obtained by taking the asymptotical expressions for $T^{(1,2)}$ in (A1) and (A2).

- hammer, M. Helm, W. D. Kollmann, H. Krehbiel and M. Schadlich, *Z. Phys. C* **3** (1979), 101
- [8] E. B. Dally, D. J. Drickey, J. M. Hauptman, C. F. May, D. H. Stork, J. A. Poirier, C. A. Rey, R. J. Wojslaw, P. F. Shepard and A. J. Lennox, *et al.* *Phys. Rev. D* **24** (1981), 1718-1735
- [9] E. B. Dally, J. M. Hauptman, J. Kubic, D. H. Stork, A. B. Watson, Z. Guzik, T. S. Nigmanov, V. D. Ryabtsov, E. N. Tsyganov and A. S. Vodopianov, *et al.* *Phys. Rev. Lett.* **48** (1982), 375-378
- [10] S. R. Amendolia, B. Badelek, G. Batignani, G. A. Beck, F. Bedeschi, E. H. Bellamy, E. Bertolucci, D. Bettoni, H. Bilokon and G. Bologna, *et al.* *Phys. Lett. B* **146** (1984), 116-120
- [11] S. R. Amendolia *et al.* [NA7], *Nucl. Phys. B* **277** (1986), 168
- [12] J. Volmer *et al.* [Jefferson Lab F(pi)], *Phys. Rev. Lett.* **86** (2001), 1713-1716 [arXiv:nucl-ex/0010009 [nucl-ex]].
- [13] V. Tadevosyan *et al.* [Jefferson Lab F(pi)], *Phys. Rev. C* **75** (2007), 055205 [arXiv:nucl-ex/0607007 [nucl-ex]].
- [14] T. Horn *et al.* [Jefferson Lab F(pi)-2], *Phys. Rev. Lett.* **97** (2006), 192001 [arXiv:nucl-ex/0607005 [nucl-ex]].
- [15] H. P. Blok *et al.* [Jefferson Lab], *Phys. Rev. C* **78** (2008), 045202 [arXiv:0809.3161 [nucl-ex]].
- [16] G. M. Huber *et al.* [Jefferson Lab], *Phys. Rev. C* **78** (2008), 045203 [arXiv:0809.3052 [nucl-ex]].
- [17] R. R. Akhmetshin *et al.* [CMD-2], *Phys. Lett. B* **527** (2002), 161-172 [arXiv:hep-ex/0112031 [hep-ex]].
- [18] R. R. Akhmetshin *et al.* [CMD-2], *Phys. Lett. B* **578** (2004), 285-289 [arXiv:hep-ex/0308008 [hep-ex]].
- [19] M. N. Achasov, K. I. Beloborodov, A. V. Berdyugin, A. G. Bogdanchikov, A. V. Bozhenok, A. D. Bukin, D. A. Bukin, T. V. Dimova, V. P. Druzhinin and V. B. Golubev, *et al.* *J. Exp. Theor. Phys.* **101** (2005) no.6, 1053-1070 [arXiv:hep-ex/0506076 [hep-ex]].
- [20] M. N. Achasov, K. I. Beloborodov, A. V. Berdyugin, A. G. Bogdanchikov, A. V. Bozhenok, A. D. Bukin, D. A. Bukin, T. V. Dimova, V. P. Druzhinin and V. B. Golubev, *et al.* *J. Exp. Theor. Phys.* **103** (2006), 380-384 [arXiv:hep-ex/0605013 [hep-ex]].
- [21] V. M. Aul'chenko, R. R. Akhmetshin, V. S. Banzarov, L. M. Barkov, N. S. Bashtovoi, D. V. Bondarev, A. E. Bondar', A. V. Bragin, N. I. Gabyshev and D. A. Gorbachev, *et al.* *JETP Lett.* **84** (2006), 413-417 [arXiv:hep-ex/0610016 [hep-ex]].
- [22] R. R. Akhmetshin *et al.* [CMD-2], *Phys. Lett. B* **648** (2007), 28-38 [arXiv:hep-ex/0610021 [hep-ex]].
- [23] F. Ambrosino *et al.* [KLOE], *Phys. Lett. B* **670** (2009), 285-291 [arXiv:0809.3950 [hep-ex]].
- [24] B. Aubert *et al.* [BaBar], *Phys. Rev. Lett.* **103** (2009), 231801 [arXiv:0908.3589 [hep-ex]].
- [25] F. Ambrosino *et al.* [KLOE], *Phys. Lett. B* **700** (2011), 102-110 [arXiv:1006.5313 [hep-ex]].
- [26] D. Babusci *et al.* [KLOE], *Phys. Lett. B* **720** (2013), 336-343 [arXiv:1212.4524 [hep-ex]].
- [27] J. P. Lees *et al.* [BaBar], *Phys. Rev. D* **86** (2012), 032013 [arXiv:1205.2228 [hep-ex]].
- [28] A. Anastasi *et al.* [KLOE-2], *JHEP* **03** (2018), 173 [arXiv:1711.03085 [hep-ex]].
- [29] M. Ablikim *et al.* [BESIII], *Phys. Lett. B* **753** (2016), 629-638 [erratum: *Phys. Lett. B* **812** (2021), 135982] [arXiv:1507.08188 [hep-ex]].
- [30] J. Gasser and H. Leutwyler, *Annals Phys.* **158**, 142 (1984)
- [31] G. Martinelli and C. T. Sachrajda, *Nucl. Phys. B* **306** (1988), 865-889
- [32] T. Draper, R. M. Woloshyn, W. Wilcox and K. F. Liu, *Nucl. Phys. B* **318** (1989), 319-336
- [33] X. Feng, Y. Fu and L. C. Jin, *Phys. Rev. D* **101** (2020) no.5, 051502 [arXiv:1911.04064 [hep-lat]].
- [34] G. Wang *et al.* [chiQCD], *Phys. Rev. D* **104** (2021), 074502 [arXiv:2006.05431 [hep-ph]].
- [35] X. Gao, N. Karthik, S. Mukherjee, P. Petreczky, S. Syritsyn and Y. Zhao, *Phys. Rev. D* **104** (2021) no.11, 114515 [arXiv:2102.06047 [hep-lat]].
- [36] G. P. Lepage and S. J. Brodsky, *Phys. Lett. B* **87**, 359-365 (1979)
- [37] G. P. Lepage and S. J. Brodsky, *Phys. Rev. Lett.* **43**, no.21, 545-549 (1979) [erratum: *Phys. Rev. Lett.* **43**, 1625-1626 (1979)]
- [38] G. P. Lepage and S. J. Brodsky, *Phys. Rev. D* **22**, 2157 (1980) doi:10.1103/PhysRevD.22.2157
- [39] A. V. Efremov and A. V. Radyushkin, *Theor. Math. Phys.* **42**, 97-110 (1980)
- [40] A. V. Efremov and A. V. Radyushkin, *Phys. Lett. B* **94**, 245-250 (1980)
- [41] A. Duncan and A. H. Mueller, *Phys. Lett. B* **90**, 159-163 (1980)
- [42] A. Duncan and A. H. Mueller, *Phys. Rev. D* **21**, 1636 (1980)
- [43] V. L. Chernyak and A. R. Zhitnitsky, *Phys. Rept.* **112** (1984), 173
- [44] R. D. Field, R. Gupta, S. Otto and L. Chang, *Nucl. Phys. B* **186** (1981), 429-474
- [45] F. M. Dittes and A. V. Radyushkin, *Sov. J. Nucl. Phys.* **34** (1981), 293
- [46] M. H. Sarmadi, *Phys. Lett. B* **143** (1984), 471
- [47] E. Braaten and S. M. Tse, *Phys. Rev. D* **35** (1987), 2255
- [48] B. Melic, B. Nizic and K. Passek, *Phys. Rev. D* **60** (1999), 074004 [arXiv:hep-ph/9802204 [hep-ph]].
- [49] E. G. Floratos, D. A. Ross and C. T. Sachrajda, *Nucl. Phys. B* **129** (1977), 66-88 [erratum: *Nucl. Phys. B* **139** (1978), 545-546]
- [50] F. M. Dittes and A. V. Radyushkin, *Phys. Lett. B* **134** (1984), 359-362
- [51] G. R. Katz, *Phys. Rev. D* **31** (1985), 652
- [52] S. V. Mikhailov and A. V. Radyushkin, *Nucl. Phys. B* **254** (1985), 89-126

- [53] A. V. Belitsky, D. Mueller and A. Freund, Phys. Lett. B **461** (1999), 270-279 [arXiv:hep-ph/9904477 [hep-ph]].
- [54] V. M. Braun, A. N. Manashov, S. Moch and M. Strohmaier, JHEP **06**, 037 (2017) [arXiv:1703.09532 [hep-ph]].
- [55] T. Becher and M. Neubert, Phys. Lett. B **633**, 739-747 (2006) [arXiv:hep-ph/0512208 [hep-ph]].
- [56] F. Feng, Y. F. Xie, Q. C. Zhou and S. R. Tang, Comput. Phys. Commun. **265** (2021), 107982 [arXiv:2103.08507 [hep-ph]].
- [57] T. Hahn, Comput. Phys. Commun. **140** (2001), 418-431 [arXiv:hep-ph/0012260 [hep-ph]].
- [58] F. Feng, Comput. Phys. Commun. **183** (2012), 2158-2164 [arXiv:1204.2314 [hep-ph]].
- [59] A. V. Smirnov and F. S. Chuharev, Comput. Phys. Commun. **247** (2020), 106877 [arXiv:1901.07808 [hep-ph]].
- [60] A. V. Kotikov, Phys. Lett. B **254** (1991), 158-164
- [61] E. Remiddi, Nuovo Cim. A **110** (1997), 1435-1452 [arXiv:hep-th/9711188 [hep-th]].
- [62] J. M. Henn, Phys. Rev. Lett. **110** (2013), 251601 [arXiv:1304.1806 [hep-th]].
- [63] J. Gao, T. Huber, Y. Ji and Y. M. Wang, Phys. Rev. Lett. **128** (2022) no.6, 6 [arXiv:2106.01390 [hep-ph]].
- [64] V. M. Braun, A. N. Manashov, S. Moch and J. Schoenleber, Phys. Rev. D **104** (2021) no.9, 094007 [arXiv:2106.01437 [hep-ph]].
- [65] W. Chen, JHEP **02** (2020), 115 [arXiv:1902.10387 [hep-ph]].
- [66] W. Chen, Eur. Phys. J. C **81** (2021) no.3, 244 [arXiv:1912.08606 [hep-ph]].
- [67] W. Chen, Eur. Phys. J. C **80** (2020) no.12, 1173 [arXiv:2007.00507 [hep-ph]].
- [68] W. Chen, M. x. Luo, T. Z. Yang and H. X. Zhu, JHEP **01**, 131 (2024) [arXiv:2309.03832 [hep-ph]].
- [69] A. B. Goncharov, Math. Res. Lett. **5** (1998), 497-516 [arXiv:1105.2076 [math.AG]].
- [70] X. Liu and Y. Q. Ma, Comput. Phys. Commun. **283** (2023), 108565 [arXiv:2201.11669 [hep-ph]].
- [71] S. V. Mikhailov, A. V. Pimikov and N. G. Stefanis, Phys. Rev. D **93** (2016) no.11, 114018 [arXiv:1604.06391 [hep-ph]].
- [72] A. P. Bakulev, S. V. Mikhailov and N. G. Stefanis, Phys. Lett. B **508** (2001), 279-289 [erratum: Phys. Lett. B **590** (2004), 309-310] [arXiv:hep-ph/0103119 [hep-ph]].
- [73] P. Ball, V. M. Braun and A. Lenz, JHEP **05** (2006), 004 [arXiv:hep-ph/0603063 [hep-ph]].
- [74] N. G. Stefanis, Phys. Rev. D **102** (2020) no.3, 034022 [arXiv:2006.10576 [hep-ph]].
- [75] S. Cheng, A. Khodjamirian and A. V. Rusov, Phys. Rev. D **102** (2020) no.7, 074022 [arXiv:2007.05550 [hep-ph]].
- [76] N. G. Stefanis, Phys. Lett. B **738** (2014), 483-487 [arXiv:1405.0959 [hep-ph]].
- [77] L. Chang, I. C. Cloet, J. J. Cobos-Martinez, C. D. Roberts, S. M. Schmidt and P. C. Tandy, Phys. Rev. Lett. **110** (2013) no.13, 132001 [arXiv:1301.0324 [nucl-th]].
- [78] K. Raya, L. Chang, A. Bashir, J. J. Cobos-Martinez, L. X. Gutiérrez-Guerrero, C. D. Roberts and P. C. Tandy, Phys. Rev. D **93** (2016) no.7, 074017 [arXiv:1510.02799 [nucl-th]].
- [79] J. Lan, C. Mondal, S. Jia, X. Zhao and J. P. Vary, Phys. Rev. D **101** (2020) no.3, 034024 [arXiv:1907.01509 [nucl-th]].
- [80] H. M. Choi and C. R. Ji, Phys. Rev. D **91** (2015) no.1, 014018 [arXiv:1412.2507 [hep-ph]].
- [81] Q. Chang, S. J. Brodsky and X. Q. Li, Phys. Rev. D **95** (2017) no.9, 094025 [arXiv:1612.05298 [hep-ph]].
- [82] G. S. Bali *et al.* [RQCD], JHEP **08**, 065 (2019) [arXiv:1903.08038 [hep-lat]].
- [83] J. Hua *et al.* [Lattice Parton], Phys. Rev. Lett. **129** (2022) no.13, 132001 [arXiv:2201.09173 [hep-lat]].
- [84] X. Ji, Phys. Rev. Lett. **110** (2013), 262002 [arXiv:1305.1539 [hep-ph]].
- [85] X. Ji, Sci. China Phys. Mech. Astron. **57**, 1407-1412 (2014) [arXiv:1404.6680 [hep-ph]].
- [86] M. Strohmaier, *Conformal symmetry breaking and evolution equations in Quantum Chromodynamics*, Ph.D. thesis, Regensburg U. (2018).
- [87] A. P. Bakulev and V. L. Khandramai, Comput. Phys. Commun. **184** (2013) no.1, 183-193 [arXiv:1204.2679 [hep-ph]].
- [88] A. Bylinkin, C. T. Dean, S. Fegan, D. Gangadharan, K. Gates, S. J. D. Kay, I. Korover, W. B. Li, X. Li and R. Montgomery, *et al.* Nucl. Instrum. Meth. A **1052** (2023), 168238 [arXiv:2208.14575 [physics.ins-det]].

CERN-EP-2024-027
2024/02/29

CMS-TOP-22-003

Search for baryon number violation in top quark production and decay using proton-proton collisions at $\sqrt{s} = 13$ TeV

The CMS Collaboration*

Abstract

A search is presented for baryon number violating interactions in top quark production and decay. The analysis uses data from proton-proton collisions at a center-of-mass energy of 13 TeV, collected with the CMS detector at the LHC with an integrated luminosity of 138 fb^{-1} . Candidate events are selected by requiring two oppositely-charged leptons (electrons or muons) and exactly one jet identified as originating from a bottom quark. Multivariate discriminants are used to separate the signal from the background. No significant deviation from the standard model prediction is observed. Upper limits are placed on the strength of baryon number violating couplings. For the first time the production of single top quarks via baryon number violating interactions is studied. This allows the search to set the most stringent constraints to date on the branching fraction of the top quark decay to a lepton, an up-type quark (u or c), and a down-type quark (d, s, or b). The results improve the previous bounds by three to six orders of magnitude based on the fermion flavor combination of the baryon number violating interactions.

Submitted to Physical Review Letters

In the standard model (SM), the baryon number is a conserved quantum number. Its conservation, however, is not a direct consequence of fundamental symmetries within the SM, and it can be violated by nonperturbative effects [1]. The size of such violations is too small to explain the observed matter-antimatter asymmetry in the universe [2]. Certain scenarios of physics beyond the SM, such as grand unified theories [3] and supersymmetry [4], naturally include baryon number violation (BNV) and could provide a mechanism to explain this observation. Various low-energy direct searches for signatures of BNV have been conducted over the past decades, with constraints set on the BNV energy scale via processes such as nucleon [5], τ lepton [6], c [7], and b quark [8] decays. There are also stringent indirect constraints from proton stability involving heavy quarks [9] for specific theoretical assumptions [10]. Experiments at the CERN LHC provide the highest sensitivity for potential high-energy BNV processes involving the top quark. Previously, the CMS Collaboration has performed a search for BNV decays of the top quark in single lepton (electron or muon) channels in proton-proton (pp) collisions at $\sqrt{s} = 8$ TeV [11]. This Letter presents the first search for top quark BNV interactions via single top quark production in association with a lepton in pp collisions at 13 TeV in dilepton final states. The data used in the analysis correspond to an integrated luminosity of 138 fb^{-1} , collected by the CMS experiment at the LHC during 2016–2018.

Assuming the mass scale of new physics responsible for BNV processes is larger than the energy scale directly accessible at the LHC, BNV interactions of top quarks can be described through an effective Lagrangian, \mathcal{L}_{eff} . Including up to dimension-six operators, the most general effective Lagrangian that describes the BNV interactions of the top quark and a charged lepton takes the form [12]:

$$\mathcal{L}_{\text{eff}} = \frac{C_s}{\Lambda^2} \epsilon^{\alpha\beta\gamma} [\bar{t}_\alpha^c d_\gamma] [\bar{u}_\beta^c \ell] + \frac{C_t}{\Lambda^2} \epsilon^{\alpha\beta\gamma} [\bar{t}_\alpha^c \ell] [\bar{u}_\beta^c d_\gamma] + \text{h.c.}, \quad (1)$$

where d , u , and ℓ are down-type quark, up-type quark, and charged-lepton fields, respectively, where the superscript “c” denotes charged conjugated fields. Colors are labeled by greek indices, Λ is the generic scale of new physics, and C_s and C_t are fermion-flavor-dependent effective couplings. The s and t labels in Eq. (1) denote that the new physics scale may be linked to the mass of a heavy mediator exchanged in the s or t channels, respectively [12]. No specific chirality is assumed for the BNV interactions. These effective BNV four-fermion interactions open new top quark decay and production channels at the LHC. Figure 1 displays representative Feynman diagrams for single top quark production (“ST mode”) and top quark decay (“TT mode”) via BNV interactions in top quark-antiquark pair production ($t\bar{t}$).

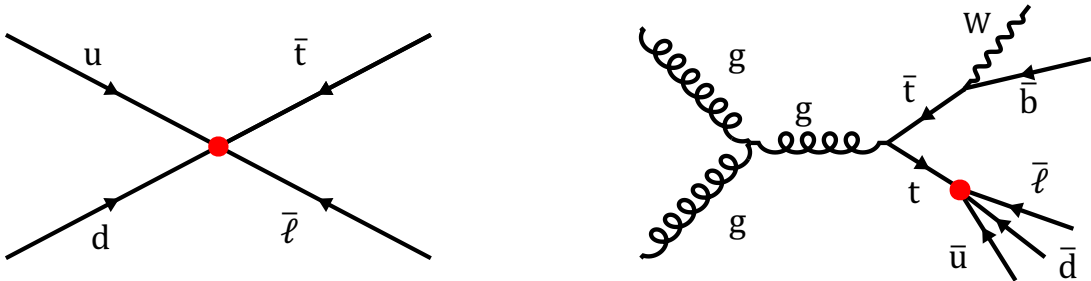


Figure 1: Representative Feynman diagrams for single top quark production (left) and top quark decays (right) via BNV interactions. The red circles mark the BNV vertices.

This analysis uses events in dileptonic final states (e^+e^- , $e^\pm\mu^\mp$, and $\mu^+\mu^-$) where one lepton is produced via the BNV interaction and a second lepton comes from the decay of the W boson produced in the dominant $t \rightarrow bW$ decay. The strength of the twelve flavor combinations of

top quark four-fermion BNV interactions are probed in these final states. These take the form $t\ell q_u q_d$, where ℓ can be an electron or muon, q_u can be an up or charm quark, and q_d can be any down-type quark.

The central feature of the CMS apparatus is a superconducting solenoid of 6 m internal diameter, providing a magnetic field of 3.8 T. Within the solenoid volume are a silicon pixel and strip tracker, a lead tungstate crystal electromagnetic calorimeter, and a brass and scintillator hadron calorimeter, each composed of a barrel and two endcap sections. Forward calorimeters extend the pseudorapidity (η) coverage provided by the barrel and endcap detectors. Muons are measured in gas-ionization detectors embedded in the steel flux-return yoke outside the solenoid. A more detailed description of the CMS detector, together with a definition of the coordinate system used and the relevant kinematic variables, can be found in Ref. [13].

The data are modeled by Monte Carlo (MC) simulations of the signal and background processes. Simulated events are produced with event generator programs using the next-to-next-to-leading order (NNLO) parton distribution function (PDF) sets from NNPDF3.1 [14]. Parton showering and hadronization are done with PYTHIA v8.240 [15] using the underlying-event tune CP5 [16]. Generated events undergo a full simulation of the detector response using GEANT4 [17]. The presence of simultaneous pp collisions in the same or nearby bunch crossings, referred to as pileup (PU), is modeled by superimposing inelastic pp interactions, simulated using PYTHIA, on all MC events. Simulated events are then reweighted to reproduce the PU distribution observed in data.

Contributions to the background include SM $t\bar{t}$ production, single top quark production in association with a W boson (tW), W or Z bosons produced in association with $t\bar{t}$ ($t\bar{t}+W/Z$), Drell–Yan in association with jets (DY+jets) processes, W+jets production, and diboson processes (including WW, WZ, and ZZ). The contribution from quantum chromodynamics (QCD) multijet production is found to be negligible. The POWHEG v2.0 next-to-leading order (NLO) MC generator is used to simulate the SM $t\bar{t}$, tW, and diboson events [18–20]. The MADGRAPH5_aMC@NLO v2.6.5 generator is used to simulate the $t\bar{t}+W/Z$, DY+jets, W+jets, and diboson events [21]. The $t\bar{t}$ sample is normalized to the cross section calculated at NNLO in QCD including resummation of next-to-next-to-leading logarithmic (NNLL) soft-gluon terms with the TOP++2.0 program [22], 832_{-29}^{+20} (scale) ± 35 (PDF + α_s) pb, where α_s is the strong coupling. To improve the modeling of the transverse momentum (p_T) spectrum of the top quark in POWHEG, simulated SM $t\bar{t}$ events are weighted as a function of the p_T of the top quark to match the expectations at NNLO QCD accuracy, including electroweak corrections [23]. Other simulated samples are normalized to their cross section predictions at NNLO (for DY+jets and W+jets [24]), NLO+NNLL (for tW production [25]), or NLO (for the diboson and $t\bar{t}+W/Z$ processes [26, 27]).

The simulated signal samples are generated using the MADGRAPH5_aMC@NLO v2.6.5 generator with the TopBNV model [12] at leading order in QCD. The top quark BNV signal sample has two independent components: (i) ST mode, and (ii) TT mode, as shown in Fig. 1. Independent samples are generated for the various possible fermion flavor combinations. The top quark mass and width are set to 172.5 and 1.33 GeV, respectively. There is no interference considered between the BNV signal and SM processes and the BNV couplings affect only the signal yield. Since the BNV couplings are probed individually, signal samples are generated separately for nonzero C_t and C_s couplings, assuming $\Lambda = 1$ TeV. The BNV signal cross sections and the branching fractions for the BNV top quark decays depend quadratically on C/Λ^2 [12]. Theoretical cross sections for single top quark production and top quark decays via the BNV interactions are shown in Table 1. The dominant signal process is the ST mode because

of its larger cross section. Final-state particles in the ST mode also have a harder p_T spectrum compared to SM processes and the TT mode [12]. Therefore, the analysis is optimized with respect to the ST mode signatures and the TT mode contribution is added for completeness.

Table 1: Theoretical inclusive cross sections, in units of pico barn (pb), for single top quark production (ST) and top quark-antiquark pair production with the decay (TT) via BNV interactions, assuming a top quark mass of 172.5 GeV, the top quark decay width 1.33 GeV, $\Lambda = 1$ TeV, and $C_t = 1$ or $C_s = 1$. The uncertainties arising from the choice of the renormalization and factorization scales and PDFs are given as $(\sigma \pm \text{Scale} \pm \text{PDF})$. Here, the sum of the two cross sections is given where $\ell = e$ or μ .

Process	$\sigma(C_t = 1)$ [pb]	$\sigma(C_s = 1)$ [pb]
ST (t ℓ ud)	$31.5 \pm 2.1 \pm 1.0$	$10.7 \pm 0.7 \pm 0.4$
ST (t ℓ us)	$8.1 \pm 0.3 \pm 0.5$	$2.8 \pm 0.1 \pm 0.2$
ST (t ℓ ub)	$3.31 \pm 0.13 \pm 0.06$	$1.14 \pm 0.05 \pm 0.02$
ST (t ℓ cd)	$2.77 \pm 0.22 \pm 0.01$	$0.96 \pm 0.01 \pm 0.07$
ST (t ℓ cs)	$0.79 \pm 0.02 \pm 0.11$	$0.27 \pm 0.01 \pm 0.04$
ST (t ℓ cb)	$0.28 \pm 0.03 \pm 0.04$	$0.10 \pm 0.01 \pm 0.01$
TT	$0.007 \pm 0.002 \pm 0.001$	$0.007 \pm 0.002 \pm 0.001$

Events were selected online during data taking by a combination of single-electron and di-electron triggers for the e^+e^- events as in Refs. [28, 29]. Single-muon triggers are used for the $e^\pm\mu^\mp$ and $\mu^+\mu^-$ events, as described in Ref. [30]. The particle-flow (PF) algorithm aims at reconstructing individual particles (photons, charged and neutral hadrons, muons, and electrons) by combining information from the various components of the CMS detector [31]. The primary vertex is taken to be the vertex corresponding to the hardest scattering in the event, evaluated using tracking information alone, as described in Section 9.4.1 of Ref. [32]. Electron and muon candidates [33, 34] are required to lie within $|\eta| < 2.4$ to keep them within the silicon tracker coverage. Electron candidates in the transition region between barrel and endcap calorimeters ($1.44 < |\eta| < 1.57$) are removed. The same high- p_T lepton identification and isolation criteria described in Ref. [30] are used to reject nonprompt leptons. Events are required to have exactly two opposite-sign leptons. To operate well above the trigger threshold, the selected electron (muon) should have $p_T > 35(53)$ GeV. Selected events are divided based on their lepton flavors into three mutually exclusive categories: e^+e^- , $e^\pm\mu^\mp$, and $\mu^+\mu^-$. To suppress backgrounds, especially from the DY+jets processes, we reject events in which the two leptons have an invariant mass below 106 GeV.

Jets are reconstructed from the PF candidates using the anti- k_T clustering algorithm with a distance parameter of 0.4 [35, 36]. We select jets with $|\eta| < 2.4$ and $p_T > 30$ GeV. Jets originating from b quarks (b jets) are identified (b-tagged) using the DEEPJET algorithm [37] with an average b tagging efficiency of 68% and a light quark and gluon jet misidentification rate of 1.1%. Events are required to have exactly one b-tagged jet. The missing transverse momentum (\vec{p}_T^{miss}) is defined as the negative vector \vec{p}_T sum of all PF particles, and its magnitude is denoted as p_T^{miss} [38]. Events with $p_T^{\text{miss}} < 60$ GeV are rejected to further suppress the DY+jets events.

The selected events in the signal region have exactly one opposite-sign lepton pair with invariant mass greater than 106 GeV, $p_T^{\text{miss}} > 60$ GeV, and exactly one b-tagged jet irrespective of the number of untagged jets. The dominant background is the $t\bar{t}$ process ($\sim 89\%$), followed by the tW ($\sim 9\%$) and DY+jets ($\sim 1\%$) processes. Signal selection efficiencies for the ST (TT) mode of

2.8 (1.1)% for $t\bar{t}ud$ flavor combination are obtained with respect to an inclusive MC sample, assuming $C_s = 0$ and nonzero C_t .

In the ST mode, the lepton and top quark are produced directly from the annihilation of the incoming quarks, and are Lorentz-boosted and approximately back-to-back. The subleading lepton in the ST mode is primarily from the top quark decay chain. To use these specific features of the signal events, the four-momentum vectors of the top quarks are reconstructed from the decay products: the subleading lepton, the neutrino, and the b jet candidate. The neutrino p_T can be inferred from the \vec{p}_T^{miss} . The longitudinal momentum of the neutrino is inferred assuming energy-momentum conservation at the W boson decay vertex and constraining the W boson mass to 80.4 GeV as discussed in Ref. [39].

A boosted decision tree (BDT) [40, 41] is employed to distinguish signal from the sum of the background processes. Independent signal and background samples are used for training the BDT. A merged sample from $t\bar{t}$, tW , and DY+jets background events, weighted by their cross sections, is used as the background training and testing sample. For the signal, events from various BNV flavor combinations of the ST mode are merged with equal weights and are used in the BDT training and testing. Ten variables are inputs to the BDT: the transverse momenta of the leading lepton (ℓ_1), subleading lepton (ℓ_2), and the top quark candidate (t); the distances between the leading and subleading leptons [$\Delta R(\ell_1, \ell_2) = \sqrt{(\eta^{\ell_1} - \eta^{\ell_2})^2 + (\phi^{\ell_1} - \phi^{\ell_2})^2}$] and $\Delta R(\ell_1, t)$; the azimuthal angles between the leading and subleading leptons [$\Delta\phi(\ell_1, \ell_2) = |\phi^{\ell_1} - \phi^{\ell_2}|$] and $\Delta\phi(\ell_1, t)$; the invariant mass and p_T of the dilepton system; and $|p_T^t - p_T^{\ell_1}| / |p_T^t + p_T^{\ell_1}|$.

The templates describing the BDT distributions for the signal and background events are taken from simulation. The normalization of the DY+jets background, which is important in the e^+e^- and $\mu^+\mu^-$ channels, is determined by applying a scale factor to the simulation derived from data in a control region where the reconstructed dilepton mass is close to the Z boson mass [42].

The list of uncertainties considered and the techniques used to estimate their values are very similar to those in Ref. [43]. We consider uncertainties in the integrated luminosity [44–46], pileup effects [47], trigger, lepton identification [33, 48], and b tagging [37, 49] efficiencies, in the calculation of p_T^{miss} , and those related to the jet energy scale and resolution [50]. Uncertainties arising from choices in signal and $t\bar{t}$ modeling include PDFs, renormalization and factorization scales, and initial- and final-state QCD radiation. The uncertainty arising from the modeling of the top quark p_T spectrum is evaluated by the renormalization and factorization scales at NNLO QCD accuracy, including NLO electroweak corrections [23]. Modeling uncertainties from the matching of the matrix element level calculation to the parton shower simulation, the modeling of the underlying event defined in PYTHIA tunes, and the models of color reconnection are considered for the SM $t\bar{t}$ process, as described in Ref. [51]. The $t\bar{t}$ and signal modeling uncertainties apply only to the signal acceptance. Normalization uncertainties of 5, 10, and 30% are considered for the $t\bar{t}$, tW , and other processes based on experimental measurements [51, 52], respectively. An additional 20% normalization uncertainty is added for DY+jets processes to account for PU mismodeling in large p_T^{miss} events.

Figure 2 shows the BDT discriminant distributions for events in the three channels (e^+e^- , $e^\pm\mu^\mp$, and $\mu^+\mu^-$) passing the event selection for the three data-taking years (2016–2018) combined. To illustrate signal distributions, simulated “teud” and “t μ ud” samples are included in the figure, assuming $\Lambda = 1$ TeV and $C_t = C_s = 1$. Signal events are well separated from background events. To extract the signal contribution, a simultaneous binned maximum-likelihood fit is performed of the BDT output distributions in the signal region for three years and three

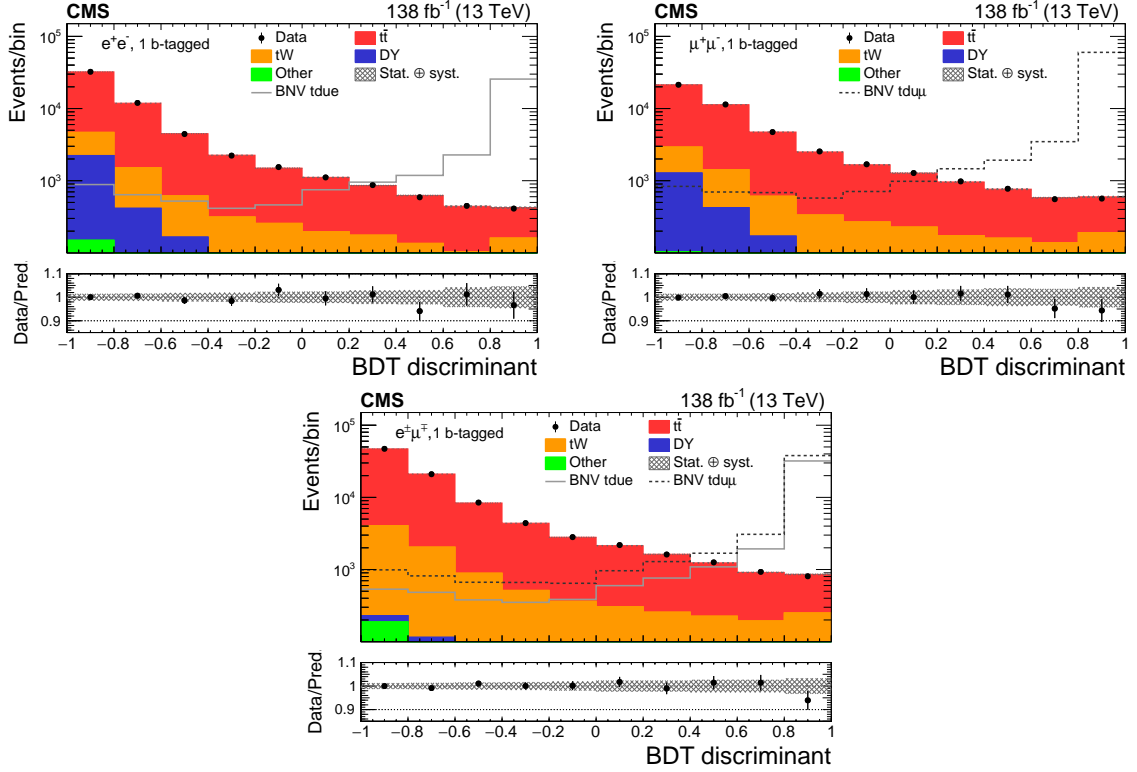


Figure 2: The BDT output distributions for data (points) and backgrounds (histograms) for the e^+e^- (upper left), $\mu^+\mu^-$ (right), and $e^+\mu^+$ (lower) channels, including the ratio of data to the predicted total background yield. The hatched bands indicate the total uncertainty (statistical and systematic added in quadrature) for the SM background predictions. The predicted yields of the backgrounds and the uncertainty bands are shown after the simultaneous fits for the signal-plus-background hypothesis. Examples of the predicted signal contribution for the BNV interactions via $tWue$ (solid gray line) and $tWud$ (dashed black line) vertices are shown.

channels, with the systematic uncertainties described above treated as nuisance parameters. The best fit for the BNV effective couplings is consistent with zero and no significant excess over the background expectations is observed. The sources of systematic uncertainty with the largest impact on the estimated signal contribution depend on the fermion flavor combination of the BNV interactions. The three main sources of uncertainty that are common among the BNV interactions are uncertainties in the normalization of the SM tW process, muon energy scale, and modeling of the top quark p_T spectrum in the SM $t\bar{t}$ simulation. The exclusion limits are calculated using the asymptotic approximation of the CL_s method [53]. The adequacy of the asymptotic approximation has been validated with pseudo-experiments. The limit-setting procedure is performed for each individual BNV coupling while setting the other BNV couplings to zero. The observed and expected limits at 95% confidence level (CL) on the BNV effective coupling strengths are listed in Table 2. The limits on the strengths of the BNV couplings are translated to limits on the branching fractions for the BNV top quark decays. The differences between different quark flavor combination stems mainly from the different PDFs involved in the production mode. The results for limits on various BNV branching fractions are displayed in Fig. 3. Tabulated results are provided in the HEPData record for this analysis [54].

In summary, a search for baryon number violation (BNV) in events with top quarks is performed using the LHC proton-proton collision data at a center-of-mass energy of 13 TeV. The

Table 2: Expected and observed 95% CL upper limits on the BNV effective couplings and top quark BNV branching fractions.

Vertex	C_x	C_x/Λ^2 [TeV ⁻²] Exp.	C_x/Λ^2 [TeV ⁻²] Obs.	\mathcal{B}_x [10 ⁻⁶] Exp.	\mathcal{B}_x [10 ⁻⁶] Obs.
teud	<i>s</i>	0.055	0.048	0.015	0.011
	<i>t</i>	0.031	0.027	0.005	0.003
t μ ud	<i>s</i>	0.046	0.036	0.010	0.006
	<i>t</i>	0.025	0.020	0.003	0.002
tecd	<i>s</i>	0.207	0.184	0.208	0.164
	<i>t</i>	0.114	0.102	0.063	0.050
t μ cd	<i>s</i>	0.178	0.141	0.153	0.095
	<i>t</i>	0.100	0.080	0.048	0.030
teus	<i>s</i>	0.115	0.101	0.063	0.050
	<i>t</i>	0.064	0.056	0.019	0.015
t μ us	<i>s</i>	0.102	0.079	0.050	0.030
	<i>t</i>	0.056	0.043	0.015	0.009
tecs	<i>s</i>	0.448	0.403	0.973	0.786
	<i>t</i>	0.243	0.218	0.286	0.229
t μ cs	<i>s</i>	0.394	0.311	0.752	0.468
	<i>t</i>	0.217	0.169	0.228	0.138
teub	<i>s</i>	0.199	0.178	0.191	0.154
	<i>t</i>	0.109	0.097	0.057	0.045
t μ ub	<i>s</i>	0.168	0.134	0.136	0.087
	<i>t</i>	0.095	0.076	0.044	0.028
tecb	<i>s</i>	0.718	0.657	2.503	2.090
	<i>t</i>	0.405	0.367	0.795	0.652
t μ cb	<i>s</i>	0.703	0.564	2.393	1.521
	<i>t</i>	0.386	0.307	0.722	0.455

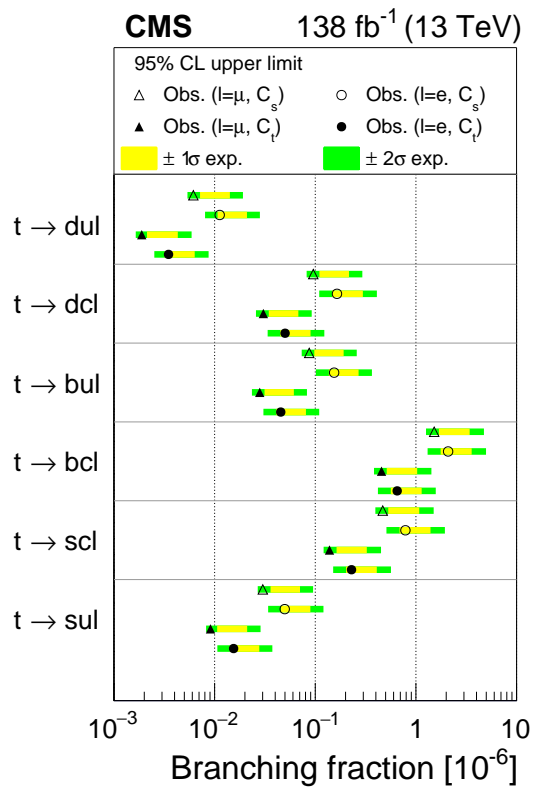


Figure 3: The observed upper limits on the branching fractions of the top quark BNV decays are shown with circle and triangle shapes for electron and muon couplings, respectively. The observed limits corresponding to the C_t and C_s coefficients are shown with filled and open markers, respectively. The yellow light (green dark) bands indicate the range within plus or minus one (two) standard deviations bands around the expected limits.

analysis explores baryon number violating effects in single top quark production for the first time. Data were collected by the CMS experiment in 2016–2018 and correspond to an integrated luminosity of 138 fb^{-1} . Events with a lepton pair and exactly one b-tagged jet are selected. A boosted decision tree (BDT) is used to separate signal events from background events. A binned maximum likelihood fit to the BDT output distribution is performed to search for the BNV processes. Considering BNV vertices in the production of top quarks dramatically increases the sensitivity of this search. No significant excess of events over the background prediction is observed. Upper limits are placed on the strengths of the BNV couplings, which are multiple orders of magnitude more stringent than the previous limits [11].

Acknowledgments

We congratulate our colleagues in the CERN accelerator departments for the excellent performance of the LHC and thank the technical and administrative staffs at CERN and at other CMS institutes for their contributions to the success of the CMS effort. In addition, we gratefully acknowledge the computing centers and personnel of the Worldwide LHC Computing Grid and other centers for delivering so effectively the computing infrastructure essential to our analyses. Finally, we acknowledge the enduring support for the construction and operation of the LHC, the CMS detector, and the supporting computing infrastructure provided by the following funding agencies: SC (Armenia), BMBWF and FWF (Austria); FNRS and FWO (Belgium); CNPq, CAPES, FAPERJ, FAPERGS, and FAPESP (Brazil); MES and BNSF (Bulgaria); CERN; CAS, MoST, and NSFC (China); MINCIENCIAS (Colombia); MSES and CSF (Croatia); RIF (Cyprus); SENESCYT (Ecuador); ERC PRG, RVTT3 and MoER TK202 (Estonia); Academy of Finland, MEC, and HIP (Finland); CEA and CNRS/IN2P3 (France); SRNSF (Georgia); BMBF, DFG, and HGF (Germany); GSRI (Greece); NKFIH (Hungary); DAE and DST (India); IPM (Iran); SFI (Ireland); INFN (Italy); MSIP and NRF (Republic of Korea); MES (Latvia); LMTLT (Lithuania); MOE and UM (Malaysia); BUAP, CINVESTAV, CONACYT, LNS, SEP, and UASLP-FAI (Mexico); MOS (Montenegro); MBIE (New Zealand); PAEC (Pakistan); MES and NSC (Poland); FCT (Portugal); MESTD (Serbia); MCIN/AEI and PCTI (Spain); MOSTR (Sri Lanka); Swiss Funding Agencies (Switzerland); MST (Taipei); MHESI and NSTDA (Thailand); TUBITAK and TENMAK (Turkey); NASU (Ukraine); STFC (United Kingdom); DOE and NSF (USA).

References

- [1] G. 't Hooft, "Symmetry breaking through Bell-Jackiw anomalies", *Phys. Rev. Lett.* **37** (1976) 8, doi:10.1103/PhysRevLett.37.8.
- [2] A. D. Sakharov, "Violation of CP Invariance, C asymmetry, and baryon asymmetry of the universe", *Pisma Zh. Eksp. Teor. Fiz.* **5** (1967) 32, doi:10.1070/PU1991v034n05ABEH002497.
- [3] H. Georgi and S. L. Glashow, "Unity of all elementary particle forces", *Phys. Rev. Lett.* **32** (1974) 438, doi:10.1103/PhysRevLett.32.438.
- [4] S. Weinberg, "Supersymmetry at ordinary energies. 1. masses and conservation laws", *Phys. Rev. D* **26** (1982) 287, doi:10.1103/PhysRevD.26.287.
- [5] Super-Kamiokande Collaboration, "Search for proton decay via $p \rightarrow e^+ \pi^0$ and $p \rightarrow \mu^+ \pi^0$ with an enlarged fiducial volume in Super-Kamiokande I-IV", *Phys. Rev. D* **102** (2020) 112011, doi:10.1103/PhysRevD.102.112011, arXiv:2010.16098.

- [6] LHCb Collaboration, “Searches for violation of lepton flavour and baryon number in tau lepton decays at LHCb”, *Phys. Lett. B* **724** (2013) 36, doi:10.1016/j.physletb.2013.05.063, arXiv:1304.4518.
- [7] BESIII Collaboration, “Search for baryon- and lepton-number violating decays $D^0 \rightarrow \bar{p}e^+$ and $D^0 \rightarrow pe^-$ ”, *Phys. Rev. D* **105** (2022) 032006, doi:10.1103/PhysRevD.105.032006, arXiv:2112.10972.
- [8] BaBar Collaboration, “Searches for the baryon- and lepton-number violating decays $B^0 \rightarrow \Lambda_c^+ \ell^-$, $B^- \rightarrow \Lambda \ell^-$, and $B^- \rightarrow \bar{\Lambda} \ell^-$ ”, *Phys. Rev. D* **83** (2011) 091101, doi:10.1103/PhysRevD.83.091101, arXiv:1101.3830.
- [9] W.-S. Hou, M. Nagashima, and A. Soddu, “Baryon number violation involving higher generations”, *Phys. Rev. D* **72** (2005) 095001, doi:10.1103/PhysRevD.72.095001, arXiv:hep-ph/0509006.
- [10] M. E. McCracken et al., “Search for baryon-number and lepton-number violating decays of Λ hyperons using the CLAS detector at Jefferson Laboratory”, *Phys. Rev. D* **92** (2015) 072002, doi:10.1103/PhysRevD.92.072002, arXiv:1507.03859.
- [11] CMS Collaboration, “Search for baryon number violation in top-quark decays”, *Phys. Lett. B* **731** (2014) 173, doi:10.1016/j.physletb.2014.02.033, arXiv:1310.1618.
- [12] Z. Dong et al., “Baryon number violation at the LHC: the top option”, *Phys. Rev. D* **85** (2012) 016006, doi:10.1103/PhysRevD.85.016006, arXiv:1107.3805.
- [13] CMS Collaboration, “The CMS experiment at the CERN LHC”, *JINST* **3** (2008) S08004, doi:10.1088/1748-0221/3/08/S08004.
- [14] NNPDF Collaboration, “Parton distributions from high-precision collider data”, *Eur. Phys. J. C* **77** (2017) 663, doi:10.1140/epjc/s10052-017-5199-5, arXiv:1706.00428.
- [15] T. Sjöstrand et al., “An introduction to PYTHIA 8.2”, *Comput. Phys. Commun.* **191** (2015) 159, doi:10.1016/j.cpc.2015.01.024, arXiv:1410.3012.
- [16] CMS Collaboration, “Extraction and validation of a new set of CMS PYTHIA8 tunes from underlying-event measurements”, *Eur. Phys. J. C* **80** (2020) 4, doi:10.1140/epjc/s10052-019-7499-4, arXiv:1903.12179.
- [17] GEANT4 Collaboration, “GEANT4 — a simulation toolkit”, *Nucl. Instrum. Meth. A* **506** (2003) 250, doi:10.1016/S0168-9002(03)01368-8.
- [18] P. Nason, “A new method for combining NLO QCD with shower Monte Carlo algorithms”, *JHEP* **11** (2004) 040, doi:10.1088/1126-6708/2004/11/040, arXiv:0409146.
- [19] S. Alioli, P. Nason, C. Oleari, and E. Re, “A general framework for implementing NLO calculations in shower Monte Carlo programs: the POWHEG BOX”, *JHEP* **06** (2010) 043, doi:10.1007/JHEP06(2010)043, arXiv:1002.2581.
- [20] S. Frixione, P. Nason, and C. Oleari, “Matching NLO QCD computations with parton shower simulations: the POWHEG method”, *JHEP* **11** (2007) 070, doi:10.1088/1126-6708/2007/11/070, arXiv:0709.2092.


-
- [21] J. Alwall et al., “The automated computation of tree-level and next-to-leading order differential cross sections, and their matching to parton shower simulations”, *JHEP* **07** (2014) 079, doi:10.1007/JHEP07(2014)079, arXiv:1405.0301.
- [22] M. Czakon and A. Mitov, “Top++: A program for the calculation of the top-pair cross-section at hadron colliders”, *Comput. Phys. Commun.* **185** (2014) 2930, doi:10.1016/j.cpc.2014.06.021, arXiv:1112.5675.
- [23] M. Czakon et al., “Top-pair production at the LHC through NNLO QCD and NLOEW”, *JHEP* **10** (2017) 186, doi:10.1007/JHEP10(2017)186, arXiv:1705.04105.
- [24] Y. Li and F. Petriello, “Combining QCD and electroweak corrections to dilepton production in FEWZ”, *Phys. Rev. D* **86** (2012) 094034, doi:10.1103/PhysRevD.86.094034, arXiv:1208.5967.
- [25] N. Kidonakis, “Two-loop soft anomalous dimensions for single top quark associated production with W^- or H^- ”, *Phys. Rev. D* **82** (2010) 054018, doi:10.1103/PhysRevD.82.054018, arXiv:1005.4451.
- [26] J. M. Campbell, R. K. Ellis, and C. Williams, “Vector boson pair production at the LHC”, *JHEP* **07** (2011) 018, doi:10.1007/JHEP07(2011)018, arXiv:1105.0020.
- [27] F. Maltoni, D. Pagani, and I. Tsinikos, “Associated production of a top-quark pair with vector bosons at NLO in QCD: impact on $t\bar{t}H$ searches at the LHC”, *JHEP* **02** (2016) 113, doi:10.1007/JHEP02(2016)113, arXiv:1507.05640.
- [28] CMS Collaboration, “Measurement of the $t\bar{t}$ production cross section, the top quark mass, and the strong coupling constant using dilepton events in pp collisions at $\sqrt{s} = 13$ TeV”, *Eur. Phys. J. C* **79** (2019) 368, doi:10.1140/epjc/s10052-019-6863-8, arXiv:1812.10505.
- [29] CMS Collaboration, “The CMS trigger system”, *JINST* **12** (2017) P01020, doi:10.1088/1748-0221/12/01/P01020, arXiv:1609.02366.
- [30] CMS Collaboration, “Search for resonant and nonresonant new phenomena in high-mass dilepton final states at $\sqrt{s} = 13$ TeV”, *JHEP* **07** (2021) 208, doi:10.1007/JHEP07(2021)208, arXiv:2103.02708.
- [31] CMS Collaboration, “Particle-flow reconstruction and global event description with the CMS detector”, *JINST* **12** (2017) P10003, doi:10.1088/1748-0221/12/10/P10003, arXiv:1706.04965.
- [32] CMS Collaboration, “Technical proposal for the Phase-II upgrade of the Compact Muon Solenoid”, CMS Technical Proposal CERN-LHCC-2015-010, CMS-TDR-15-02, 2015.
- [33] CMS Collaboration, “Performance of electron reconstruction and selection with the CMS detector in proton-proton collisions at $\sqrt{s} = 8$ TeV”, *JINST* **10** (2015) P06005, doi:10.1088/1748-0221/10/06/P06005, arXiv:1502.02701.
- [34] CMS Collaboration, “Performance of the CMS muon detector and muon reconstruction with proton-proton collisions at $\sqrt{s} = 13$ TeV”, *JINST* **13** (2018) P06015, doi:10.1088/1748-0221/13/06/P06015, arXiv:1804.04528.
- [35] M. Cacciari, G. P. Salam, and G. Soyez, “The anti- k_T jet clustering algorithm”, *JHEP* **04** (2008) 063, doi:10.1088/1126-6708/2008/04/063, arXiv:0802.1189.

- [36] M. Cacciari, G. P. Salam, and G. Soyez, “FastJet user manual”, *Eur. Phys. J. C* **72** (2012) 1896, doi:10.1140/epjc/s10052-012-1896-2, arXiv:1111.6097.
- [37] CMS Collaboration, “Identification of heavy-flavour jets with the CMS detector in pp collisions at 13 TeV”, *JINST* **13** (2018) P05011, doi:10.1088/1748-0221/13/05/P05011, arXiv:1712.07158.
- [38] CMS Collaboration, “Performance of missing transverse momentum reconstruction in proton-proton collisions at $\sqrt{s} = 13$ TeV using the CMS detector”, *JINST* **14** (2019) P07004, doi:10.1088/1748-0221/14/07/P07004, arXiv:1903.06078.
- [39] CMS Collaboration, “Cross section measurement of t -channel single top quark production in pp collisions at $\sqrt{s} = 13$ TeV”, *Phys. Lett. B* **772** (2017) 752, doi:10.1016/j.physletb.2017.07.047, arXiv:1610.00678.
- [40] H. Voss, A. Höcker, J. Stelzer, and F. Tegenfeldt, “TMVA, the toolkit for multivariate data analysis with ROOT”, in *XIth International Workshop on Advanced Computing and Analysis Techniques in Physics Research (ACAT)*, p. 40. 2007. arXiv:physics/0703039. [PoS(ACAT)040]. doi:10.22323/1.050.0040.
- [41] J. R. Quinlan, “Simplifying decision trees”, *Int. J. Man-Mach. Stud.* **27** (1987) 221, doi:10.1016/S0020-7373(87)80053-6.
- [42] CMS Collaboration, “Measurement of the top quark pair production cross section in proton-proton collisions at $\sqrt{s} = 13$ TeV”, *Phys. Rev. Lett.* **116** (2016) 052002, doi:10.1103/PhysRevLett.116.052002, arXiv:1510.05302.
- [43] CMS Collaboration, “Search for charged-lepton flavor violation in top quark production and decay in pp collisions at $\sqrt{s} = 13$ TeV”, *JHEP* **06** (2022) 082, doi:10.1007/JHEP06(2022)082, arXiv:2201.07859.
- [44] CMS Collaboration, “Precision luminosity measurement in proton-proton collisions at $\sqrt{s} = 13$ TeV in 2015 and 2016 at CMS”, *Eur. Phys. J. C* **81** (2021) 800, doi:10.1140/epjc/s10052-021-09538-2, arXiv:2104.01927.
- [45] CMS Collaboration, “CMS luminosity measurement for the 2017 data-taking period at $\sqrt{s} = 13$ TeV”, CMS Physics Analysis Summary CMS-PAS-LUM-17-004, 2017.
- [46] CMS Collaboration, “CMS luminosity measurement for the 2018 data-taking period at $\sqrt{s} = 13$ TeV”, CMS Physics Analysis Summary CMS-PAS-LUM-18-002, 2018.
- [47] CMS Collaboration, “Measurement of the inelastic proton-proton cross section at $\sqrt{s} = 13$ TeV”, *JHEP* **07** (2018) 161, doi:10.1007/JHEP07(2018)161, arXiv:1802.02613.
- [48] CMS Collaboration, “Performance of CMS muon reconstruction in pp collision events at $\sqrt{s} = 7$ TeV”, *JINST* **7** (2012) P10002, doi:10.1088/1748-0221/7/10/P10002, arXiv:1206.4071.
- [49] CMS Collaboration, “Performance summary of AK4 jet b tagging with data from proton-proton collisions at 13 TeV with the CMS detector”, CMS Detector Performance Note CMS-DP-2023-005, 2023.
- [50] CMS Collaboration, “Jet energy scale and resolution in the CMS experiment in pp collisions at 8 TeV”, *JINST* **12** (2017) P02014, doi:10.1088/1748-0221/12/02/P02014, arXiv:1607.03663.









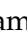


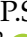


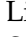
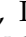


- [51] CMS Collaboration, “Measurements of $t\bar{t}$ differential cross sections in proton-proton collisions at $\sqrt{s} = 13$ TeV using events containing two leptons”, *JHEP* **02** (2019) 149, doi:10.1007/JHEP02(2019)149, arXiv:1811.06625.
- [52] CMS Collaboration, “Measurement of the production cross section for single top quarks in association with W bosons in proton-proton collisions at $\sqrt{s} = 13$ TeV”, *JHEP* **10** (2018) 117, doi:10.1007/JHEP10(2018)117, arXiv:1805.07399.
- [53] A. L. Read, “Presentation of search results: The CL_s technique”, *J. Phys. G* **28** (2002) 2693, doi:10.1088/0954-3899/28/10/313.
- [54] HEPData record for this analysis, 2023. doi:10.17182/hepdata.138414.

A The CMS Collaboration




Yerevan Physics Institute, Yerevan, Armenia

A. Hayrapetyan, A. Tumasyan¹ 


Institut für Hochenergiephysik, Vienna, Austria

W. Adam , J.W. Andrejkovic, T. Bergauer , S. Chatterjee , K. Damanakis , M. Dragicevic , P.S. Hussain , M. Jeitler² , N. Krammer , A. Li , D. Liko , I. Mikulec , J. Schieck² , R. Schöfbeck , D. Schwarz , M. Sonawane , S. Templ , W. Waltenberger , C.-E. Wulz² 














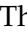
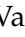

Universiteit Antwerpen, Antwerpen, Belgium

M.R. Darwish³ , T. Janssen , P. Van Mechelen 











Vrije Universiteit Brussel, Brussel, Belgium

E.S. Bols , J. D'Hondt , S. Dansana , A. De Moor , M. Delcourt , S. Lowette , I. Makarenko , D. Müller , S. Tavernier , M. Tytgat⁴ , G.P. Van Onsem , S. Van Putte , D. Vannerom 










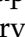
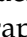
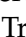
Université Libre de Bruxelles, Bruxelles, Belgium

B. Clerbaux , A.K. Das, G. De Lentdecker , H. Evard , L. Favart , P. Gianneios , D. Hohov , J. Jaramillo , A. Khalilzadeh, F.A. Khan , K. Lee , M. Mahdavihorrani , A. Malara , S. Paredes , L. Thomas , M. Vanden Bemden , C. Vander Velde , P. Vanlaer 







Ghent University, Ghent, Belgium

M. De Coen , D. Dobur , Y. Hong , J. Knolle , L. Lambrecht , G. Mestdach, K. Mota Amarilo , C. Rendón, A. Samalan, K. Skovpen , N. Van Den Bossche , J. van der Linden , L. Wezenbeek 





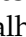
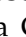












Université Catholique de Louvain, Louvain-la-Neuve, Belgium

A. Benecke , A. Bethani , G. Bruno , C. Caputo , C. Delaere , I.S. Donertas , A. Giammanco , Sa. Jain , V. Lemaitre, J. Lidrych , P. Mastrapasqua , T.T. Tran , S. Wertz 

Centro Brasileiro de Pesquisas Físicas, Rio de Janeiro, Brazil

G.A. Alves , E. Coelho , C. Hensel , T. Menezes De Oliveira , A. Moraes , P. Rebello Teles , M. Soeiro

Universidade do Estado do Rio de Janeiro, Rio de Janeiro, Brazil





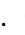

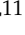

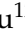
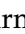
















W.L. Aldá Júnior , M. Alves Gallo Pereira , M. Barroso Ferreira Filho , H. Brandao Malbouisson , W. Carvalho , J. Chinellato⁵, E.M. Da Costa , G.G. Da Silveira⁶ , D. De Jesus Damiao , S. Fonseca De Souza , R. Gomes De Souza, J. Martins⁷ , C. Mora Herrera , L. Mundim , H. Nogima , J.P. Pinheiro , A. Santoro , A. Sznajder , M. Thiel , A. Vilela Pereira 














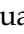



















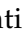







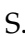




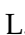








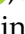
















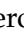












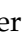




Universidade Estadual Paulista, Universidade Federal do ABC, São Paulo, Brazil

C.A. Bernardes⁶ , L. Calligaris , T.R. Fernandez Perez Tomei , E.M. Gregores , P.G. Mercadante , S.F. Novaes , B. Orzari , Sandra S. Padula 

Institute for Nuclear Research and Nuclear Energy, Bulgarian Academy of Sciences, Sofia, Bulgaria

A. Aleksandrov , G. Antchev , R. Hadjiiska , P. Iaydjiev , M. Misheva , M. Shopova , G. Sultanov 

University of Sofia, Sofia, BulgariaA. Dimitrov , L. Litov , B. Pavlov , P. Petkov , A. Petrov , E. Shumka **Instituto De Alta Investigación, Universidad de Tarapacá, Casilla 7 D, Arica, Chile**S. Keshri , S. Thakur **Beihang University, Beijing, China**T. Cheng , T. Javaid , L. Yuan **Department of Physics, Tsinghua University, Beijing, China**Z. Hu , J. Liu, K. Yi^{8,9} **Institute of High Energy Physics, Beijing, China**G.M. Chen¹⁰ , H.S. Chen¹⁰ , M. Chen¹⁰ , F. Iemmi , C.H. Jiang, A. Kapoor¹¹ , H. Liao , Z.-A. Liu¹² , R. Sharma¹³ , J.N. Song¹², J. Tao , C. Wang¹⁰, J. Wang , Z. Wang¹⁰, H. Zhang **State Key Laboratory of Nuclear Physics and Technology, Peking University, Beijing, China**A. Agapitos , Y. Ban , A. Levin , C. Li , Q. Li , Y. Mao, S.J. Qian , X. Sun , D. Wang , H. Yang, L. Zhang , C. Zhou **Sun Yat-Sen University, Guangzhou, China**Z. You **University of Science and Technology of China, Hefei, China**K. Jaffel , N. Lu **Nanjing Normal University, Nanjing, China**G. Bauer¹⁴**Institute of Modern Physics and Key Laboratory of Nuclear Physics and Ion-beam Application (MOE) - Fudan University, Shanghai, China**X. Gao¹⁵ **Zhejiang University, Hangzhou, Zhejiang, China**Z. Lin , C. Lu , M. Xiao **Universidad de Los Andes, Bogota, Colombia**C. Avila , D.A. Barbosa Trujillo, A. Cabrera , C. Florez , J. Fraga , J.A. Reyes Vega**Universidad de Antioquia, Medellin, Colombia**J. Mejia Guisao , F. Ramirez , M. Rodriguez , J.D. Ruiz Alvarez **University of Split, Faculty of Electrical Engineering, Mechanical Engineering and Naval Architecture, Split, Croatia**D. Giljanovic , N. Godinovic , D. Lelas , A. Sculac **University of Split, Faculty of Science, Split, Croatia**M. Kovac , T. Sculac **Institute Rudjer Boskovic, Zagreb, Croatia**P. Bargassa , V. Brigljevic , B.K. Chitroda , D. Ferencek , K. Jakovcic, S. Mishra , A. Starodumov¹⁶ , T. Susa **University of Cyprus, Nicosia, Cyprus**A. Attikis , K. Christoforou , A. Hadjiagapiou, S. Konstantinou , J. Mousa , C. Nicolaou, F. Ptochos , P.A. Razis , H. Rykaczewski, H. Saka , A. Stepennov 


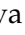




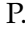





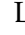
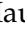


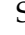





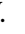






Charles University, Prague, Czech RepublicM. Finger , M. Finger Jr. , A. Kveton **Escuela Politecnica Nacional, Quito, Ecuador**E. Ayala **Universidad San Francisco de Quito, Quito, Ecuador**E. Carrera Jarrin **Academy of Scientific Research and Technology of the Arab Republic of Egypt, Egyptian Network of High Energy Physics, Cairo, Egypt**S. Elgammal¹⁷, A. Ellithi Kamel¹⁸**Center for High Energy Physics (CHEP-FU), Fayoum University, El-Fayoum, Egypt**A. Lotfy , M.A. Mahmoud **National Institute of Chemical Physics and Biophysics, Tallinn, Estonia**K. Ehataht , M. Kadastik, T. Lange , S. Nandan , C. Nielsen , J. Pata , M. Raidal , L. Tani , C. Veelken **Department of Physics, University of Helsinki, Helsinki, Finland**H. Kirschenmann , K. Osterberg , M. Voutilainen **Helsinki Institute of Physics, Helsinki, Finland**S. Bharthuar , E. Brücken , F. Garcia , K.T.S. Kallonen , R. Kinnunen, T. Lampén , K. Lassila-Perini , S. Lehti , T. Lindén , L. Martikainen , M. Myllymäki , M.m. Rantanen , H. Siikonen , E. Tuominen , J. Tuominiemi **Lappeenranta-Lahti University of Technology, Lappeenranta, Finland**P. Luukka , H. Petrow **IRFU, CEA, Université Paris-Saclay, Gif-sur-Yvette, France**M. Besancon , F. Couderc , M. Dejardin , D. Denegri, J.L. Faure, F. Ferri , S. Ganjour , P. Gras , G. Hamel de Monchenault , V. Lohezic , J. Malcles , J. Rander, A. Rosowsky , M.Ö. Sahin , A. Savoy-Navarro¹⁹ , P. Simkina , M. Titov , M. Tornago **Laboratoire Leprince-Ringuet, CNRS/IN2P3, Ecole Polytechnique, Institut Polytechnique de Paris, Palaiseau, France**F. Beaudette , A. Buchot Perraguin , P. Busson , A. Cappati , C. Charlot , M. Chiusi , F. Damas , O. Davignon , A. De Wit , I.T. Ehle , B.A. Fontana Santos Alves , S. Ghosh , A. Gilbert , R. Granier de Cassagnac , A. Hakimi , B. Harikrishnan , L. Kalipoliti , G. Liu , J. Motta , M. Nguyen , C. Ochando , L. Portales , R. Salerno , J.B. Sauvan , Y. Sirois , A. Tarabini , E. Vernazza , A. Zabi , A. Zghiche **Université de Strasbourg, CNRS, IPHC UMR 7178, Strasbourg, France**J.-L. Agram²⁰ , J. Andrea , D. Apparú , D. Bloch , J.-M. Brom , E.C. Chabert , C. Collard , S. Falke , U. Goerlach , C. Grimault, R. Haeberle , A.-C. Le Bihan , M. Meena , G. Saha , M.A. Sessini , P. Van Hove **Institut de Physique des 2 Infinis de Lyon (IP2I), Villeurbanne, France**S. Beauceron , B. Blancon , G. Boudoul , N. Chanon , J. Choi , D. Contardo , P. Depasse , C. Dozen²¹ , H. El Mamouni, J. Fay , S. Gascon , M. Gouzevitch , C. Greenberg, G. Grenier , B. Ille , I.B. Laktineh, M. Lethuillier , L. Mirabito, S. Perries, A. Purohit , M. Vander Donckt , P. Verdier , J. Xiao **Georgian Technical University, Tbilisi, Georgia**

G. Adamov, I. Lomidze , Z. Tsamalaidze¹⁶ 

RWTH Aachen University, I. Physikalisches Institut, Aachen, Germany

V. Botta , L. Feld , K. Klein , M. Lipinski , D. Meuser , A. Pauls , N. Röwert ,
M. Teroerde 

RWTH Aachen University, III. Physikalisches Institut A, Aachen, Germany

S. Diekmann , A. Dodonova , N. Eich , D. Eliseev , F. Engelke , J. Erdmann,
M. Erdmann , P. Fackeldey , B. Fischer , T. Hebbeker , K. Hoepfner , F. Ivone ,
A. Jung , M.y. Lee , F. Mausolf , M. Merschmeyer , A. Meyer , S. Mukherjee ,
D. Noll , F. Nowotny, A. Pozdnyakov , Y. Rath, W. Redjeb , F. Rehm, H. Reithler ,
U. Sarkar , V. Sarkisovi , A. Schmidt , A. Sharma , J.L. Spah , A. Stein ,
F. Torres Da Silva De Araujo²² , S. Wiedenbeck , S. Zaleski



























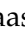







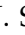
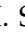



RWTH Aachen University, III. Physikalisches Institut B, Aachen, Germany

C. Dziwok , G. Flügge , W. Haj Ahmad²³ , T. Kress , A. Nowack , O. Pooth ,
A. Stahl , T. Ziemons , A. Zotz 



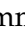


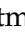


















Deutsches Elektronen-Synchrotron, Hamburg, Germany

H. Aarup Petersen , M. Aldaya Martin , J. Alimena , S. Amoroso, Y. An , S. Baxter ,
M. Bayatmakou , H. Becerril Gonzalez , O. Behnke , A. Belvedere , S. Bhattacharya ,
F. Blekman²⁴ , K. Borras²⁵ , A. Campbell , A. Cardini , C. Cheng, F. Colombina ,
S. Consuegra Rodríguez , G. Correia Silva , M. De Silva , G. Eckerlin, D. Eckstein ,
L.I. Estevez Banos , O. Filatov , E. Gallo²⁴ , A. Geiser , A. Giraldi , V. Guglielmi ,
M. Guthoff , A. Hinzmann , A. Jafari²⁶ , L. Jeppe , N.Z. Jomhari , B. Kaech ,
M. Kasemann , C. Kleinwort , R. Kogler , M. Komm , D. Krücker , W. Lange,
D. Leyva Pernia , K. Lipka²⁷ , W. Lohmann²⁸ , R. Mankel , I.-A. Melzer-Pellmann ,
M. Mendizabal Morentin , A.B. Meyer , G. Milella , A. Mussgiller , L.P. Nair ,
A. Nürnberg , Y. Otariid, J. Park , D. Pérez Adán , E. Ranken , A. Raspereza ,
B. Ribeiro Lopes , J. Rübenach, A. Saggio , M. Scham^{29,25} , S. Schnake²⁵ , P. Schütze ,
C. Schwanenberger²⁴ , D. Selivanova , K. Sharko , M. Shchedrolosiev , R.E. Sosa Ri-
cardo , D. Stafford, F. Vazzoler , A. Ventura Barroso , R. Walsh , Q. Wang , Y. Wen ,
K. Wichmann, L. Wiens²⁵ , C. Wissing , Y. Yang , A. Zimmermann Castro Santos 

University of Hamburg, Hamburg, Germany

A. Albrecht , S. Albrecht , M. Antonello , S. Bein , L. Benato , S. Bollweg,
M. Bonanomi , P. Connor , K. El Morabit , Y. Fischer , E. Garutti , A. Grohsjean ,
J. Haller , H.R. Jabusch , G. Kasieczka , P. Keicher, R. Klanner , W. Korcari ,
T. Kramer , V. Kutzner , F. Labe , J. Lange , A. Lobanov , C. Matthies , A. Mehta ,
L. Moureaux , M. Mrowietz, A. Nigamova , Y. Nissan, A. Paasch , K.J. Pena Rodriguez ,
T. Quadfasel , B. Raciti , M. Rieger , D. Savoii , J. Schindler , P. Schleper ,
M. Schröder , J. Schwandt , M. Sommerhalder , H. Stadie , G. Steinbrück , A. Tews,
M. Wolf 

Karlsruher Institut fuer Technologie, Karlsruhe, Germany

S. Brommer , M. Burkart, E. Butz , T. Chwalek , A. Dierlamm , A. Droll, N. Fal-
termann , M. Giffels , A. Gottmann , F. Hartmann³⁰ , R. Hofsaess , M. Horzela ,
U. Husemann , J. Kieseler , M. Klute , R. Koppenhöfer , J.M. Lawhorn , M. Link,
A. Lintuluoto , B. Maier , S. Maier , S. Mitra , M. Mormile , Th. Müller , M. Neukum,
M. Oh , E. Pfeffer , M. Presilla , G. Quast , K. Rabbertz , B. Regnery , N. Shadskiy ,
I. Shvetsov , H.J. Simonis , M. Toms , N. Trevisani , R.F. Von Cube , M. Wassmer ,
S. Wieland , F. Wittig, R. Wolf , X. Zuo 

Institute of Nuclear and Particle Physics (INPP), NCSR Demokritos, Aghia Paraskevi, Greece

G. Anagnostou, G. Daskalakis , A. Kyriakis, A. Papadopoulos³⁰, A. Stakia 

National and Kapodistrian University of Athens, Athens, Greece

P. Kontaxakis , G. Melachroinos, Z. Painesis , A. Panagiotou, I. Papavergou , I. Paraskevas , N. Saoulidou , K. Theofilatos , E. Tziaferi , K. Vellidis , I. Zisopoulos 

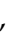



National Technical University of Athens, Athens, Greece

G. Bakas , T. Chatzistavrou, G. Karapostoli , K. Kousouris , I. Papakrivopoulos , E. Siamarkou, G. Tsipolitis, A. Zacharopoulou

University of Ioánnina, Ioánnina, Greece

K. Adamidis, I. Bestintzanos, I. Evangelou , C. Foudas, C. Kamtsikis, P. Katsoulis, P. Kokkas , P.G. Kosmoglou Kioseoglou , N. Manthos , I. Papadopoulos , J. Strologas 


HUN-REN Wigner Research Centre for Physics, Budapest, Hungary

M. Bartók³¹ , C. Hajdu , D. Horvath^{32,33} , K. Márton, A.J. Rádli³⁴ , F. Sikler , V. Veszpremi 

MTA-ELTE Lendület CMS Particle and Nuclear Physics Group, Eötvös Loránd University, Budapest, Hungary

M. Csanád , K. Farkas , M.M.A. Gadallah³⁵ , Á. Kadlecik , P. Major , K. Mandal , G. Pásztor , G.I. Veres 




Faculty of Informatics, University of Debrecen, Debrecen, Hungary

P. Raics, B. Ujvari , G. Zilizi 















Institute of Nuclear Research ATOMKI, Debrecen, Hungary

G. Bencze, S. Czellar, J. Molnar, Z. Szillasi

Karoly Robert Campus, MATE Institute of Technology, Gyongyos, Hungary

T. Csorgo³⁶ , F. Nemes³⁶ , T. Novak 

Panjab University, Chandigarh, India

J. Babbar , S. Bansal , S.B. Beri, V. Bhatnagar , G. Chaudhary , S. Chauhan , N. Dhingra³⁷ , A. Kaur , A. Kaur , H. Kaur , M. Kaur , S. Kumar , K. Sandeep , T. Sheokand, J.B. Singh , A. Singla 














University of Delhi, Delhi, India

A. Ahmed , A. Bhardwaj , A. Chhetri , B.C. Choudhary , A. Kumar , A. Kumar , M. Naimuddin , K. Ranjan , S. Saumya 



Saha Institute of Nuclear Physics, HBNI, Kolkata, India

S. Baradia , S. Barman³⁸ , S. Bhattacharya , S. Dutta , S. Dutta, S. Sarkar

Indian Institute of Technology Madras, Madras, India


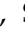





M.M. Ameen , P.K. Behera , S.C. Behera , S. Chatterjee , P. Jana , P. Kalbhor , J.R. Komaragiri³⁹ , D. Kumar³⁹ , P.R. Pujahari , N.R. Saha , A. Sharma , A.K. Sikdar , S. Verma 

Tata Institute of Fundamental Research-A, Mumbai, India



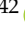








S. Dugad, M. Kumar , G.B. Mohanty , P. Suryadevara

Tata Institute of Fundamental Research-B, Mumbai, India




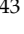




A. Bala , S. Banerjee , R.M. Chatterjee, R.K. Dewanjee⁴⁰ , M. Guchait , Sh. Jain 

A. Jaiswal , S. Karmakar , S. Kumar , G. Majumder , K. Mazumdar , S. Parolia ,
A. Thachayath 

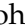
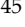

National Institute of Science Education and Research, An OCC of Homi Bhabha National Institute, Bhubaneswar, Odisha, India

S. Bahinipati⁴¹ , C. Kar , D. Maity⁴² , P. Mal , T. Mishra , V.K. Muraleedharan Nair Bindhu⁴² , K. Naskar⁴² , A. Nayak⁴² , P. Sadangi, S.K. Swain , S. Varghese⁴² ,
D. Vats⁴² 





Indian Institute of Science Education and Research (IISER), Pune, India

S. Acharya⁴³ , A. Alpana , S. Dube , B. Gomber⁴³ , B. Kansal , A. Laha , B. Sahu⁴³ ,
S. Sharma , K.Y. Vaish


Isfahan University of Technology, Isfahan, Iran

H. Bakhshiansohi⁴⁴ , E. Khazaie⁴⁵ , M. Zeinali⁴⁶ 











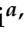
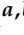



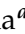
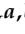
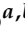


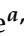




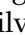

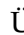




Institute for Research in Fundamental Sciences (IPM), Tehran, Iran

S. Chenarani⁴⁷ , S.M. Etesami , M. Khakzad , M. Mohammadi Najafabadi 

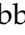
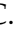


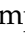






















University College Dublin, Dublin, Ireland

M. Grunewald 


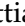



INFN Sezione di Bari^a, Università di Bari^b, Politecnico di Bari^c, Bari, Italy

M. Abbrescia^{a,b} , R. Aly^{a,c,48} , A. Colaleo^{a,b} , D. Creanza^{a,c} , B. D'Anzi^{a,b} ,
N. De Filippis^{a,c} , M. De Palma^{a,b} , A. Di Florio^{a,c} , W. Elmetenawee^{a,b,48} ,
L. Fiore^a , G. Iaselli^{a,c} , M. Louka^{a,b} , G. Maggi^{a,c} , M. Maggi^a , I. Margjeka^{a,b} ,
V. Mastrapasqua^{a,b} , S. My^{a,b} , S. Nuzzo^{a,b} , A. Pellecchia^{a,b} , A. Pompili^{a,b} ,
G. Pugliese^{a,c} , R. Radogna^a , G. Ramirez-Sanchez^{a,c} , D. Ramos^a , A. Ranieri^a ,
L. Silvestris^a , F.M. Simone^{a,b} , Ü. Sözbilir^a , A. Stamerra^a , R. Venditti^a ,
P. Verwilligen^a , A. Zaza^{a,b} 

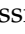







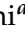


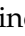

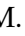



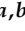

INFN Sezione di Bologna^a, Università di Bologna^b, Bologna, Italy

G. Abbiendi^a , C. Battilana^{a,b} , L. Borgonovi^a , R. Campanini^{a,b} , P. Capiluppi^{a,b} ,
A. Castro^{a,b} , F.R. Cavallo^a , M. Cuffiani^{a,b} , G.M. Dallavalle^a , T. Diotallevi^{a,b} ,
F. Fabbri^a , A. Fanfani^{a,b} , D. Fasanella^{a,b} , P. Giacomelli^a , L. Giommi^{a,b} ,
C. Grandi^a , L. Guiducci^{a,b} , S. Lo Meo^{a,49} , L. Lunerti^{a,b} , S. Marcellini^a ,
G. Masetti^a , F.L. Navarria^{a,b} , A. Perrotta^a , F. Primavera^{a,b} , A.M. Rossi^{a,b} ,
T. Rovelli^{a,b} , G.P. Siroli^{a,b} 

INFN Sezione di Catania^a, Università di Catania^b, Catania, Italy

S. Costa^{a,b,50} , A. Di Mattia^a , R. Potenza^{a,b} , A. Tricomi^{a,b,50} , C. Tuve^{a,b} 

INFN Sezione di Firenze^a, Università di Firenze^b, Firenze, Italy

P. Assiouras^a , G. Barbagli^a , G. Bardelli^{a,b} , B. Camaiani^{a,b} , A. Cassese^a ,
R. Ceccarelli^a , V. Ciulli^{a,b} , C. Civinini^a , R. D'Alessandro^{a,b} , E. Focardi^{a,b} ,
T. Kello^a , G. Latino^{a,b} , P. Lenzi^{a,b} , M. Lizzo^a , M. Meschini^a , S. Paoletti^a ,
A. Papanastassiou^{a,b} , G. Sguazzoni^a , L. Viliani^a 





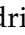

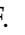





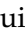



INFN Laboratori Nazionali di Frascati, Frascati, Italy

L. Benussi , S. Bianco , S. Meola⁵¹ , D. Piccolo 

INFN Sezione di Genova^a, Università di Genova^b, Genova, Italy

P. Chatagnon^a , F. Ferro^a , E. Robutti^a , S. Tosi^{a,b} 









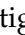

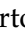
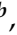

INFN Sezione di Milano-Bicocca^a, Università di Milano-Bicocca^b, Milano, Italy

A. Benaglia^a , G. Boldrini^{a,b} , F. Brivio^a , F. Cetorelli^a , F. De Guio^{a,b} , M.E. Dinardo^{a,b} , P. Dini^a , S. Gennai^a , R. Gerosa^{a,b} , A. Ghezzi^{a,b} , P. Govoni^{a,b} , L. Guzzi^a , M.T. Lucchini^{a,b} , M. Malberti^a , S. Malvezzi^a , A. Massironi^a , D. Menasce^a , L. Moroni^a , M. Paganoni^{a,b} , D. Pedrini^a , B.S. Pinolini^a , S. Ragazzi^{a,b} , T. Tabarelli de Fatis^{a,b} , D. Zuolo^a












INFN Sezione di Napoli^a, Università di Napoli 'Federico II'^b, Napoli, Italy; Università della Basilicata^c, Potenza, Italy; Scuola Superiore Meridionale (SSM)^d, Napoli, Italy

S. Buontempo^a , A. Cagnotta^{a,b} , F. Carnevali^{a,b} , N. Cavallo^{a,c} , F. Fabozzi^{a,c} , A.O.M. Iorio^{a,b} , L. Lista^{a,b,52} , P. Paolucci^{a,30} , B. Rossi^a , C. Sciacca^{a,b} 


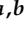

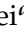
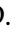


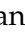





INFN Sezione di Padova^a, Università di Padova^b, Padova, Italy; Università di Trento^c, Trento, Italy

R. Ardino^a , P. Azzi^a , N. Bacchetta^{a,53} , D. Bisello^{a,b} , P. Bortignon^a , G. Bortolato^{a,b} , A. Bragagnolo^{a,b} , R. Carlin^{a,b} , P. Checchia^a , T. Dorigo^a , F. Gasparini^{a,b} , U. Gasparini^{a,b} , E. Lusiani^a , M. Margoni^{a,b} , F. Marini^a , G. Maron^{a,54} , M. Michelotto^a , M. Migliorini^{a,b} , J. Pazzini^{a,b} , P. Ronchese^{a,b} , R. Rossin^{a,b} , F. Simonetto^{a,b} , G. Strong^a , M. Tosi^{a,b} , A. Triossi^{a,b} , S. Ventura^a , H. Yarar^{a,b} , M. Zanetti^{a,b} , P. Zotto^{a,b} , A. Zucchetta^{a,b}

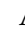
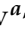

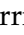



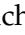

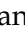



INFN Sezione di Pavia^a, Università di Pavia^b, Pavia, Italy

S. Abu Zeid^{a,55} , C. Aimè^{a,b} , A. Braghieri^a , S. Calzaferri^a , D. Fiorina^a , P. Montagna^{a,b} , V. Re^a , C. Riccardi^{a,b} , P. Salvini^a , I. Vai^{a,b} , P. Vitulo^{a,b} 



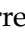

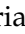
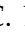


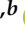




INFN Sezione di Perugia^a, Università di Perugia^b, Perugia, Italy

S. Ajmal^{a,b} , G.M. Bilei^a , D. Ciangottini^{a,b} , L. Fanò^{a,b} , M. Magherini^{a,b} , G. Mantovani^{a,b} , V. Mariani^{a,b} , M. Menichelli^a , F. Moscatelli^{a,56} , A. Rossi^{a,b} , A. Santocchia^{a,b} , D. Spiga^a , T. Tedeschi^{a,b} 

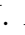
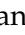
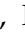

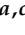








INFN Sezione di Pisa^a, Università di Pisa^b, Scuola Normale Superiore di Pisa^c, Pisa, Italy; Università di Siena^d, Siena, Italy






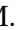



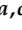


P. Asenov^{a,b} , P. Azzurri^a , G. Bagliesi^a , R. Bhattacharya^a , L. Bianchini^{a,b} , T. Boccali^a , E. Bossini^a , D. Bruschini^{a,c} , R. Castaldi^a , M.A. Ciocci^{a,b} , M. Cipriani^{a,b} , V. D'Amante^{a,d} , R. Dell'Orso^a , S. Donato^a , A. Giassi^a , F. Ligabue^{a,c} , D. Matos Figueiredo^a , A. Messineo^{a,b} , M. Musich^{a,b} , F. Palla^a , A. Rizzi^{a,b} , G. Rolandi^{a,c} , S. Roy Chowdhury^a , T. Sarkar^a , A. Scribano^a , P. Spagnolo^a , R. Tenchini^a , G. Tonelli^{a,b} , N. Turini^{a,d} , F. Vaselli^{a,c} , A. Venturi^a , P.G. Verdini^a

INFN Sezione di Roma^a, Sapienza Università di Roma^b, Roma, Italy





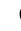
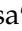
C. Baldenegro Barrera^{a,b} , P. Barria^a , C. Basile^{a,b} , M. Campana^{a,b} , F. Cavallari^a , L. Cunqueiro Mendez^{a,b} , D. Del Re^{a,b} , E. Di Marco^a , M. Diemoz^a , F. Errico^{a,b} , E. Longo^{a,b} , P. Meridiani^a , J. Mijuskovic^{a,b} , G. Organtini^{a,b} , F. Pandolfi^a , R. Paramatti^{a,b} , C. Quaranta^{a,b} , S. Rahatlou^{a,b} , C. Rovelli^a , F. Santanastasio^{a,b} , L. Soffi^a

INFN Sezione di Torino^a, Università di Torino^b, Torino, Italy; Università del Piemonte Orientale^c, Novara, Italy

N. Amapane^{a,b} , R. Arcidiacono^{a,c} , S. Argiro^{a,b} , M. Arneodo^{a,c} , N. Bartosik^a , R. Bellan^{a,b} , A. Bellora^{a,b} , C. Biino^a , C. Borca^{a,b} , N. Cartiglia^a , M. Costa^{a,b} , R. Covarelli^{a,b} , N. Demaria^a , L. Finco^a , M. Grippo^{a,b} , B. Kiani^{a,b} , F. Legger^a , F. Luongo^{a,b} , C. Mariotti^a , L. Markovic^{a,b} , S. Maselli^a , A. Mecca^{a,b} , E. Migliore^{a,b} , M. Monteno^a , R. Mulargia^a , M.M. Obertino^{a,b} , G. Ortona^a

L. Pacher^{a,b} , N. Pastrone^a , M. Pelliccioni^a , M. Ruspa^{a,c} , F. Siviero^{a,b} , V. Sola^{a,b} , A. Solano^{a,b} , A. Staiano^a , C. Tarricone^{a,b} , D. Trocino^a , G. Umoret^{a,b} , E. Vlasov^{a,b} , R. White^a 

INFN Sezione di Trieste^a, Università di Trieste^b, Trieste, Italy

S. Belforte^a , V. Candelise^{a,b} , M. Casarsa^a , F. Cossutti^a , K. De Leo^a , G. Della Ricca^{a,b} 



Kyungpook National University, Daegu, Korea

S. Dogra , J. Hong , C. Huh , B. Kim , D.H. Kim , J. Kim, H. Lee, S.W. Lee , C.S. Moon , Y.D. Oh , M.S. Ryu , S. Sekmen , Y.C. Yang 

Department of Mathematics and Physics - GWNU, Gangneung, Korea

M.S. Kim 

Chonnam National University, Institute for Universe and Elementary Particles, Kwangju, Korea

G. Bak , P. Gwak , H. Kim , D.H. Moon 

Hanyang University, Seoul, Korea

E. Asilar , D. Kim , T.J. Kim , J.A. Merlin

Korea University, Seoul, Korea

S. Choi , S. Han, B. Hong , K. Lee, K.S. Lee , S. Lee , J. Park, S.K. Park, J. Yoo 











Kyung Hee University, Department of Physics, Seoul, Korea

J. Goh , S. Yang 








Sejong University, Seoul, Korea

H. S. Kim , Y. Kim, S. Lee



Seoul National University, Seoul, Korea

J. Almond, J.H. Bhyun, J. Choi , W. Jun , J. Kim , S. Ko , H. Kwon , H. Lee , J. Lee , J. Lee , B.H. Oh , S.B. Oh , H. Seo , U.K. Yang, I. Yoon 

University of Seoul, Seoul, Korea

W. Jang , D.Y. Kang, Y. Kang , S. Kim , B. Ko, J.S.H. Lee , Y. Lee , I.C. Park , Y. Roh, I.J. Watson 

Yonsei University, Department of Physics, Seoul, Korea

S. Ha , H.D. Yoo 




Sungkyunkwan University, Suwon, Korea

M. Choi , M.R. Kim , H. Lee, Y. Lee , I. Yu 


College of Engineering and Technology, American University of the Middle East (AUM), Dasman, Kuwait

T. Beyrouthy

Riga Technical University, Riga, Latvia

K. Dreimanis , A. Gaile , G. Pikurs, A. Potrebko , M. Seidel 

University of Latvia (LU), Riga, Latvia

N.R. Strautnieks 




Vilnius University, Vilnius, Lithuania

M. Ambrozas , A. Juodagalvis , A. Rinkevicius , G. Tamulaitis 

National Centre for Particle Physics, Universiti Malaya, Kuala Lumpur, Malaysia

N. Bin Norjoharuddeen , I. Yusuff⁵⁷ , Z. Zolkapli

Universidad de Sonora (UNISON), Hermosillo, Mexico

J.F. Benitez , A. Castaneda Hernandez , H.A. Encinas Acosta, L.G. Gallegos Maríñez, M. León Coello , J.A. Murillo Quijada , A. Sehrawat , L. Valencia Palomo 





Centro de Investigacion y de Estudios Avanzados del IPN, Mexico City, Mexico

G. Ayala , H. Castilla-Valdez , H. Crotte Ledesma, E. De La Cruz-Burelo , I. Heredia-De La Cruz⁵⁸ , R. Lopez-Fernandez , C.A. Mondragon Herrera, A. Sánchez Hernández 


Universidad Iberoamericana, Mexico City, Mexico

C. Oropeza Barrera , M. Ramírez García 

Benemerita Universidad Autonoma de Puebla, Puebla, Mexico

I. Bautista , I. Pedraza , H.A. Salazar Ibarguen , C. Uribe Estrada 

University of Montenegro, Podgorica, Montenegro

I. Bubanja, N. Raicevic 

University of Canterbury, Christchurch, New Zealand

P.H. Butler 

National Centre for Physics, Quaid-I-Azam University, Islamabad, Pakistan

A. Ahmad , M.I. Asghar, A. Awais , M.I.M. Awan, H.R. Hoorani , W.A. Khan 







AGH University of Krakow, Faculty of Computer Science, Electronics and Telecommunications, Krakow, Poland

V. Avati, L. Grzanka , M. Malawski 

National Centre for Nuclear Research, Swierk, Poland

H. Bialkowska , M. Bluj , B. Boimska , M. Górski , M. Kazana , M. Szeleper , P. Zalewski 






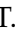





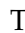

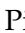


Institute of Experimental Physics, Faculty of Physics, University of Warsaw, Warsaw, Poland

K. Bunkowski , K. Doroba , A. Kalinowski , M. Konecki , J. Krolikowski , A. Muhammad 



Warsaw University of Technology, Warsaw, Poland

K. Pozniak , W. Zabolotny 



Laboratório de Instrumentação e Física Experimental de Partículas, Lisboa, Portugal

M. Araujo , D. Bastos , C. Beirão Da Cruz E Silva , A. Boletti , M. Bozzo , T. Camporesi , G. Da Molin , P. Faccioli , M. Gallinaro , J. Hollar , N. Leonardo , T. Niknejad , A. Petrilli , M. Pisano , J. Seixas , J. Varela , J.W. Wulff







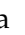




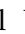
Faculty of Physics, University of Belgrade, Belgrade, Serbia











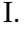
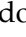




P. Adzic , P. Milenovic 

VINCA Institute of Nuclear Sciences, University of Belgrade, Belgrade, Serbia

M. Dordevic , J. Milosevic , V. Rekovic

Centro de Investigaciones Energéticas Medioambientales y Tecnológicas (CIEMAT), Madrid, Spain









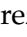
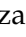




M. Aguilar-Benitez, J. Alcaraz Maestre , Cristina F. Bedoya , Oliver M. Carretero , M. Cepeda , M. Cerrada , N. Colino , B. De La Cruz , A. Delgado Peris , A. Escalante Del Valle , D. Fernández Del Val , J.P. Fernández Ramos , J. Flix 

M.C. Fouz , O. Gonzalez Lopez , S. Goy Lopez , J.M. Hernandez , M.I. Josa , D. Moran , C. M. Morcillo Perez , Á. Navarro Tobar , C. Perez Dengra , A. Pérez-Calero Yzquierdo , J. Puerta Pelayo , I. Redondo , D.D. Redondo Ferrero , L. Romero, S. Sánchez Navas , L. Urda Gómez , J. Vazquez Escobar , C. Willmott








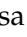


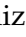





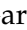

Universidad Autónoma de Madrid, Madrid, Spain

J.F. de Trocóniz 

Universidad de Oviedo, Instituto Universitario de Ciencias y Tecnologías Espaciales de Asturias (ICTEA), Oviedo, Spain

B. Alvarez Gonzalez , J. Cuevas , J. Fernandez Menendez , S. Folgueras , I. Gonzalez Caballero , J.R. González Fernández , P. Leguina , E. Palencia Cortezon , C. Ramón Álvarez , V. Rodríguez Bouza , A. Soto Rodríguez , A. Trapote , C. Vico Villalba , P. Vischia 


Instituto de Física de Cantabria (IFCA), CSIC-Universidad de Cantabria, Santander, Spain

S. Bhowmik , S. Blanco Fernández , J.A. Brochero Cifuentes , I.J. Cabrillo , A. Calderon , J. Duarte Campderros , M. Fernandez , G. Gomez , C. Lasiosa García , C. Martinez Rivero , P. Martinez Ruiz del Arbol , F. Matorras , P. Matorras Cuevas , E. Navarrete Ramos , J. Piedra Gomez , L. Scodellaro , I. Vila , J.M. Vizan Garcia 

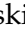
University of Colombo, Colombo, Sri Lanka

M.K. Jayananda , B. Kailasapathy⁵⁹ , D.U.J. Sonnadara , D.D.C. Wickramarathna 








University of Ruhuna, Department of Physics, Matara, Sri Lanka

W.G.D. Dharmaratna⁶⁰ , K. Liyanage , N. Perera , N. Wickramage 

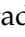

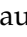
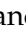









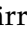







CERN, European Organization for Nuclear Research, Geneva, Switzerland















D. Abbaneo , C. Amendola , E. Auffray , G. Auzinger , J. Baechler, D. Barney , A. Bermúdez Martínez , M. Bianco , B. Bilin , A.A. Bin Anuar , A. Bocci , C. Botta , E. Brondolin , C. Caillol , G. Cerminara , N. Chernyavskaya , D. d'Enterria , A. Dabrowski , A. David , A. De Roeck , M.M. Defranchis , M. Deile , M. Dobson , L. Forthomme , G. Franzoni , W. Funk , S. Giani, D. Gigi, K. Gill , F. Glege , L. Gouskos , M. Haranko , J. Hegeman , B. Huber, V. Innocente , T. James , P. Janot , O. Kaluzinska , S. Laurila , P. Lecoq , E. Leutgeb , C. Lourenço , L. Malgeri , M. Mannelli , A.C. Marini , M. Matthewman, F. Meijers , S. Mersi , E. Meschi , V. Milosevic , F. Monti , F. Moortgat , M. Mulders , I. Neutelings , S. Orfanelli, F. Pantaleo , G. Petrucciani , A. Pfeiffer , M. Pierini , D. Piparo , H. Qu , D. Rabadý , M. Rovere , H. Sakulin , S. Scarfi , C. Schwick, M. Selvaggi , A. Sharma , K. Shchelina , P. Silva , P. Sphicas⁶¹ , A.G. Stahl Leiton , A. Steen , S. Summers , D. Treille , P. Tropea , A. Tsirou, D. Walter , J. Wanczyk⁶² , J. Wang, S. Wuchterl , P. Zehetner , P. Zejdl , W.D. Zeuner

Paul Scherrer Institut, Villigen, Switzerland








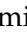
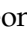
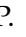
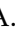




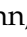
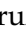


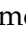

T. Bevilacqua⁶³ , L. Caminada⁶³ , A. Ebrahimi , W. Erdmann , R. Horisberger , Q. Ingram , H.C. Kaestli , D. Kotlinski , C. Lange , M. Missiroli⁶³ , L. Noehte⁶³ , T. Rohe 

ETH Zurich - Institute for Particle Physics and Astrophysics (IPA), Zurich, Switzerland

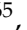
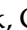


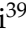


T.K. Aarrestad , K. Androsov⁶² , M. Backhaus , A. Calandri , C. Cazzaniga , K. Datta , A. De Cosa , G. Dissertori , M. Dittmar, M. Donegà , F. Eble , M. Galli , K. Gedia , F. Glessgen , C. Grab , N. Härringer , T.G. Harte, D. Hits , W. Lustermann , A.-M. Lyon , R.A. Manzoni , M. Marchegiani , L. Marchese 

C. Martin Perez , A. Mascellari⁶² , F. Nessi-Tedaldi , F. Pauss , V. Perovic , S. Pigazzini , C. Reissel , T. Reitenspiess , B. Ristic , F. Riti , R. Seidita , J. Steggemann⁶² , D. Valsecchi , R. Wallny 



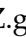




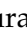




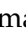

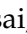




Universität Zürich, Zurich, Switzerland

C. Amsler⁶⁴ , P. Bäertschi , M.F. Canelli , K. Cormier , J.K. Heikkilä , M. Huwiler , W. Jin , A. Jofrehei , B. Kilminster , S. Leontsinis , S.P. Liechti , A. Macchiolo , P. Meiring , U. Molinatti , A. Reimers , P. Robmann , S. Sanchez Cruz , M. Senger , F. Stäger , Y. Takahashi , R. Tramontano 

National Central University, Chung-Li, Taiwan

C. Adloff⁶⁵ , D. Bhowmik , C.M. Kuo , W. Lin , P.K. Rout , P.C. Tiwari³⁹ , S.S. Yu 














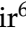
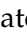
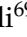




National Taiwan University (NTU), Taipei, Taiwan

L. Ceard , Y. Chao , K.F. Chen , P.s. Chen , Z.g. Chen , A. De Iorio , W.-S. Hou , T.h. Hsu , Y.w. Kao , R. Khurana , G. Kole , Y.y. Li , R.-S. Lu , E. Paganis , X.f. Su , J. Thomas-Wilsker , L.s. Tsai , H.y. Wu , E. Yazgan 

High Energy Physics Research Unit, Department of Physics, Faculty of Science, Chulalongkorn University, Bangkok, Thailand

C. Asawatangtrakuldee , N. Srimanobhas , V. Wachirapusanand 

Çukurova University, Physics Department, Science and Art Faculty, Adana, Turkey

D. Agyel , F. Boran , Z.S. Demiroglu , F. Dolek , I. Dumanoglu⁶⁶ , E. Eskut , Y. Guler⁶⁷ , E. Gurpinar Guler⁶⁷ , C. Isik , O. Kara , A. Kayis Topaksu , U. Kiminsu , G. Onengut , K. Ozdemir⁶⁸ , A. Polatoz , B. Tali⁶⁹ , U.G. Tok , S. Turkcapar , E. Uslan , I.S. Zorbakir 


Middle East Technical University, Physics Department, Ankara, Turkey

M. Yalvac⁷⁰ 


Bogazici University, Istanbul, Turkey

B. Akgun , I.O. Atakisi , E. Gülmez , M. Kaya⁷¹ , O. Kaya⁷² , S. Tekten⁷³ 

Istanbul Technical University, Istanbul, Turkey

A. Cakir , K. Cankocak^{66,74} , G.G. Dincer , Y. Komurcu , S. Sen⁷⁵ 

Istanbul University, Istanbul, Turkey

O. Aydilek²³ , S. Cerci⁶⁹ , V. Epshteyn , B. Hacisahinoglu , I. Hos⁷⁶ , B. Kaynak , S. Ozkorucuklu , O. Potok , H. Sert , C. Simsek , C. Zorbilmez 


Yildiz Technical University, Istanbul, Turkey

B. Isildak⁷⁷ , D. Sunar Cerci⁶⁹ 








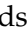
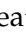
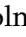



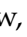
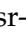
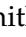
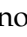
Institute for Scintillation Materials of National Academy of Science of Ukraine, Kharkiv, Ukraine

A. Boyaryntsev , B. Grynyov 


















National Science Centre, Kharkiv Institute of Physics and Technology, Kharkiv, Ukraine

L. Levchuk 


























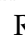








University of Bristol, Bristol, United Kingdom

D. Anthony , J.J. Brooke , A. Bundock , F. Bury , E. Clement , D. Cussans , H. Flacher , M. Glowacki , J. Goldstein , H.F. Heath , M.-L. Holmberg , L. Kreczko , S. Paramesvaran , L. Robertshaw , S. Seif El Nasr-Storey , V.J. Smith , N. Stylianou⁷⁸ , K. Walkingshaw Pass




Rutherford Appleton Laboratory, Didcot, United Kingdom

A.H. Ball, K.W. Bell , A. Belyaev⁷⁹ , C. Brew , R.M. Brown , D.J.A. Cockerill , C. Cooke , K.V. Ellis, K. Harder , S. Harper , J. Linacre , K. Manolopoulos, D.M. Newbold , E. Olaiya, D. Petyt , T. Reis , A.R. Sahasransu , G. Salvi , T. Schuh, C.H. Shepherd-Themistocleous , I.R. Tomalin , T. Williams 

Imperial College, London, United Kingdom

R. Bainbridge , P. Bloch , C.E. Brown , O. Buchmuller, V. Cacchio, C.A. Carrillo Montoya , G.S. Chahal⁸⁰ , D. Colling , J.S. Dancu, I. Das , P. Dauncey , G. Davies , J. Davies, M. Della Negra , S. Fayer, G. Fedi , G. Hall , M.H. Hassanshahi , A. Howard, G. Iles , M. Knight , J. Langford , J. León Holgado , L. Lyons , A.-M. Magnan , S. Malik, M. Mieskolainen , J. Nash⁸¹ , M. Pesaresi , B.C. Radburn-Smith , A. Richards, A. Rose , K. Savva , C. Seez , R. Shukla , A. Tapper , K. Uchida , G.P. Uttley , L.H. Vage, T. Virdee³⁰ , M. Vojinovic , N. Wardle , D. Winterbottom 






Brunel University, Uxbridge, United Kingdom

K. Coldham, J.E. Cole , A. Khan, P. Kyberd , I.D. Reid 

Baylor University, Waco, Texas, USA

S. Abdullin , A. Brinkerhoff , B. Caraway , E. Collins , J. Dittmann , K. Hatakeyama , J. Hiltbrand , B. McMaster , M. Saunders , S. Sawant , C. Sutantawibul , J. Wilson 






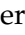














Catholic University of America, Washington, DC, USA

R. Bartek , A. Dominguez , C. Huerta Escamilla, A.E. Simsek , R. Uniyal , A.M. Vargas Hernandez 














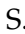

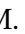

The University of Alabama, Tuscaloosa, Alabama, USA

B. Bam , R. Chudasama , S.I. Cooper , S.V. Gleyzer , C.U. Perez , P. Rumerio⁸² , E. Usai , R. Yi 



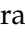




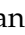











Boston University, Boston, Massachusetts, USA

A. Akpinar , D. Arcaro , C. Cosby , Z. Demiragli , C. Erice , C. Fangmeier , C. Fernandez Madrazo , E. Fontanesi , D. Gastler , F. Golf , S. Jeon , I. Reed , J. Rohlf , K. Salyer , D. Sperka , D. Spitzbart , I. Suarez , A. Tsatsos , S. Yuan , A.G. Zecchinelli 




Brown University, Providence, Rhode Island, USA

G. Benelli , X. Coubez²⁵, D. Cutts , M. Hadley , U. Heintz , J.M. Hogan⁸³ , T. Kwon , G. Landsberg , K.T. Lau , D. Li , J. Luo , S. Mondal , M. Narain[†] , N. Pervan , S. Sagir⁸⁴ , F. Simpson , M. Stamenkovic , X. Yan , W. Zhang






University of California, Davis, Davis, California, USA

S. Abbott , J. Bonilla , C. Brainerd , R. Breedon , H. Cai , M. Calderon De La Barca Sanchez , M. Chertok , M. Citron , J. Conway , P.T. Cox , R. Erbacher , F. Jensen , O. Kukral , G. Mocellin , M. Mulhearn , D. Pellett , W. Wei , Y. Yao , F. Zhang 














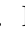









University of California, Los Angeles, California, USA

M. Bachtis , R. Cousins , A. Datta , G. Flores Avila, J. Hauser , M. Ignatenko , M.A. Iqbal , T. Lam , E. Manca , A. Nunez Del Prado, D. Saltzberg , V. Valuev 



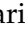





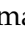







University of California, Riverside, Riverside, California, USA

R. Clare , J.W. Gary , M. Gordon, G. Hanson , W. Si , S. Wimpenny[†] 

University of California, San Diego, La Jolla, California, USA

J.G. Branson , S. Cittolin , S. Cooperstein , D. Diaz , J. Duarte , L. Giannini , J. Guiang , R. Kansal , V. Krutelyov , R. Lee , J. Letts , M. Masciovecchio , F. Mokhtar , S. Mukherjee , M. Pieri , M. Quinnan , B.V. Sathia Narayanan , V. Sharma , M. Tadel , E. Vourliotis , F. Würthwein , Y. Xiang , A. Yagil 


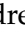








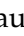





University of California, Santa Barbara - Department of Physics, Santa Barbara, California, USA

A. Barzdukas , L. Brennan , C. Campagnari , J. Incandela , J. Kim , A.J. Li , P. Masterson , H. Mei , J. Richman , U. Sarica , R. Schmitz , F. Setti , J. Sheplock , D. Stuart , T.Á. Vami , S. Wang 



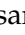
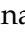
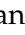


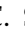





California Institute of Technology, Pasadena, California, USA

A. Bornheim , O. Cerri , A. Latorre , J. Mao , H.B. Newman , G. Reales Gutiérrez , M. Spiropulu , J.R. Vlimant , C. Wang , S. Xie , R.Y. Zhu 





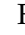



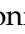
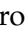







Carnegie Mellon University, Pittsburgh, Pennsylvania, USA

J. Alison , S. An , M.B. Andrews , P. Bryant , M. Cremonesi , V. Dutta , T. Ferguson , A. Harilal , C. Liu , T. Mudholkar , S. Murthy , P. Palit , M. Paulini , A. Roberts , A. Sanchez , W. Terrill 




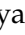
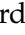





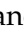
























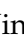
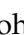


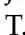
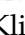
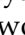



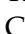



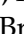


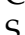

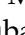

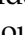


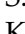
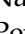





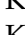


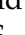
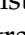


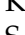
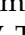
University of Colorado Boulder, Boulder, Colorado, USA

J.P. Cumalat , W.T. Ford , A. Hart , A. Hassani , G. Karathanasis , N. Manganelli , A. Perloff , C. Savard , N. Schonbeck , K. Stenson , K.A. Ulmer , S.R. Wagner , N. Zipper 

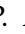


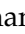
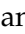















Cornell University, Ithaca, New York, USA

J. Alexander , S. Bright-Thonney , X. Chen , D.J. Cranshaw , J. Fan , X. Fan , S. Hogan , P. Kotamnives , J. Monroy , M. Oshiro , J.R. Patterson , J. Reichert , M. Reid , A. Ryd , J. Thom , P. Wittich , R. Zou 

Fermi National Accelerator Laboratory, Batavia, Illinois, USA



M. Albrow , M. Alyari , O. Amram , G. Apollinari , A. Apresyan , L.A.T. Bauerdick , D. Berry , J. Berryhill , P.C. Bhat , K. Burkett , J.N. Butler , A. Canepa , G.B. Cerati , H.W.K. Cheung , F. Chlebana , G. Cummings , J. Dickinson , I. Dutta , V.D. Elvira , Y. Feng , J. Freeman , A. Gandrakota , Z. Gecse , L. Gray , D. Green , A. Grummer , S. Grünendahl , D. Guerrero , O. Gutsche , R.M. Harris , R. Heller , T.C. Herwig , J. Hirschauer , L. Horyn , B. Jayatilaka , S. Jindariani , M. Johnson , U. Joshi , T. Klijsma , B. Klima , K.H.M. Kwok , S. Lammel , D. Lincoln , R. Lipton , T. Liu , C. Madrid , K. Maeshima , C. Mantilla , D. Mason , P. McBride , P. Merkel , S. Mrenna , S. Nahn , J. Ngadiuba , D. Noonan , V. Papadimitriou , N. Pastika , K. Pedro , C. Pena⁸⁵ , F. Ravera , A. Reinsvold Hall⁸⁶ , L. Ristori , E. Sexton-Kennedy , N. Smith , A. Soha , L. Spiegel , S. Stoynev , J. Strait , L. Taylor , S. Tkaczyk , N.V. Tran , L. Uplegger , E.W. Vaandering , A. Whitbeck , I. Zoi 

University of Florida, Gainesville, Florida, USA

C. Aruta , P. Avery , D. Bourilkov , L. Cadamuro , P. Chang , V. Cherepanov , R.D. Field , E. Koenig , M. Kolosova , J. Konigsberg , A. Korytov , K. Matchev , N. Menendez , G. Mitselmakher , K. Mohrman , A. Muthirakalayil Madhu , N. Rawal , D. Rosenzweig , S. Rosenzweig , J. Wang 

Florida State University, Tallahassee, Florida, USA





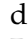




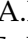











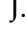
T. Adams , A. Al Kadhim , A. Askew , S. Bower , R. Habibullah , V. Hagopian , R. Hashmi , R.S. Kim , S. Kim , T. Kolberg , G. Martinez , H. Prosper , P.R. Prova 

M. Wulansatiti , R. Yohay , J. Zhang






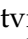





Florida Institute of Technology, Melbourne, Florida, USA

B. Alsufyani, M.M. Baarmand , S. Butalla , S. Das , T. Elkafrawy⁵⁵ , M. Hohlmann ,
R. Kumar Verma , M. Rahmani, E. Yanes












University of Illinois Chicago, Chicago, USA, Chicago, USA

M.R. Adams , A. Baty , C. Bennett, R. Cavanaugh , R. Escobar Franco , O. Evdokimov , C.E. Gerber , M. Hawksworth, A. Hingrajiya, D.J. Hofman , J.h. Lee ,
D. S. Lemos , A.H. Merrit , C. Mills , S. Nanda , G. Oh , B. Ozek , D. Pilipovic ,
R. Pradhan , E. Prifti, T. Roy , S. Rudrabhatla , M.B. Tonjes , N. Varelas , Z. Ye ,
J. Yoo 









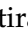


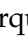

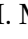






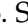
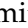


The University of Iowa, Iowa City, Iowa, USA

M. Alhusseini , D. Blend, K. Dilsiz⁸⁷ , L. Emediato , G. Karaman , O.K. Köseyan , J.-
P. Merlo, A. Mestvirishvili⁸⁸ , J. Nachtman , O. Neogi, H. Ogul⁸⁹ , Y. Onel , A. Penzo ,
C. Snyder, E. Tiras⁹⁰ 









Johns Hopkins University, Baltimore, Maryland, USA

B. Blumenfeld , L. Corcodilos , J. Davis , A.V. Gritsan , L. Kang , S. Kyriacou ,
P. Maksimovic , M. Roguljic , J. Roskes , S. Sekhar , M. Swartz 

The University of Kansas, Lawrence, Kansas, USA

A. Abreu , L.F. Alcerro Alcerro , J. Anguiano , P. Baringer , A. Bean , Z. Flowers ,
D. Grove , J. King , G. Krintiras , M. Lazarovits , C. Le Mahieu , J. Marquez ,
N. Minafra , M. Murray , M. Nickel , M. Pitt , S. Popescu⁹¹ , C. Rogan , C. Royon ,
R. Salvatico , S. Sanders , C. Smith , Q. Wang , G. Wilson 








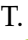

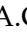
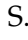
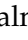



Kansas State University, Manhattan, Kansas, USA

B. Allmond , A. Ivanov , K. Kaadze , A. Kalogeropoulos , D. Kim, Y. Maravin ,
J. Natoli , D. Roy , G. Sorrentino 















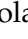

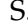



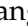
Lawrence Livermore National Laboratory, Livermore, California, USA

F. Rebassoo , D. Wright 


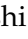
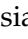
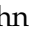



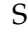
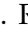

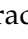
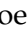


University of Maryland, College Park, Maryland, USA

A. Baden , A. Belloni , Y.M. Chen , S.C. Eno , N.J. Hadley , S. Jabeen ,
R.G. Kellogg , T. Koeth , Y. Lai , S. Lascio , A.C. Mignerey , S. Nabili , C. Palmer ,
C. Papageorgakis , M.M. Paranjpe, L. Wang 

Massachusetts Institute of Technology, Cambridge, Massachusetts, USA

J. Bendavid , I.A. Cali , M. D'Alfonso , J. Eysermans , C. Freer , G. Gomez-Ceballos ,
M. Goncharov, G. Grosso, P. Harris, D. Hoang, D. Kovalskyi , J. Krupa , L. Lavezzo ,
Y.-J. Lee , K. Long , A. Novak , C. Paus , D. Rankin , C. Roland , G. Roland ,
S. Rothman , G.S.F. Stephans , Z. Wang , B. Wyslouch , T. J. Yang 













University of Minnesota, Minneapolis, Minnesota, USA

B. Crossman , B.M. Joshi , C. Kapsiak , M. Krohn , D. Mahon , J. Mans ,
B. Marzocchi , S. Pandey , M. Revering , R. Rusack , R. Saradhy , N. Schroeder ,
N. Strobbe , M.A. Wadud 

University of Mississippi, Oxford, Mississippi, USA

L.M. Cremaldi 

















University of Nebraska-Lincoln, Lincoln, Nebraska, USA

K. Bloom , D.R. Claes , G. Haza , J. Hossain , C. Joo , I. Kravchenko , J.E. Siado , W. Tabb , A. Vagnerini , A. Wightman , F. Yan , D. Yu 





State University of New York at Buffalo, Buffalo, New York, USA

H. Bandyopadhyay , L. Hay , I. Iashvili , A. Kharchilava , M. Morris , D. Nguyen , S. Rappoccio , H. Rejeb Sfar, A. Williams 








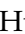





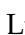












Northeastern University, Boston, Massachusetts, USA

G. Alverson , E. Barberis , J. Dervan, Y. Haddad , Y. Han , A. Krishna , J. Li , M. Lu , G. Madigan , R. Mccarthy , D.M. Morse , V. Nguyen , T. Orimoto , A. Parker , L. Skinnari , B. Wang , D. Wood 









Northwestern University, Evanston, Illinois, USA

S. Bhattacharya , J. Bueghly, Z. Chen , S. Dittmer , K.A. Hahn , Y. Liu , Y. Miao , D.G. Monk , M.H. Schmitt , A. Taliercio , M. Velasco
















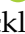
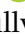

University of Notre Dame, Notre Dame, Indiana, USA

G. Agarwal , R. Band , R. Bucci, S. Castells , A. Das , R. Goldouzian , M. Hildreth , K.W. Ho , K. Hurtado Anampa , T. Ivanov , C. Jessop , K. Lannon , J. Lawrence , N. Loukas , L. Lutton , J. Mariano, N. Marinelli, I. Mcalister, T. McCauley , C. Mcgrady , C. Moore , Y. Musienko¹⁶ , H. Nelson , M. Osherson , A. Piccinelli , R. Ruchti , A. Townsend , Y. Wan, M. Wayne , H. Yockey, M. Zarucki , L. Zygalá 


The Ohio State University, Columbus, Ohio, USA

A. Basnet , B. Bylsma, M. Carrigan , L.S. Durkin , C. Hill , M. Joyce , M. Nunez Ornelas , K. Wei, B.L. Winer , B. R. Yates 













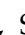






Princeton University, Princeton, New Jersey, USA

F.M. Addesa , H. Bouchamaoui , P. Das , G. Dezoort , P. Elmer , A. Frankenthal , B. Greenberg , N. Haubrich , G. Kopp , S. Kwan , D. Lange , A. Loeliger , D. Marlow , I. Ojalvo , J. Olsen , A. Shevelev , D. Stickland , C. Tully 




University of Puerto Rico, Mayaguez, Puerto Rico, USA

S. Malik 




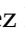







Purdue University, West Lafayette, Indiana, USA

A.S. Bakshi , V.E. Barnes , S. Chandra , R. Chawla , A. Gu , L. Gutay, M. Jones , A.W. Jung , D. Kondratyev , A.M. Koshy, M. Liu , G. Negro , N. Neumeister , G. Paspalaki , S. Piperov , V. Scheurer, J.F. Schulte , M. Stojanovic , J. Thieman , A. K. Viridi , F. Wang , W. Xie 


Purdue University Northwest, Hammond, Indiana, USA

J. Dolen , N. Parashar , A. Pathak 


Rice University, Houston, Texas, USA

D. Acosta , T. Carnahan , K.M. Ecklund , P.J. Fernández Manteca , S. Freed, P. Gardner, F.J.M. Geurts , W. Li , O. Miguel Colin , B.P. Padley , R. Redjimi, J. Rotter , E. Yigitbasi , Y. Zhang 







University of Rochester, Rochester, New York, USA

A. Bodek , P. de Barbaro , R. Demina , J.L. Dulemba , A. Garcia-Bellido , O. Hindrichs , A. Khukhunaishvili , N. Parmar, P. Parygin⁹² , E. Popova⁹² , R. Taus 

The Rockefeller University, New York, New York, USA

K. Goulianos 


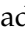
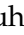




Rutgers, The State University of New Jersey, Piscataway, New Jersey, USA

B. Chiarito, J.P. Chou , S.V. Clark , D. Gadkari , Y. Gershtein , E. Halkiadakis , M. Heindl , C. Houghton , D. Jaroslowski , O. Karacheban²⁸ , I. Laflotte , A. Lath , R. Montalvo, K. Nash, H. Routray , P. Saha , S. Salur , S. Schnetzer, S. Somalwar , R. Stone , S.A. Thayil , S. Thomas, J. Vora , H. Wang





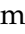


University of Tennessee, Knoxville, Tennessee, USA

H. Acharya, D. Ally , A.G. Delannoy , S. Fiorendi , S. Higginbotham , T. Holmes , A.R. Kanuganti , N. Karunarathna , L. Lee , E. Nibigira , S. Spanier




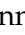


Texas A&M University, College Station, Texas, USA

D. Aebi , M. Ahmad , O. Bouhali⁹³ , R. Eusebi , J. Gilmore , T. Huang , T. Kamon⁹⁴ , H. Kim , S. Luo , R. Mueller , D. Overton , D. Rathjens , A. Safonov








Texas Tech University, Lubbock, Texas, USA

N. Akchurin , J. Damgov , V. Hegde , A. Hussain , Y. Kazhykarim, K. Lamichhane , S.W. Lee , A. Mankel , T. Peltola , I. Volobouev

Vanderbilt University, Nashville, Tennessee, USA

E. Appelt , Y. Chen , S. Greene, A. Gurrola , W. Johns , R. Kunnawalkam Elayavalli , A. Melo , F. Romeo , P. Sheldon , S. Tuo , J. Velkovska , J. Viinikainen


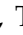




University of Virginia, Charlottesville, Virginia, USA

B. Cardwell , B. Cox , J. Hakala , R. Hirosky , A. Ledovskoy , C. Neu , C.E. Perez Lara 

Wayne State University, Detroit, Michigan, USA

P.E. Karchin 

University of Wisconsin - Madison, Madison, Wisconsin, USA

A. Aravind, S. Banerjee , K. Black , T. Bose , S. Dasu , I. De Bruyn , P. Everaerts , C. Galloni, H. He , M. Herndon , A. Herve , C.K. Koraka , A. Lanaro, R. Loveless , J. Madhusudanan Sreekala , A. Mallampalli , A. Mohammadi , S. Mondal, G. Parida , L. Pétré , D. Pinna, A. Savin, V. Shang , V. Sharma , W.H. Smith , D. Teague, H.F. Tsoi , W. Vetens , A. Warden

Authors affiliated with an institute or an international laboratory covered by a cooperation agreement with CERN

S. Afanasiev , V. Andreev , Yu. Andreev , T. Aushev , M. Azarkin , I. Azhgirey , A. Babaev , A. Belyaev , V. Blinov⁹⁵ , E. Boos , V. Borshch , D. Budkouski , V. Bunichev , V. Chekhovsky, R. Chistov⁹⁵ , M. Danilov⁹⁵ , A. Dermenev , T. Dimova⁹⁵ , D. Druzhkin⁹⁶ , M. Dubinin⁸⁵ , L. Dudko , G. Gavrilo , V. Gavrilo , S. Gninenko , V. Golovtsov , N. Golubev , I. Golutvin , I. Gorbunov , A. Gribushin , Y. Ivanov , V. Kachanov , V. Karjavine , A. Karneyev , V. Kim⁹⁵ , M. Kirakosyan, D. Kirpichnikov , M. Kirsanov , V. Klyukhin , D. Konstantinov , V. Korenkov , A. Kozyrev⁹⁵ , N. Krasnikov , A. Lanev , P. Levchenko⁹⁷ , N. Lychkovskaya , V. Makarenko , A. Malakhov , V. Matveev⁹⁵ , V. Murzin , A. Nikitenko^{98,99} , S. Obraztsov , V. Oreshkin , V. Palichik , V. Perelygin , M. Perfilov, S. Petrushanko , S. Polikarpov⁹⁵ , V. Popov , O. Radchenko⁹⁵ , R. Ryutin, M. Savina , V. Savrin , V. Shalaev , S. Shmatov , S. Shulha , Y. Skovpen⁹⁵ , S. Slabospitskii , V. Smirnov , D. Sosnov , V. Sulimov , E. Tcherniaev , A. Terkulov , O. Teryaev , I. Tlisova , A. Toropin , L. Uvarov , A. Uzunian , P. Volkov , A. Vorobyev[†], G. Vorotnikov , N. Voytishin , B.S. Yuldashev¹⁰⁰, A. Zarubin , I. Zhizhin , A. Zhokin

†: Deceased

¹Also at Yerevan State University, Yerevan, Armenia

²Also at TU Wien, Vienna, Austria

³Also at Institute of Basic and Applied Sciences, Faculty of Engineering, Arab Academy for Science, Technology and Maritime Transport, Alexandria, Egypt

⁴Also at Ghent University, Ghent, Belgium

⁵Also at Universidade Estadual de Campinas, Campinas, Brazil

⁶Also at Federal University of Rio Grande do Sul, Porto Alegre, Brazil

⁷Also at UFMS, Nova Andradina, Brazil

⁸Also at Nanjing Normal University, Nanjing, China

⁹Now at The University of Iowa, Iowa City, Iowa, USA

¹⁰Also at University of Chinese Academy of Sciences, Beijing, China

¹¹Also at China Center of Advanced Science and Technology, Beijing, China

¹²Also at University of Chinese Academy of Sciences, Beijing, China

¹³Also at China Spallation Neutron Source, Guangdong, China

¹⁴Now at Henan Normal University, Xinxiang, China

¹⁵Also at Université Libre de Bruxelles, Bruxelles, Belgium

¹⁶Also at an institute or an international laboratory covered by a cooperation agreement with CERN

¹⁷Now at British University in Egypt, Cairo, Egypt

¹⁸Now at Cairo University, Cairo, Egypt

¹⁹Also at Purdue University, West Lafayette, Indiana, USA

²⁰Also at Université de Haute Alsace, Mulhouse, France

²¹Also at Department of Physics, Tsinghua University, Beijing, China

²²Also at The University of the State of Amazonas, Manaus, Brazil

²³Also at Erzincan Binali Yildirim University, Erzincan, Turkey

²⁴Also at University of Hamburg, Hamburg, Germany

²⁵Also at RWTH Aachen University, III. Physikalisches Institut A, Aachen, Germany

²⁶Also at Isfahan University of Technology, Isfahan, Iran

²⁷Also at Bergische University Wuppertal (BUW), Wuppertal, Germany

²⁸Also at Brandenburg University of Technology, Cottbus, Germany

²⁹Also at Forschungszentrum Jülich, Juelich, Germany

³⁰Also at CERN, European Organization for Nuclear Research, Geneva, Switzerland

³¹Also at Institute of Physics, University of Debrecen, Debrecen, Hungary

³²Also at Institute of Nuclear Research ATOMKI, Debrecen, Hungary

³³Now at Universitatea Babeş-Bolyai - Facultatea de Fizica, Cluj-Napoca, Romania

³⁴Also at MTA-ELTE Lendület CMS Particle and Nuclear Physics Group, Eötvös Loránd University, Budapest, Hungary

³⁵Also at Physics Department, Faculty of Science, Assiut University, Assiut, Egypt

³⁶Also at HUN-REN Wigner Research Centre for Physics, Budapest, Hungary

³⁷Also at Punjab Agricultural University, Ludhiana, India

³⁸Also at University of Visva-Bharati, Santiniketan, India

³⁹Also at Indian Institute of Science (IISc), Bangalore, India

⁴⁰Also at Birla Institute of Technology, Mesra, Mesra, India

⁴¹Also at IIT Bhubaneswar, Bhubaneswar, India

⁴²Also at Institute of Physics, Bhubaneswar, India

⁴³Also at University of Hyderabad, Hyderabad, India

⁴⁴Also at Deutsches Elektronen-Synchrotron, Hamburg, Germany

⁴⁵Also at Department of Physics, Isfahan University of Technology, Isfahan, Iran

- ⁴⁶Also at Sharif University of Technology, Tehran, Iran
- ⁴⁷Also at Department of Physics, University of Science and Technology of Mazandaran, Behshahr, Iran
- ⁴⁸Also at Helwan University, Cairo, Egypt
- ⁴⁹Also at Italian National Agency for New Technologies, Energy and Sustainable Economic Development, Bologna, Italy
- ⁵⁰Also at Centro Siciliano di Fisica Nucleare e di Struttura Della Materia, Catania, Italy
- ⁵¹Also at Università degli Studi Guglielmo Marconi, Roma, Italy
- ⁵²Also at Scuola Superiore Meridionale, Università di Napoli 'Federico II', Napoli, Italy
- ⁵³Also at Fermi National Accelerator Laboratory, Batavia, Illinois, USA
- ⁵⁴Also at Laboratori Nazionali di Legnaro dell'INFN, Legnaro, Italy
- ⁵⁵Also at Ain Shams University, Cairo, Egypt
- ⁵⁶Also at Consiglio Nazionale delle Ricerche - Istituto Officina dei Materiali, Perugia, Italy
- ⁵⁷Also at Department of Applied Physics, Faculty of Science and Technology, Universiti Kebangsaan Malaysia, Bangi, Malaysia
- ⁵⁸Also at Consejo Nacional de Ciencia y Tecnología, Mexico City, Mexico
- ⁵⁹Also at Trincomalee Campus, Eastern University, Sri Lanka, Nilaveli, Sri Lanka
- ⁶⁰Also at Saegis Campus, Nugegoda, Sri Lanka
- ⁶¹Also at National and Kapodistrian University of Athens, Athens, Greece
- ⁶²Also at Ecole Polytechnique Fédérale Lausanne, Lausanne, Switzerland
- ⁶³Also at Universität Zürich, Zurich, Switzerland
- ⁶⁴Also at Stefan Meyer Institute for Subatomic Physics, Vienna, Austria
- ⁶⁵Also at Laboratoire d'Annecy-le-Vieux de Physique des Particules, IN2P3-CNRS, Annecy-le-Vieux, France
- ⁶⁶Also at Near East University, Research Center of Experimental Health Science, Mersin, Turkey
- ⁶⁷Also at Konya Technical University, Konya, Turkey
- ⁶⁸Also at Izmir Bakircay University, Izmir, Turkey
- ⁶⁹Also at Adiyaman University, Adiyaman, Turkey
- ⁷⁰Also at Bozok Universiteleri Rektörlüğü, Yozgat, Turkey
- ⁷¹Also at Marmara University, Istanbul, Turkey
- ⁷²Also at Milli Savunma University, Istanbul, Turkey
- ⁷³Also at Kafkas University, Kars, Turkey
- ⁷⁴Now at Istanbul Okan University, Istanbul, Turkey
- ⁷⁵Also at Hacettepe University, Ankara, Turkey
- ⁷⁶Also at Istanbul University - Cerrahpasa, Faculty of Engineering, Istanbul, Turkey
- ⁷⁷Also at Yildiz Technical University, Istanbul, Turkey
- ⁷⁸Also at Vrije Universiteit Brussel, Brussel, Belgium
- ⁷⁹Also at School of Physics and Astronomy, University of Southampton, Southampton, United Kingdom
- ⁸⁰Also at IPPP Durham University, Durham, United Kingdom
- ⁸¹Also at Monash University, Faculty of Science, Clayton, Australia
- ⁸²Also at Università di Torino, Torino, Italy
- ⁸³Also at Bethel University, St. Paul, Minnesota, USA
- ⁸⁴Also at Karamanoğlu Mehmetbey University, Karaman, Turkey
- ⁸⁵Also at California Institute of Technology, Pasadena, California, USA
- ⁸⁶Also at United States Naval Academy, Annapolis, Maryland, USA
- ⁸⁷Also at Bingöl University, Bingöl, Turkey
- ⁸⁸Also at Georgian Technical University, Tbilisi, Georgia

⁸⁹Also at Sinop University, Sinop, Turkey

⁹⁰Also at Erciyes University, Kayseri, Turkey

⁹¹Also at Horia Hulubei National Institute of Physics and Nuclear Engineering (IFIN-HH), Bucharest, Romania

⁹²Now at an institute or an international laboratory covered by a cooperation agreement with CERN

⁹³Also at Texas A&M University at Qatar, Doha, Qatar

⁹⁴Also at Kyungpook National University, Daegu, Korea

⁹⁵Also at another institute or international laboratory covered by a cooperation agreement with CERN

⁹⁶Also at Universiteit Antwerpen, Antwerpen, Belgium

⁹⁷Also at Northeastern University, Boston, Massachusetts, USA

⁹⁸Also at Imperial College, London, United Kingdom

⁹⁹Now at Yerevan Physics Institute, Yerevan, Armenia

¹⁰⁰Also at Institute of Nuclear Physics of the Uzbekistan Academy of Sciences, Tashkent, Uzbekistan

Measurement of Proton-Induced Reactions on Lanthanum from 55–200 MeV by Stacked-Foil Activation

Jonathan T. Morrell,¹ Ellen M. O’Brien,¹ Michael Skulski,² Andrew S. Voyles,³ Dmitri G. Medvedev,² Veronika Mocko,¹ Lee A. Bernstein,^{4,3} and C. Etienne Vermeulen¹

¹*Los Alamos National Laboratory, Los Alamos, NM 87545, USA*

²*Brookhaven National Laboratory, Upton, NY 11973, USA*

³*University of California, Berkeley, Berkeley, CA 94720, USA*

⁴*Lawrence Berkeley National Laboratory, Berkeley, CA 94720, USA*

(Dated: February 29, 2024)

Cerium-134 is an isotope desired for applications as a chemical analogue to the promising therapeutic radionuclide ²²⁵Ac, for use in bio-distribution assays as an *in vivo* generator of the short-lived positron-emitting isotope ¹³⁴La. In the 50–100 MeV energy range relevant to the production of ¹³⁴Ce by means of high-energy proton bombardment of lanthanum, existing cross section data are discrepant and have gaps at important energies. To address these deficiencies, a series of 17 ¹³⁹La foils (99.919% natural abundance) were irradiated in two stacked-target experiments: one at the Los Alamos National Laboratory’s Isotope Production Facility (IPF) with an incident proton energy of 100 MeV, and a second at Brookhaven National Laboratory’s Brookhaven Linac Isotope Producer (BLIP) with an incident proton energy of 200 MeV — a complete energy range spanning approximately 55–200 MeV. Cross sections are reported for 30 products of ¹³⁹La(p,x) reactions (representing up to 55% of the total non-elastic cross section), in addition to 24 residual products measured in the ^{nat}Cu and ^{nat}Ti foils that were used as proton flux monitors. The measured production cross sections for ¹³⁹La reactions were compared to literature data as well as default calculations from the nuclear reaction modeling codes TALYS, EMPIRE and ALICE, as well as the TENDL-2023 library. The default calculations typically exhibited poor predictive capability, due to the complexity of multiple interacting physics models in this energy range, and deficiencies in pre-equilibrium reaction modeling. Building upon previous efforts to evaluate proton-induced reactions in this energy range, a parameter adjustment procedure was performed upon the optical model and the two-component exciton model using the TALYS-2.0 code. This resulted in an improvement in ¹³⁹La(p,x) cross sections for applications including isotope production, over default predictions.

I. INTRODUCTION

Proton accelerators operating in the approximately 10–200 MeV energy range are advantageous for the production of radioisotopes having characteristics of simultaneous high activity and high *specific* activity, *i.e.*, having a high ratio of the desired radionuclide to “cold” (stable) impurities. These characteristics are generally advantageous to the field of nuclear medicine for the creation of radiopharmaceuticals used in the diagnosis and treatment of various diseases, such as cancers. For example, one such radionuclide we are interested in producing is ¹³⁴Ce, which has applications as a positron-emitting analogue of the therapeutic isotope ²²⁵Ac.

Actinium-225 is an alpha-emitting radionuclide that is currently under study for the treatment of various forms of cancer, such as advanced prostate cancer and acute myeloid leukemia [1–3]. With a half-life of 9.9203 (3) days, ²²⁵Ac quickly decays to ²⁰⁹Bi through the emission of four 5–8 MeV α particles and two β^- particles, with the longest-lived intermediate decay product being the

3.234 (7) h ²⁰⁹Pb [4–8]. Having a characteristic range of 50–100 μm in human tissue, these emitted alpha particles have a high likelihood of killing cancerous cells while sparing nearby healthy tissue, provided a sufficiently specific cancer-targeting vector. One example of a promising vector is PSMA-617 (prostate-specific membrane antigen), which has shown efficacy (defined as a decrease in prostate-specific antigen, or PSA, serum concentration of $\geq 50\%$) in 66% of patients afflicted with advanced (metastatic) prostate cancer, according to a recent meta-analysis [9].

An important aspect of treatment planning in targeted radionuclide therapy is the ability to assay the bio-distribution of the injected radiopharmaceutical, typically with clinical positron-emission tomography (PET) scanners [10]. Unfortunately, ²²⁵Ac lacks positron emissions in any of its decay products, negating the possibility of performing such scans directly. Instead, the therapeutic targeting vector must be radiolabeled with a positron-emitting chemical analogue of actinium. Recent studies have demonstrated the ability of ¹³⁴Ce to act as a PET imaging surrogate for drug conjugates in-

corporating ^{225}Ac for long-term tumor targeting [11–13]. Cerium-134 decays with a half-life of 3.16 (4) days to ^{134}La ($T_{1/2} = 6.45$ (16) min), which emits a positron in approximately 64% of decays [14]. Therefore, ^{134}Ce , acting as a chemical analogue to actinium, serves as an *in-vivo* generator of the positron-emitter ^{134}La .

Cerium-134 could be produced by proton accelerators using natural targets of lanthanum, cerium, praseodymium, neodymium or even samarium, however the (p,6n) reaction on ^{139}La (99.9119% natural abundance) is generally predicted to have the highest ^{134}Ce yield of these options. The $^{140}\text{Ce}(p,7n)^{134}\text{Pr}$ production route is theoretically interesting because it could produce ^{134}Ce with a higher radiopurity than using a lanthanum target; however, the ≈ 11 min half-life of ^{134}Pr is too short for practical radiochemical separations, which may take several hours to days [14]. By this time, the product ^{134}Ce would be chemically indistinguishable from the target material, and therefore the separation would be impossible.

Currently available cross section data for the $^{139}\text{La}(p,6n)^{134}\text{Ce}$ reaction extends from approximately 50–90 MeV [15–17]. However, there are only two data points above 70 MeV, where the peak of the cross section is expected, and the three available data sets are generally discrepant beyond their reported error margins, leading to calls for improvements in these data [18]. The primary goal of this study was to address these discrepancies with additional measurements in the 55–100 MeV energy range, as well as to extend the data set with measurements up to approximately 200 MeV, which would characterize the preequilibrium tail for the ^{134}Ce product. This was done using the stacked-foil activation technique, in which a set of thin foils are simultaneously irradiated with a proton beam, such that the beam loses energy as it passes through each foil in the stack [19, 20]. By measuring the induced radioactivity for each foil in the stack, the radionuclide production cross sections can be inferred as a function of proton energy. One benefit of this technique is that while the experiment was designed around the measurement of the (p,6n) cross section, many more radionuclide production cross sections could be simultaneously determined. In this experiment, 30 distinct reaction channels were observed in the lanthanum targets, comprising an estimated 55% of the total non-elastic cross section (based on the TENDL-2023 non-elastic cross section), with an additional 24 products measured in the $^{\text{nat}}\text{Cu}$ and $^{\text{nat}}\text{Ti}$ foils used as proton flux monitors. This represents the most extensive measurement of proton-induced reactions on lanthanum to date, and the first measurement above 100 MeV. The resulting data set provides an exquisite sensitivity to the nuclear reaction processes relevant to the formation of the associated radionuclides, such as preequilibrium particle emission.

These data were used to qualitatively assess the predictions of various nuclear reaction modeling codes, as well as to determine how well the fitting procedure developed in Fox *et al.* for the existing lanthanum data set (previously extending only up to 90 MeV) extrapolated to the new 100–200 MeV measurements [21]. While the extrapolation was generally better than the default predictions, there was considerable room for improvement, which we performed with an optimization of selected preequilibrium and optical model parameters using the TALYS-2.0 code [22]. As part of this optimization procedure we compared various optimization algorithms, figure-of-merit weighting procedures, and sensitivities for various TALYS parameters. These results are vital to improving the quality of nuclear data evaluations for these high-energy charged particle reaction pathways.

II. EXPERIMENTAL METHODS AND MATERIALS

In this work, a number of proton-induced nuclear reaction cross sections were measured using the stacked-foil activation method. These measurements were performed as part of a Tri-lab collaboration between Los Alamos National Laboratory (LANL), Brookhaven National Laboratory (BNL) and Lawrence Berkeley National Laboratory (LBNL). Two sets of foils were irradiated: one at the LANL Isotope Production Facility (IPF) with an incident proton energy of 100 MeV, and a second at the BNL Brookhaven Linac Isotope Producer (BLIP) with 200 MeV protons. We will be referring to these irradiations as the “LANL stack” and the “BNL stack” respectively.

II.1. Stack Design and Irradiations

In the stacked-foil (sometimes called stacked-target) activation method, a set of thin foils are arranged in a “stack” and irradiated with charged particles: protons in this case. As the proton beam traverses each successive foil in the stack, its average energy is degraded via stopping interactions within the foils, such that each foil is activated at a slightly lower proton energy than the foil preceding it. Each foil was paired with multiple “monitor” foils, which served as a measure of the beam current and energy at each point in the stack. In our experiment, additional “degraders” made of thick pieces of aluminum or copper were used to further decrease the energy between each set of foils. Following a stacked-foil irradiation, the proton-induced reaction products created in each foil are assayed via gamma spectrometry. The assayed production rates for each isotope, R_i , are related to the foil’s areal density, ρr , the average proton current, I_p ,

and the cross section for the production of each isotope, σ_i according to

$$R_i = (\rho r) I_p \sigma_i \quad (1)$$

where the standard units for R_i , ρr , I_p and σ_i are s^{-1} , $atoms \cdot cm^{-2}$, s^{-1} and cm^2 , respectively. Using this equation, the reaction cross section can be calculated so long as the beam current and areal densities are well-known. This is often referred to as the “thin-target” activation equation [19, 20]. It is based on the assumption that both the proton current and the cross section are approximately constant within the foil — which can only be the case for foils thin enough such that their energy degradation is much less than the incident proton energy. An additional feature of these experiments is in the determination of proton beam currents, I_p , using “monitor” foils, rather than external diagnostics such as a Faraday cup — the use of which is precluded by the physical layouts of both the IPF and BLIP irradiation stations. This monitor foil method relies upon the activation of thin foils having well-characterized “monitor reaction” cross sections, and using Eq. 1 to calculate I_p using a known value of σ_i .

Our experiment consisted of two separate irradiations: one stack of ten lanthanum foils irradiated at the LANL IPF with 100 MeV protons, and a stack of seven lanthanum foils irradiated at the BNL BLIP with 200 MeV protons. The lanthanum foils used in this experiment were identical for both irradiations, all of at least 99% purity by metals basis, purchased from Goodfellow Corporation (Coraopolis, PA 15108, USA). These consisted of natural (*i.e.*, non-enriched) lanthanum metal, which is constituted of 99.9119% ^{139}La and the remainder of ^{138}La [23]. Each foil had a nominal thickness of 25 μm and was approximately 25.4 mm square. Oxidation of the lanthanum metal was minimized by handling the foils inside of a glove box with an inert (dry argon) cover gas. Figure 1 shows a typical preparation of one of the lanthanum foils used in the experiment. Slight oxidation can be seen along the lower edge of the foil, however, oxidation in the beam-strike area (center) was minimal prior to irradiation.

Prior to irradiation, the dimensions and masses of each of these foils were measured in the argon-filled glovebox, with a 1–2% accuracy in the areal density. The foils were then suspended in the center of a plastic mounting frame, sealed between two pieces of 3M 5413-Series Kapton polyimide film tape, which consist of a 25 μm polyimide backing material and a $\approx 43 \mu\text{m}$ layer of acrylic adhesive. The adhesive was specifically chosen to be free of silicon, which under proton bombardment has been shown to lead to the production of ^{24}Na : a contaminant that would interfere with the $^{27}\text{Al}(p,x)^{24}\text{Na}$ monitor reaction channel, and also produce an unwanted

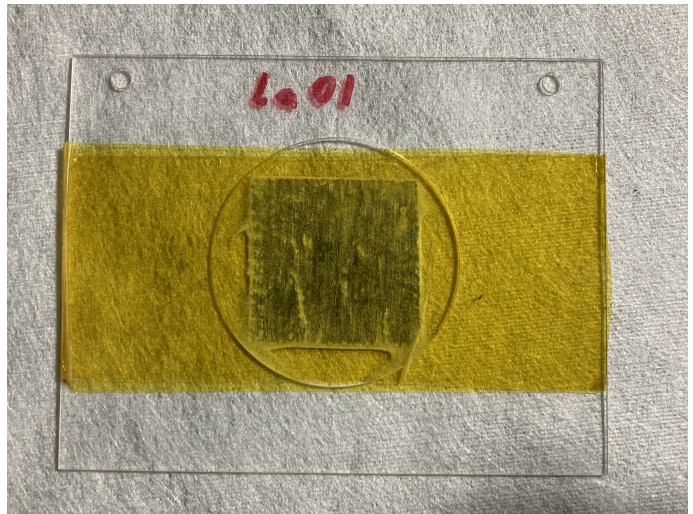


FIG. 1: Photo of an individual lanthanum foil sealed in Kapton polyimide tape, and secured to the acrylic frame before the irradiation.

γ -ray spectrometry background in the form of 1.368 and 2.754 MeV photo-peaks and associated Compton scattering events [19, 24]. The mounting frames were also machined out of acrylic, for this same reason.

The LANL stack made use of natural titanium and copper as monitor foils, observing the ^{46}Sc and ^{48}V monitor reaction products in titanium and ^{62}Zn , ^{65}Zn , ^{56}Co and ^{58}Co in copper. In the BNL stack, aluminum was used instead of titanium, where the ^{22}Na and ^{24}Na monitor channels were observed. All of these foils were cut from sheets of 25 μm nominal thickness into approximately 25.4 mm squares, which were also measured, weighed and mounted to their frames in Kapton tape in a similar manner as described for the lanthanum foils. For both stacks, one monitor foil of each material was co-irradiated with each lanthanum foil, such that there were 20 monitor foils irradiated in the LANL stack and 14 in the BNL stack. The respective metals-basis purities for the titanium, copper and aluminum monitor foils used in this experiment were 99.95%, 99.99% and 99.999%, respectively.

The degraders used in the LANL stack were made from 110-Copper alloy sheets for degraders 1–4 and 6065-Aluminum alloy sheets for degraders 5–9, with thicknesses ranging from approximately 0.6–1.5 mm. The BNL stack made use of 110-Copper degraders, machined from plates ranging between 3.7–5.1 mm in thickness. Each degrader was also carefully measured and weighed to determine its areal density. Finally, a stainless steel “profile monitor” foil was placed in front of and behind each stack, with a nominal thickness of 100 μm . The purpose of these foils was to be used as a post-irradiation check of the beamspot entering and exiting the stack, by mapping the induced activation profile with

radiochromic film (Gafchromic EBT3). For both irradiations, the profile monitor foils confirmed that the beam was well-contained within the approximately 25 mm by 25 mm area of the foils, in the center of the stack. The complete specifications of both BNL and LANL stacks can be found in Appendix B.

Since both IPF and BLIP are high-power production facilities with water-cooled irradiation stations that are only accessible remotely, and require that all materials be introduced into a hot cell and handled with telemanipulators, a specially designed sample irradiation box was required for both irradiations. It was critical that this sample irradiation box was leak tight, as the lanthanum foils would rapidly oxidize if exposed to the cooling water. This had the added benefit of significantly minimizing surface contamination on the foils. Photos of the target boxes used in the LANL and BNL irradiations can be seen in Fig. 2, with red arrows indicating the direction of the incident beam. Both target boxes were relatively similar in design. They were both machined from aluminum, with a cutout in the front to minimize the thickness of the entrance window, and both had a water-tight seal provided by an aluminum lid (not pictured) that bolts to the top of the box. In both cases, the experimental foils in each compartment between degraders — La, Cu and Ti for LANL and La, Cu and Al for BNL — were bundled together into packets using baling wire, to aid in sample retrieval with hot cell telemanipulators after the irradiation.

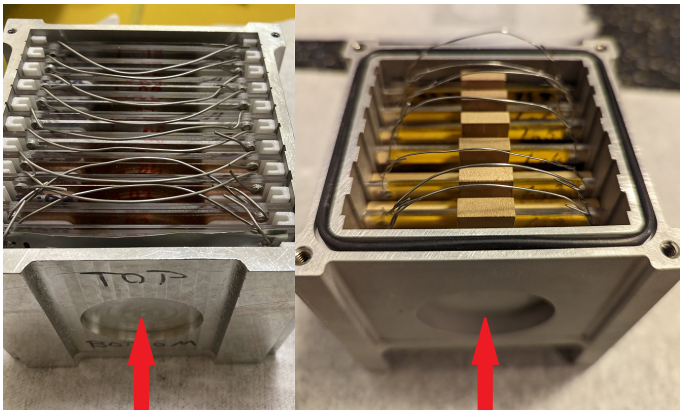


FIG. 2: Photos of the experimental target boxes used in the LANL (left) and BNL (right) irradiations.

Individual foil packets can be seen bundled together with wire, for ease of manipulation inside of the hot cells. The red arrows indicate the orientation of the incident proton beam.

Both stacks were irradiated with a nominal beam current of 200 nA for a duration of 1 hour, 6 seconds at LANL and 1 hour, 1 minute at BNL. The LANL irradiation took place on 13 September, 2022 and the BNL irradiation took place on 17 March, 2023. Both facilities utilized an inductive pickup current monitor, with cur-

rent readings recorded at a frequency of approximately 20 times per minute. The resolution of each current monitor was 1 nA, and the beam current was stable over the duration of both irradiations with an RMS fluctuation less than 3 nA. The measurements of the inductive pickup current monitors agreed quite well with the current determined using the monitor foils in the first (highest-energy) compartment. However, scattering and absorption of protons within the stacks themselves caused the beam current to drop as the beam traversed the stack.

II.2. Gamma Spectrometry

Following each irradiation the target boxes were retrieved from each respective hot cell, and the foils were separated and placed into individual plastic bags made of 50 μm thick polyethylene in order to prevent the spread of radioactive contamination during the gamma-ray assay. The time between end-of-bombardment and the first count of the lanthanum foils was approximately 2 hours at LANL and 1 hour at BNL, which meant the product with the shortest half-life that was independently measured was $^{132\text{m}}\text{La}$, with a half-life of 24.3(5) min [25]. The gamma counting process had differences between each site, but in general, short, initial counts were taken at the respective production facilities to capture the short-lived products, after which the foils were transferred to a secondary on-site counting laboratory where the gamma-ray background was lower. All gamma-ray assays were performed using mechanically cooled High-Purity Germanium (HPGe) detectors.

At LANL, the first counts of the lanthanum foils were performed using an ORTEC GEM p-type coaxial HPGe detector (model GEM20P-PLUS), at a distance ranging from 35–44 cm from the entrance window of the detector. These counts ranged in duration from 2–4 minutes, with the five highest-energy foils being counted twice, and the five lowest-energy foils being counted once. Following this, all the foils were transferred to a secondary on-site counting laboratory — internally referred to as “TarDIS” — which houses two ORTEC GEM p-type coaxial HPGe detectors (model GEM20P4-70-PL). All of the three detectors described utilize transistor-reset preamplifiers, which allowed for count rates of approximately 3 kHz at a dead-time of approximately 5%, while still maintaining good energy resolution (approximately 1.85 keV FWHM at 1.33 MeV). At the TarDIS counting lab, the count plan was to cycle all of the foils between both detectors over a 45 day period, with the count length increasing from 10 minutes at the beginning of the period to 24 hours at the end. However, one of the two detectors suffered an electronic malfunction after approximately 36 hours, and was replaced with the GEM20P-PLUS that had been used previously at the IPF loca-

tion. Initially the foils were counted 45 cm from the detector face, and were gradually brought closer in as they decayed, to as close as 10 cm. The same Eckert & Ziegler source set was used to calibrate all three detectors, which consisted of ^{152}Eu , ^{133}Ba , ^{137}Cs and ^{60}Co sealed point sources, of known activity (provided by the manufacturer) with a listed 95% confidence interval of $\pm 3\%$.

At BNL, two ORTEC GEM p-type coaxial HPGe detectors were used for the initial lanthanum foil counts at the BLIP facility — one having a transistor-reset preamplifier and another having a standard charge-sensitive preamplifier. Each of the 7 lanthanum foils were counted once on each detector, for approximately 10 minutes per count, at a distance of 62 cm on the charge-sensitive detector and 45 cm on the transistor-reset detector. Lead shielding was used to minimize the environmental background in the detector, however the samples were sufficiently far from the lead shielding so as to avoid substantial Compton-scattered background and lead x-rays. After the BLIP counts, the foils were transferred to a separate on-site counting laboratory, where three p-type HPGe detectors were utilized for gamma counting: an ORTEC IDM-200-V, an ORTEC Trans-SPEC-DX-100T, and an ORTEC GEM20P4-70-PL. The IDM and Trans-SPEC utilize charge-sensitive preamplifiers, while the GEM20P4 makes use of a transistor-reset preamplifier. The lanthanum foils were preferentially counted on the transistor-reset detector for the sake of improved statistics, however each lanthanum, copper and aluminum foil was counted on every detector to minimize the potential of systematic effects arising from any single detector. The foil-to-detector counting distances varied from 10–59 cm, depending on the detector, the foil being counted and the decay time. The BLIP and on-site detectors were all calibrated using the same source set: ^{152}Eu , ^{133}Ba , ^{137}Cs , ^{60}Co , and ^{241}Am point sources procured from Eckert & Ziegler, with a listed 95% confidence interval of $\pm 3\%$. After 7 days of counting at the BNL on-site counting laboratory, the foils were shipped to the TarDIS laboratory used in the LANL irradiation, where they were counted on the two ORTEC GEM20P4-70-PL detectors for an additional 35 day period, at a distance of 10 cm. The calibration source set was the same as previously described for that location.

III. DATA ANALYSIS

The residual nuclide production cross sections were extracted from the measured gamma-ray spectra in a consistent manner for both irradiations. The open-source CURIE python library was used for isotope identification and to extract the number of measured counts from each photopeak in the measured spectra, as well as to

generate the response functions (energy, resolution and efficiency) for each detector [26]. CURIE was also used to calculate production rates for each product isotope based on the peak fits in each foil. For the monitor foils, these production rates were used to calculate the beam current witnessed by each foil, and CURIE was used to determine the proton energy distributions within each foil. These calculated proton energies were then refined using a variance minimization procedure. Finally, the beam currents from the monitor foils were used to calculate the residual nuclide production cross sections from the production rates measured in the lanthanum foils, according to Eq. 1. The uncertainties in the reported cross sections are attributable to: statistical and systematic uncertainties from the peak fits, uncertainties in isotope half-lives and decay gamma branching ratios, uncertainties in the measured foil areal density, systematic uncertainties from the production rate determination, uncertainty in the evaluated monitor cross sections, and uncertainty in the detector efficiency.

III.1. Calibration and Peak Fitting

The analysis of the measured gamma-ray spectra was performed using the CURIE python library. The detector response functions consisted of energy, resolution and efficiency calibrations which were determined from a set of calibration standards of known activity, as described in Section II.2. This procedure was performed for each detector, at every distance that was used to count the experimental foils. Because the BNL foils were counted at BNL and LANL, with two different sets of calibration sources used between them, a cross-calibration was performed to ensure the detector efficiencies were consistent between the two sites. The calibration functions for the energy and resolution calibration were quadratic and linear, respectively, whereas the efficiency function used by CURIE consists of a semi-empirical “physical” efficiency model, based on the work of Vidmar *et al.* [27].

The main advantage of using such a model for the efficiency is in its ability to extrapolate well to energies above which calibration data are available, as demonstrated in Fig. 3. The black, dashed line shows the original fit to the efficiency data which were taken from the calibration sources, for which the photopeak energy ranged from 53.1622 keV (a minor line in ^{133}Ba) to a maximum energy of 1528.1 keV, from ^{152}Eu [28, 29]. However, the gamma spectra collected from the experimental foils extended as high as the 3009.645 keV gamma line in ^{56}Co , well above the highest calibration energy [30].

To correctly estimate the detector efficiencies above approximately 1500 keV, an extrapolation procedure was performed from the spectra collected during the exper-

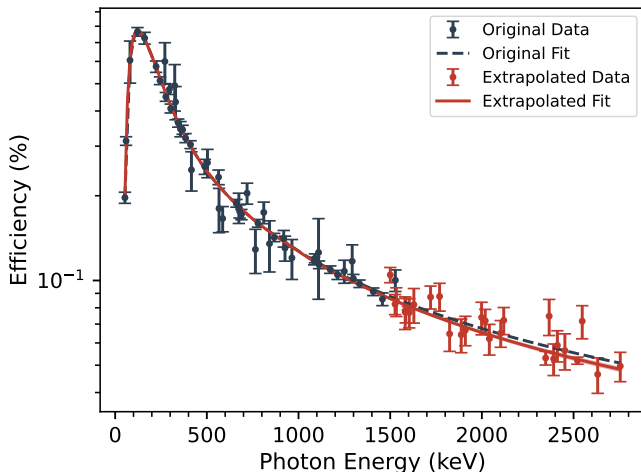


FIG. 3: Comparison of “physical” efficiency model fit to original efficiency data taken from the calibration sources (black, dashed line), versus the fit to efficiency data that was extrapolated from the experimental foil measurements (red, solid line).

iment, using isotopes having decay gammas both below 1500 keV (known efficiency) *and* above 1500 keV (unknown efficiency). The high-energy efficiency was estimated by multiplying the known low-energy efficiency by the appropriate ratios of I_γ and measured photopeak counts. Examples of isotopes with gamma emissions both above and below 150 keV that were used in this extrapolation are $^{133\text{m}}\text{Ce}$, $^{129\text{m}}\text{Ba}$, ^{132}La and ^{56}Co . This extrapolation is also shown in Fig. 3 as red points, with the solid red line indicating a fit to both the calibration data (black points) and the extrapolated data (red points). As can be seen, the original calibration (dashed black) extrapolated very well to higher energy. This would likely *not* have been the case for a log-polynomial fit to the same data.

Minor correction factors were applied to the efficiency, with a geometry correction factor accounting for the fact that the experimental “source” (activated foil) was not a perfect point source, but rather a distributed source over the beam-strike area. An additional correction factor accounted for attenuation through the Kapton tape and polyethylene encapsulation, as well as within the foils themselves (self-attenuation). The attenuation correction factors were derived from the XCOM library of photon attenuation coefficients [31, 32]. These corrections were generally quite small, with the largest geometry correction being 0.35% and the largest attenuation correction being 7.91%.

An example of a collected γ -ray spectrum with peaks fit using the CURIE code can be seen in Fig. 4. In general, the resolution of the HPGe detectors was quite good, such that there were very few peaks which could

not be resolved due to issues such as interference from neighboring lines. However, certain isotopes share decay gammas of the *exact* same energy, for example $^{132\text{m}}\text{La}$ and $^{132\text{g}}\text{La}$, which both decay into ^{132}Ba and therefore have a number of identical lines. In these cases, the overlapping peaks were excluded in favor of isolated decay gammas from those isotopes. Fig. 4 also illustrates the advantage of using a semi-automated peak fitting code like CURIE for the analysis, as the spectrum is clearly very complex and contains too many individual gamma lines for identifying and/or fitting individual peaks to be practical. In total, the entire data set (comprised of spectra from both irradiations) contained approximately 75,000 individual peak fits from 644 gamma spectra.

III.2. Production Rate Determination

The production rates were determined for each individual isotope by first using the number of counts, N_c , from each observed photopeak, and calculating the corresponding number of decays according to:

$$N_D = \frac{N_c}{I_\gamma \epsilon(E_\gamma)} \frac{t_{\text{real}}}{t_{\text{live}}} \quad (2)$$

where I_γ is the gamma branching ratio, $\epsilon(E_\gamma)$ is the detector efficiency at energy E_γ , and t_{real} and t_{live} are the real and live times of the data acquisition system, respectively. These decays are associated with a given start and stop time, t_{start} and t_{stop} . The CURIE library implements the general solution to the Bateman equations for radioactive production and decay [33], and solves for the production rates of any number of isotopes in a decay chain (originating from the same parent radionuclide) by taking advantage of the fact that the Bateman solutions are additive, and converting the problem into a linear system of the form:

$$\vec{M} \cdot \vec{R} = \vec{N}_D \quad (3)$$

where \vec{N}_D is a vector of observed decays for all isotopes in the chain, \vec{R} is a vector of production rates, and \vec{M} is a matrix of decays calculated from a decay chain of unit production rates for a single isotope in \vec{R} , during the interval t_{start} to t_{stop} of the associated element of \vec{N}_D . While CURIE only implements this approach for decay chains with a single parent isotope, this methodology was extended to work for multiple decay chains feeding the same isotopes, which was required in this work to fit the $A = 132$ and $A = 133$ decay chains.

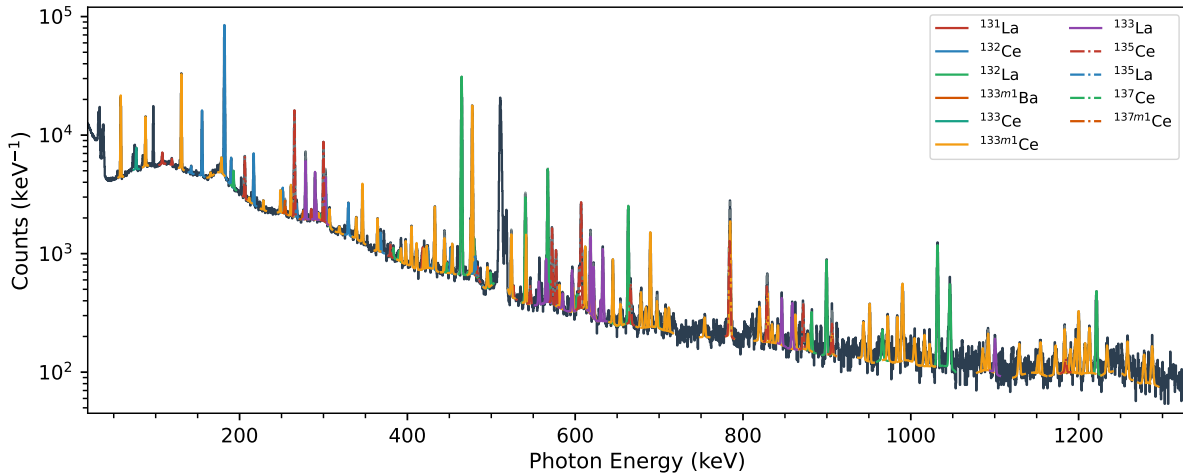


FIG. 4: Example of a gamma-ray spectrum with peaks identified and fit using CURIE – from the first lanthanum foil in the LANL stack, irradiated with approximately 91.3 MeV protons. This spectrum was collected approximately 4 hours after the end-of-bombardment.

An example of this fit to the $A = 133$ decay chain is shown in Fig. 5, which fit the production rates of ^{133m}Ce , ^{133g}Ce , ^{133}La and ^{133m}Ba . While ^{133g}Ba is likely also independently produced, it was not quantified with sufficient sensitivity to distinguish its independently produced activity from in-feeding from the other isotopes. Such an approach is very necessary in this case, as both ^{133m}Ce and ^{133g}Ce decay into ^{133}La (*i.e.*, ^{133}La has two parent isotopes), and all isotopes in this system feed into ^{133g}Ba . Therefore, there is neither a simple equation for calculating the production rate of a given isotope from measured activities, nor for calculating the measured activities from the number of observed decays.

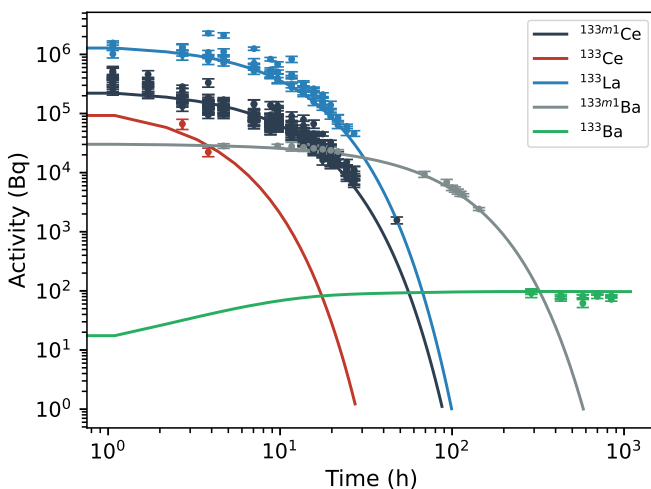


FIG. 5: Example of a fit to the $A = 133$ decay chain in a lanthanum foil irradiated with approximately 160 MeV protons at BNL.

The half-lives and major gamma branching ratios used for each of the isotopes observed in this study are listed in Tables X and XI in Appendix C. The uncertainties in the half-lives and gamma branching ratios were used in the determination of the uncertainties in production rates, however in general these were much smaller than the systematic uncertainties associated with the gamma counting process.

One additional feature of this data set was the presence of secondary (mostly thermal) neutrons, resulting from spallation reactions in the stack, and subsequent thermalization in the surrounding cooling water. This could potentially inflate our determination of reaction rates through (n,x) reactions resulting in the same product. Conveniently, we were able to use the ^{140}La ($T_{1/2} = 1.67855(12)$ d) product, resulting from neutron capture on the lanthanum foils, as a neutron flux monitor [34]. This was used in combination with a FLUKA Monte Carlo simulation to determine the neutron flux profile throughout the stack [35], showing that only the ^{64}Cu production rate in the copper monitor foils had a non-negligible contribution from secondary neutrons (from the capture reaction on ^{63}Cu). This effect has been corrected for in the reported cross sections.

III.3. Beam Currents and Energy Determination

The proton beam currents witnessed by each foil in each of the two irradiated stacks were determined using a set of monitor foils, which have well-characterized reaction channels that are included in the list of beam monitor reactions from the IAEA charged-particle cross

section database for medical radionuclide production [36]. This method is well described in other publications [19, 21], and has some advantages and disadvantages compared to other methods of measuring beam current. The main disadvantage is that the accuracy of the measured cross sections cannot exceed that of the monitor reaction cross sections, and in particular, any unknown systematic errors in the monitor cross sections will be applied (proportionally) to the measured cross sections. However, these effects can be mitigated by using multiple monitor reaction channels in multiple foil materials, and by comparing the monitor foil-derived beam currents to beam currents determined by electronic measurement, such as an inductive-pickup current monitor. The main advantage of this method is that it can correctly account for beam current losses within the stack, which would not be observable with an electronic beam current monitor. Also, issues such as electron suppression or other sources of “dark current” do not impact the measurement.

The beam current for an individual monitor channel is calculated from a measured production rate, R_i , using Eq. 1 where the cross section used is the flux-averaged cross section:

$$\bar{\sigma} = \frac{\int_0^\infty \sigma(E)\psi(E)dE}{\int_0^\infty \psi(E)dE} \quad (4)$$

where $\sigma(E)$ is the recommended cross section from the IAEA beam monitor library [36], and $\psi(E)$ is the proton flux calculated using a 1-D Monte Carlo stopping power code implemented in CURIE, which uses the Anderson & Ziegler formalism for stopping powers [26, 37]. This treatment accounts for the beam straggling which occurs towards the back of the stack. This was particularly significant for the BNL data set, which was degraded from 200 MeV incident energy down to just under 100 MeV in the rear foil.

The measured beam currents from each reaction channel as a function of proton energy were compiled for both stacks, and fit with a linear function ($I = I_0 + m \cdot E$) for the BNL stack and a square-root function ($I = I_0 + m \cdot \sqrt{E - 45}$) for the LANL stack. The measured per-channel beam currents and attending fits can be seen in Fig. 6, with the LANL stack shown in the upper panel and the BNL stack shown in the lower panel.

One complication for the BNL stack was that only the $^{27}\text{Al}(p,x)^{22}\text{Na}$ and $^{\text{nat}}\text{Cu}(p,x)^{58}\text{Co}$ reactions have recommended cross sections above 100 MeV, despite many experimental measurements in this energy region for the production of ^{24}Na (from ^{27}Al) and ^{56}Co , ^{62}Zn and ^{65}Zn (from $^{\text{nat}}\text{Cu}$), which were all observed reaction products in the monitor foils, and have IAEA-recommended cross sections below 100 MeV. To improve the quality of the beam current determination for the BNL stack,

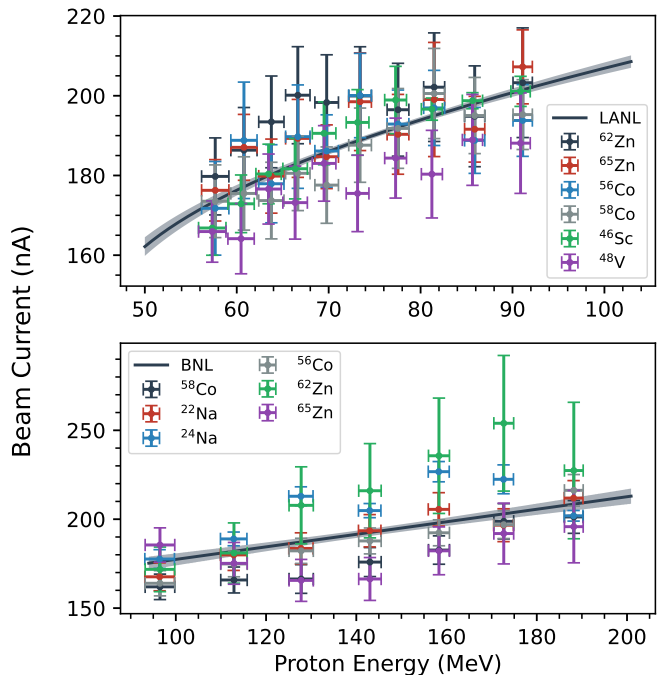


FIG. 6: Beam currents measured in each of the 6 monitor reaction channels utilized by the LANL stack (top) and BNL stack (bottom). The black line on each plot indicates a fit to the calculated beam currents as a function of energy.

a down-selected set of experimental data were used to generate monitor reaction cross sections in this energy region. This was done by performing a regression of the following 3-parameter log-polynomial function to the down-selected cross section data:

$$\sigma(E) = \sigma_{100} + \left(\frac{c_1}{E} \ln(E - 60)^2 + \frac{c_2}{E} \ln(E - 60) + \frac{c_3}{E} \right) (E - 100) \quad (5)$$

where σ_{100} is the IAEA-recommended cross section for that channel at 100 MeV, and c_1 , c_2 and c_3 are adjustable parameters. This functional form was selected to ensure that the fitted cross section agreed with the IAEA evaluation at 100 MeV. The resulting fits to these additional monitor channels can be seen in Appendix A. There were significant discrepancies between our apparent cross sections and the $^{\text{nat}}\text{Cu}(p,x)^{58}\text{Co}$ IAEA reference cross sections, which may indicate the need for future study of this channel [36].

The energy distributions predicted by the Anderson-Ziegler calculation in CURIE were adjusted using a “variance minimization” methodology, similar to the methods described in Graves *et al.* and Voyles *et al.* [19, 20]. In

this approach, a multiplier to the areal densities of all stack elements ($\Delta\rho$), as well as the incident energy (E_0) are treated as free parameters, and are varied in order to minimize a goodness-of-fit parameter: in this case the reduced χ^2 (or χ^2_ν). The purpose of this is not to presume that the densities of the stack elements or the incident energy were not well-known, but rather to correct for unaccounted systematics in the calculation of the proton energy spectra. A plot showing the calculation of the χ^2_ν for variation of $\Delta\rho$ and E_0 for the LANL stack can be seen in Fig. 7. For the LANL stack, the optimum E_0 and $\Delta\rho$ were found to be 99 MeV and -6.65%. For the BNL stack, only $\Delta\rho$ was optimized using this method, as there was not sufficient sensitivity of χ^2_ν to the incident energy. The resulting optimum density change for the BNL stack was found to be +1.75%.

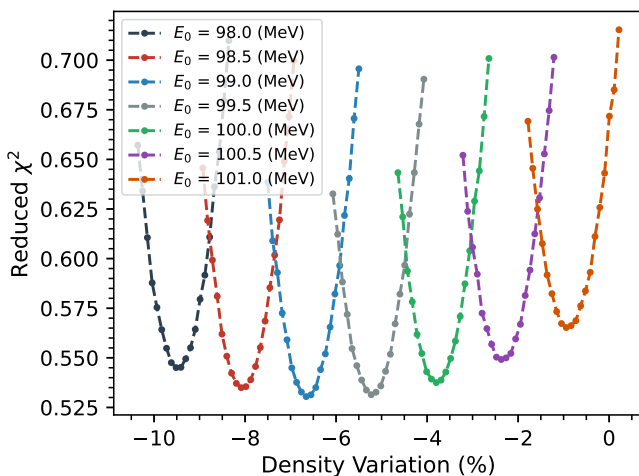


FIG. 7: Reduced χ^2 of the fit to the LANL monitor foil data, plotted as a function of degrader density variation and incident proton energy.

IV. RESULTS AND DISCUSSION

The cross sections for the products observed in this work were calculated from the measured production rates, R_i , the areal densities (ρr) and monitor-foil derived beam currents I_p , using Eq. 1. The uncertainties in the cross sections were calculated as the quadrature sum of the uncertainties from these three sources. The results of these measurements are tabulated in Table I for the ^{139}La products, Table II for products in the copper foils, and similarly in Table III for titanium products. The results for selected reaction channels that are of particular interest for medical applications or from a nuclear reaction modeling perspective are discussed below.

The results are shown in comparison to previous measurements from Tárkányi *et al.*, Morrell *et al.* and Becker *et al.* [15–17]. In general, the results show good agreement with previous measurements. Interestingly, the ^{134}Ce production cross section above 100 MeV was much larger than expected, which could have implications for medical isotope production applications. This work represents the first measurement of proton-induced reactions on lanthanum above 100 MeV, as well as the first measurement of many of these reaction products. Notably, the observation of ^{130}Ce represents the first measurement of an exclusive (p,10n) excitation function (*i.e.*, a cross section curve measured at multiple energies, including the threshold) in this energy range.

In addition, we compare our results to the TENDL-2023 evaluation, as well as default predictions from TALYS-2.0, EMPIRE-3.2.3, and ALICE-20 [22, 38–40]. A complete description of the default models used by each of these codes that are relevant to intermediate-energy proton-induced reactions can be found in Fox *et al.* [21]. The relevant differences are in the optical models (Koning-Delaroche in TALYS and EMPIRE versus Becchetti-Greenlees in ALICE), the level density models (CT Fermi gas in TALYS, enhanced GSM in EMPIRE, and shell-dependent Kataria-Ramamurthy in ALICE) as well as the default preequilibrium models. TALYS implements a two-component exciton model, which has been parameterized with a global fit to emission spectra for $A \geq 24$ and incident energies between 7 and 200 MeV [41]. The default preequilibrium model in EMPIRE is PCROSS, a more simplistic one-component exciton model, while ALICE makes use of the Hybrid Monte-Carlo Simulation (HMS) precompound decay model. Additionally, the treatment of angular momentum in ALICE is generally poorer than the other two codes, which tends to lead to inaccurate isomeric ratio predictions. Overall, all three codes struggled to predict many of the multi-particle-out channels, which would seem to indicate a deficiency in the preequilibrium models used by these codes. A selected parameter adjustment using the TALYS-2.0 code was performed in this work, which is described in Section V, and the results are shown here for comparison.

IV.1. $^{139}\text{La}(p,6n)^{134}\text{Ce}$ Cross Section

Cerium-134 is a challenging isotope to quantify, due to its relatively weak gamma-emission probability, with the 0.209(15)%, 130.4 keV gamma being the strongest emission [14]. Because the ^{134}Ce production cross section is generally quite high in the energy region explored in this work, it is not the counting statistics that are a challenge. Rather, it is the fact that in this photon energy range there is a significant Compton background for most types of HPGe detectors, including those used in this measure-

TABLE I: Summary of lanthanum cross sections measured in this work. Subscripts (c) and (i) indicate cumulative and independently measured cross sections, respectively. The subscript ($m+$) indicates the cross section includes contributions from one or more isomers of the same product isotope, but is otherwise independent of feeding from other products. Uncertainties are given in the least significant digit, *i.e.*, 188.4(21) means 188.4 ± 2.1 , *etc.*

$^{139}\text{La}(p,x)$ Production cross sections (mb)									
E_p (MeV)	188.3(21)	172.8(22)	158.5(23)	143.2(25)	127.9(27)	113.1(29)	96.7(33)	91.3(11)	86.1(11)
	81.7(11)	77.8(12)	73.7(12)	70.0(13)	66.9(13)	64.1(14)	61.1(14)	58.0(15)	-
$^{139}\text{Ce}_{(m+)}$	4.04(28)	4.53(28)	5.02(30)	5.52(28)	6.18(40)	6.49(26)	7.66(46)	7.96(27)	8.14(29)
	8.89(30)	8.49(31)	9.48(33)	9.61(34)	11.28(38)	10.86(39)	11.55(40)	12.33(49)	-
$^{137m}\text{Ce}_{(i)}$	14.53(55)	16.90(61)	18.28(67)	20.59(73)	23.82(85)	26.75(99)	31.4(13)	34.0(12)	36.9(12)
	39.9(14)	40.4(14)	44.9(16)	47.6(16)	54.4(19)	56.7(19)	60.0(21)	67.3(24)	-
$^{137g}\text{Ce}_{(i)}$	-	5.3(13)	5.26(84)	3.9(18)	7.5(20)	4.8(22)	-	13.4(18)	13.5(13)
	11.5(27)	14.3(31)	18.0(37)	21.0(23)	22.9(36)	24.0(28)	22.6(27)	27.2(39)	-
$^{136}\text{Cs}_{(m+)}$	0.506(31)	0.490(28)	0.431(23)	0.388(19)	0.321(18)	0.255(17)	0.176(12)	0.1038(75)	0.101(23)
	0.097(18)	0.150(67)	-	0.229(62)	0.131(30)	0.134(16)	0.093(12)	0.082(20)	-
$^{135}\text{La}_{(i)}$	86.3(54)	121.4(91)	104.3(84)	121.2(74)	136.3(87)	162(12)	161(14)	134.5(87)	147(11)
	141.8(83)	139.5(94)	141(10)	139(11)	149(12)	145(12)	140(12)	140(11)	-
$^{135}\text{Ce}_{(m+)}$	24.73(91)	28.3(10)	31.6(11)	35.8(12)	44.7(15)	52.0(18)	67.0(25)	76.8(25)	85.0(28)
	97.1(31)	103.3(34)	129.3(42)	157.8(52)	208.3(68)	256.6(84)	319(10)	410(14)	-
$^{135m}\text{Ba}_{(i)}$	17.42(71)	18.18(71)	17.00(61)	16.59(61)	15.91(61)	15.01(63)	12.64(50)	11.51(61)	11.33(69)
	8.76(34)	8.48(45)	6.44(48)	7.96(63)	6.12(71)	-	-	-	-
$^{134}\text{Ce}_{(i)}$	30.2(23)	35.1(28)	35.2(20)	39.9(16)	49.5(20)	62.2(25)	87.0(35)	97.9(34)	118.2(40)
	151.5(51)	181.3(59)	239.4(78)	265.2(87)	285.9(94)	244.0(80)	179.8(61)	107.4(41)	-
$^{133}\text{La}_{(i)}$	106.0(38)	119.7(41)	124.8(42)	145.7(49)	164.7(56)	169.1(59)	169.5(64)	187.6(60)	183.1(59)
	130.8(42)	88.7(28)	57.6(18)	24.56(78)	12.62(40)	4.41(14)	-	-	-
$^{133m}\text{Ce}_{(i)}$	16.49(59)	18.48(64)	21.81(73)	27.08(90)	37.5(13)	45.6(16)	73.2(27)	110.6(35)	123.6(40)
	133.0(42)	98.4(31)	67.0(21)	30.91(99)	11.02(35)	2.540(82)	0.500(16)	-	-
$^{133g}\text{Ce}_{(i)}$	3.32(12)	3.75(13)	4.72(16)	5.45(18)	7.15(24)	9.04(32)	14.17(53)	19.84(64)	23.25(74)
	25.03(80)	20.79(66)	14.81(47)	8.26(26)	2.982(95)	0.640(21)	-	-	-
$^{133m}\text{Ba}_{(i)}$	20.97(75)	20.98(72)	20.34(68)	19.64(65)	18.28(62)	15.25(53)	10.53(39)	10.57(34)	8.48(27)
	6.81(22)	5.59(18)	5.23(17)	5.33(17)	6.05(19)	6.59(21)	7.32(24)	9.30(30)	-
$^{132m}\text{La}_{(i)}$	43.7(16)	42.1(15)	49.5(17)	58.7(20)	68.5(23)	63.4(22)	38.6(14)	33.9(11)	19.75(63)
	9.68(31)	3.96(13)	1.420(45)	-	-	-	-	-	-
$^{132}\text{Cs}_{(i)}$	5.53(21)	5.22(19)	4.64(16)	4.26(15)	3.71(13)	3.17(12)	2.74(11)	2.527(84)	2.499(85)
	2.399(79)	2.156(74)	1.961(66)	1.703(58)	1.469(52)	1.096(38)	0.690(26)	0.386(14)	-
$^{132}\text{Ce}_{(m+)}$	17.38(63)	18.23(63)	21.47(72)	26.15(87)	36.7(12)	50.0(18)	58.5(22)	71.4(23)	37.1(12)
	14.48(46)	3.20(10)	0.508(16)	-	-	-	-	-	-
$^{131}\text{La}_{(c)}$	66.9(26)	73.1(27)	79.8(30)	89.9(33)	97.1(37)	84.1(33)	16.70(88)	6.94(55)	1.82(32)
$^{131}\text{Ba}_{(m+)}$	20.8(14)	18.9(13)	13.8(14)	10.3(15)	8.2(18)	4.2(15)	7.88(70)	12.18(64)	15.29(59)
	-	20.49(66)	21.15(68)	16.28(52)	12.38(40)	6.83(22)	2.791(93)	0.685(25)	-
$^{130}\text{Ce}_{(i)}$	7.31(41)	7.67(51)	9.63(47)	11.80(61)	11.18(46)	2.84(32)	-	-	-
$^{129}\text{Cs}_{(m+)}$	30.0(11)	24.35(84)	20.37(69)	18.26(61)	16.81(57)	14.70(52)	7.81(29)	-	1.660(85)
$^{129m}\text{Ba}_{(c)}$	10.07(36)	9.41(33)	8.09(27)	6.54(22)	4.65(16)	4.85(17)	3.27(12)	-	-
$^{129g}\text{Ba}_{(c)}$	32.6(12)	34.3(12)	33.9(11)	25.61(85)	10.63(36)	5.87(21)	3.51(13)	3.18(10)	1.939(62)
$^{128}\text{Ba}_{(c)}$	35.7(13)	32.0(12)	24.42(87)	15.34(54)	13.50(48)	10.14(37)	0.701(31)	-	-
$^{127}\text{Xe}_{(c)}$	33.7(13)	26.2(10)	23.08(83)	19.79(70)	11.26(46)	2.17(10)	0.701(34)	-	-
$^{127}\text{Cs}_{(c)}$	34.8(16)	28.8(12)	23.49(93)	19.10(96)	12.62(76)	-	-	-	-
$^{126}\text{I}_{(i)}$	0.766(81)	0.743(85)	0.413(31)	0.262(30)	0.33(10)	-	-	-	-
$^{126}\text{Ba}_{(c)}$	6.79(44)	4.14(30)	3.75(35)	2.84(29)	1.32(28)	-	-	-	-
$^{125}\text{Xe}_{(c)}$	16.58(66)	12.64(45)	7.98(28)	2.856(99)	1.380(54)	0.556(26)	-	-	-
$^{125}\text{Cs}_{(c)}$	19.5(44)	14.0(27)	8.9(19)	-	-	-	-	-	-
$^{123}\text{Xe}_{(c)}$	4.31(23)	2.084(90)	1.261(72)	0.622(64)	-	-	-	-	-
$^{123}\text{I}_{(i)}$	1.51(25)	1.047(86)	0.745(85)	0.352(77)	-	-	-	-	-

TABLE II: Summary of copper cross sections measured in this work. The uncertainty format and subscript designations (c), (i) and ($m+$) remain the same as in Table I. Products which were used as beam current monitors (and are therefore somewhat circular) are indicated with a *, *e.g.* $^{65}\text{Zn}_{(i)}^*$.

$^{\text{nat}}\text{Cu}(\text{p},\text{x})$ Production cross sections (mb)									
E_p (MeV)	188.2(21)	172.7(22)	158.3(23)	143.0(25)	127.8(27)	112.9(29)	96.5(33)	91.1(11)	85.9(11)
	81.5(11)	77.5(12)	73.4(12)	69.8(13)	66.6(13)	63.8(14)	60.8(14)	57.7(15)	-
$^{65}\text{Zn}_{(i)}^*$	1.240(77)	1.450(92)	1.565(78)	1.589(85)	1.717(97)	1.96(11)	2.42(11)	2.512(81)	2.523(81)
	2.82(19)	2.90(13)	3.27(18)	3.28(10)	3.59(15)	3.65(16)	4.07(14)	4.16(14)	-
$^{64}\text{Cu}_{(i)}$	24.8(12)	29.1(25)	32.2(34)	30.6(13)	37.5(13)	35.0(25)	41.7(17)	37.3(19)	40.1(27)
	43.9(16)	40.0(49)	42.7(23)	47.2(35)	48.7(24)	49.0(29)	50.6(20)	49.7(26)	-
$^{62}\text{Zn}_{(i)}^*$	2.19(10)	2.74(11)	2.89(12)	3.09(13)	3.54(13)	3.75(19)	4.55(20)	4.96(19)	5.16(17)
	5.77(22)	6.04(21)	6.70(26)	7.26(26)	8.03(30)	8.56(30)	9.29(32)	10.36(37)	-
$^{61}\text{Cu}_{(c)}$	31.2(16)	37.2(17)	38.3(16)	39.2(18)	44.4(20)	45.9(22)	53.3(25)	56.2(21)	61.1(22)
	65.4(23)	69.2(25)	74.9(26)	79.6(28)	82.9(29)	85.4(30)	86.2(31)	89.6(32)	-
$^{60}\text{Co}_{(m+)}$	10.89(71)	11.47(62)	11.50(63)	11.22(53)	11.14(54)	10.98(44)	11.25(52)	-	11.8(16)
	14.0(60)	10.59(98)	13.8(50)	9.99(70)	13.6(56)	10.38(73)	14.7(23)	11.00(60)	-
$^{59}\text{Fe}_{(i)}$	1.206(49)	1.158(42)	1.138(40)	1.069(36)	1.024(50)	0.953(34)	0.837(35)	0.793(28)	0.787(27)
	0.787(43)	0.771(27)	0.741(85)	0.720(26)	0.695(27)	0.630(23)	0.577(54)	0.496(16)	-
$^{58}\text{Co}_{(m+)}^*$	42.9(18)	44.6(20)	43.2(16)	44.3(17)	44.8(18)	47.3(17)	48.2(18)	50.5(17)	50.4(18)
	51.0(23)	47.4(17)	44.1(14)	39.1(15)	37.0(12)	33.1(12)	31.4(10)	30.4(11)	-
$^{57}\text{Ni}_{(c)}$	1.848(81)	1.955(82)	1.905(81)	1.938(88)	1.947(87)	1.845(85)	1.570(76)	1.467(78)	1.280(58)
	1.213(47)	1.118(58)	1.261(53)	1.377(70)	1.576(65)	1.827(74)	2.09(10)	2.28(10)	-
$^{57}\text{Co}_{(i)}$	41.5(18)	41.8(17)	41.8(17)	42.5(19)	42.4(18)	41.6(18)	40.1(19)	40.3(17)	38.2(13)
	36.6(13)	35.1(12)	35.3(13)	36.5(13)	40.2(15)	43.2(15)	48.8(20)	54.1(19)	-
$^{56}\text{Ni}_{(c)}$	0.140(21)	0.128(16)	0.144(23)	0.141(15)	0.115(10)	0.0781(53)	0.0701(68)	-	0.096(10)
	-	0.108(12)	-	0.132(22)	-	-	-	-	-
$^{56}\text{Mn}_{(i)}$	2.331(92)	2.50(10)	2.39(13)	1.945(69)	1.988(75)	1.508(56)	1.123(58)	1.162(49)	1.144(47)
	1.084(62)	1.047(43)	0.993(44)	0.734(70)	0.614(56)	0.490(39)	0.408(44)	0.340(31)	-
$^{56}\text{Co}_{(c)}^*$	12.67(48)	12.17(46)	12.29(44)	12.21(44)	11.81(41)	11.06(41)	10.10(40)	10.53(39)	10.76(36)
	12.22(47)	12.81(44)	14.09(62)	12.76(46)	11.49(66)	8.22(30)	5.71(35)	2.73(10)	-
$^{55}\text{Co}_{(c)}$	2.005(85)	2.014(83)	2.006(93)	1.870(82)	1.735(67)	1.568(84)	1.619(85)	1.719(85)	1.529(64)
	1.238(51)	0.916(53)	0.465(28)	0.211(28)	0.105(18)	0.061(17)	0.042(11)	0.053(15)	-
$^{54}\text{Mn}_{(i)}$	16.69(62)	15.46(57)	14.76(68)	13.57(55)	11.90(49)	10.45(40)	6.94(30)	6.18(20)	4.68(15)
	3.90(15)	3.55(17)	3.68(20)	3.98(15)	4.53(21)	-	-	-	-
$^{52}\text{Mn}_{(c)}$	5.31(21)	4.89(20)	4.20(16)	3.61(13)	2.68(11)	1.959(77)	1.763(77)	1.752(61)	1.250(43)
	0.841(31)	0.394(16)	-	0.047(16)	-	-	-	-	-
$^{51}\text{Cr}_{(c)}$	11.65(46)	9.75(38)	8.16(31)	6.36(24)	5.09(21)	3.94(17)	1.464(88)	-	-
$^{48}\text{V}_{(i)}^*$	1.957(71)	1.454(56)	1.072(37)	0.691(24)	0.449(15)	0.300(13)	0.0553(48)	-	-

TABLE III: Summary of titanium cross sections measured in this work. The uncertainty format and subscript designations (c), (i) and ($m+$) remain the same as in Table I. Products which were used as beam current monitors (and are therefore somewhat circular) are indicated with a *, *e.g.* $^{48}\text{V}_{(i)}^*$.

$^{\text{nat}}\text{Ti}(\text{p},\text{x})$ Production cross sections (mb)									
E_p (MeV)	90.9(11)	85.6(11)	81.2(11)	77.3(12)	73.1(12)	69.5(13)	66.3(13)	63.5(14)	60.5(14)
$^{48}\text{V}_{(i)}^*$	7.15(27)	7.84(28)	8.11(30)	8.96(32)	9.30(33)	10.53(38)	10.75(43)	11.81(43)	11.93(51)
$^{48}\text{Sc}_{(i)}$	2.50(30)	2.60(33)	2.49(36)	2.68(38)	2.48(41)	2.23(47)	2.33(47)	2.05(39)	1.98(35)
$^{47}\text{Sc}_{(i)}$	19.87(86)	20.13(69)	20.11(89)	20.76(79)	20.5(11)	20.97(69)	20.97(71)	21.06(68)	21.14(69)
$^{46}\text{Sc}_{(m+)}^*$	39.5(15)	40.8(14)	41.9(14)	43.9(15)	44.5(15)	45.9(15)	46.0(15)	48.1(16)	49.1(17)
$^{44\text{m}}\text{Sc}_{(i)}$	18.38(70)	19.35(81)	20.53(79)	21.45(81)	20.94(79)	19.56(84)	17.94(83)	16.63(76)	14.26(63)
$^{43}\text{Sc}_{(c)}$	27.6(53)	28.7(56)	24.9(63)	26.5(66)	-	-	-	-	-
$^{43}\text{K}_{(c)}$	1.706(82)	1.619(98)	1.497(64)	1.402(57)	1.366(54)	1.369(59)	1.298(45)	1.383(47)	1.437(59)
$^{42}\text{K}_{(i)}$	5.81(44)	6.01(40)	5.87(40)	6.39(44)	6.10(42)	6.60(43)	6.41(42)	6.22(42)	5.26(34)

ment, arising from higher energy gamma-rays scattering out of the detector. Additionally, above proton energies of approximately 60 MeV, the ($T_{1/2} = 11.50$ day) product ^{131}Ba is produced, which has a 2.18(3)% gamma emission at 133.617 keV, which may interfere with the 130.4 keV ^{134}Ce emission depending on the resolution of the detector.

Instead, the preferred signature for ^{134}Ce is the 5.04(20)%, 604.721 keV gamma emitted by its decay product ^{134}La . Lanthanum-134 has a half-life of only 6.45 minutes, much shorter than the 3.16 day half-life of ^{134}Ce , which means it reaches secular equilibrium with ^{134}Ce after only a few hours. However, even this approach is not foolproof, as the ($T_{1/2} = 17.7$ h) ^{135}Ce isotope produced via the (p,5n) channel emits multiple gamma-rays which overlap at this energy, meaning it must have time to sufficiently decay (≈ 7 days) before the ^{134}La decay can be observed without contamination.

The measured cross sections for ^{134}Ce production can be seen in Fig. 8 in comparison to other measurements and theoretical predictions. The most notable result is that the measured cross sections were much higher than theoretical predictions in the 100–200 MeV energy region. This may have implications for bulk production of this isotope for medical applications, as it would imply a higher production rate at facilities utilizing these higher energy beams than theoretical estimates had previously suggested.

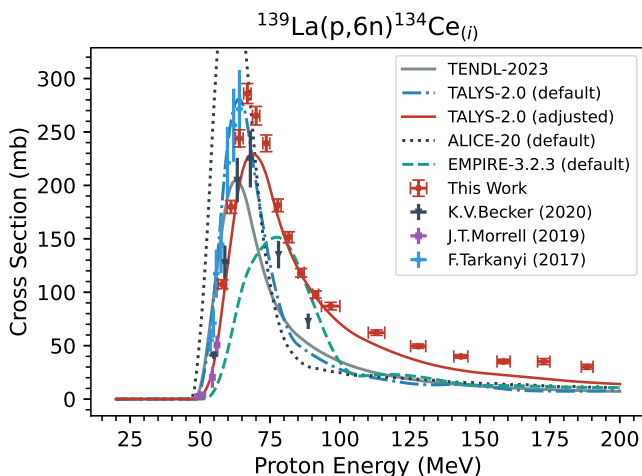


FIG. 8: Measured cross sections for the $^{139}\text{La}(p,6n)^{134}\text{Ce}$ reaction.

In general these results agree quite well with previous measurements. However, there is a significant difference in the two highest energy data points from Becker *et al.*, which is not explained by the reported error margins. One potential source of discrepancy could be the choice of gamma line used for quantifying ^{134}Ce , as the Becker *et al.* measurement relied solely upon the 0.209%, 130.4 keV

gamma branch discussed previously. While that gamma decay was observed in this work, it was supplemented with the ^{134}La decay gamma at 604.721 keV, which typically had lower peak fitting uncertainties than the 130.4 keV gamma.

In addition to under-predicting the cross section at high energy, the default models generally struggled to predict the centroid energy of the “compound peak”, though not as significantly as has been reported in previous versions of these codes [16]. We expect this is due to differences in the predicted neutron emission spectra arising from the different level densities and preequilibrium reaction models used by each code, which would affect how much energy is “carried away” by these neutrons prior to the nucleus reaching a compound state. In the adjusted TALYS-2.0 model, this effect has been improved, though not completely corrected, with modifications to the default preequilibrium parameters, to be discussed in more detail below.

IV.2. $^{139}\text{La}(p,n)^{139}\text{Ce}$ Cross Section

The product ^{139}Ce was measured via its 79.90(5)% intensity, 165.86 keV gamma emission, which was clearly observable several days after the end-of-bombardment due to this isotope’s relatively long half-life of 137.641(20) days. This also included feeding from the ^{139m}Ce isomer, which has a half-life of only 57.58(32) s, and decays via a 100% isomeric transition to the ground state. The measured cross sections for the $^{139}\text{La}(p,n)^{139}\text{Ce}_{(m+)}$ channel can be seen in Fig. 9.

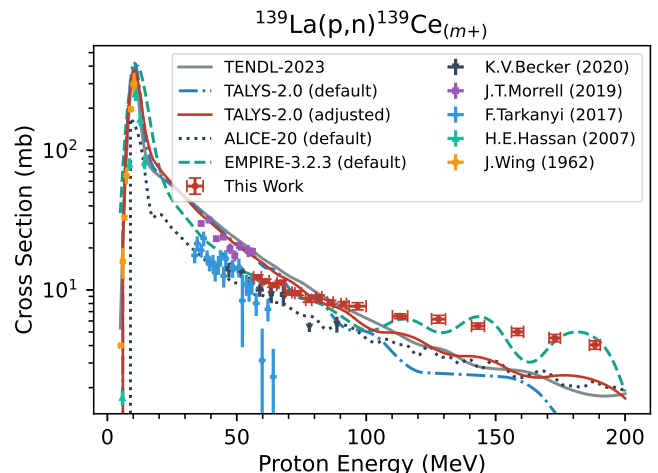


FIG. 9: Measured cross sections for the $^{139}\text{La}(p,n)^{139}\text{Ce}$ reaction.

The results agree quite well with most of the existing measurements, although there is a large amount of scat-

ter in these data. It is unclear why this might be the case, as the 165.86 keV gamma line is well-isolated from contaminants and quite strong, but could be attributed to poor counting statistics in these measurements if the lanthanum foil were not counted a sufficient length of time — in our experiment the 165.86 keV line typically had a count rate below 1 s^{-1} .

In general the reaction modeling is quite good, with ALICE generally performing best at low energy and EMPIRE being the best code at predicting the high-energy behavior. Similar to the (p,6n) channel, the cross section in the 100–200 MeV region was higher than most of the codes predicted, although by a far smaller percentage. This may also have significance for medical isotope production applications, as ^{139}Ce is the primary contaminant of concern when producing ^{134}Ce , due to its long half-life and inability to be chemically separated from ^{134}Ce [11, 13]. Therefore, this cross section sets a fundamental lower limit to the possible radiopurity with which ^{134}Ce can be produced.

IV.3. $^{139}\text{La}(p,3n)^{137m,g}\text{Ce}$ Cross Sections

Both the isomer ($J_\pi = 11/2^-$) and ground state ($J_\pi = 3/2^+$) of ^{137}Ce were independently observed in this work, formed through the (p,3n) reaction channel. The measured cross sections for the formation of these products are shown in Fig. 10.

The ^{137m}Ce isomer decays with a 1.433(13) day half-life, mostly via an isomeric transition to the ground state, accompanied by a 254.29 keV gamma emission with an 11.1(4)% branching ratio. This allowed the production of the isomer to be quantified relatively accurately. Unfortunately, the fact that the isomer feeds into the shorter-lived ($T_{1/2} = 9.0(3)$ h) ground state makes the quantification of the ground state population somewhat difficult. This is compounded by the relatively weak gamma-emission probability of the ground state, with a 1.680(84)% intense 447.15 keV gamma being the strongest emission. Distinguishing the independent ^{137}Ce ground state production from isomeric feeding required fitting spectra shortly (a few hours) after the end-of-bombardment, where the signal-to-noise ratio of the 447.15 keV gamma line was quite low due to the Compton continuum arising from many higher energy gamma decays. Therefore the uncertainty on this cross section was generally very large, and a few of the BNL data points were omitted as the uncertainty was greater than 50%.

In both the isomer and ground state, there is good agreement with existing measurements. While there is a significant amount of fluctuation in the ground state data, this is generally within the large error bounds that

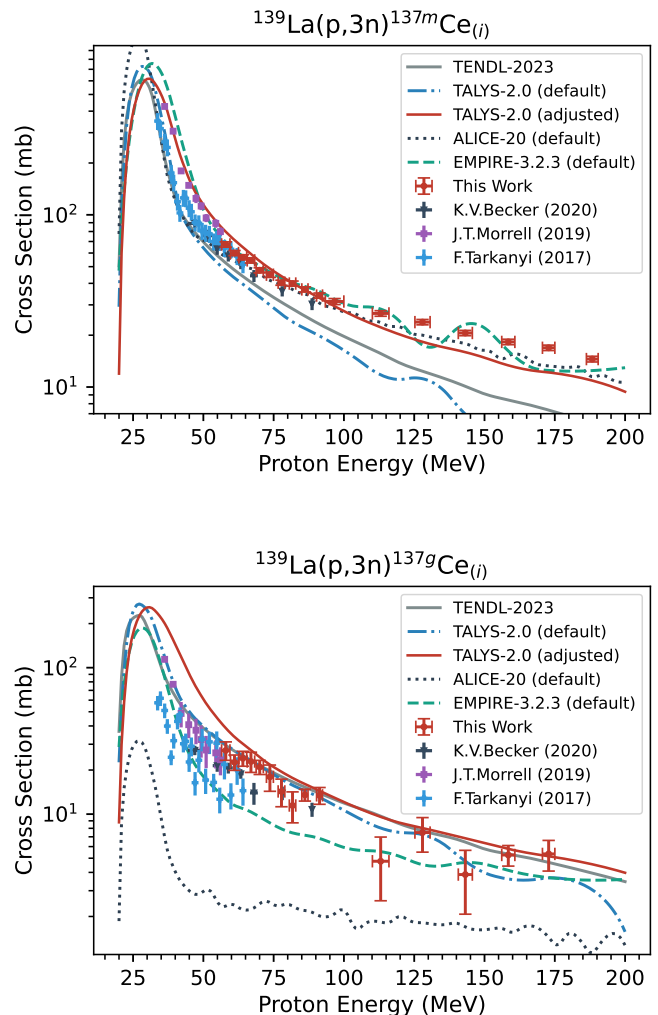


FIG. 10: Measured cross sections for the $^{139}\text{La}(p,3n)^{137m}\text{Ce}$ (top) and $^{139}\text{La}(p,3n)^{137g}\text{Ce}$ (bottom) reactions.

arise from the difficulty described above. Most of the reaction modeling codes produced reasonable predictions of the ^{137m}Ce (isomer) population, with ALICE-20 giving the best result across the span of energies. However, ALICE greatly under-predicted the ground state population, and due to the rather large variability in the measured data for ^{137g}Ce , it is unclear which of the other models performed best. Because most of the (p,3n) cross section populates the isomer, the total cross section for this channel is relatively well-predicted by the models, with only ALICE greatly over-predicting the m/g (isomer-to-ground state) ratio. This is in accordance with a general observation of relatively poor angular momentum modeling in ALICE [21, 42].

IV.4. $^{139}\text{La}(p,5n)^{135}\text{Ce}$ Cross Section

The population of ^{135}Ce via the (p,5n) reaction channel was relatively well-quantified, due to a large number of intense gamma emissions ranging from 119.52 keV ($I_\gamma = 1.30(9)\%$) to 1184.09 keV ($I_\gamma = 1.09(5)\%$), six of which had a gamma branching ratio greater than 10%. This cross section also includes the population of the ^{135m}Ce isomer, as its 20(1) second half-life was too short to be independently measured before it decayed with a 100% isomeric transition to the ground state. The measured cross sections for this channel are plotted in Fig. 11.

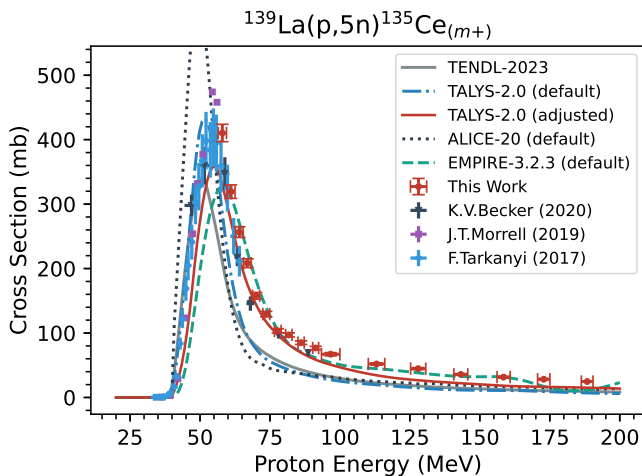


FIG. 11: Measured cross sections for the $^{139}\text{La}(p,5n)^{135}\text{Ce}$ reaction.

The results of this work show excellent agreement with previous measurements, likely due to the large production cross section and high accuracy with which this isotope's activity can be quantified. TALYS and ALICE show good agreement in the prediction of the compound peak, though ALICE somewhat over-estimates the maximum cross section. EMPIRE struggled to predict both the centroid energy and magnitude of the compound peak, although it has the best prediction above ≈ 70 MeV. This could be a result of better preequilibrium modeling parameters used in the EMPIRE exciton model. However, it could also be a numerical artifact arising from EMPIRE's limitations on the number of tracked ejectile particles, essentially forcing the cross section to be artificially higher at high energies.

For medical isotope production applications, ^{135}Ce ($T_{1/2} = 17.7(3)$ h) is the longest-lived contaminant to ^{134}Ce production, aside from the much longer-lived ^{139}Ce , and cannot be chemically removed. However, because the ^{135}Ce half-life is shorter than ^{134}Ce , the radiopurity of ^{134}Ce can be improved by waiting for ^{135}Ce to decay away — although the decay time cannot be so

long that the $^{134}\text{Ce}/^{139}\text{Ce}$ ratio is significantly impacted. Because of the trade-off between ^{135}Ce and ^{139}Ce impurity, it is essential to measure the magnitude and energy dependence of each of these cross sections if one is to optimize the ^{134}Ce production scenario.

IV.5. $^{139}\text{La}(p,7n)^{133m,g}\text{Ce}$ Cross Sections

The isomer ($J_\pi = 9/2^-$) and ground state ($J_\pi = 1/2^+$) of ^{133}Ce were accurately quantified via a large number of gamma decays in the ($T_{1/2} = 5.1(3)$ h) isomer, and the 15.9(23)% intense 76.9 keV gamma emission from the ($T_{1/2} = 97(4)$ min) ground state. Unlike the (p,3n) reaction populating ^{137}Ce , the ground state of ^{133}Ce was relatively straightforward to independently quantify due to the isomer exclusively decaying to ^{133}La , with no population of the ground state of ^{133}Ce . The main challenge associated with these (p,7n) channels was to ensure consistency with the other products in the overlapping $A = 133$ decay chains: ^{133}La , ^{133m}Ba and ^{133g}Ba . However, this did not have any impact on the accuracy of the $^{133m,g}\text{Ce}$ products themselves. The measured cross sections can be seen in Fig. 12.

The experimental data on these channels are quite sparse, with only four measurements of ^{133m}Ce from Becker *et al.* and two from Tárkányi *et al.* [15, 17]. However, where they overlap, the agreement is quite good. The consistency of the measurements in this and other channels would seem to indicate that the beam current determination and energy assignments of the various measurements agree quite well, and that any systematic differences are likely attributable to specifics of the activity determination (counting, peak-fitting, decay-corrections, *etc.*) associated with individual isotopes, rather than some global difference.

For both ^{133m}Ce and ^{133g}Ce , no particular reaction model gives a satisfactory prediction of the cross section. Most of the models over-predict the ground state population and under-predict the isomer, except for EMPIRE which under-predicts them both. Once again, ALICE gives very poor predictions of the m/g ratio, with almost no population of the isomer. Also, the default codes give generally poor predictions of the centroid energy of the compound peak and the overall shape, which we likely attribute to the preequilibrium modeling.

IV.6. $^{139}\text{La}(p,10n)^{130}\text{Ce}$ Cross Section

While many other reaction channels were observed, one final product isotope that is particularly interesting is ^{130}Ce , resulting from the exclusive (p,10n) reaction

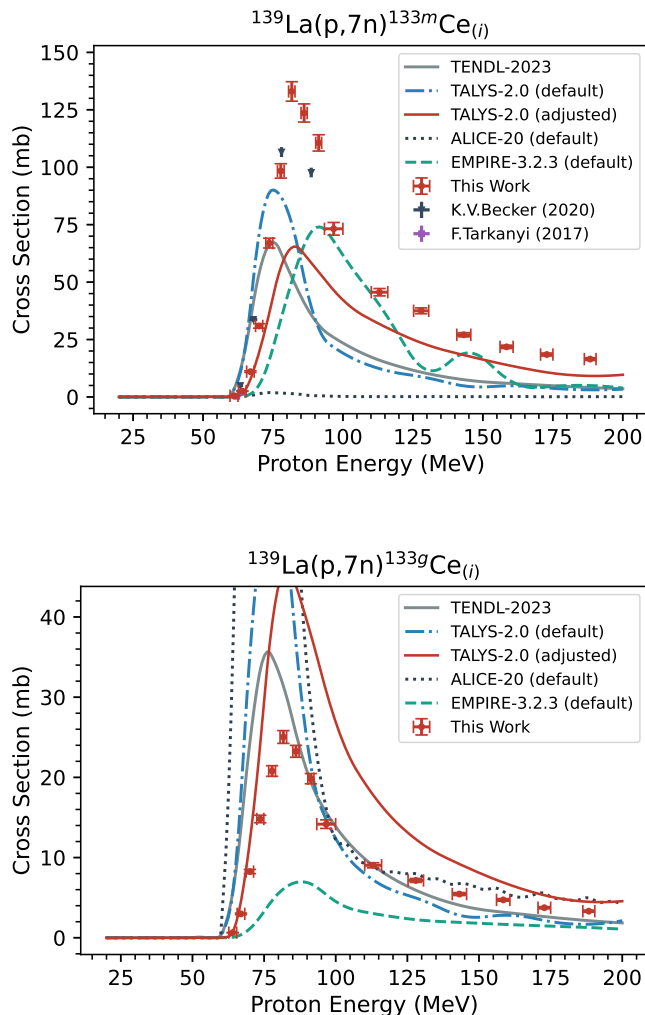


FIG. 12: Measured cross sections for the $^{139}\text{La}(p,7n)^{133m}\text{Ce}$ (top) and $^{139}\text{La}(p,7n)^{133g}\text{Ce}$ (bottom) reactions.

on ^{139}La . We believe that this represents the first measurement of an independent, exclusive (p,10n) excitation function in this energy range in the literature. While there are two measurements of the $^{124}\text{Sn}(p,10n)^{115}\text{Sb}$ reaction on tin targets enriched in ^{124}Sn from Alexandryan *et al.* and Balabekyan *et al.*, they were each only measured at one energy point — 660 MeV and 3.65 GeV, respectively — and therefore did not capture either the threshold of the reaction or the shape of its excitation function [43, 44]. Also, while there are several measurements of residual products resulting from (p,10n) reactions, they are either cumulative cross sections or include contributions from other target isotopes.

While ^{130}Ce does have uniquely identifying gamma emissions, the initial counts after end-of-bombardment had contaminating gamma lines in the ^{130}Ce peaks, and

therefore the 357.4 keV ($I_\gamma = 81(4)\%$) gamma from ^{130}La was used to quantify the ^{130}Ce production rate instead. Because of the 8.7(1) min half-life of ^{130}La , after approximately 90 minutes of decay the entire ^{130}La population was attributable to ^{130}Ce decay, which was confirmed by fitting the decay of the 357.4 keV line with the 22.9(5) minute half-life of ^{130}Ce . The results of this measurement are plotted in Fig. 13.

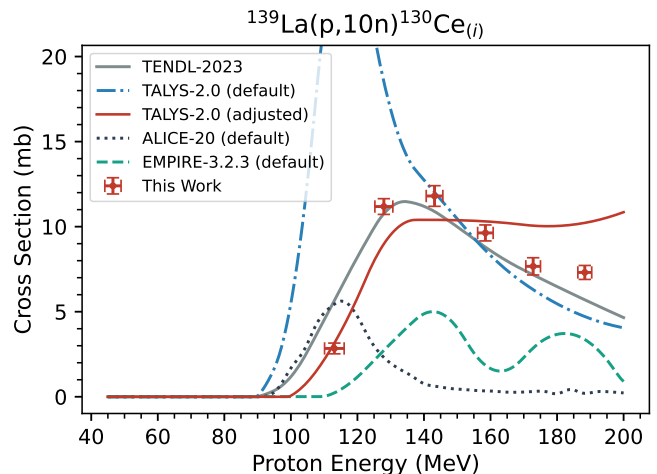


FIG. 13: Measured cross sections for the $^{139}\text{La}(p,10n)^{130}\text{Ce}$ reaction.

The results are significantly discrepant with the modeled cross sections, indicating that a significant parameter adjustment is necessary. Interestingly, the measurement showed almost no compound peak. Although it is possible there are not enough energy points to resolve the compound peak, the data seem to suggest that the compound mechanism is significantly damped in this channel, and presumably for higher (p,xn) channels as well.

V. CHARGED PARTICLE REACTION MODELING

The comparison of the cross sections measured in this work to the three nuclear reaction modeling codes TALYS, EMPIRE and ALICE, as well as TENDL-2023, showed a clear need for a parameter adjustment from the default models. Additionally, while the adjusted parameter set from Fox *et al.* fit the available data well, it did not extrapolate to our new measurements above 100 MeV. In this work, we apply a modified version of the TALYS-based residual product fitting procedure that was introduced in Fox *et al.* to the new set of measured cross sections [21]. In conjunction with literature data, these new measurements represent up to approximately 55% of the entire non-elastic cross section of proton reactions on lanthanum, for a combined 30 reaction

channels, ranging in energy from 4.5–188.4 MeV. This provided a unique opportunity to explore the nuclear reaction physics of this system. The motivation for using TALYS over other reaction modeling codes has been well described in Fox *et al.*, but we will reiterate the benefits to TALYS being the accessibility of this code (and its underlying models), as well as the perception that the two-component exciton model employed by TALYS is the most physically justified out of the default models in the most prominently used codes (*e.g.* EMPIRE, CoH, ALICE) [21, 22, 39, 40, 45].

V.1. Fitting Procedure

The parameter adjustment procedure used to improve the predicted cross sections was inspired by the recent work of Fox *et al.*, which proposed a particular sequence of parameters to be optimized, with the specific goal of fitting high-energy proton-induced reaction data [21]. Our general approach can be outlined as follows:

1. Down-select data to strongest, independently measured reaction channels. We will refer to this as “training” data.
2. Choose a goodness-of-fit metric to be optimized.
3. Optimize base-model selection parameters, *e.g.*, `ldmodel`, `strength`, `deuteronomp` and `alphaomp`.
4. Adjust major optical model parameters, primarily `rvadjust` and `avadjust` for both neutrons and protons.
5. Adjust major preequilibrium exciton model parameters, primarily `M2constant`, `M2limit` and `M2shift`.
6. Adjust minor parameters, *e.g.*, `Rgamma`, `Cstrip a`, *etc.*
7. Iterate through steps 4–6 until convergence in the goodness-of-fit metric.
8. Validate using the unused (cumulative) channels excluded from step 1.

There are three primary differences between the proposed approach and the work of Fox *et al.* First, we adjusted the optical model parameters before other parameters, rather than after the preequilibrium optimization. This was motivated by the fact that optical model parameters determine the magnitude of the non-elastic cross section, which should be fixed before modifying parameters which affect channel-to-channel competition. Second, we greatly increased the number of parameters

considered in the optimization, particularly the neutron optical model parameters and additional preequilibrium model parameters: specifically the `Rnunu`, `Rnupi`, `Rpinu` and `Rpipi` modifiers to the matrix element, as well as `Rgamma`. Finally, we did not perform any isotope-specific level density adjustments using the `ptable` parameter, however this would certainly be useful if one wished to provide the best interpolation of the data.

While a number of parameter optimization algorithms were considered for this work, the method with the best performance (best improvement over default TALYS) was actually the simplest method: sequentially optimizing one parameter at a time. Conventional regression and simulated annealing methods were also attempted, but failed to produce a satisfactory result. This method of sequentially optimizing the parameters for specific models within TALYS has a number of advantages over less physically-motivated evaluation methods. One of the most obvious advantages is that TALYS contains over 400 adjustable parameters, some of which are numerical, some are yes/no, some require a choice from a number of options, and some even require a file input. This means that one could not optimize *all* parameters in TALYS using conventional methods such as linear regression, and even if one were to use a more global optimization approach such as a machine learning model, there are likely not enough experimental data available to train such a model on the full parameter space. Instead, a physically-motivated evaluation approach allows one to down-select to a much smaller subset of parameters, based on which parameters are relevant to the data being fit, as well as eliminating parameters which have been well-constrained by other experiments. Even then, there may still be dozens of relevant parameters to a data set like the stacked-foil measurement performed here, which may overwhelm a conventional regression algorithm, particularly when the effects of one parameter are highly correlated with another. We hypothesize that the strong sensitivities and correlations of our problem to these parameters are the reason that sequential parameter optimization provided the best results.

Following the procedure outlined above, we selected our “training” data set from the 18 largest cross sections in Table I which were independently measured, including products with contributions from an isomer but no feeding from other isotopes, *i.e.*, cross sections subscripted (*i*) or (*m+*). The 12 remaining cross section channels were reserved for validation. In Fox *et al.* two goodness-of-fit metrics were used: reduced- χ^2 (χ_v^2) weighted by the maximum cross section in a channel, and χ_v^2 weighted by the integrated cross section in a channel. The reasoning behind using a weighted χ_v^2 is that the larger reaction channels (either by maximum or integrated cross section) contain more information relevant to the models being optimized, and thus should be weighted heavier than the minor channels. Because we preferred to optimize on a

TABLE IV: Summary of TALYS-2.0 base-model selection parameters.

Parameter	Best	Sensitivity	Default	Options
<code>ldmodel</code>	5	84.2	1	1–6
<code>strength</code>	10	46.1	9	1–10
<code>deuteronomp</code>	2	21.6	1	1–5
<code>alphaomp</code>	4	8.48	6	1–8
<code>preeqspin</code>	3	2.08	1	1–3

TABLE V: Summary of optical model parameters explored in TALYS-2.0 modeling. Parameters at the limits of the constraints are indicated with a *. Defaults for all parameters were 1.

Parameter	Best	Sensitivity	Constraints
<code>rvadjust n</code>	0.977	4523	0.95–1.05
<code>avadjust n</code>	1.076	291	0.75–1.25
<code>rvadjust p</code>	0.9*	59.1	0.9–1.1
<code>avadjust p</code>	1.0118	30.8	0.7–1.3
<code>w1adjust n</code>	4*	5.79	0.25–4
<code>w2adjust n</code>	1.51	8.92	0.25–4
<code>w1adjust p</code>	4*	18.5	0.25–4
<code>w2adjust p</code>	1.83	19.3	0.25–4

single figure-of-merit, we opted to use the average of these two (max and integral) weights. Also, because ^{134}Ce is a reaction channel with particular value for applications, the weight for the ^{134}Ce channel was selectively doubled.

The first set of parameters to be optimized were related to selection of the base-models, such as level density and gamma strength. The sensitivity to each base-model parameter was first calculated, in order to decide if the parameter should be included, as well as to inform the optimization order. Because these are discrete parameters, the “sensitivity” was calculated as the maximum percentage change (not necessarily improvement) in weighted- χ^2_ν , out of the whole set of options. The base-model parameters were then optimized in order of highest sensitivity. The resulting “best” model selection, range of options, default options and sensitivities are given for each of the 5 considered parameters in Table IV. It was found that `ldmodel` 5 and `strength` 10 were the best options, corresponding to the Gogny Hartree-Fock-Bogolyubov (HFB) level densities and Skyrme (HFB) + QRPA corrected strength tables, respectively [46, 47]. Also, note that each model was run with the option `bins` 0, which scales the number of excitation energy bins as the incident energy increases.

Following the base-model selections, the continuous-variable parameters were optimized iteratively, beginning with the optical model parameters. For the optical model and preequilibrium parameters, the sensitivity was calculated as $d\chi^2_\nu/dp$, or the ratio of percent change

TABLE VI: Summary of preequilibrium parameters explored in TALYS-2.0 modeling. Parameters at the limits of the constraints are indicated with a *. Defaults for `Rnnu` and `Rgamma` were 1.5 and 2.0, respectively, all others were 1.

Parameter	Best	Sensitivity	Constraints
<code>M2constant</code>	1.055	134	0.2–5
<code>M2shift</code>	1.196	109	0.2–5
<code>M2limit</code>	1.926	37.1	0.2–5
<code>Rnnu</code>	1.66	33.3	0.1–10
<code>Rnupi</code>	0.16	35.7	0.1–10
<code>Rpinu</code>	2.21	38.0	0.1–10
<code>Rpipi</code>	0.1*	6.65	0.1–10
<code>Rgamma</code>	0.1*	0.1	0.1–10
<code>Cstrip a</code>	0.1*	4.2	0.1–10

in weighted- χ^2_ν to the percent change in the parameter — evaluated at the default value for that parameter. This was used to inform the order in which the parameters were optimized, as well as the range of allowed values. Parameters with very high sensitivities, such as `rvadjust n`, were constrained to be much closer to the default values. Additionally, because `rvadjust` and `avadjust` correspond to the width and diffuseness of the optical-model well potential, which have fairly well-constrained systematics, the allowed range of values was more limited than for other parameters [48]. The resulting optimized optical model parameters, as well as the associated sensitivities and parameter constraints, are given in Table V. In most cases the imposed constraints were more strict than those required by TALYS. Because of the relatively large sensitivity of these calculations to optical model parameters, the resulting “best” values were very near the default values, with the exception of `w1adjust` for both protons and neutrons, which relate to the magnitude of the imaginary component of the optical model potential, primarily impacting the elastic to non-elastic cross section ratio.

The same approach was taken for optimizing the preequilibrium parameters, with the results shown in Table VI. The most significant change (from defaults) was to `M2limit`, which affects the asymptotic behavior of the exciton transition rates. This seemed to be necessary to account for the significant enhancement (over default predictions) of the preequilibrium tail seen in most of the (p,xn) channels, which occurred above 100 MeV. The effects of this are quite apparent in the (p,6n) and (p,8n) cross sections plotted in Fig. 14, where almost every other prediction is a factor of 2–5 low in this energy region. Other significant changes were to `Rgamma`, which is a competing mechanism for de-excitation to neutron emission, as well as to `Cstrip a`, which affects the magnitude of the preequilibrium contributions to (p, α) channels.

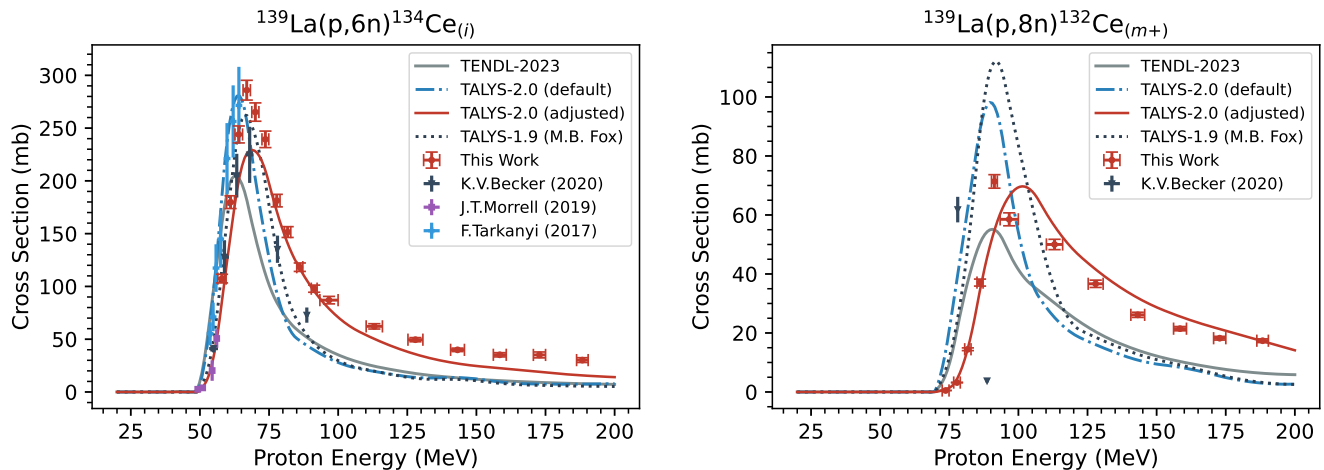


FIG. 14: Comparison of predicted and observed cross sections for the ^{134}Ce (left) and ^{132}Ce (right) products, which were used as training data for the parameter adjustments.

TABLE VII: Summary of TALYS-2.0 modeling results.

Source	Training χ^2_ν	Validation χ^2_ν
TENDL-2023	633	412
TALYS-2.0 default	2012	4769
TALYS-2.0 adjusted	73.5	3663
TALYS-1.9 (M.B. Fox)	638	5515
EMPIRE-3.2.3 default	879	3515
ALICE-20 default	6741	7.11×10^4

The completed parameter adjustment resulted in significant improvements to cross section predictions in the “training” data set, over default predictions. The resulting improvement in the weighted- χ^2_ν figure-of-merit can be seen in Table VII, in comparison to TENDL-2023, default predictions from TALYS-2.0, EMPIRE-3.2.3, ALICE-20 as well as the parameter adjustment resulting from the work of M.B. Fox *et al.*, which was calculated with TALYS-1.9 as this was the TALYS version used in that work [21]. While the Fox adjustment performed well on the data that was available at the time, that data did not include any energies above 100 MeV, and unfortunately as a result did not extrapolate well to the new 100–200 MeV measurements collected in this work. However, the Fox parameters still represent an improvement over default predictions.

We also performed a validation of the parameter adjustments against the various other predictions, using the unused “validation” data set, mostly comprising the cumulative channels. The weighted- χ^2_ν for the validation data are also given in Table VII, where the weights were again determined as the average of the two weighting methods (max and integral) from the Fox *et al.* work [21]. Two of the 12 validation channels are also plotted

in Fig. 15, with additional results plotted in Figs. 16 and 17. In general, the fit to the validation data set was much worse than the training set, as one might expect. However, the fit still represents an improvement over all of the modeling codes run with default values, as well as over the Fox adjustment (for reasons previously discussed). Our adjustment performed worse than the TENDL-2023 evaluation on the validation data, which seems to be attributed to a significant over-prediction of many barium and iodine channels. This could be due to over-fitting, *i.e.*, using too many parameters in our adjustment, or could be due to making adjustments that were too large and are therefore non-physical. While this does highlight the challenges of performing reaction evaluations on incomplete data sets, and the need for more work on this topic, the improvement over default predictions for both training and validation data sets implies some amount of physical consistency in our adjustments.

VI. SUMMARY AND CONCLUSIONS

In this work we conducted two stacked-foil irradiations — at the LANL Isotope Production Facility and the BNL Brookhaven Linac Isotope Producer — resulting in 30 measurements of $^{139}\text{La}(p,x)$ cross section channels in the 55–200 MeV proton energy range. Many of these cross sections represent the first observation of certain reaction products, and for all of the observed products this represents the first set of measurements above 100 MeV. Additionally, the fidelity of certain channels between 70–100 MeV was improved with measurements at additional proton energies, notably ^{134}Ce . The ^{134}Ce product represents a significant interest to the medical isotope production community. The reported finding that the cross

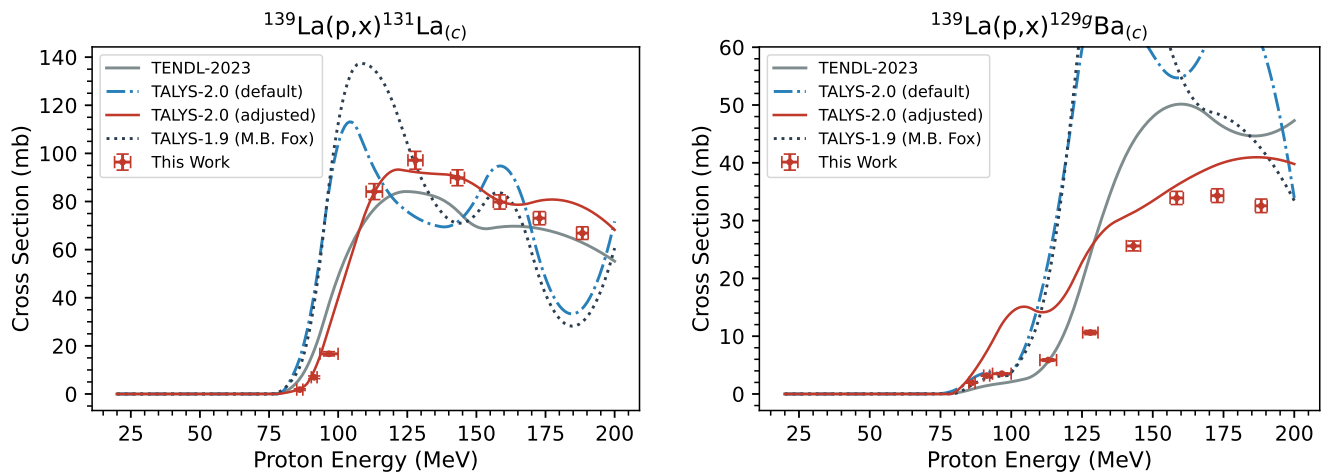


FIG. 15: Comparison of predicted and observed cross sections for the ^{131}La (left) and ^{129g}Ba (right) products, which were used to validate the parameter adjustments.

section was higher than predicted above 100 MeV is likely to be of interest for that application. Also, we believe the $^{139}\text{La}(p,10n)^{130}\text{Ce}$ reaction measured in this work to be the first measurement of an exclusive $(p,10n)$ excitation function reported in the literature. In general, the significant discrepancies between the observed cross sections and default model predictions suggests a need to use caution when relying upon such predictions for applications where little or no experimental data exist.

The cross sections measured in this work represent a significant proportion of the non-elastic cross section, which we estimate to be as high as 55% of the entire non-elastic cross section. The extensive nature of this data set enabled a comprehensive parameter adjustment for the $p+^{139}\text{La}$ system. Using the TALYS-2.0 nuclear reaction modeling code, parameter adjustments were made to the optical model and to the two-component exciton model for preequilibrium. The adjustment procedure resulted in an improvement in the overall fit to the measured data, which we believe to be physically consistent based on an improvement in cumulative reaction channels which were not used as part of the data set for the parameter optimization. The results corroborate previous findings suggesting the need to incorporate residual product excitation functions into exciton model parameterization studies, particularly at high energy [21].

The analysis code used to convert the spectra into cross sections, as well as the gamma-ray spectra and all other raw data generated during this work, have been stored in a LANL archive, and are available upon request to the corresponding author. Upon publication, the cross section data will be incorporated into EXFOR [49].

ACKNOWLEDGEMENTS

We wish to acknowledge our thanks to the operators of the LANL IPF for their assistance and support during the LANL irradiation: Anthony Koppi, Ross Capon and Nathan Kollarik. Additionally, we thank the BNL BLIP operators Henryk Chelminski and David O'Rourke. We are grateful to Ben Stein for the use of the LANL glove-box for the preparation and storage of the lanthanum foils. We acknowledge Deepak Raparia, head of the Pre-Injector Systems group at BNL-CAD for supporting the BLIP beam tuning. We would also like to thank the LANSCE Accelerator Operations support staff, and acknowledge the support from the LANSCE radiological control technicians. Additionally, we are grateful to Patrick Sullivan and Vicki Litton for their support with radiological controls at BNL.

This research is supported by the U.S. Department of Energy Isotope Program, managed by the Office of Science for Isotope R&D and Production. This work was carried out under Lawrence Berkeley National Laboratory (Contract No. DE-AC02-05CH11231), Los Alamos National Laboratory (Contract No. 89233218CNA000001) and Brookhaven National Laboratory (Contract No. DEAC02-98CH10886).

This material is approved for public release; distribution unlimited (LA-UR-24-21320).

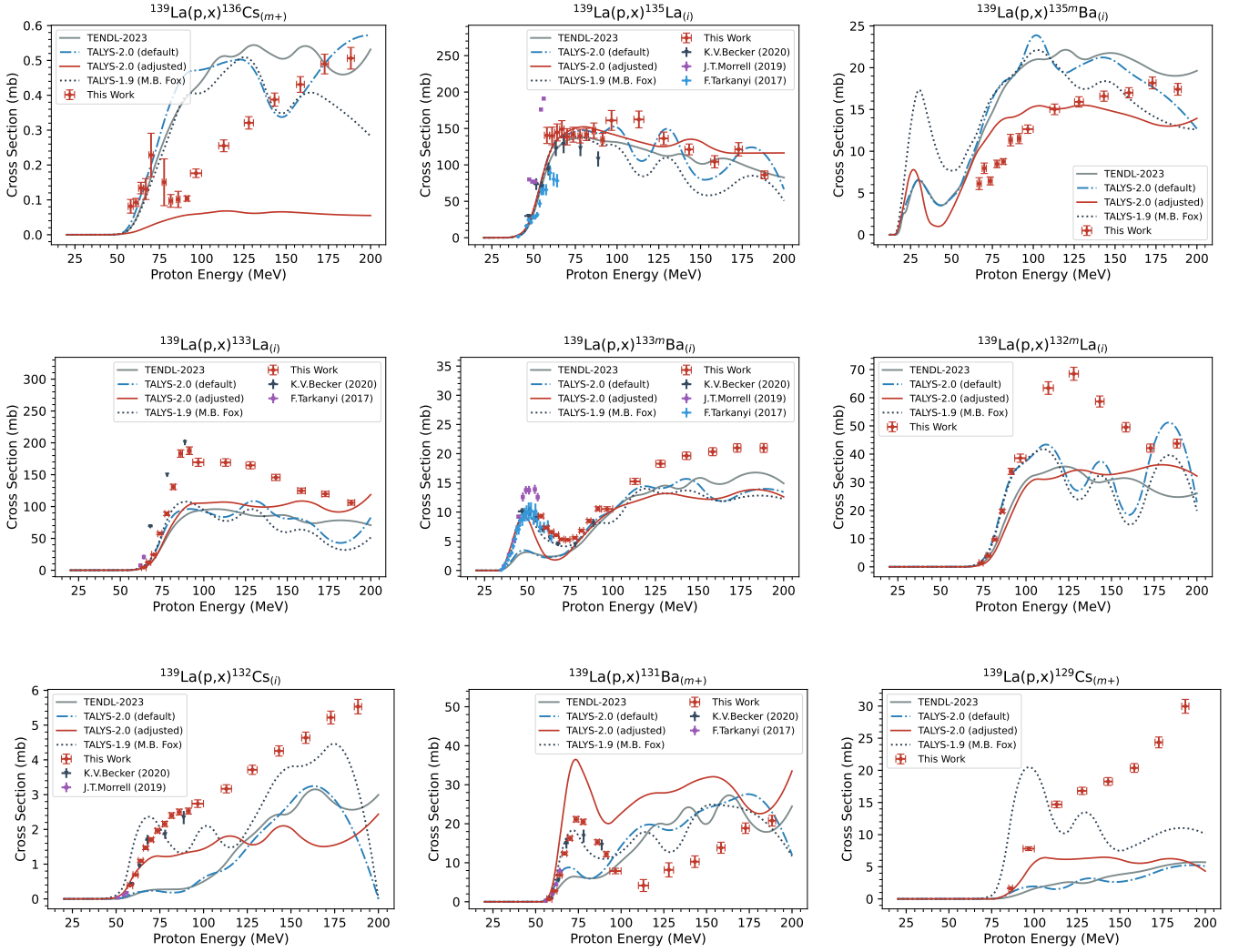


FIG. 16: Comparison of measured cross sections to TENDL-2023 and TALYS-2.0 predictions using default parameters, the parameter adjustments of Fox *et al.*, and the adjustments performed in this work [21].

- [1] C. Kratochwil, F. Bruchertseifer, F. L. Giesel, M. Weis, F. A. Verburg, F. Mottaghy, K. Kopka, C. Apostolidis, U. Haberkorn, and A. Morgenstern, 225Ac-PSMA-617 for PSMA-Targeted α -Radiation Therapy of Metastatic Castration-Resistant Prostate Cancer, *Journal of Nuclear Medicine* **57**, 1941 (2016), <https://jnm.snmjournals.org/content/57/12/1941.full.pdf>.
- [2] N. L. of Medicine (US), A Study of JNJ-69086420, an Actinium-225-Labeled Antibody Targeting Human Kallikrein-2 (hK2) for Advanced Prostate Cancer, <https://clinicaltrials.gov/study/NCT04644770> (2024), Identifier NCT04644770.
- [3] N. L. of Medicine (US), Venetoclax and Lintuzumab-Ac225 in AML Patients, <https://clinicaltrials.gov/study/NCT03867682> (2023), Identifier NCT03867682.
- [4] A. Jain, R. Raut, and J. Tuli, Nuclear Data Sheets for A = 225, *Nuclear Data Sheets* **110**, 1409 (2009).
- [5] A. K. Jain, S. Singh, S. Kumar, and J. K. Tuli, Nuclear Data Sheets for A = 221, *Nuclear Data Sheets* **108**, 883 (2007).
- [6] F. Kondev, E. McCutchan, B. Singh, K. Banerjee, S. Bhattacharya, A. Chakraborty, S. Garg, N. Jovancevic, S. Kumar, S. Rathi, T. Roy, J. Lee, and R. Shearman, Nuclear Data Sheets for A=217, *Nuclear Data Sheets* **147**, 382 (2018).
- [7] M. Basunia, Nuclear Data Sheets for A = 213, *Nuclear Data Sheets* **108**, 633 (2007).
- [8] J. Chen and F. Kondev, Nuclear Data Sheets for A = 209, *Nuclear Data Sheets* **126**, 373 (2015).
- [9] J. Ma, L. Li, T. Liao, W. Gong, and C. Zhang, Efficacy and Safety of 225Ac-PSMA-617-Targeted Alpha Therapy in Metastatic Castration-Resistant Prostate Cancer: A Systematic Review and Meta-Analysis, *Frontiers in Oncology* **12** (2022).

- [10] R. M. Pallares and R. J. Abergel, Development of radiopharmaceuticals for targeted alpha therapy: Where do we stand?, *Frontiers in Medicine* **9**, 10.3389/fmed.2022.1020188 (2022).
- [11] T. Bailey, V. Mocko, K. Shield, D. An, A. Akin, E. Birnbaum, M. Brugh, J. Cooley, J. Engle, M. Fassbender, S. Gauny, A. Lakes, F. Nortier, E. O'Brien, S. Thieman, F. White, C. Vermeulen, S. Kozimor, and R. Abergel, Developing the ^{134}Ce and ^{134}La pair as companion positron emission tomography diagnostic isotopes for ^{225}Ac and ^{227}Th radiotherapeutics, *Nature Chemistry* **13** (2021).
- [12] T. A. Bailey, J. N. Wacker, D. D. An, K. P. Carter, R. C. Davis, V. Mocko, J. Larrabee, K. M. Shield, M. N. Lam, C. H. Booth, and R. J. Abergel, Evaluation of ^{134}Ce as a PET imaging surrogate for antibody drug conjugates incorporating ^{225}Ac , *Nuclear Medicine and Biology* **110-111**, 28 (2022).
- [13] K. N. Bobba, A. P. Bidkar, N. Meher, C. Fong, A. Wadhwa, S. Dhrona, A. Sorlin, S. Bidlingmaier, B. Shuere, J. He, D. M. Wilson, B. Liu, Y. Seo, H. F. VanBrocklin, and R. R. Flavell, Evaluation of $^{134}\text{Ce}/^{134}\text{La}$ as a PET Imaging Theranostic Pair for ^{225}Ac alpha-Radiotherapeutics, *Journal of Nuclear Medicine* 10.2967/jnumed.122.265355 (2023).
- [14] A. Sonzogni, Nuclear Data Sheets for A = 134, *Nuclear Data Sheets* **103**, 1 (2004).
- [15] F. Tárkányi, A. Hermanne, F. Ditrói, and S. Takács, Activation cross section data of proton induced nuclear reactions on lanthanum in the 34–65 MeV energy range and application for production of medical radionuclides, *Journal of Radioanalytical and Nuclear Chemistry* **312**, 691 (2017).
- [16] Morrell, Jonathan T., Voyles, Andrew S., Basunia, M. S., Batchelder, Jon C., Matthews, Eric F., and Bernstein, Lee A., Measurement of $^{139}\text{La}(p,x)$ cross sections from 35–60 MeV by stacked-target activation, *Eur. Phys. J. A* **56**, 13 (2020).
- [17] K. Becker, E. Vermeulen, C. Kutyreff, E. O'Brien, J. Morrell, E. Birnbaum, L. Bernstein, F. Nortier, and J. Engle, Cross section measurements for proton induced reactions on natural La, *Nuclear Instruments and Methods in Physics Research Section B: Beam Interactions with Materials and Atoms* **468**, 81 (2020).
- [18] S. Qaim, New directions in nuclear data research for accelerator-based production of medical radionuclides, *Journal of Radioanalytical and Nuclear Chemistry* (2024).
- [19] A. S. Voyles, L. A. Bernstein, E. R. Birnbaum, J. W. Engle, S. A. Graves, T. Kawano, A. M. Lewis, and F. M. Nortier, Excitation functions for (p,x) reactions of niobium in the energy range of $E_p = 40\text{--}90\text{ MeV}$, *Nuclear Instruments and Methods in Physics Research Section B: Beam Interactions with Materials and Atoms* **429**, 53 (2018).
- [20] S. A. Graves, P. A. Ellison, T. E. Barnhart, H. F. Valdivinos, E. R. Birnbaum, F. M. Nortier, R. J. Nickles, and J. W. Engle, Nuclear excitation functions of proton-induced reactions ($E_p = 35\text{--}90\text{ MeV}$) from Fe, Cu, and Al, *Nuclear Instruments and Methods in Physics Research Section B: Beam Interactions with Materials and Atoms* **386**, 44 (2016).
- [21] M. B. Fox, A. S. Voyles, J. T. Morrell, L. A. Bernstein, A. M. Lewis, A. J. Koning, J. C. Batchelder, E. R. Birnbaum, C. S. Cutler, D. G. Medvedev, F. M. Nortier, E. M. O'Brien, and C. Vermeulen, Investigating high-energy proton-induced reactions on spherical nuclei: Implications for the preequilibrium exciton model, *Phys. Rev. C* **103**, 034601 (2021).
- [22] Koning, Arjan, Hilaire, Stephane, and Goriely, Stephane, TALYS: modeling of nuclear reactions, *Eur. Phys. J. A* **59**, 131 (2023).
- [23] W. Huang, M. Wang, F. Kondev, G. Audi, and S. Naimi, The AME 2020 atomic mass evaluation (I). Evaluation of input data, and adjustment procedures*, *Chinese Physics C* **45**, 030002 (2021).
- [24] R. Firestone, Nuclear Data Sheets for A = 24, *Nuclear Data Sheets* **108**, 2319 (2007).
- [25] Y. Khazov, A. Rodionov, S. Sakharov, and B. Singh, Nuclear Data Sheets for A=132, *Nuclear Data Sheets* **104**, 497 (2005).
- [26] J. T. Morrell, *Curie: A python toolkit to aid in the analysis of experimental nuclear data* (2019–), [Online; accessed January 24, 2024].
- [27] T. Vidmar, M. Korun, A. Likar, and R. Martinčič, A semi-empirical model of the efficiency curve for extended sources in gamma-ray spectrometry, *Nuclear Instruments and Methods in Physics Research Section A: Accelerators, Spectrometers, Detectors and Associated Equipment* **470**, 533 (2001).
- [28] Y. Khazov, A. Rodionov, and F. Kondev, Nuclear Data Sheets for A = 133, *Nuclear Data Sheets* **112**, 855 (2011).
- [29] M. Martin, Nuclear Data Sheets for A = 152, *Nuclear Data Sheets* **114**, 1497 (2013).
- [30] H. Junde, H. Su, and Y. Dong, Nuclear Data Sheets for A = 56, *Nuclear Data Sheets* **112**, 1513 (2011).
- [31] M. J. Berger, J. H. Hubbell, S. M. Seltzer, J. Chang, J. S. Coursey, R. Sukumar, D. S. Zucker, and K. Olsen, XCOM: Photon cross section database (version 1.5), (2010).
- [32] J. H. Hubbell and S. M. Seltzer, *Tables of X-ray mass attenuation coefficients and mass energy-absorption coefficients 1 keV to 20 MeV for elements Z= 1 to 92 and 48 additional substances of dosimetric interest*, Tech. Rep. (National Inst. of Standards and Technology-PL, Gaithersburg, MD (United States, 1995).
- [33] H. Bateman, The solution of a system of differential equations occurring in the theory of radioactive transformations, *In Proc. Cambridge Philos. Soc.* **15**, 423 (1910).
- [34] N. Nica, Nuclear Data Sheets for A=140, *Nuclear Data Sheets* **154**, 1 (2018).
- [35] G. Battistoni, T. Boehlen, F. Cerutti, P. W. Chin, L. S. Esposito, A. Fassò, A. Ferrari, A. Lechner, A. Empl, A. Mairani, A. Mereghetti, P. G. Ortega, J. Ranft, S. Roesler, P. R. Sala, V. Vlachoudis, and G. Smirnov, Overview of the FLUKA code, *Annals of Nuclear Energy* **82**, 10 (2015), joint International Conference on Supercomputing in Nuclear Applications and Monte Carlo 2013, SNA + MC 2013. Pluri- and Trans-disciplinarity, Towards New Modeling and Numerical Simulation Paradigms.
- [36] A. Hermanne, A. V. Ignatyuk, R. Capote, B. V. Carlson, J. W. Engle, M. A. Kellett, T. Kibédi, G. Kim, F. G. Kondev, M. Hussain, O. Lebeda, A. Luca, Y. Nagai, H. Naik, A. L. Nichols, F. M. Nortier, S. V. Suryanarayana, S. Takács, F. T. Tárkányi, and M. Verpelli, Reference Cross Sections for Charged-particle Monitor Reactions, *Nuclear Data Sheets* **148**, 338 (2018).

- [37] J. F. Ziegler, M. Ziegler, and J. Biersack, SRIM – The stopping and range of ions in matter (2010), **Nuclear Instruments and Methods in Physics Research Section B: Beam Interactions with Materials and Atoms** **268**, 1818 (2010), 19th International Conference on Ion Beam Analysis.
- [38] D. Rochman, A. J. Koning, J. C. Sublet, M. Fleming, E. Bauge, S. Hilaire, P. Romain, B. Morillon, H. Duarte, S. Goriely, *et al.*, The TENDL library: Hope, reality and future, in *EPJ web of conferences*, Vol. 146 (EDP Sciences, 2017) p. 02006.
- [39] M. Herman, R. Capote, B. Carlson, P. Obložinský, M. Sin, A. Trkov, H. Wienke, and V. Zerkin, EMPIRE: Nuclear Reaction Model Code System for Data Evaluation, **Nuclear Data Sheets** **108**, 2655 (2007), special Issue on Evaluations of Neutron Cross Sections.
- [40] M. Blann and J. Bisplinghoff, Code ALICE/LIVERMORE 82 (1982).
- [41] A. Koning and M. Duijvestijn, A global pre-equilibrium analysis from 7 to 200 MeV based on the optical model potential, **Nuclear Physics A** **744**, 15 (2004).
- [42] M. B. Fox, A. S. Voyles, J. T. Morrell, L. A. Bernstein, J. C. Batchelder, E. R. Birnbaum, C. S. Cutler, A. J. Koning, A. M. Lewis, D. G. Medvedev, F. M. Nortier, E. M. O'Brien, and C. Vermeulen, Measurement and modeling of proton-induced reactions on arsenic from 35 to 200 MeV, **Phys. Rev. C** **104**, 064615 (2021).
- [43] V. Alexandryan, G. Ivazyan, A. Balabekyan, A. Danagulyan, V. Kalinnikov, V. Stegailov, and J. Frána, Study of isomeric ratios of proton-nucleus cross sections on tin isotopes, *Physics of Atomic Nuclei - PHYS ATOM NUCL-ENGL TR* **59**, 560 (1996).
- [44] A. Balabekyan, A. Danagulyan, J. Drnoyan, N. Demekhina, J. Adam, V. Kalinnikov, M. Krivopustov, V. Pronskikh, V. Stegailov, A. Solnyshkin, P. Caloun, and V. Tsoupko-Sitnikov, Investigation of spallation reactions on ^{120}Sn and (d, xn) , (d, pxn) , (p, xn) , and (p, pxn) reactions on enriched tin isotopes, **Physics of Atomic Nuclei - PHYS ATOM NUCL-ENGL TR** **68**, 171 (2005).
- [45] T. Kawano, CoH3: The Coupled-Channels and Hauser-Feshbach Code, in *Compound-Nuclear Reactions*, edited by J. Escher, Y. Alhassid, L. A. Bernstein, D. Brown, C. Fröhlich, P. Talou, and W. Younes (Springer International Publishing, Cham, 2021) pp. 27–34.
- [46] S. Goriely, S. Hilaire, and A. J. Koning, Improved microscopic nuclear level densities within the Hartree-Fock-Bogoliubov plus combinatorial method, **Phys. Rev. C** **78**, 064307 (2008).
- [47] S. Goriely, S. Hilaire, S. Péru, and K. Sieja, Gogny-HFB+QRPA dipole strength function and its application to radiative nucleon capture cross section, **Phys. Rev. C** **98**, 014327 (2018).
- [48] A. J. Koning and J. P. Delaroche, Local and global nucleon optical models from 1 keV to 200 MeV, **Nuclear Physics A** **713**, 231 (2003).
- [49] N. Otuka, E. Dupont, V. Semkova, B. Pritychenko, A. Blokhin, M. Aikawa, S. Babykina, M. Bossant, G. Chen, S. Dunaeva, R. Forrest, T. Fukahori, N. Furutachi, S. Ganesan, Z. Ge, O. Gritzay, M. Herman, S. Hlavač, K. Katō, B. Lalremruata, Y. Lee, A. Makinaga, K. Matsumoto, M. Mikhaylyukova, G. Pikulina, V. Pronyaev, A. Saxena, O. Schwerer, S. Simakov, N. Soppera, R. Suzuki, S. Takács, X. Tao, S. Taova, F. Tárkányi, V. Varlamov, J. Wang, S. Yang, V. Zerkin, and Y. Zhuang, Towards a More Complete and Accurate Experimental Nuclear Reaction Data Library (EXFOR): International Collaboration Between Nuclear Reaction Data Centres (NRDC), **Nuclear Data Sheets** **120**, 272 (2014).
- [50] P. K. Joshi, B. Singh, S. Singh, and A. K. Jain, Nuclear Data Sheets for $A = 139$, **Nuclear Data Sheets** **138**, 1 (2016).
- [51] E. Browne and J. Tuli, Nuclear Data Sheets for $A = 137$, **Nuclear Data Sheets** **108**, 2173 (2007).
- [52] E. McCutchan, Nuclear Data Sheets for $A=136$, **Nuclear Data Sheets** **152**, 331 (2018).
- [53] B. Singh, A. A. Rodionov, and Y. L. Khazov, Nuclear Data Sheets for $A = 135$, **Nuclear Data Sheets** **109**, 517 (2008).
- [54] Y. Khazov, I. Mitropolsky, and A. Rodionov, Nuclear Data Sheets for $A = 131$, **Nuclear Data Sheets** **107**, 2715 (2006).
- [55] B. Singh, Nuclear Data Sheets for $A = 130$, **Nuclear Data Sheets** **93**, 33 (2001).
- [56] J. Timar, Z. Elekes, and B. Singh, Nuclear Data Sheets for $A = 129$, **Nuclear Data Sheets** **121**, 143 (2014).
- [57] Z. Elekes and J. Timar, Nuclear Data Sheets for $A = 128$, **Nuclear Data Sheets** **129**, 191 (2015).
- [58] A. Hashizume, Nuclear Data Sheets for $A = 127$, **Nuclear Data Sheets** **112**, 1647 (2011).
- [59] H. Iimura, J. Katakura, and S. Ohya, Nuclear Data Sheets for $A=126$, **Nuclear Data Sheets** **180**, 1 (2022).
- [60] J. Katakura, Nuclear Data Sheets for $A = 125$, **Nuclear Data Sheets** **112**, 495 (2011).
- [61] J. Chen, Nuclear Data Sheets for $A=123$, **Nuclear Data Sheets** **174**, 1 (2021).
- [62] E. Browne and J. Tuli, Nuclear Data Sheets for $A = 65$, **Nuclear Data Sheets** **111**, 2425 (2010).
- [63] A. L. Nichols, B. Singh, and J. K. Tuli, Nuclear Data Sheets for $A = 62$, **Nuclear Data Sheets** **113**, 973 (2012).
- [64] K. Zuber and B. Singh, Nuclear Data Sheets for $A = 61$, **Nuclear Data Sheets** **125**, 1 (2015).
- [65] E. Browne and J. Tuli, Nuclear Data Sheets for $A = 60$, **Nuclear Data Sheets** **114**, 1849 (2013).
- [66] M. S. Basunia, Nuclear Data Sheets for $A=59$, **Nuclear Data Sheets** **151**, 1 (2018).
- [67] C. D. Nesaraja, S. D. Geraedts, and B. Singh, Nuclear Data Sheets for $A = 58$, **Nuclear Data Sheets** **111**, 897 (2010).
- [68] M. Bhat, Nuclear data sheets update for $A = 57$, **Nuclear Data Sheets** **67**, 195 (1992).
- [69] H. Junde, Nuclear Data Sheets for $A = 55$, **Nuclear Data Sheets** **109**, 787 (2008).
- [70] H. Junde and H. Su, Nuclear Data Sheets for $A = 54$, **Nuclear Data Sheets** **107**, 1393 (2006).
- [71] J. Huo, S. Huo, and C. Ma, Nuclear Data Sheets for $A = 52$, **Nuclear Data Sheets** **108**, 773 (2007).
- [72] J. Wang and X. Huang, Nuclear Data Sheets for $A=51$, **Nuclear Data Sheets** **144**, 1 (2017).
- [73] J. Chen, Nuclear Data Sheets for $A=48$, **Nuclear Data Sheets** **179**, 1 (2022).
- [74] T. Burrows, Nuclear Data Sheets for $A = 47$, **Nuclear Data Sheets** **108**, 923 (2007).
- [75] S.-C. Wu, Nuclear Data Sheets for $A = 46$, **Nuclear Data Sheets** **91**, 1 (2000).
- [76] J. Chen and B. Singh, Nuclear Structure and Decay Data for $A=44$ Isobars, **Nuclear Data Sheets** **190**, 1 (2023).

- [77] B. Singh and J. Chen, Nuclear Data Sheets for $A = 43$, *Nuclear Data Sheets* **126**, 1 (2015).
- [78] J. Chen and B. Singh, Nuclear Data Sheets for $A = 42$, *Nuclear Data Sheets* **135**, 1 (2016).
- [79] M. S. Basunia, Nuclear Data Sheets for $A = 22$, *Nuclear Data Sheets* **127**, 69 (2015).

Appendix A: Cross Sections

Plots of additional cross sections measured in this work that were not discussed in the main text are shown in Figs. 17 and 18.

Plots of the monitor reaction cross sections that were extrapolated to the 100–200 MeV energy range are shown in Fig. 19, in comparison with the “effective” cross sections that are constituted by the measured beam currents.

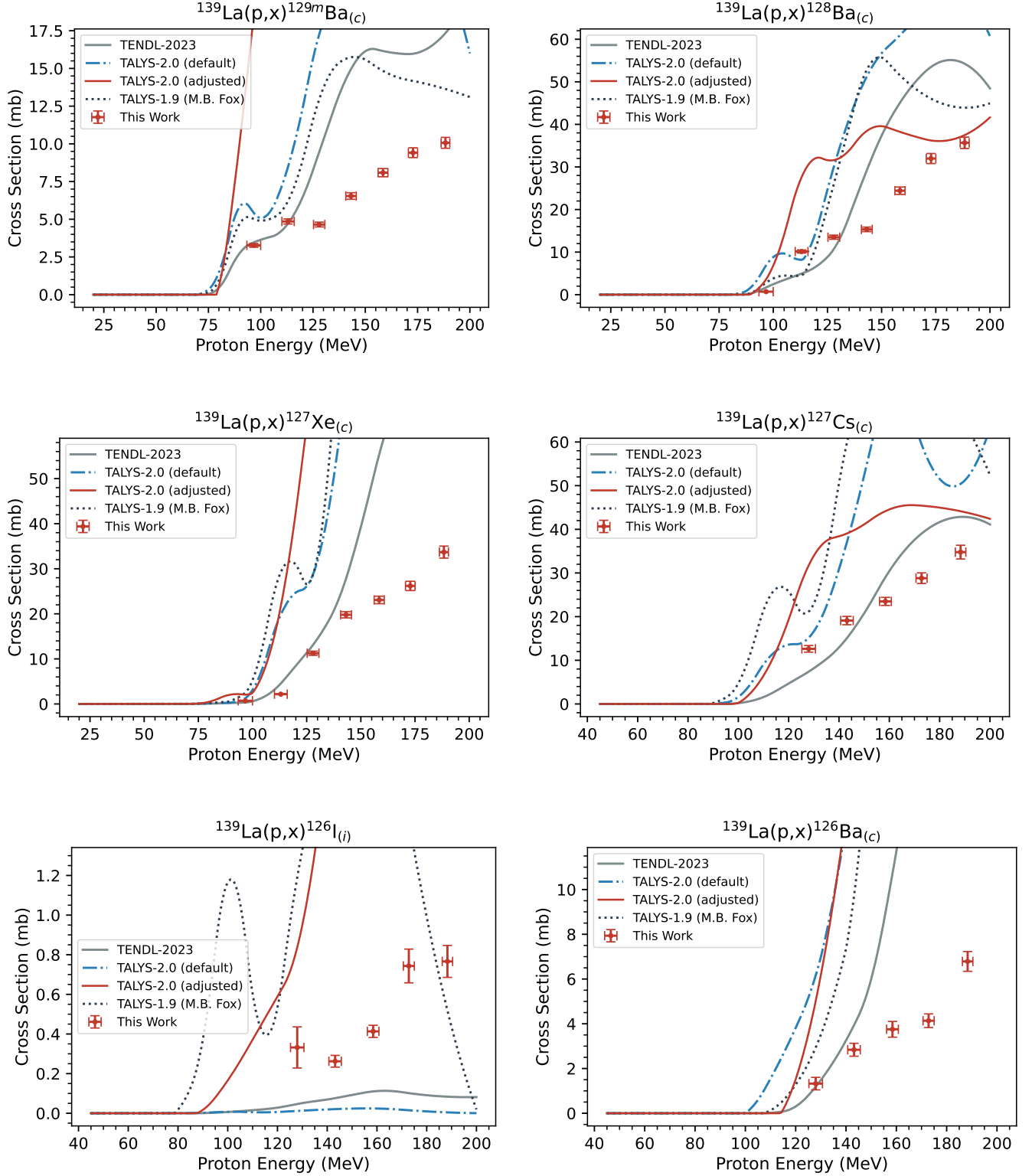


FIG. 17: Comparison of measured cross sections to TENDL-2023 and TALYS-2.0 predictions using default parameters, the parameter adjustments of Fox *et al.*, and the adjustments performed in this work [21].

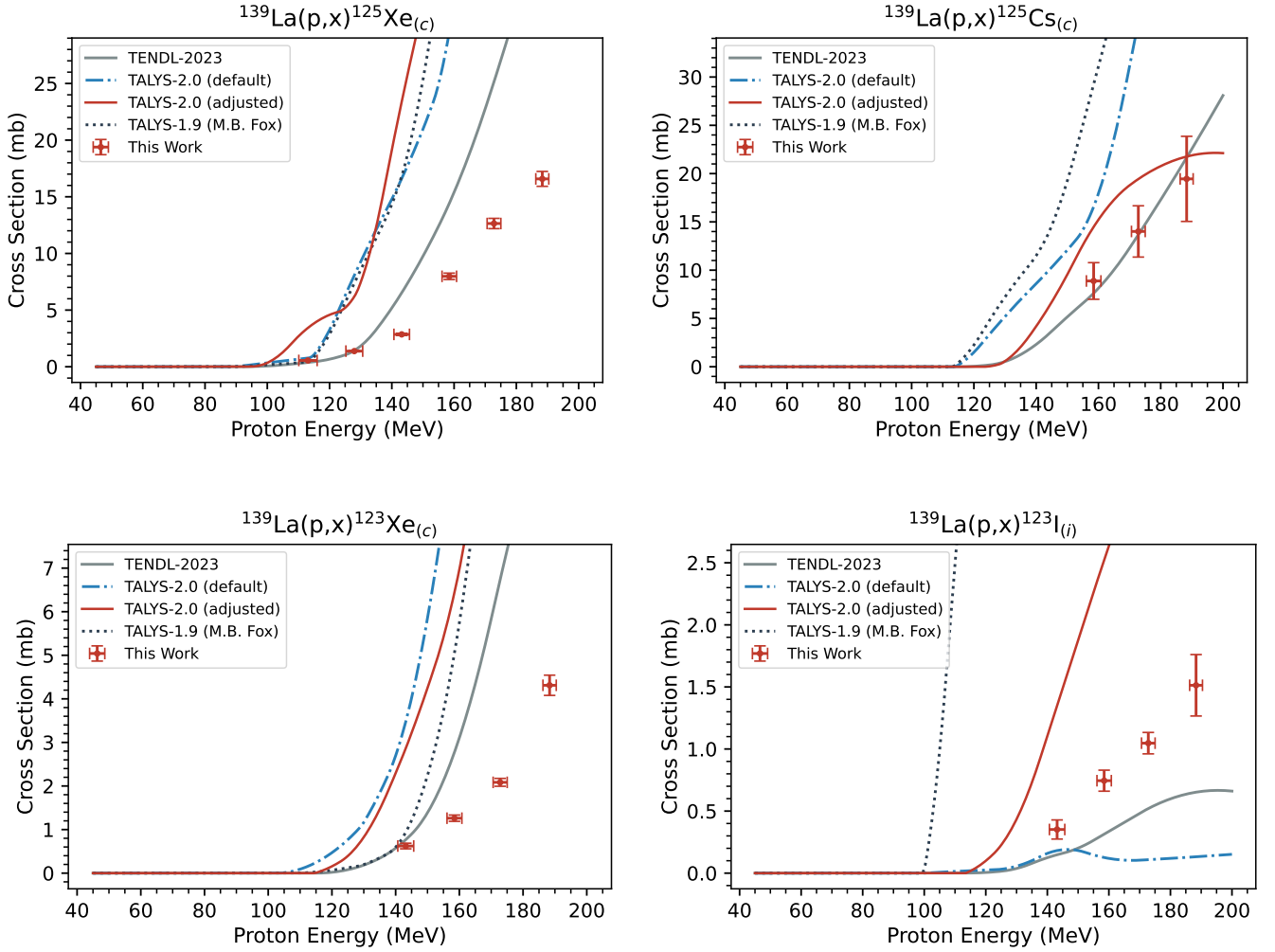


FIG. 18: Comparison of measured cross sections to TENDL-2023 and TALYS-2.0 predictions using default parameters, the parameter adjustments of Fox *et al.*, and the adjustments performed in this work [21].

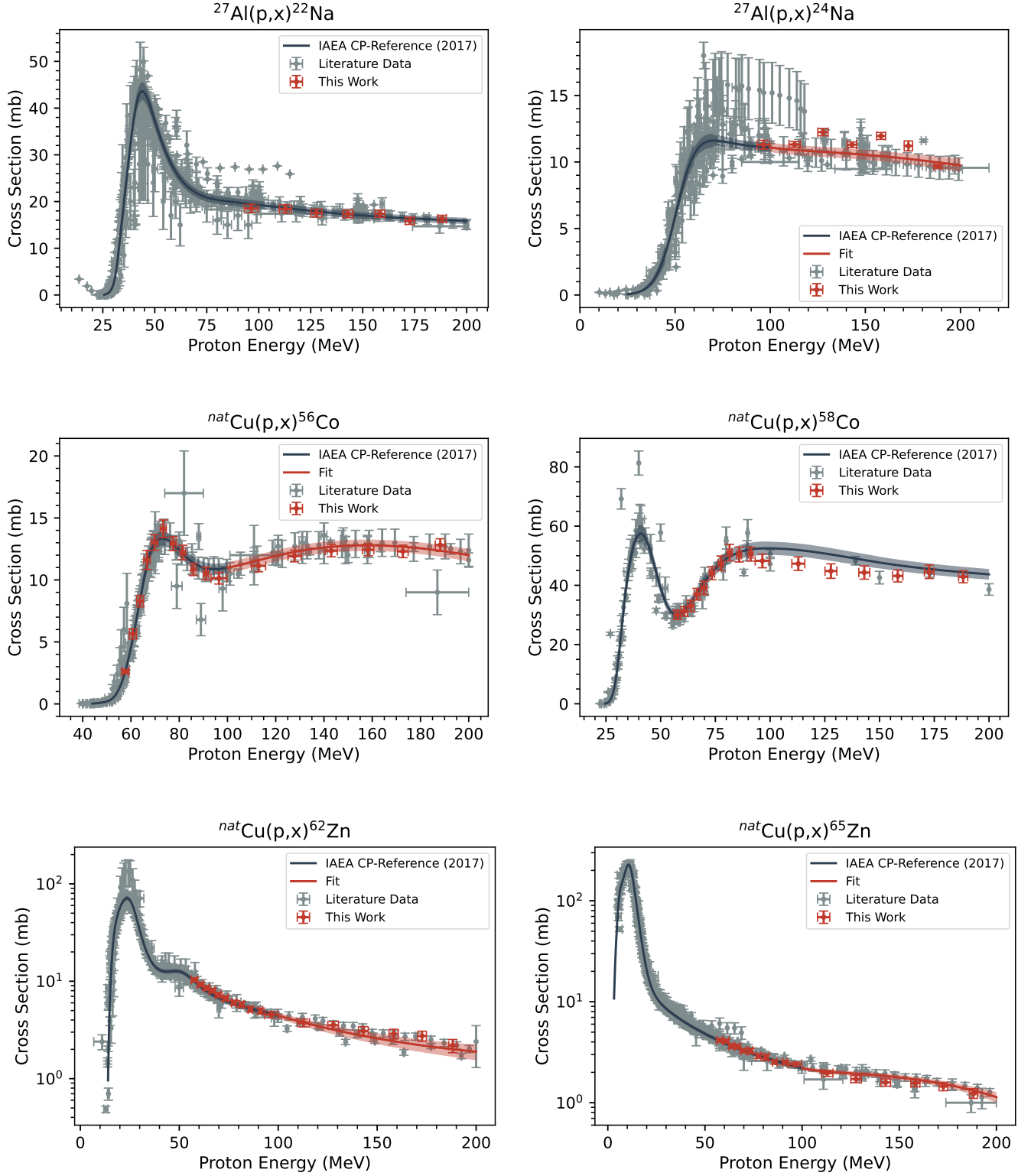


FIG. 19: Experimental and evaluated monitor cross sections for the production of ^{22}Na (top-left), ^{24}Na (top-right), ^{56}Co (middle-left), ^{58}Co (middle-right), ^{62}Zn (bottom-left) and ^{65}Zn (bottom-right) [36].

Appendix B: Stack Design

A list of every component of the experimental stacks used in both irradiations can be found in Table VIII for the LANL irradiation and Table IX for the BNL irradiation.

TABLE VIII: Details of the stack used in the LANL irradiation. Uncertainties are listed in the least significant digit, that is, 15.51(28) means 15.51 ± 0.28 .

Foil Id	Compound	Δx (mm)	$\rho\Delta x$ (mg/cm ²)
La01	La	0.0251	15.51(28)
Cu01	Cu	0.0213	19.05(26)
Ti01	Ti	0.0344	15.56(19)
D1	Cu	1.02	909
La02	La	0.0288	17.81(32)
Cu02	Cu	0.0214	19.15(27)
Ti02	Ti	0.0346	15.65(19)
D2	Cu	0.794	710
La03	La	0.0286	17.67(32)
Cu03	Cu	0.0208	18.61(26)
Ti03	Ti	0.034	15.37(18)
D3	Cu	0.663	593
La04	La	0.025	15.45(28)
Cu04	Cu	0.0214	19.11(27)
Ti04	Ti	0.034	15.37(18)
D4	Cu	0.67	599
La05	La	0.0251	15.48(28)
Cu05	Cu	0.0215	19.20(27)
Ti05	Ti	0.0346	15.64(19)
D5	Al	1.53	414
La06	La	0.0243	14.98(27)
Cu06	Cu	0.0213	19.05(26)
Ti06	Ti	0.0339	15.30(18)
D6	Al	1.2	324
La07	La	0.0283	17.47(32)
Cu07	Cu	0.0215	19.24(27)
Ti07	Ti	0.0343	15.49(19)
D7	Al	1.02	275
La08	La	0.0246	15.17(27)
Cu08	Cu	0.0213	19.10(27)
Ti08	Ti	0.0348	15.72(19)
D8	Al	1.02	275
La09	La	0.0241	14.85(27)
Cu09	Cu	0.0208	18.65(26)
Ti09	Ti	0.0343	15.52(19)
D9	Al	1.02	275
La10	La	0.0305	18.81(34)
Cu10	Cu	0.0208	18.63(26)
Ti10	Ti	0.0334	15.11(18)

TABLE IX: Details of the stack used in the BNL irradiation. Uncertainties are listed in the least significant digit, that is, 17.32(31) means 17.32 ± 0.31 .

Foil Id	Compound	Δx (mm)	$\rho\Delta x$ (mg/cm ²)
La01	La	0.028	17.32(31)
Cu01	Cu	0.021	18.81(26)
Al01	Al	0.0267	7.19(13)
D1	Cu	5.11	4570
La02	La	0.0272	16.77(30)
Cu02	Cu	0.0206	18.39(26)
Al02	Al	0.0274	7.40(14)
D2	Cu	4.46	3990
La03	La	0.0276	17.02(31)
Cu03	Cu	0.0212	18.98(26)
Al03	Al	0.0265	7.15(13)
D3	Cu	4.46	3990
La04	La	0.0279	17.24(31)
Cu04	Cu	0.0211	18.86(26)
Al04	Al	0.0269	7.26(13)
D4	Cu	4.12	3690
La05	La	0.0274	16.92(31)
Cu05	Cu	0.0215	19.21(27)
Al05	Al	0.0269	7.26(13)
D5	Cu	3.7	3310
La06	La	0.0277	17.09(31)
Cu06	Cu	0.0214	19.11(27)
Al06	Al	0.027	7.29(13)
D6	Cu	3.7	3310
La07	La	0.0243	14.99(27)
Cu07	Cu	0.0211	18.92(26)

Appendix C: Relevant Nuclear Data

The principal gamma-ray decay data used in the activation analysis of the lanthanum foils are given in Table X. The principal gamma-ray decay data used in the activation analysis of the aluminum, copper and titanium monitor foils are given in Table XI.

TABLE X: Principle γ -ray data for lanthanum products, from ENSDF [14, 25, 28, 50–61]. Uncertainties are listed in the least significant digit, that is, 137.641(20) d means 137.641 ± 0.020 d.

Isotope	γ Energy (keV)	I_γ (%)	$T_{1/2}$
¹³⁹ Ce	165.8575	79.90(5)	137.641(20) d
¹³⁷ Ce	447.15	1.680(84)	9.0(3) h
^{137m} Ce	254.29	11.1(4)	1.433(13) d
¹³⁶ Cs	818.514	99.7(50)	13.16(3) d
	340.547	42.2(13)	
¹³⁵ Ce	265.56	41.8(14)	17.7(3) h
	300.07	23.5(5)	
¹³⁵ La	480.51	1.520(76)	19.5(2) h
^{135m} Ba	268.218	16.00(40)	1.1958(83) d
¹³⁴ Ce	130.4	0.209(15)	3.16(4) d
¹³⁴ La	604.721	5.04(20)	6.45(16) min
¹³³ Ce	97.261	46.0(7)	1.617(67) h
	76.9	15.9(23)	
^{133m} Ce	477.22	39.3(20)	4.9(4) h
	58.39	19.3(4)	
¹³³ La	278.835	2.44(13)	3.912(8) h
	302.38	1.61(8)	
^{133m} Ba	275.925	17.69(88)	1.6208(42) d
¹³³ Ba	356.0129	62.0(31)	10.516(19) y
	80.9979	32.9(3)	
¹³² Ce	182.11	77.4(39)	3.51(11) h
	155.37	10.5(5)	
¹³² La	464.55	76.0(6)	4.8(2) h
	567.14	15.7(15)	
^{132m} La	135.8	49.0(4)	24.3(5) min
	390.51	4.8(9)	
¹³² Cs	667.714	97.6(49)	6.480(6) d
¹³¹ La	108.081	25.0(8)	59.0(2) min
	417.783	18.0(6)	
¹³¹ Ba	496.321	48.0(24)	11.50(6) d
	123.804	29.8(3)	
¹³⁰ La	357.4	81.0(4)	8.7(1) min
	550.7	25.9(19)	
¹²⁹ Ba	214.3	13.4(7)	2.23(11) h
	220.83	8.5(4)	
^{129m} Ba	1459.1	50.0(2)	2.16(2) h
	202.38	33.7(6)	
¹²⁹ Cs	371.918	30.6(17)	1.3358(25) d
	411.49	22.3(12)	
¹²⁸ Ba	273.44	14.50(72)	2.43(5) d
¹²⁸ Cs	442.901	26.8(13)	3.62(2) min
	526.557	2.41(12)	
¹²⁷ Cs	411.95	62.9(31)	6.25(10) h
	124.7	11.38(22)	
¹²⁷ Xe	202.86	68.7(34)	36.4(1) d
	172.132	25.7(9)	
¹²⁶ Ba	233.6	19.6(18)	1.667(33) h
	257.6	7.6(7)	
¹²⁶ I	388.633	35.6(6)	12.93(5) d
	666.331	32.9(7)	
¹²⁵ Cs	112.0	8.60(43)	46.7(1) min
	712.0	3.50(18)	
¹²⁵ Xe	188.418	53.8(27)	16.9(2) h
	243.378	30.0(6)	
¹²³ Xe	148.9	48.9(24)	2.08(2) h
	1093.4	2.79(25)	
¹²³ I	158.97	83.3(42)	13.2234(19) h

TABLE XI: Principle γ -ray data for monitor foil products, from ENSDF [24, 30, 62–79]. Uncertainties are listed in the least significant digit, that is, 243.93(9) d means 243.93 ± 0.09 d.

Isotope	γ Energy (keV)	I_γ (%)	$T_{1/2}$
⁶⁵ Zn	1115.539	50.04(10)	243.93(9) d
⁶³ Zn	669.62	8.20(41)	38.47(5) min
	962.06	6.5(4)	
⁶² Zn	596.56	26.0(13)	9.26(2) h
	548.35	15.3(14)	
⁶¹ Cu	282.956	12.20(61)	3.333(5) h
	656.008	10.8(20)	
⁶⁰ Cu	1332.5	88.0(44)	23.7(4) min
	1791.6	45.4(23)	
⁶⁰ Co	1332.492	99.9826(6)	5.27113(38) y
	1173.228	99.85(3)	
⁵⁹ Fe	1099.245	56.5(18)	44.495(9) d
	1291.59	43.2(14)	
⁵⁸ Co	810.7593	99.4(50)	70.86(6) d
⁵⁷ Ni	1377.63	81.7(24)	1.4833(25) d
	127.164	16.7(5)	
⁵⁷ Co	122.06065	85.60(17)	271.74(6) d
	136.47356	10.68(8)	
⁵⁶ Ni	158.38	98.8(10)	6.075(10) d
	749.95	49.5(12)	
⁵⁶ Co	846.77	99.9(50)	77.233(27) d
	1238.288	66.46(12)	
⁵⁶ Mn	846.7638	98.8(49)	2.5789(1) h
	1810.726	26.9(4)	
⁵⁵ Co	931.1	75.0(38)	17.53(3) h
	477.2	20.2(17)	
⁵⁴ Mn	834.848	99.976(1)	312.05(4) d
⁵² Mn	1434.092	100.0(14)	5.591(3) d
	935.544	94.5(13)	
⁵¹ Cr	320.0824	9.91(1)	27.7010(11) d
⁴⁸ V	983.525	99.98(4)	15.9735(25) d
	1312.106	98.2(3)	
⁴⁸ Sc	1037.522	97.60(70)	1.8196(37) d
	175.361	7.48(10)	
⁴⁷ Sc	159.381	68.30(40)	3.34920(60) d
⁴⁶ Sc	1120.545	99.9870(10)	83.790(40) d
	889.277	99.9840(10)	
⁴⁴ Sc	1157.02	99.90(40)	3.970(40) h
^{44m} Sc	271.241	86.70(30)	2.4421(42) d
	1126.06	1.200(60)	
⁴³ K	372.76	86.8(43)	22.30(10) h
	617.49	79.20(60)	
⁴² K	1524.6	18.08(90)	12.360(12) h
²⁴ Na	1368.626	99.9936(15)	14.997(12) h
	2754.007	99.855(5)	
²² Na	1274.537	99.940(14)	2.6027(10) y